INSTABILITIES IN ROLL AND SLOT COATING FLOWS

by

Neil Daniels

Submitted in accordance with the requirements for the degree of

Doctor of Philosophy

The University of Leeds

Department of Applied Mathematics

December 1998

The candidate confirms that the work submitted is his own and that appropriate credit has been given where reference has been made to the work of others.

ABSTRACT

This thesis is concerned primarily with the investigation, both analytically and numerically, of instabilities in reverse- and forward-roll and slot coating flows. Consideration is restricted to Newtonian, incompressible fluids in the absence of inertial forces.

The onset of the ribbing instability in inlet flooded, reverse roll coating is examined first by applying linear stability theory to a base flow formulated using lubrication theory. Regions of instability are established and found to be in accord with experimental observation. These results are then compared with predictions from a stability hypothesis based on a two-dimensional force balance argument. This simple criterion shows that the effect of various parameters on the stability of the downstream free surface can be ascertained by examining their influence on the pressure gradient and meniscus location. The stability hypothesis is shown to underpredict the critical capillary number and so is only sufficient for predicting stability. Results are also compared to ones obtained numerically by applying linear stability theory to finite element solutions for the entire flow field, the principal difference being that the analytical approach overpredicts the critical capillary number for the onset of instability.

A variation of inlet flooded, reverse roll coating is then studied in which the nip is fed from above by a large reservoir of fluid (i.e. a hydrostatic head). The influence of this head on the base flow (obtained using lubrication theory) and its stability is then investigated.

An improved model of the dynamic contact line, developed by Shikhmurzaev [1993a] is described in which the dynamic contact angle is no longer kept constant, but is a function of various fluid and geometrical parameters. The limit of this theory for small capillary number is incorporated into the analytical model from which its effect on the base flow and stability is examined.

Instabilities in forward roll coating are then investigated. The inlet flooded case is studied using linear stability analysis, a stability hypothesis and the finite element method. As in reverse roll coating, the stability hypothesis at the downstream free surface is sufficient for predicting stability only. The finite element method, on the other hand, leads to solutions that are in close agreement with linear stability theory, unlike the reverse roll case.

Inlet starved forward roll coating is examined next and, as with the inlet flooded case, the ribbing instability can still manifest at the downstream free surface. The presence of an instability known as bead break, noted experimentally by Malone [1992] and Gaskell *et al* [1998], is verified analytically using linear stability theory. It is then shown that a stability hypothesis applied at the upstream free surface gives an accurate description of stability (unlike at the downstream free surface).

Finally, the slot coating geometry is explored. A geometrically flexible finite element code is described for which it is possible to use various lip shapes and a roll of variable radius and location (with respect to the slot). Initially, as has always been the case in previous work reported in the literature, the numerical mesh incorporates a downstream wetting line pinned at the lip edge and the effect of the various fluid and geometrical parameters on the resultant pressure profile and upstream meniscus location is examined. These numerical results are seen to compare favourably with predictions obtained analytically using a model based on lubrication theory.

However, Sartor [1990] showed that the downstream wetting line does not always remain pinned, but can climb up the die shoulder or regress into the coating gap. This has been confirmed experimentally by Kapur [1998] who also notes that ribs only appear when operating in the unpinned regime. Hence, the case in which the downstream, static contact line has retreated from the lip edge towards the inlet is studied. Pressure profiles and meniscus locations are compared with those for the case of a pinned downstream wetting line and the numerical linear stability analysis used to determine the effect of the fluid and geometrical parameters on the stability of the downstream free surface.

PUBLICATIONS

DANIELS, N., GASKELL, P.H., SAVAGE, M.D., "The ribbing instability in reverse roll coating", Proceedings of the Second European Coating Symposium, Strasbourg, France (Ed. Bourgin, P.), pp.102-111 [1997]

This thesis is dedicated to my Father, Cedric

ACKNOWLEDGEMENTS

Firstly, I would like to thank my supervisors, Prof. M.D. Savage and Prof. P.H. Gaskell for their advice and encouragement over the last four years. Special thanks also to Dr. M. Wilson and Dr. H.M. Thompson for sharing their numerical know-how and many useful discussions and to all my other colleagues in the Coating group.

I would like to thank all my friends in the Maths Department and bridge club for making my time in Leeds so enjoyable, especially Abi, Andy, Chris, Dom, Geoff, Graham, Keith, Matt, Neil, Rich and most of all, Sarah.

Special thanks to my family, especially my parents, Elissa and Cecil, for their support and encouragement over the period of my research.

Finally, I gratefully acknowledge the financial support provided by E.P.S.R.C., Autotype International Ltd, Ilford Imaging Ltd and Felix Schoeller Ltd.

Contents

1 Introduction 1

1.1 Coating processes 2

1.2 Common features of coating processes 2

1.2.1 Free surfaces 2

1.2.2 Contact lines 5

1.3 Forward Roll coating 7

1.3.1 The inlet flooded regime 7

1.3.2 The moderately starved regime 12

1.3.3 The meniscus regime 12

1.4 Reverse roll coating 13

1.4.1 The inlet flooded regime 14

1.4.2 The meniscus regime 16

1.5 Slot coating 16

1.6 Stability of coating flows 19

1.6.1 The ribbing instability 20

1.6.2 The cascade instability 22

1.6.3 The bead break instability 24

1.7 Outline of this thesis 24

2 Methods 27

2.1 Galerkin finite element method 28

2.1.1 Introduction 28

2.1.2 Governing differential equations 30

2.1.3 Galerkin FE formulation 31

2.1.4 Free surfaces 33

2.1.5 Dynamic contact angles 35

2.1.6 Isoparametric mapping 37

2.1.7 Numerical Integration 40

2.1.8 Iterative technique 41
2.1.9 The frontal solution method 43
2.1.10 Post-processing 44
2.2 Linear stability analysis based on the FEM 46
2.2.1 Introduction 46
2.2.2 Formulation of the equations 46
2.2.3 Derivation of the Jacobian matrix 48
2.2.4 Derivation of the mass matrix 52
2.2.5 Inclusion of a dynamic contact line 53
2.2.6 Method of solution 54

3 Onset of the Ribbing Instability in Inlet Flooded Reverse Roll Coating 56
3.1 Introduction 57
3.1.1 Outline of this chapter 60
3.2 Analysis based on lubrication theory 62
3.2.1 Mathematical model 62
3.2.2 Method of solution 70
3.2.3 Discussion of Results 72
3.2.4 Comparison with the Stability Hypothesis (S.H.) 75
3.3 A computational approach 83
3.3.1 Numerical solution of the base flow 83
3.3.2 Stability of the FE base flow 87
3.4 The effect of a hydrostatic head 89
3.4.1 Mathematical model 90
3.4.2 Discussion of results 96
3.5 An improved model of the contact line region 101
3.5.1 A general model for the dynamic contact line region 101
3.5.2 Small capillary number asymptotics for the contact line 103
3.5.3 Effect of Shikhmurzaev's asymptotic theory on the base flow . . 106
3.5.4 Effect of Shikhmurzaev's asymptotic theory on the onset of ribbing 106
3.6 Conclusions 109

4 Instabilities in Forward Roll Coating 111
4.1 Introduction 112
4.1.1 Outline of this chapter 114
4.2 Inlet flooded case 119
4.2.1 Mathematical model 119

4.2.2 Method of solution 126
4.2.3 Discussion of results 127
4.2.4 Comparison with the Stability Hypothesis (S.H.) 129
4.2.5 Comparison with the computational approach 131
4.3 Inlet starved case 138
4.3.1 Mathematical Model 138
4.3.2 Discussion of results 147
4.3.3 Stability Hypothesis: downstream interface 152
4.3.4 Stability Hypothesis: upstream interface 153
4.3.5 Operability diagrams in the $Ca - H_i$ plane 155
4.4 Conclusions 161

5 Slot Coating **162**
5.1 Introduction 163
5.2 Base flow 170
5.2.1 Downstream pinned: computational approach 175
5.2.2 Downstream pinned: analytical approach 178
5.2.3 Downstream unpinned: computational approach 184
5.3 Finite element stability analysis 187
5.4 Conclusions 191

6 Conclusions **192**
6.1 General review 193
6.2 Suggestions for future work 196

A An examination of the force balance on a perturbed interface **198**

References **204**

List of Figures

1.1 Examples of self-metered coating processes. 3
1.2 Examples of pre-metered coating processes. 4
1.3 Different regimes of forward roll coating. 8
1.4 *(a)* Flow field identified by Taylor [1963]; *(b)* corresponding pressure profile. 9
1.5 Schematic of the flow structure in moderately starved, forward roll coating. 12
1.6 Schematic illustration of the flow field in *(a)* ultra-starved and *(b)* starved forward meniscus roll coating (Gaskell *et al* [1995]). 13
1.7 Different operating regimes of reverse roll coating. 14
1.8 Schematic illustration of the flow field in *(a)* ultra starved and *(b)* starved reverse meniscus roll coating (Richardson [1996]). 17
1.9 Schematic of single and multilayer slot coating. 18
1.10 Photograph of the ribbing instability (Dowson and Taylor [1979]). . . . 20
1.11 Schematic representation of the mechanism of the cascade instability (Coyle [1984]). 23

2.1 A fluid domain, Ω, with boundary $\partial\Omega$, as tessellated by finite elements. 31
2.2 The V6/P3 element, satisfying the LBB stability condition. 32
2.3 Parametrization of a free surface by the spine method. 34
2.4 Parametrization of a free surface using inter-dependent spines. 36
2.5 (a) A triangular element in global space. (b) The standard triangle, A_0, showing the local node numbering scheme and local coordinate system. . 37
2.6 Subtriangles used to define the area coordinates, L_i, of an interior point P. 38
2.7 Local node numbering of elements which have one side lying on a free surface. 39
2.8 Gauss points and corresponding weights in (a) a 4-point quadrature scheme for domain integrals, and (b) a 3-point scheme for boundary (line) integrals. 41

3.1 Schematic of an inlet flooded reverse roll coater. 58

3.2 Typical $Ca - S$ operability diagram for a given value of h_0/R showing a stable window of operation. 60
3.3 Pressure profiles for $Ca = 0.1$, $h_0/R = 0.01$ and various speed ratios. . . 67
3.4 Pressure profiles for $S = 0.5$, $h_0/R = 0.01$ and various capillary numbers. 67
3.5 Pressure profiles for $S = 0.5$, $Ca = 0.1$ and various h_0/R. 67
3.6 Film thickness predictions (H_2) against Speed ratio (S) for $h_0/R = 0.01$ with $Ca = 0.03$, 0.1. Note that both curves terminate at S^{lim} i.e. when the wetting line reaches the nip. 68
3.7 Schematic of the perturbed outflow region of an inlet flooded reverse roll coater. 69
3.8 Growth rate (Σ) against wavenumber (N) for various Ca with $h_0/R = 10^{-4}$ and $S = 0.5$. 74
3.9 Growth rate (Σ) against wavenumber (N) for various Ca with $h_0/R = 10^{-4}$ and $S = 0.595$. 74
3.10 Growth rate (Σ) against wavenumber (N) for various Ca with $h_0/R = 10^{-4}$ and $S = 0.597$. 74
3.11 Growth rate (Σ) against wavenumber (N) for various Ca with $h_0/R = 10^{-4}$ and $S = 0.61$. 74
3.12 Operability diagram in the $Ca - S$ plane for $h_0/R = 10^{-4}$. 76
3.13 Operability diagrams in the $Ca - S$ plane with varying h_0/R. 76
3.14 Graph of Ca^{max} against h_0/R, where stability is ensured if $Ca < Ca^{max}$. 77
3.15 Graph of S^{min} against h_0/R, where stability is ensured for $S > S^{min}$. . 77
3.16 Operability diagram in the $Ca - S$ plane for $h_0/R = 10^{-4}$ and various θ_d values. 78
3.17 Graph of $g(D, N = 0)$ against Ca for $h_0/R = 10^{-4}$ and $S = 0.500$. Stability is ensured (via the S.H.) if $g(D, N = 0) > 0$. 79
3.18 Operability diagram in the $Ca - S$ plane for $h_0/R = 10^{-4}$ for both the S.H. and ribbing analysis. 82
3.19 Operability diagram in the $Ca - S$ plane with varying h_0/R for both the S.H. and ribbing analysis. 82
3.20 Computational boundary conditions for the inlet flooded reverse roll coater. 84
3.21 Schematic of the grid used to tesselate the downstream region. Note that for clarity of presentation, the y-axis has been scaled and the mid-spines have been omitted. 85
3.22 Typical finite element solution showing (a) the grid with (b) corresponding streamlines. 87

3.23 A comparison of film thickness predictions (H_2) against speed ratio (S) obtained via the finite element method and lubrication theory for $Ca = 0.06$ and $R/h_0 = 85$. 88
3.24 Schematic of a reverse roll coater fed by a hydrostatic head. 90
3.25 Pressure profiles for $X_{head} = 0.50$, $Ca = 0.03$, $S = 0.50$, $h_0/R = 10^{-4}$ and various Stokes numbers. 95
3.26 Pressure profiles for $St = 0.02$, $Ca = 0.03$, $S = 0.50$, $h_0/R = 10^{-4}$ and various hydrostatic head heights. 95
3.27 Angular position of the wetting line, $\bar{\gamma}$, against X_{head} for $Ca = 0.03$, $S = 0.50$ and $h_0/R = 10^{-4}$ for four values of St. 97
3.28 Film thickness predictions (H_2) against X_{head} for $Ca = 0.03$, $S = 0.50$ and $h_0/R = 10^{-4}$ for four values of St. 97
3.29 Operability diagram in the $Ca - S$ plane showing the effect of increasing St for $X_{head} = 0.50$ and $h_0/R = 0.0005$. 99
3.30 Operability diagram in the $Ca - S$ plane showing the effect of varying X_{head} for $St = 0.02$ and $h_0/R = 0.0005$. 99
3.31 Operability diagram in the $Ca - S$ plane showing the effect of varying X_{head} for $St = 0.04$ and $h_0/R = 0.0005$. 100
3.32 Operability diagram in the $Ca - S$ plane showing the effect of varying X_{head} for $St = 0.06$ and $h_0/R = 0.0005$. 100
3.33 Schematic of the region of flow near the contact line. 103
3.34 Dependence of the dynamic contact angle, θ_d, with the capillary number based on the upper roll speed, SCa for $\theta_s = 10^o, 50^o, 90^o$. 105
3.35 Pressure profiles for $Ca = 0.05$, $S = 0.50$, $h_0/R = 0.01$ and various static contact angles. 107
3.36 Film thickness predictions (H_2) against speed ratio (S) for $Ca = 0.03$, $h_0/R = 0.01$ with three values of θ_s (the full lines); A comparison is shown with the previous model, $\theta_d = 90^o = constant$ (the dotted line). Note that all the curves terminate at S^{lim} i.e. when the wetting line reaches the nip. 107
3.37 Operability diagram in the $Ca - S$ plane for $h_0/R = 10^{-4}$ and three values of θ_s (the full lines). A comparison is shown with the previous model, $\theta_d = 90^o = constant$ (the dotted line). 108

4.1 Pictures of the steady state bead in forward meniscus coating, obtained by Gaskell *et al* [1998]. 115

4.2 Bead break in forward meniscus coating, where S has been stepped from $S = 1.05$ to $S = 1.08$ at $t = 0.0s$; Gaskell *et al* [1998]. 116
4.3 Schematic of an inlet flooded forward roll coater. 117
4.4 Schematic of an inlet starved forward roll coater. 118
4.5 Pressure profiles for $S = 1.00$ and $h_0/R = 0.001$ and various capillary numbers. 123
4.6 Pressure profiles for $Ca = 0.05$ and $h_0/R = 0.001$ and various speed ratios. 123
4.7 Pressure profiles for $S = 1.00$ and $Ca = 0.05$ and various h_0/R. 123
4.8 Schematic of the perturbed downstream meniscus region of the inlet flooded forward roll coater. 125
4.9 Growth rate (Σ) against wavenumber (N) for various Ca with $S = 1.00$ and $h_0/R = 0.001$. 128
4.10 Operability diagram in the $Ca - S$ plane for $h_0/R = 10^{-3}$. 130
4.11 Operability diagrams in the $Ca - S$ plane with varying h_0/R. 130
4.12 Schematic of the downstream meniscus region of an inlet flooded forward roll coater showing both the disturbed meniscus at $x = x_d + \epsilon$, and the original uniform meniscus at $x = x_d$. 131
4.13 Operability diagram in the $Ca - S$ plane for $h_0/R = 10^{-4}$ for both the S.H. and linear stability analysis. 132
4.14 Operability diagram in the $Ca - S$ plane with varying h_0/R for both the S.H. and linear stability analysis. 132
4.15 Computational boundary conditions for the downstream region of an inlet flooded forward roll coater. 133
4.16 Schematic of the finite element grid used to tessellate the downstream region of an inlet flooded forward roll coater. 134
4.17 Finite element grid used to form a numerical description of the base flow, together with typical streamlines. 136
4.18 A comparison of film thickness ratio (H_1/H_2) against speed ratio (S) obtained via the finite element method and lubrication theory for $Ca = 0.06$ and $h_0/R = 0.004$. 137
4.19 Pressure profiles for $h_0/R = 0.001$, $Ca = 0.10$, $S = 1.00$ and various H_i. 142
4.20 Pressure profiles for $h_0/R = 0.001$, $S = 1.00$, $H_i = 1.20$ and various Ca. 142
4.21 Pressure profiles for $h_0/R = 0.001$, $Ca = 0.10$, $H_i = 1.20$ and various S. 142
4.22 Pressure profiles for $Ca = 0.10$, $S = 1.00$, $H_i = 1.20$ and various h_0/R. . 142
4.23 Schematic of the forces acting on the perturbed upstream and downstream menisci in the $x - z$ plane. 144

4.24 Schematic of the perturbed inlet region of a starved forward roll coater. 145
4.25 Growth rate (Σ) against wavenumber (N) for various H_i with $h_0/R = 10^{-3}$, $Ca = 0.05$ and $S = 1.00$. 148
4.26 ϵ_u/ϵ_d against wavenumber (N) for various H_i with $h_0/R = 10^{-3}$, $Ca = 0.05$ and $S = 1.00$. 149
4.27 ϵ_u/ϵ_d against wavenumber (N) for further, various values of H_i with $h_0/R = 10^{-3}$, $Ca = 0.05$ and $S = 1.00$. 149
4.28 Growth rate (Σ) against wavenumber (N) for various H_i with $h_0/R = 10^{-3}$, $Ca = 0.01$ and $S = 1.00$. 151
4.29 ϵ_u/ϵ_d against wavenumber (N) for various H_i with $h_0/R = 10^{-3}$, $Ca = 0.01$ and $S = 1.00$. 151
4.30 Graph of $g_d(D, N = 0)$ against H_i (with its surface tension (A) and pressure gradient (B) components) for $h_0/R = 10^{-3}$, $Ca = 0.05$ and $S = 1.00$. 153
4.31 Graph of $g_u(U, N = 0)$ against H_i for $h_0/R = 10^{-3}$, $Ca = 0.01$ and $S = 1.00$, where stability is ensured (via the S.H.) if $g_u(U, N = 0) < 0$. . 156
4.32 Graph of $g_u(U, N = 0)$ against Ca for $h_0/R = 10^{-3}$, $H_i = 0.35$ and $S = 1.00$, where stability is ensured (via the S.H.) if $g_u(U, N = 0) < 0$. . 156
4.33 Graph of $g_u(U, N = 0)$ against S for $h_0/R = 10^{-3}$, $H_i = 0.35$ and $Ca = 0.01$, where stability is ensured (via the S.H.) if $g_u(U, N = 0) < 0$. 156
4.34 Operability diagram in the $Ca - H_i$ plane for $S = 0.50$ and $h_0/R = 0.001$. 158
4.35 Operability diagram in the $Ca - H_i$ plane for $S = 1.00$ and $h_0/R = 0.001$. 158
4.36 Operability diagram in the $Ca - H_i$ plane for $S = 1.50$ and $h_0/R = 0.001$. 158
4.37 Operability diagram in the $Ca - H_i$ plane for $S = 1.00$ and $h_0/R = 0.005$. 159
4.38 Operability diagram in the $Ca - H_i$ plane for $S = 1.00$ and $h_0/R = 0.001$. 159
4.39 Operability diagram in the $Ca - H_i$ plane for $S = 1.00$ and $h_0/R = 0.0002$. 159
4.40 Operability diagram in the $Ca - H_i$ plane for $S = 1.00$ and $h_0/R = 0.001$ obtained using both a linear stability analysis (L.S.A.) and stability hypothesis (S.H.). 160

5.1 Main features of a slot coater. 163
5.2 Various possible positions of the downstream static wetting line. 164
5.3 Influence of the flow rate on the shape of the coating bead. The flow rate is increasing from (a) to (f) (Durst and Wagner [1997]). 165
5.4 Coating window and flow instabilities for variable vacuum pressure, web speed and film thickness (Sartor [1990]). 166

5.5 Various die designs of the slot coater. Figures (a), (b) and (c) are from Kageyama and Yoshida [1986]. Figures (d) and (e) are from O'Brien [1984] and figure (f) is from Aitken [1964]. 167
5.6 Schematic of a slot coater with variable geometry. 170
5.7 Computational boundary conditions for the slot coater. 171
5.8 Schematic of the grid employed by Silliman and Scriven [1980] to tessellate the downstream region of a slot coater. Note that, for the sake of clarity, the mid-spines have been omitted. 172
5.9 Schematic of the grid used to tessellate the slot coater. Note that for clarity the mid-spines have been omitted. 173
5.10 Finite element grid containing 1711 nodes and 776 elements. 174
5.11 Possible flow structures in slot coating (Sartor [1990]). 175
5.12 Typical streamlines obtained using an FE grid with 1711 nodes. Flow conditions: (a) $Ca = 0.05$, $\lambda = 0.40$, $pb = -50.0$, $\alpha = \beta = \gamma = 0.0$, $H_2 = 1.00$, $X_d = 5.00$, $H_i = 1.00$, $X_c = 0.00$ and $R = 10^8$; (b) as (a) with $\lambda = 0.25$; (c) as (a) with $H_i = 2.50$; (d) as (c) with $\lambda = 0.24$; (e) as (b) with $\alpha = 0.10$, $\beta = -0.05$ and $\gamma = 0.15$; (f) as (b) with $R = 200.0$ and $H_2 = 1.50$. 177
5.13 Pressure profiles for $\alpha = 0.00$, $Ca = 0.05$, $XM_d = 4.50$, $pb = -50.0$, $H_2 = 1.0$ and various λ. 179
5.14 Pressure profiles for $\lambda = 0.50$, $Ca = 0.05$, $XM_d = 4.50$, $pb = -50.0$, $H_2 = 1.0$ and various α. 179
5.15 Pressure profiles for $\alpha = 0.05$, $\lambda = 0.50$, $Ca = 0.05$, $pb = -50.0$, $H_2 = 1.0$ and various XM_d. 179
5.16 Dynamic wetting line x-location against capillary number (Ca) for $\alpha = 0.00$, $\lambda = 0.50$, $XM_d = 4.50$, $pb = -50.0$ and $H_2 = 1.0$. 180
5.17 Dynamic wetting line x-location against back pressure (pb) for $\alpha = 0.00$, $\lambda = 0.50$, $Ca = 0.05$, $XM_d = 4.50$ and $H_2 = 1.0$. 180
5.18 Dynamic wetting line x-location against H_2 for $\alpha = 0.00$, $\lambda = 0.50$, $Ca = 0.05$, $XM_d = 4.50$ and $pb = -50.0$. 180
5.19 Comparison of pressure profiles predicted using lubrication theory with like results obtained using the FE method. 184
5.20 Pressure profiles for $\alpha = 0.0575$, $Ca = 0.05$, $\phi = 145.0°$, $pb = -50.0$, $H_2 = 1.00$ and various λ. 186
5.21 Pressure profiles for $\lambda = 0.60$, $Ca = 0.05$, $\phi = 145.0°$, $pb = -50.0$, $H_2 = 1.00$ and various α. 186

5.22 Pressure profiles for $\alpha = 0.05$, $\lambda = 0.60$, $\phi = 145.0°$, $pb = -50.0$, $H_2 = 1.00$ and various Ca. 186
5.23 Pressure profiles for $\alpha = 0.05$, $\lambda = 0.60$, $Ca = 0.05$, $pb = -50.0$, $H_2 = 1.00$ and various ϕ. 186
5.24 Growth rate (eigenvalue) against wavenumber for various λ with $\alpha = 0.0575$, $Ca = 0.05$ $\phi = 145°$, $pb = -50.0$ and $H_2 = 1.00$. 189
5.25 Growth rate (eigenvalue) against wavenumber for various α with $\lambda = 0.60$, $Ca = 0.05$ $\phi = 145.0°$, $pb = -50.0$ and $H_2 = 1.00$. 189
5.26 Growth rate (eigenvalue) against wavenumber for various ϕ with $\lambda = 0.60$, $\alpha = 0.0575$, $Ca = 0.05$, $pb = -50.0$ and $H_2 = 1.00$. 190
5.27 Growth rate (eigenvalue) against wavenumber for various Ca with $\lambda = 0.60$, $\alpha = 0.05$ $\phi = 145.0°$, $pb = -50.0$ and $H_2 = 1.00$. 190

A.1 Solution for the perturbed flow, showing Σ, $g(D)$ and $g'(D)$ against wavenumber (N) for $h_0/R = 10^{-4}$, $Ca = 0.01$ and $S = 0.5$. 201
A.2 Solution for the perturbed flow, showing Σ, $g(D)$ and $g'(D)$ against wavenumber (N) for $h_0/R = 10^{-4}$, $Ca = 0.0193$ and $S = 0.5$. 201
A.3 Solution for the perturbed flow, showing Σ, $g(D)$ and $g'(D)$ against wavenumber (N) for $h_0/R = 10^{-4}$, $Ca = 0.0260$ and $S = 0.5$. 202
A.4 Solution for the perturbed flow, showing Σ, $g(D)$ and $g'(D)$ against wavenumber (N) for $h_0/R = 10^{-4}$, $Ca = 0.00342$ and $S = 0.5$. 202
A.5 Solution for the perturbed flow, showing Σ, $g(D)$ and $g'(D)$ against wavenumber (N) for $h_0/R = 10^{-4}$, $Ca = 0.05$ and $S = 0.5$. 203

NOMENCLATURE

Most of the symbols used in this thesis have different meanings in different chapters and so are not listed here, but introduced and defined later. Below are listed those symbols which have a general meaning, although their specific definitions depend on the context.

Ca	Capillary number
Ca^{max}	Critical Ca below which no ribs occur (for any S)
$Ca*$	Critical capillary number marking the onset of instability
n	Wavenumber
N	Dimensionless wavenumber
p	Liquid pressure
P	Dimensionless liquid pressure
Re	Reynolds number
S	Speed ratio
S^{min}	Critical S above which no ribs occur (for any Ca)
St	Stokes number
u, v, w	Velocity components
U, V, W	Dimensionless velocity components
x, y, z	Cartesian components
X, Y, Z	Dimensionless cartesian components
μ	Dynamic viscosity
ν	Kinematic viscosity
ρ	Density
σ	Eigenvalue
Σ	Dimensionless eigenvalue

Chapter 1

Introduction

Contents

1.1 Coating processes 2
1.2 Common features of coating processes 2
1.2.1 Free surfaces 2
1.2.2 Contact lines 5
1.3 Forward Roll coating 7
1.3.1 The inlet flooded regime 7
1.3.2 The moderately starved regime 12
1.3.3 The meniscus regime 12
1.4 Reverse roll coating 13
1.4.1 The inlet flooded regime 14
1.4.2 The meniscus regime 16
1.5 Slot coating 16
1.6 Stability of coating flows 19
1.6.1 The ribbing instability 20
1.6.2 The cascade instability 22
1.6.3 The bead break instability 24
1.7 Outline of this thesis 24

1.1 Coating processes

Coating is a process by which a continuous, thin film of liquid is deposited onto a moving substrate. A gas (usually air) is replaced by a liquid prior to drying or solidification. Such processes are considered successful if the liquid film produced is of uniform thickness and free from any imperfections. Coating flows are important in a wide range of industries, for example in the manufacture of food packaging, adhesive tapes and photographic film. All the industries are subject to economic driving forces which demand high operating speeds.

Coating devices can be categorised into two classes: *self-metering* and *pre-metering*. Self-metered coaters are those in which the amount of fluid applied to the substrate depends on the properties of the fluid and the geometry and operating conditions of the coater. Examples of common self-metered coaters are forward, reverse and dip coating (see figure 1.1). Alternatively, pre-metered coaters are those in which the amount of fluid applied to the substrate is controlled directly by the operator; all fluid entering the system is deposited on the substrate allowing the coated film thickness to be controlled to within precise limits. These coaters also have the capability to produce multi-layer films by the simultaneous deposition of more than one liquid. Examples of common pre-metered coaters are slot, slide and curtain coaters (see figure 1.2).

1.2 Common features of coating processes

All coating flows share common features, two of which being a liquid-gas interface (commonly referred to as a *free surface* or *meniscus*) and a contact line. Both these features are discussed below.

1.2.1 Free surfaces

Interfaces are very thin layers across which the density varies rapidly from that of the bulk liquid to that of the bulk gas. These steep density gradients, which are effectively discontinuities, give rise to the property known as *surface tension*, which produces an isotropic capillary stress within the meniscus. However, since the interfacial layers are negligibly thin (compared to macroscopic length scales) they are conveniently approximated as mathematical surfaces with zero-thickness.

The presence of one or more free surfaces greatly complicates the theoretical analysis

(a) Forward roll coater

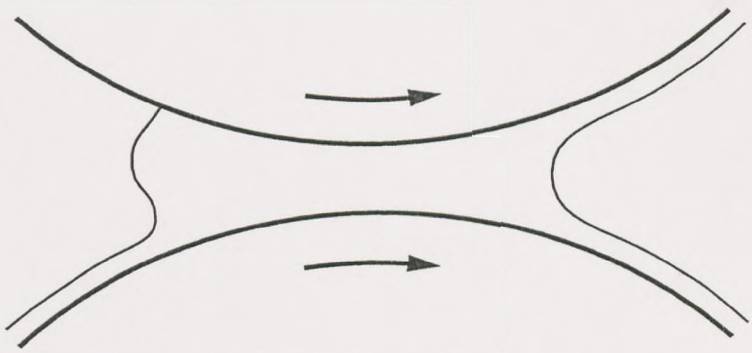

(b) Reverse roll coater

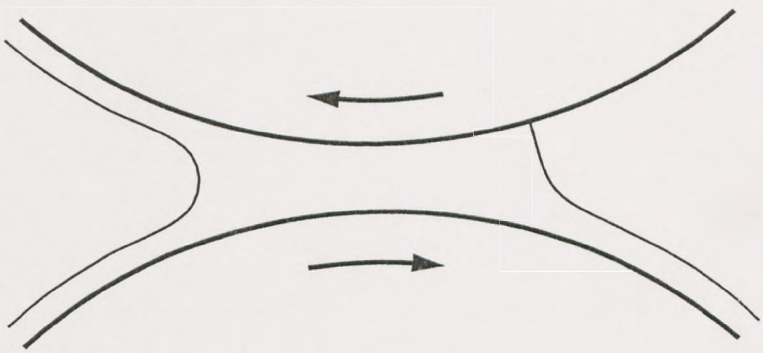

(c) Dip coater

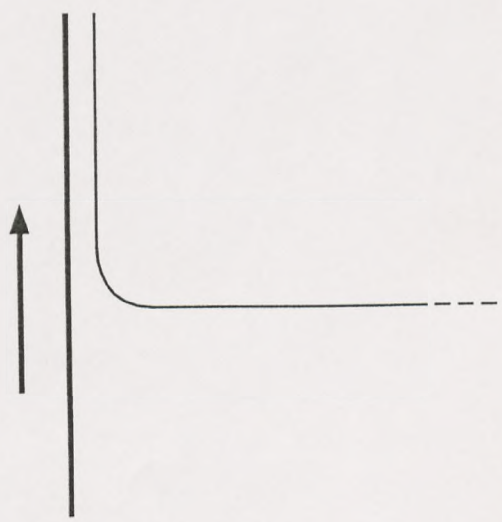

Figure 1.1: Examples of self-metered coating processes.

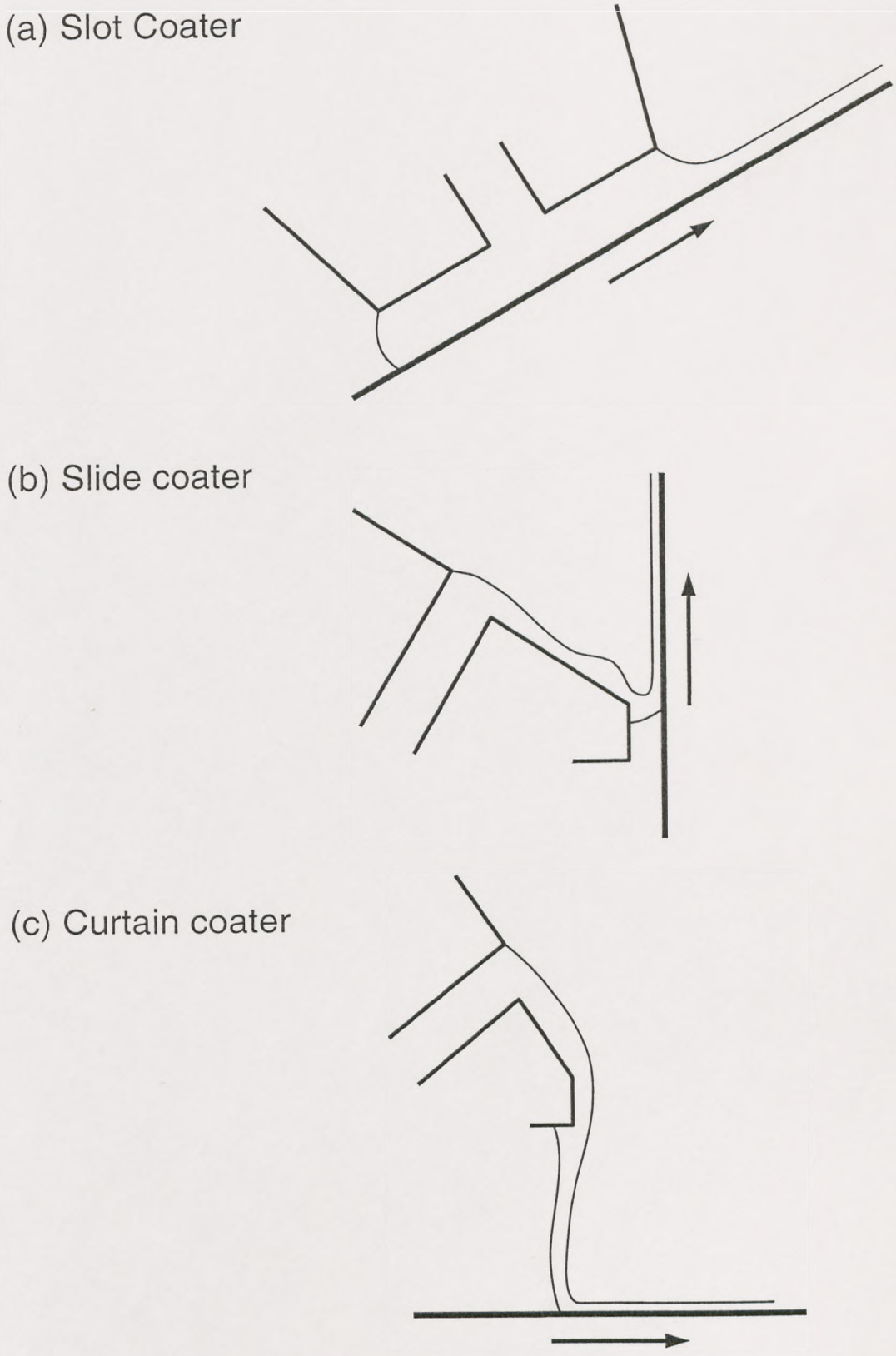

Figure 1.2: Examples of pre-metered coating processes.

of coating flows as their location and thus the extent of the fluid domain are unknown *a priori*. Further, the curvature of a free surface is important and can substantially change as the operating parameters are varied. Such difficulties can be overcome by the use of computational methods (see chapter 2) or alternatively by approximating the meniscus by a simple shape, such as the arc of a circle (see chapters 3, 4 and 5).

1.2.2 Contact lines

Since the aim of all coating processes is to replace the gas at a solid surface by a layer of liquid, at some stage of the process the three phases must meet. This *contact line* can be of two types:

1. a *static contact line*, which is stationary relative to the solid surface, or
2. a *dynamic contact*, or *wetting line*, which moves relative to the solid surface

Despite their practical importance, much is still unknown about the physics of contact lines, though recent advances have been made by Shikhmurzaev [1993a,1993b,1994,1996].

On the scale of macroscopic flows, the liquid-gas interface appears to intersect the solid surface at a well defined angle, θ_c, measured through the liquid and termed the *apparent* contact angle. The advancing contact line (i.e. the motion by which a liquid displaces a gas from a solid surface) has attracted considerable attention from both theoreticians and experimentalists, who have noted a number of features associated with this phenomenon:

- The nature of the spreading of liquids over the surface is rolling (see Dussan and Davis [1974]) i.e. in a finite time, material points which are initially located on the meniscus arrive at the solid surface. Note, however, recent work by Savelski *et al* [1995] suggests that this is not always the case (see chapter 3).

- The apparent dynamic contact angle grows from the static value, θ_c, to some limiting value, θ_{max}, as the speed of the solid surface increases (Schwartz and Tejada [1972], Burley and Kennedy [1976], Gutoff and Kendrick [1982]). The value of θ_{max} depends on the contacting media (Schwartz and Tejada [1972]) and although for most systems it is 180° (Burley and Kennedy [1976]), for some it is considerably less (Elliot and Riddifold [1967]).

- At very low contact line speeds, less than $U = U_c$ say, the motion of the contact line is unsteady and spasmodic, often referred to as *slip stick*. At contact line

speeds greater than U_c, the contact line speed is very smooth (Dussan and Davis [1974]).

- At a certain line speed, which depends on the materials of the system, an instability of the contact line motion occurs. The contact line takes on a *sawtooth* form and bubbles begin to entrain in the fluid, clearly an undesirable effect which can seriously impair the quality of the final coated layer (Burley and Kennedy [1976], Blake and Ruschak [1979], Gutoff and Kendrick [1982], Burley and Jolley [1984]).

Local analysis in the neighbourhood of a static contact line reveals a stress singularity which is inversely proportional to the square root of the distance from the line (Richardson [1970]). This singularity is integrable i.e. the total shear force on the solid boundary remains bounded. Further, Silliman and Scriven [1980] showed, by means of a finite element method, that the usual no-slip condition on velocity at the solid surface was adequate for flows near static contact lines. On the other hand, for flows which include a dynamic contact line, the classical formulation of the problem (Moffatt [1964], Huh and Scriven [1971]) gives rise to a non-integrable shear stress singularity i.e. to an infinite force exerted by the fluid on the solid. Such singularities are a result of the velocity at the wetting line being multi-valued i.e. dependent on the direction from which one approaches the wetting line.

To incorporate a dynamic wetting line into a mathematical model, the usual approach is to allow slip in the region close to it. This removes the singularity, but has several drawbacks, including:

- the actual *rolling* type motion for the liquid is replaced by a *sliding* motion such that the contact line always consists of the same material points, thereby changing the qualitative nature of the fluid flow (see, for example, Shikhmurzaev [1993a]).

- the dependence of the dynamic contact angle on the hydrodynamic and geometrical parameters cannot be determined from this approach and, as in the classical approach (Moffatt [1964]), must be specified. Clearly this method cannot incorporate the features associated with the contact angle which were found experimentally (see above).

- an unknown slip length must be introduced measuring the distance from the contact line over which slip occurs. Dussan [1976] investigated the effects of using different slip models and concluded that while the flow fields on the slip length scale are quite different, the global flow field is unchanged.

A more rigorous treatment of the flow near a wetting line requires a knowledge of the 'fundamental physics' at hand. Recent work by Shikhmurzaev [1993a,1993b,1994,1996] sheds new light on the mathematical modelling of wetting lines by introducing the concept of *surface tension gradients* near the contact line, which the flow itself gives rise to. Unfortunately, his analysis introduces several physical parameters which are difficult to measure experimentally, but has the significant advantage of being able to determine the contact angle and slip length as part of the solution. This model has yet to be incorporated into any numerical code, perhaps due to its complexity, although it is possible to use the asymptotic theory for small capillary number (see Shikhmurzaev [1993a,1994,1996], Summers, Gaskell, Thompson and Savage [1998] and chapter 3).

In sections, 1.3-1.5, three specific coating processes are examined in detail, namely forward, reverse and slot coating.

1.3 Forward Roll coating

Figure 1.3 shows the three possible coating regimes in forward roll coating (see Malone [1992]) which are identified below.

1. The *inlet flooded* regime refers to conditions where the fluid extends far upstream of the nip, the flow rate through which is controlled only by the physical properties of the coater and the fluid. There is a *rolling bank* of fluid far upstream of the nip, where excess liquid runs back over the incoming film (Schneider [1962]).

2. As the inlet flux is reduced, the rolling bank diminishes and disappears as the upstream free surface advances into the nip. This is commonly referred to as the *moderately starved* regime and the thickness of the inlet film is of the order of the minimum gap between the cylinders.

3. By reducing the inlet flux further still, the *meniscus* or *ultra starved* regime is entered where the thickness of the inlet film is much less than the roll separation. The upstream free surface is now located close to the nip.

1.3.1 The inlet flooded regime

Sometimes termed the fully-flooded case, this regime has been thoroughly investigated using experimental, analytical and computational techniques. Taylor [1963] suggested that the flow divides into two regions, one being a 2-dimensional region of recirculating fluid in the immediate vicinity of the downstream meniscus and the other an area

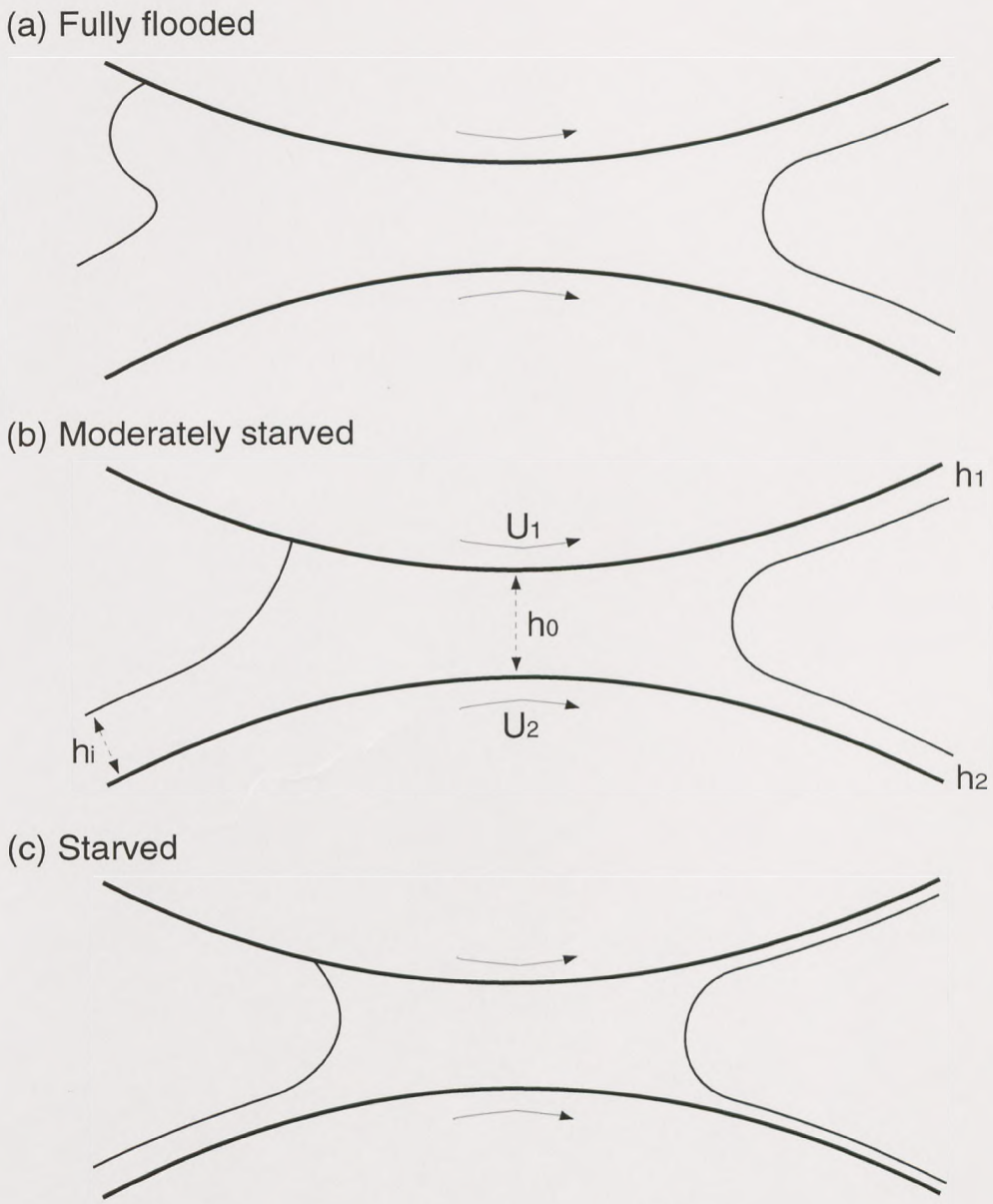

Figure 1.3: Different regimes of forward roll coating.

of almost rectilinear flow further upstream, see figure 1.4. These observations have been confirmed experimentally by Schneider [1962] and Malone [1992]. Upstream of the minimum gap, the geometry is convergent causing a large positive pressure, whereas downstream, the diverging gap results in a sub-ambient pressure which then relaxes through the recirculation region to capillary pressure at the meniscus.

Since the gap between the rolls is small and slowly varying and the flow in the middle of the domain is approximately unidirectional, mathematical models have been developed

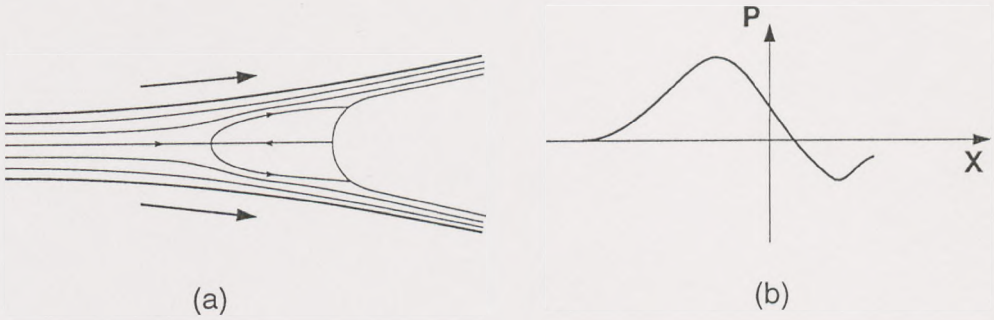

Figure 1.4: *(a)* Flow field identified by Taylor [1963]; *(b)* corresponding pressure profile.

based on the Reynolds lubrication equation,

$$\frac{\partial}{\partial x}\left[h^3(x)\frac{\partial p}{\partial x}\right] = 12\mu\bar{U}\frac{dh}{dx}, \tag{1.1}$$

where p is the pressure, $h(x)$ the gap between the rolls, μ the viscosity of the liquid and $\bar{U} = \frac{1}{2}(U_1 + U_2)$ the average roll speed (see Savage [1984]). Equation (1.1) is solved for the pressure distribution by specifying conditions on pressure or its gradient at the boundaries. In an inlet-flooded roll coater, the upstream meniscus lies far upstream of the nip and so one boundary condition is that the pressure tends to its ambient value, p_a, there i.e.

$$p(-\infty) = p_a. \tag{1.2}$$

A second pressure condition is supplied by the balance of ambient, surface tension and liquid pressures at the meniscus (see Batchelor [1967]),

$$p(x = d) = -\frac{T}{r_d} + p_a, \tag{1.3}$$

where $x = d$ and r_d are the location and radius of curvature of the downstream meniscus respectively and T is the surface tension of the liquid. Note that conditions (1.2) and (1.3) can be simplified by arbitrarily defining $p_a = 0$.

Since the location of the meniscus is unknown, another boundary condition is required. One such condition comes from Reynolds [1886] assumption that the pressure and its gradient vanish at the meniscus, i.e.

$$p(x = d) = \left.\frac{\partial p}{\partial x}\right|_{x=d} = 0. \tag{1.4}$$

This is also referred to as the *Swift-Steiber* conditions following the independent work by Swift [1931] and Steiber [1933]. However, this condition is unable to predict the sub-ambient pressure loop. Hopkins [1957] suggested that since the domain of applicability

of (1.1) terminates at the first stagnation point, the boundary conditions should be imposed there. He proposed that for equal roll speeds, velocity and shear stress are zero at this point i.e.

$$u = \frac{\partial u}{\partial y} = 0. \tag{1.5}$$

This *separation* condition is usually applied in conjunction with the additional assumption that the fluid pressure is constant throughout the reverse flow region and predicts the sub-ambient pressure loop seen experimentally. Birkoff and Hays [1963] referred to (1.5) as the *Prandtl-Hopkins* condition in recognition of Prandtl's similar work in the field of boundary layer separation.

Coyne and Elrod [1970,1971] considered the case of a film separating away from a stationary flat plate and being drawn by a nearby parallel moving plate. By assuming a quadratic velocity profile normal to the free surface and plug flow in the outflow boundary, they derived the following expression for the pressure gradient at the free surface by matching the inlet and outlet fluxes,

$$\frac{\partial p}{\partial x} = \frac{6\mu U}{h_d^2}\left[1 - \frac{2h_\infty}{h_d}\right], \tag{1.6}$$

where h_d is the height of the gap at the wetting line and h_∞ is the film thickness at the outflow boundary. They then used this condition to solve Reynolds equation for the pressure in the two roll problem and obtained good agreement with experimental observations for the location of the meniscus.

Experimental, computational and analytical predictions for the film split ratio, h_1/h_2 (where h_1 and h_2 are the final film thicknesses on the upper and lower rolls respectively), have been obtained by several authors. Benkreira, Edwards and Wilkinson [1981] found with their sets of rollers that h_1/h_2 is largely independent of the roll radii ratio but strongly dependent on the speed ratio, $S = U_1/U_2$, and summarised their results in the form

$$\frac{h_1}{h_2} = 0.87S^{0.65} \quad 0.03 \leq S \leq 14.9. \tag{1.7}$$

In general agreement, Coyle [1984] and Coyle *et al* [1986] found that their computational results, which neglect gravity, could be fitted by

$$\frac{h_1}{h_2} = S^{0.65} \quad 0.1 \leq S \leq 10.0. \tag{1.8}$$

Ruschak [1985] modelled the roll surfaces as flat plates (i.e. $h_0/R \ll 1$) and, by using viscous lifting theory, derived the expression

$$\frac{h_1}{h_2} = S^{\frac{2}{3}}, \tag{1.9}$$

which he showed to be valid as $Ca \to 0$, where $Ca = \mu U/T$ is the capillary number. For higher values of Ca he showed that the expression could be written in the approximate form

$$\frac{h_1}{h_2} = S^{\frac{1}{2}}, \tag{1.10}$$

which is identical to the form predicted by Savage [1982], who used a *separation* model. The discrepancy between the above power law indices led Savage [1992] and Gaskell, Savage and Thompson [1998] to question the applicability of these conditions when $S \neq 0$ or 1. They calculated the 2-dimensional velocity field to $O(h_0/R)^{\frac{1}{2}}$ and the condition $U = V = 0$ was used to locate the downstream stagnation point, resulting in the algebraic expression

$$\frac{h_1}{h_2} = \frac{S(S+3)}{1+3S}, \tag{1.11}$$

which is in close agreement with experimental results for $1 < S < 10$.

Note that the analytical models based on lubrication theory assume unidirectional flow and so cannot predict the 2-dimensional flow near the downstream meniscus. This has led to the introduction of powerful numerical techniques in order to obtain a more accurate representation of the flow field (see chapter 2).

Using the finite element method, Coyle *et al* [1986] showed that for $S \neq 1$, some fluid is transferred from the slower to faster moving roll by means of a weak asymmetric jet. The existence of such a jet was confirmed experimentally by Lodge [1994] and then analytically by Gaskell *et al* [1996] (using 2-dimensional flow analysis).

Experiments performed by Rees [1993] show that under certain operating conditions, a weak asymmetric jet can transfer fluid from the upper to lower roll, even when $S = 1$. The existence of such a jet was attributed to gravity and was later verified numerically by Walker [1995]. Walker [1995] also found that with the rolls vertically aligned, gravity can have a significant effect on the film split ratio at low S, in agreement with Benkreira *et al* [1981], Decre *et al* [1995] and Gaskell, Lodge and Savage [1996]. Walker also investigated the behaviour of flows with unequal roll radii.

1.3.2 The moderately starved regime

Reducing the supply of liquid to the nip such that the rolling bank of fluid disappears results in the *moderately starved* regime. The first experimental study of this regime was performed by Malone [1992]. Gaskell, Summers, Savage and Thompson [1995] used the finite element method to show that this regime is characterised by two regions of recirculating flow near the free surfaces, separated by a region of quasi-unidirectional flow, see figure 1.5.

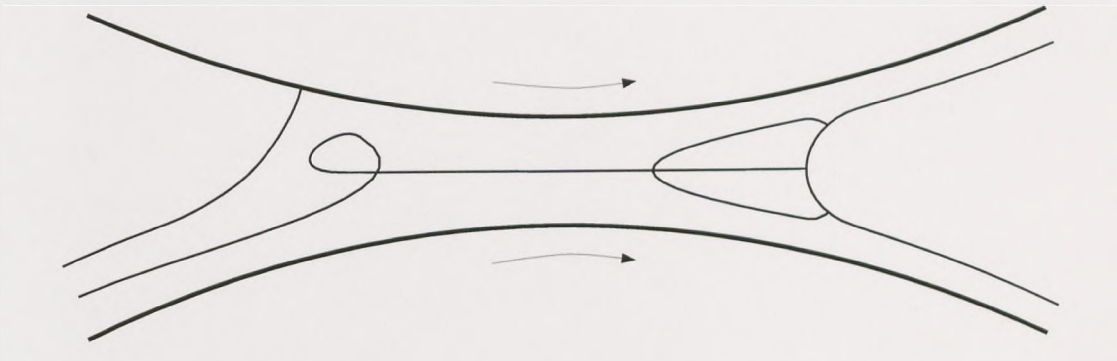

Figure 1.5: Schematic of the flow structure in moderately starved, forward roll coating.

1.3.3 The meniscus regime

Although this regime has been operated in by industry for many years (see Gaskell *et al* [1995]), it was not investigated until recently. Malone [1992] examined the flow experimentally and noted that the flow structure is vastly different from that of the inlet flooded and moderately starved cases. Indeed, he found that the flow domain consists of a small bead of liquid which contains two recirculations. Thompson [1992] formulated a boundary value problem to model this flow by neglecting the flux through the bead, which was modelled as a rectangular domain by approximating the rolls as horizontal planes and the menisci as vertical stress-free planes. The streamlines obtained using this *zero flux model* were similar to those seen by Malone [1992].

Gaskell *et al* [1995] solved the full problem both numerically, using the finite element method, and analytically, using lubrication theory in conjunction with viscous lifting theory and arc of circle approximations for the menisci. Predictions for the pressure profile and film split ratio obtained using the lubrication model were seen to have good agreement with numerical solutions. The model was also able to predict critical flow rates at which the flow structure changed. Their numerical solutions revealed that when using starved inlets, liquid could be transferred from the lower to upper roll by means of

a *primary* and/or *secondary* transfer jet, as shown in figure 1.6. However, the flux could be reduced to an *ultra starved* regime such that only a primary transfer jet existed. Note that above a critical value of flux only the secondary transfer jet is present (see figure 1.5).

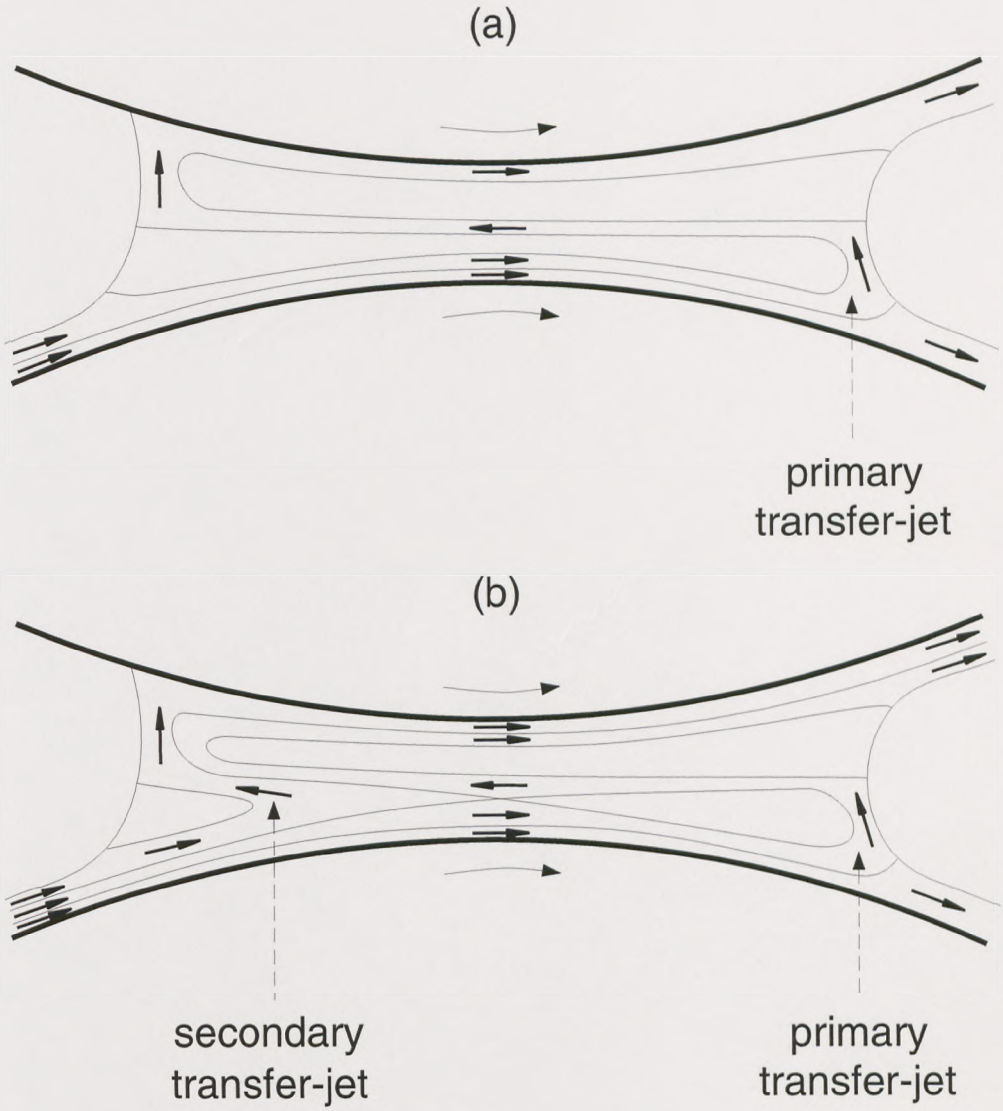

Figure 1.6: Schematic illustration of the flow field in *(a)* ultra-starved and *(b)* starved forward meniscus roll coating (Gaskell *et al* [1995]).

1.4 Reverse roll coating

Reverse roll coating, involving the flow in the narrow gap between two co-rotating cylinders, has not received quite the same attention as the forward case. Experiments by Gaskell, Innes and Savage [1996] showed that a moderately starved regime does not

exist in reverse roll coating. Thus, the only two modes of operation are the inlet flooded and meniscus regimes (see figure 1.7).

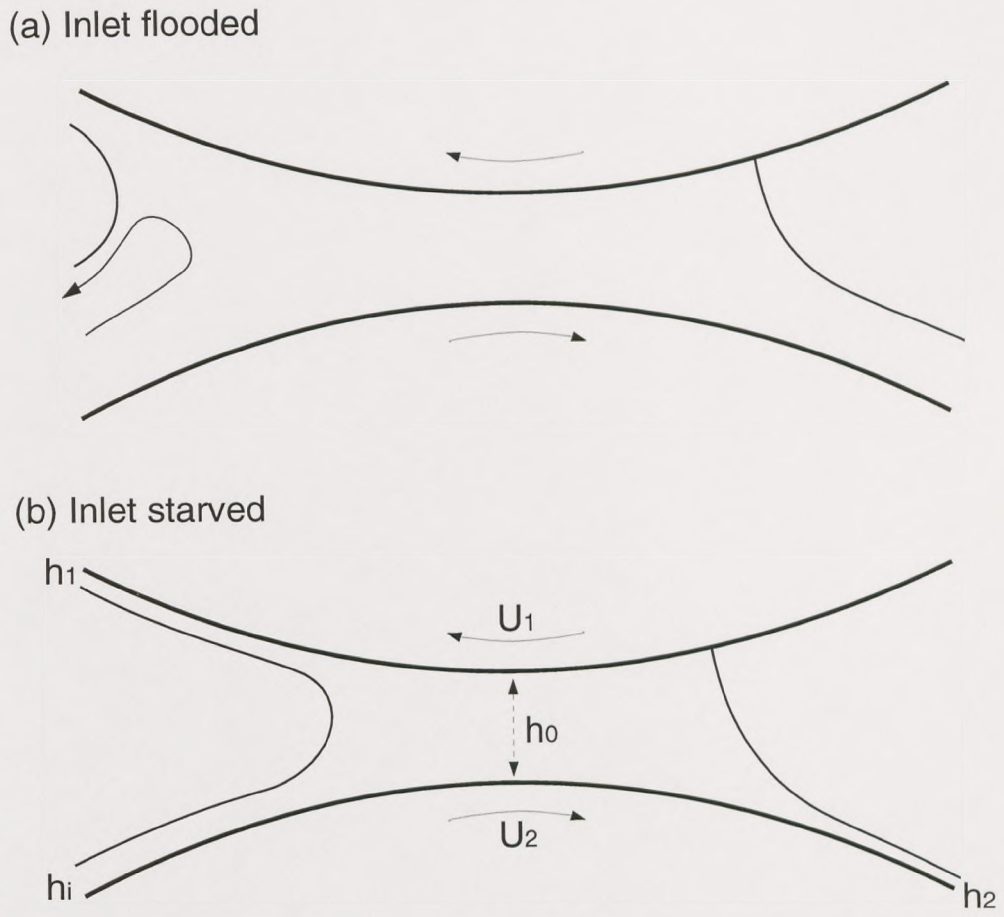

Figure 1.7: Different operating regimes of reverse roll coating.

1.4.1 The inlet flooded regime

Several mathematical studies have been made using lubrication theory to describe inlet flooded reverse roll coating (see Cheng and Savage [1978], Ho and Holland [1978] and Greener and Middleman [1981]) - all these models predict a simple linear relationship between the dimensionless downstream film thickness, H_2, and speed ratio, S,

$$H_2 = \frac{h_2}{h_0} = K(1 - S), \tag{1.12}$$

where $0.615 \leq K \leq 0.665$, depending on the boundary conditions chosen to solve (1.1). Note that this relationship predicts negative film thicknesses if $S > 1$ and so such models are only valid if $S \leq 1$.

Ho and Holland [1978] assumed that the downstream film is carried off by a horizontal web which meets the lower roll tangentially at the nip, at which point the pressure is zero. This led to the coefficient $K = 2/3$, which is identical to the case when the rolls are fully submerged. Using the Reynolds condition (1.4) gives $K = 0.613$ (see Coyle [1984], Greener and Middleman [1981]) although, as with the forward case, this model is unable to predict a sub-ambient pressure loop. Alternatively, applying the Prandtl-Hopkins conditions, equation (1.5), yields $K = 0.652$ and a sub-ambient pressure loop is then predicted.

Experimental data by Coyle [1984] demonstrated that models based on lubrication theory only predict H_2 accurately at low values of speed ratio. He also showed that H_2 is highly dependent on Ca, a relationship not seen via (1.12), although agreement with lubrication models improves as Ca decreases - this is because as Ca decreases the meniscus moves away from the nip, thus increasing the range of values of S over which the lubrication models may be applied.

Fukazawa, Benjamin and Scriven [1992] realised that, by extending the lubrication model to incorporate more realistic boundary conditions at the downstream meniscus, the film thickness prediction could be improved and so they modelled the downstream meniscus using an arc of circle approximation and applied the Landau-Levich [1942] expression (see chapter 3) at the downstream outlet. However, their analytical results are only valid for small Ca.

Coyle [1984], Coyle, Macosko and Scriven [1990a], Fukazawa *et al* [1992] and Richardson [1996] all obtained numerical solutions, using the finite element method, which are in broad agreement with experiment. Grald, Chakrabarti and Subbiah [1994] examined the flow using a spectral element approach and their results are in accord with those of Coyle *et al* [1990a], which show that as S increases from zero, H_2 decreases in precisely the manner predicted by (1.12). However, at some higher value of S, H_2 reaches a minimum beyond which it increases sharply. Coyle's results show that the minimum film thickness, H_2^{min}, corresponds to the point at which the wetting line passes through the nip and the sharp upturn in H_2 follows once the wetting line moves upstream of the nip. In addition, he showed that decreasing Ca has little effect on H_2 at low values of S, but shifts the H_2^{min} to a higher value of S.

1.4.2 The meniscus regime

Using a finite element approach, two free surface, reverse roll coating was first investigated numerically by Coyle [1984]. He studied the region of parameter space where the inlet film thickness was greater than the minimum gap and, for this case, showed that the solution downstream of the nip is almost identical to that produced via the inlet flooded finite element model. It was thus concluded that the contact line is of primary importance in the formation of the downstream film. Grald *et al* [1994] solved the problem using the spectral element method and their results, produced via the commercial package 'Nekton', are in good agreement with Coyle [1984].

Fukazawa *et al* [1992] extended their viscocapillary model to incorporate the upstream free surface by modelling it with the arc of a circle. However, their model lacked an upstream boundary condition and was therefore unable to determine H_2 as part of the solution. Richardson [1996] refined and developed this viscocapillary model which did predict H_2.

Malone [1992] and Gaskell, Innes and Savage [1998] showed that, as with forward roll coating, the flow structures in starved and flooded inlets are quite different. Richardson [1996] used his viscocapillary model to predict the critical flow rates at which the flow structure changed and then used the finite element method to examine the various structures. He reported two mechanisms by which liquid can be transferred from the inlet to upper outlet film. In deference to Gaskell *et al* [1995], these were termed the primary and secondary transfer jets, see figure 1.8.

1.5 Slot coating

The slot coater is a pre-metered device which allows the thickness of the coated layer to be controlled within precise limits. It also allows several coatings to be applied simultaneously (see figure 1.9) and, for these reasons, is very commonly used in industry (see O'Brien [1984], Cameron, Alfred and Hills [1986], Sartor [1990] and Cohen [1993]).

The process consists of a web moving with velocity U, under a die of varying height $h(x)$. Liquid is fed through the narrow feed slot(s) between the upstream and downstream lips, and separates from the downstream lip to form a uniform film of thickness h_∞. The region of liquid confined between the upstream and downstream menisci is known as the coating bead.

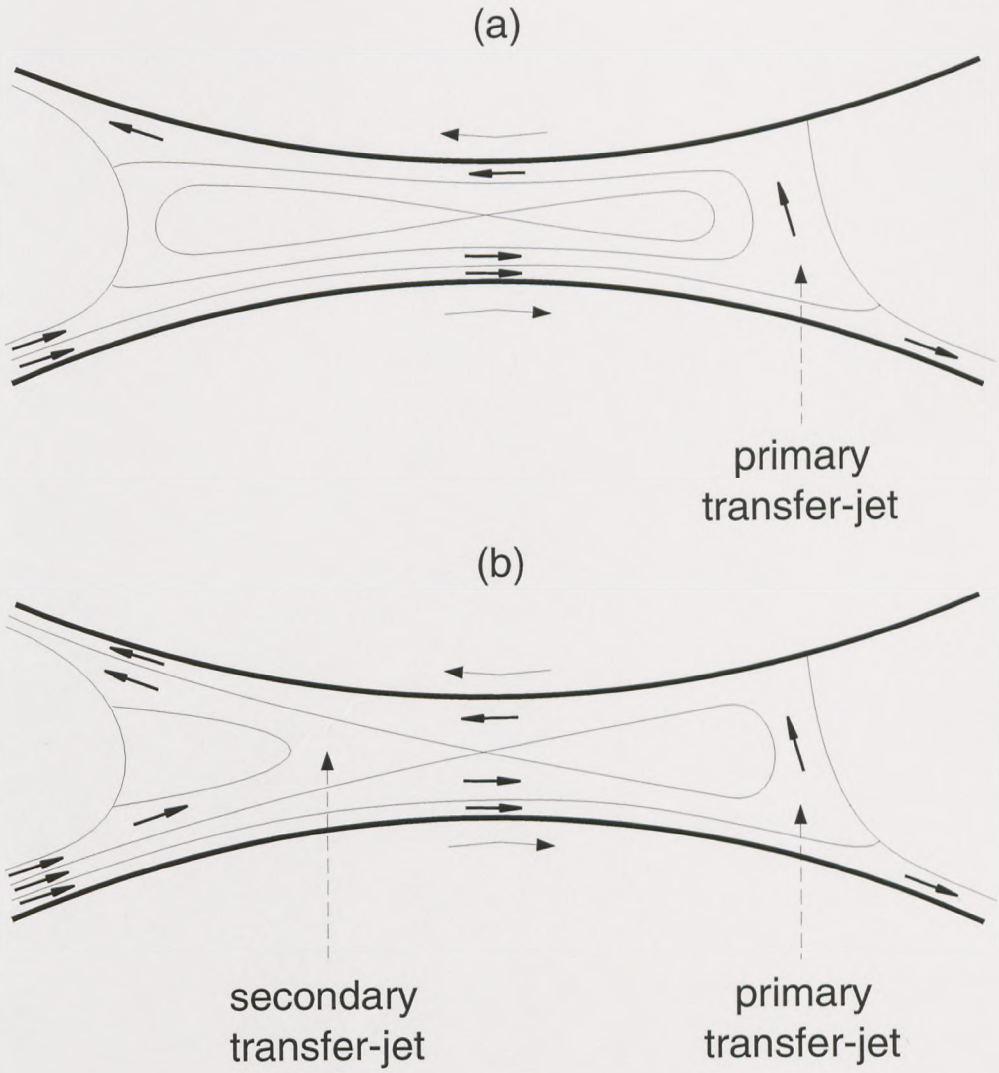

Figure 1.8: Schematic illustration of the flow field in *(a)* ultra starved and *(b)* starved reverse meniscus roll coating (Richardson [1996]).

Coyne and Elrod [1969], analysing only the flow in the downstream region, derived the asymptotic behaviour of the liquid layer thickness as $x \to \infty$. Later, by assuming a quadratic velocity distribution tangential to the meniscus, they solved for the flow along the free surface and determined the meniscus shape, which they showed to depend only on Ca for a given contact angle (see Coyne and Elrod [1970]). Their analysis showed that under certain conditions, a stagnation point is located on the free surface at a film height of $3h_\infty$ and also determined the dimensionless radius of curvature of the meniscus as a function of Ca.

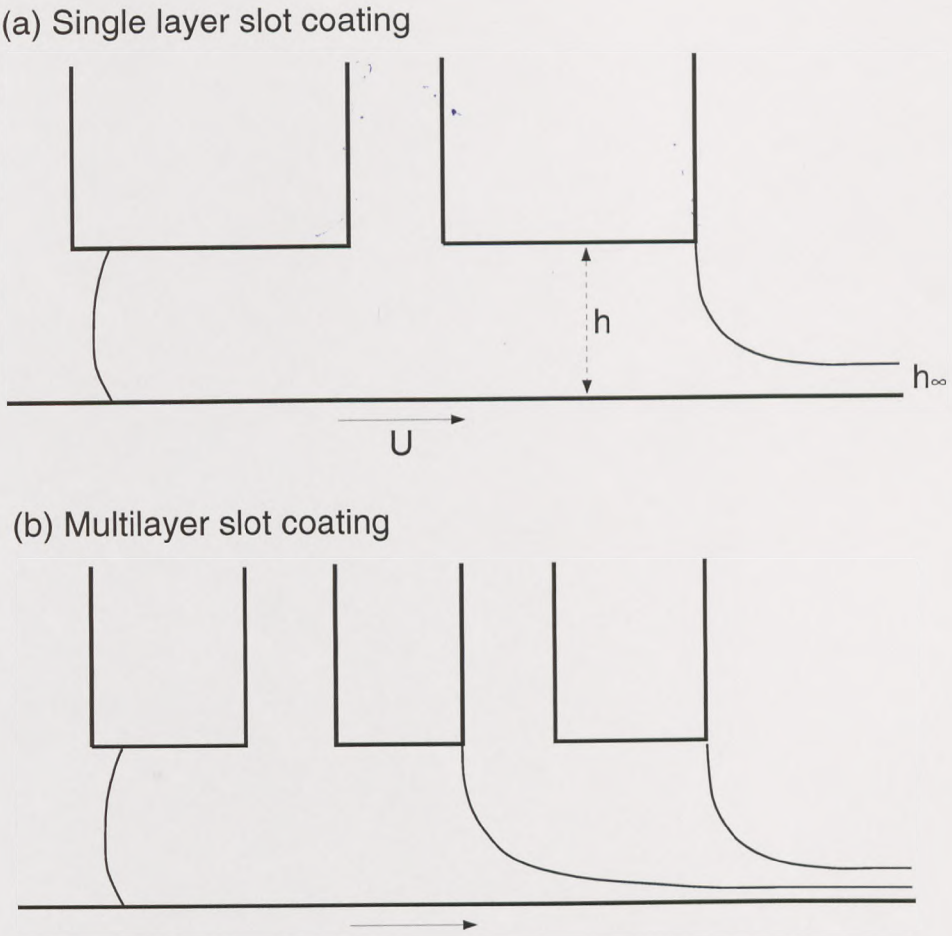

Figure 1.9: Schematic of single and multilayer slot coating.

Ruschak [1976] analysed the parameter bounds for which the slot coater is able to produce films of uniform thickness, although he neglected viscous effects, thus assuming that the upstream and downstream lip lengths are negligible so that the capillary pressure alone sets the bounds on coating bead operability. His model was also only valid for low flow rate and web speeds and assumed that the downstream static contact line is pinned at the edge of the downstream lip. Higgins and Scriven [1980] extended this work to include viscous effects.

If the pressure outside the downstream meniscus is atmospheric, Higgins and Scriven's [1980] analysis also explains why a vacuum pressure must often be applied at the upstream meniscus, as suggested by Beguin [1954]. Having such a back pressure moves the upstream free surface away from the inlet and is in fact necessary when the gap clearance is greater than twice the wet film thickness. This pressure difference, which can reach values of $3000Pa$, can be achieved with the help of a vacuum box (see Wood-

worth, Winkler and Jackson [1982]). The coating bead can be similarly stabilised by electrostatic or magnetic assist, the latter evidently being of use only with magnetic liquids.

Silliman and Scriven [1980], Saito and Scriven [1981], Carter [1985] and Thompson [1992] simulated the downstream end of the problem using the finite element method (see chapter 2) and they produced velocity and pressure profiles over a wide range of operating parameters. The full, two free surface problem (see chapter 5) was investigated numerically by Sartor [1990], Durst and Wagner [1997] (using a finite element analysis) and Grald, Chakrabarti and Subbiah [1994] (using a spectral element method). Sartor [1990] also conducted an experimental study of the flow field which compared well with his numerical predictions.

The main geometric features which can be altered are the die lengths, angles and their separation from the web. The purpose of making these changes is to modify the flow and related pressure field to enlarge the operating window of the process. Sartor [1990] investigated numerically, experimentally and analytically (using Higgins and Scriven's [1980] 2-dimensional analysis) the effect of various possible geometries on the lower vacuum limit and maximum speed of coating.

Note that in the literature, authors have generally assumed that the downstream static contact line is pinned at the edge of the slot. Sartor [1990] showed that this is not necessarily the case and found that the meniscus can detach from the edge and either wet past it and climb along the shoulder of the slot wall or regress into the coating gap along the downstream lip. The climbing effect was verified experimentally by Lodge [1993] and then examined computationally by Richardson and Storey [1993] and Kapur [1998]. Kapur [1998] also demonstrated experimentally the regression of the contact line under certain operating conditions. If the downstream contact line is unpinned, this will clearly affect the operability diagram predicted by Higgins and Scriven [1980] as the coating gap would then be narrower or wider than the assumed one.

1.6 Stability of coating flows

A major problem in the coating industry is the appearance, under certain operating conditions, of instabilities which give rise to coating defects, and hence it is necessary to determine the critical conditions (i.e. flow parameters) at which they arise. An example

of such an instability is *ribbing*, which appears in all the coating flows described above. In inlet flooded, reverse roll coating there is an additional instability known as *cascade* which occurs at large speed ratios, whereas in both the forward and reverse inlet starved roll coaters, *bead break* may arise.

1.6.1 The ribbing instability

The ribbing instability is a steady, spatially periodic, 3-dimensional disturbance of a free surface which is observed as lines of crests and troughs in the direction of the moving web, see figure 1.10. Avoidance of ribbing tends to require lower roll speeds, less

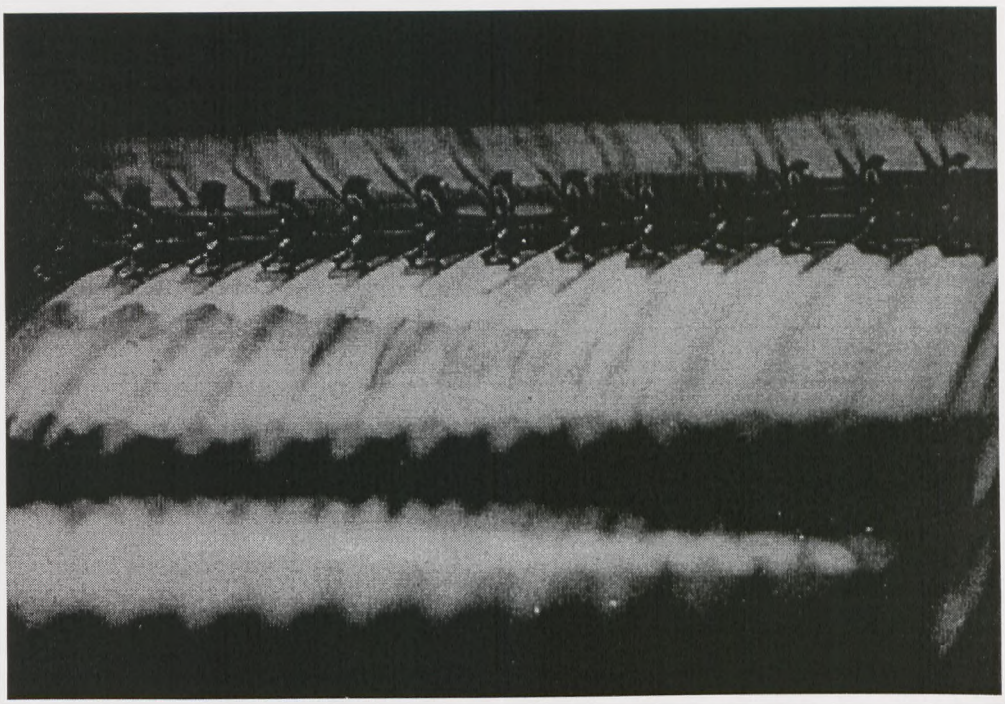

Figure 1.10: Photograph of the ribbing instability (Dowson and Taylor [1979]).

viscous fluids and thicker wet coatings. These requirements are in direct opposition to the economic driving forces for high production rates and low solvent usage.

Accurate predictions for the onset of ribbing require a theoretical analysis of both the base flow and its response to 3-dimensional disturbances of small amplitude. The base flow between pairs of rigid rolls has been extensively studied. When h_0/R is small, the flow in the gap region is almost rectilinear and the Navier-Stokes equations are well approximated by lubrication theory. Downstream of the nip the liquid splits into film(s) which attach to the roll(s). Close to this film split meniscus, the flow field is 2-dimensional and an accurate description of it would involve solving the Navier-Stokes

equations. Nevertheless, a common and effective approach has been to proceed with the lubrication approximation and adopt suitable boundary conditions at the film split meniscus. Pearson [1960] first introduced a linearised stability analysis, yet his model was restricted by an absence of appropriate boundary conditions to determine the location of the downstream meniscus. Savage [1977] and Fall [1978] used Coyne and Elrod's [1970] model of the flow near the meniscus and a steady-state linear stability analysis to investigate the cylinder-plane and wide angled spreader geometries respectively. Again following Pearson, Savage [1984] analysed the stability of the base flow in the equal speed, forward roll coater. Subsequently, Carter and Savage [1987] examined the unequal speed case. Fall [1982] went on to consider the stability of the 2-dimensional flow between a roll and a flat plate in which he included the time dependent response so as to obtain growth rate as a function of wavenumber.

An alternative approach to ascertain stability was developed by Bixler [1982], who applied ideas from linear stability theory to extend the finite element method in order to determine the stability of a free surface coating flow. The finite element method (as summarized by Kistler and Scriven [1983]) was found to be a powerful tool and made it computationally possible to solve complicated fluid flows with considerable accuracy whilst also making it no longer necessary to use the lubrication approximation near a meniscus. Neglecting gravity and inertia, this approach was used by Coyle [1984] (followed by Coyle *et al* [1990]) to solve for the stability of the half problem of equal speed, inlet flooded forward roll coating, the results of which showed areas of parameter space where the system was stable. Christodoulou [1989] included the inertia terms and investigated the stability of slide coating as various geometrical parameters were varied.

An approximate way to determine the stability of an interface was independently derived by Pitts and Greiller [1961] and Savage [1977]. By considering a force balance at the downstream interface, it was shown that this free surface would remain stable to small disturbances provided

$$\frac{d}{dx}\left(p + \frac{T}{r}\right) \; < \; 0, \tag{1.13}$$

where r represents the radius of curvature of the meniscus and p the pressure. The accuracy of this stability hypothesis, in comparison to the linear stability analysis, will be investigated in chapters 3 and 4.

1.6.2 The cascade instability

In reverse roll coating, at speed ratio values above a critical value, an instability known as *cascade* appears. Its effect is to leave a periodic cross-web disturbance in the direction of the moving web, the frequency of which increases with decreasing gap width (between the rolls). Large bubbles are simultaneously entrained on the upper roll, often being larger in size than the minimum gap. Whereas transition to ribbing as parameters vary is gradual, the transition to cascade is quite sharp. In addition, whereas ribs of small amplitude are often acceptable, the cascade instability produces a coating which is completely unacceptable.

The onset of cascade was first investigated by Booth [1970], who identified regions of instability in the $Ca - S$ plane. Coyle [1984] produced similar operability diagrams, although over a much larger region of parameter space. It is difficult to determine the nature of this instability experimentally because the dynamic contact line is situated close to the nip and so not easily observable. However, Coyle [1984] suggested the following mechanism, which can explain the observed oscillations in film thickness and the entrainment of large bubbles on the upper roll (see figure 1.11): As the speed ratio is increased, the wetting line moves towards the nip and the film thickness decreases. At a critical speed ratio, S^*, the wetting line is located at the nip and the film thickness is at a minimum. For $S > S^*$, the wetting line is positioned upstream of the nip so the gap height at the contact line, and hence the film thickness, increase. At another critical speed ratio (beyond $S = S^*$), S^L, the film thickness is equal to the minimum gap between the rolls and so the film reattaches to the upper roll, leading to a reduction in the film thickness. A large pocket of air is formed on the upper roll which then moves upstream from the minimum gap position. This value of S is too great for the wetting line to remain at the nip, i.e. $S^L > S^*$, and so it moves back to its original upstream position. Again, the film reattaches to the upper roll and the cycle repeats.

Note that at values of S near the onset of cascade, there is a very small clearance between the upper roll and film. The air boundary layer brought in on the upper roll has to turn around near the wetting line and flow back out of the gap, thus creating a high speed, high shear air flow which could generate waves on the liquid film and in itself cause instability. Hence a 3-dimensional, time dependent solution of the Navier-Stokes equation, including the effect of air flow, would be required in order to predict the flow that arises close to and during the cascade instability.

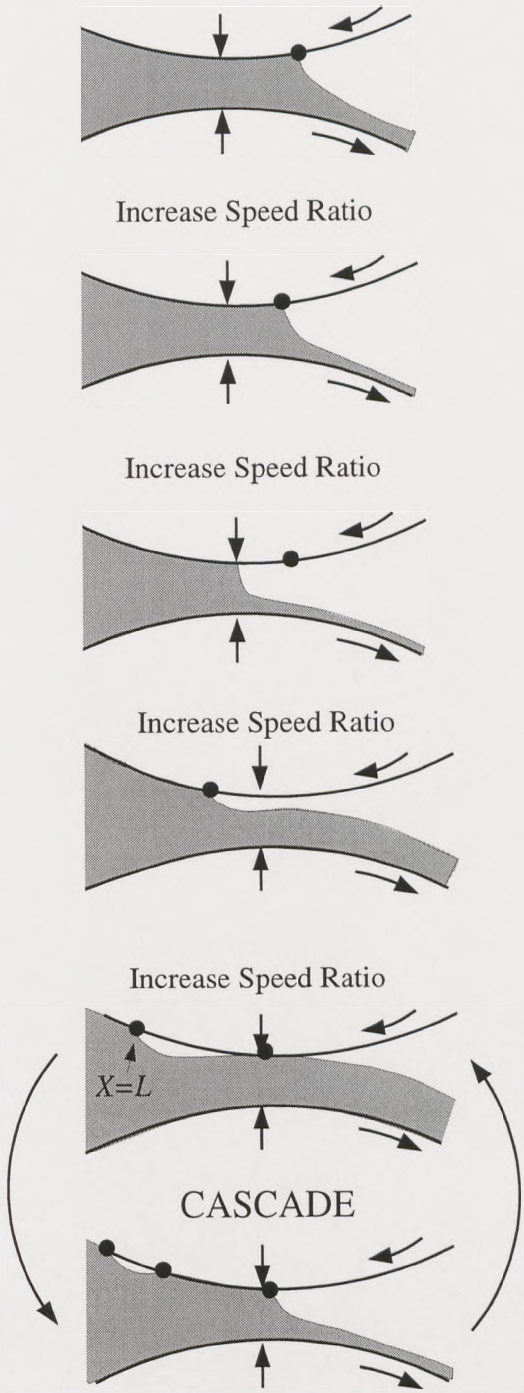

Figure 1.11: Schematic representation of the mechanism of the cascade instability (Coyle [1984]).

The experiments by Coyle [1984] also show that the onset of cascade shifts to a higher value of S as Ca is decreased, but is relatively insensitive to the minimum gap width.

1.6.3 The bead break instability

Whilst operating in the reverse meniscus regime, experiments performed by Malone [1992] suggested that the cascade instability does not occur since the final film thickness is then also dependent on the amount of fluid arriving at the nip. However, Malone [1992], Gaskell, Kapur and Savage [1998] and Kapur [1998] showed that, for rolls operating in both the reverse and forward mode, another instability known as *bead break* can then appear. They showed, for the forward case, that increasing Ca or S moved the upstream meniscus to the same side of the nip as the downstream meniscus. A further increase in Ca or S led to the acceleration of the upstream meniscus towards the downstream meniscus, at which point the entire bead collapsed, thus the term bead break. This instability is described further in chapter 4.

In the reverse case, Kapur [1998] observed a similar phenomenon, in which increasing S caused the downstream meniscus to accelerate towards the upstream again causing the bead to collapse.

1.7 Outline of this thesis

The general aim of this thesis is to investigate, both analytically and numerically, instabilities in reverse, forward and slot coating flows. Consideration is restricted to Newtonian, incompressible fluids in the absence of inertial forces. The Galerkin finite element method, which is used to obtain numerical solutions for the flow domain for all three of these processes, is outlined in chapter 2. A numerical technique for analysing the stability of these flows, based on linear stability theory, is then described.

In chapter 3, the inlet flooded regime of reverse roll coating is investigated for which, as has already been shown in section 1.6, two prominent instabilities may appear - ribbing at low S and cascade at high S. These instabilities are separated by a stable window of operation in which a uniform film can be produced. The size of the stable window can vary as parameters, such as the gap width, vary. In this chapter, only the ribbing instability is examined as the cascade instability forms a separate topic of interest in its own right and, as previously stated, would require a time dependent solution of the Navier-Stokes equation. By considering a 3-dimensional disturbance to a 2-dimensional

base flow calculated using lubrication theory, regions of instability in the $Ca - S$ control space are established. Results obtained using this linear stability analysis are then compared with predictions from the stability hypothesis (1.13) and results acquired using the numerical methods outlined in chapter 2.

A variation of inlet flooded, reverse roll coating is then examined in which the nip is fed from above by a large reservoir of fluid i.e. a hydrostatic head. The effect of this head on the base flow and stability is investigated, again by applying linear stability analysis to lubrication theory.

Finally, an improved model of the dynamic contact line, developed by Shikhmurzaev [1993a], is described in which the dynamic contact angle is no longer kept constant, but is a function of various fluid and geometrical parameters. The limit of this theory for small capillary number is then incorporated into the analytical model from which its effect on the base flow and its stability is examined.

The first aim of chapter 4 is to investigate the ribbing instability in inlet flooded, forward roll coating in the absence of gravity. As in the reverse case, by considering a 3-dimensional perturbation to a 2-dimensional base flow, regions of instability in the Ca - S plane are established and compared to those predicted by (1.13) and the numerical finite element stability approach.

Instabilities in the inlet starved case, where the inlet is fed by an incoming film of prescribed thickness, are then examined. An examination of the bead break phenomenon is performed and the effect of the upstream free surface on downstream ribbing examined. This is achieved analytically using 3-dimensional linear stability theory, the results from which are compared to predictions obtained using a stability hypothesis on both the upstream and downstream free surfaces. Note that the stability of the upstream free surface has already been investigated by Gaskell *et al* [1998] who studied the bead break instability by considering only 2-dimensional perturbations to the base flow. In addition, they did not consider the effect of the incoming film thickness which is included in the model presented here.

Experiments by Kapur [1998] show that ribbing on the downstream meniscus of a slot coater only occurs when the downstream static wetting line is not pinned, but free to move along the downstream die lip. These experiments have prompted the investigation

in chapter 5 of the ribbing instability on the downstream free surface of a slot coater. Firstly, a finite element base flow for the case of a pinned downstream is found and the effect of various fluid and geometrical parameters considered. The resulting pressure profiles and upstream meniscus locations are compared to those predicted via a model based on lubrication theory. A finite element base flow with an unpinned downstream is then found, and the resulting pressure profiles and meniscus locations are compared with those from the pinned case. Finally, linear stability theory is applied to this unpinned case and the effect of various fluid and geometrical parameters on the stability of the flow are examined. Note that instabilities on the upstream free surface are not examined since a comprehensively different finite element mesh would be required.

Chapter 6 summarises the main results obtained in this thesis and provides suggestions for future work.

Chapter 2

Methods

Contents

2.1 Galerkin finite element method 28

2.1.1 Introduction 28

2.1.2 Governing differential equations 30

2.1.3 Galerkin FE formulation 31

2.1.4 Free surfaces 33

2.1.5 Dynamic contact angles 35

2.1.6 Isoparametric mapping 37

2.1.7 Numerical Integration 40

2.1.8 Iterative technique 41

2.1.9 The frontal solution method 43

2.1.10 Post-processing 44

2.2 Linear stability analysis based on the FEM 46

2.2.1 Introduction 46

2.2.2 Formulation of the equations 46

2.2.3 Derivation of the Jacobian matrix 48

2.2.4 Derivation of the mass matrix 52

2.2.5 Inclusion of a dynamic contact line 53

2.2.6 Method of solution 54

2.1 Galerkin finite element method

2.1.1 Introduction

In the previous chapter, it was described how roll coating flows can be modelled analytically using lubrication theory. Such models reduce the problem to a one-dimensional system subject to simple boundary conditions on velocity and pressure, with the Reynolds number set to zero. Further, it is often necessary to assume a small Ca to obtain suitable boundary conditions at an outlet, e.g. the Landau-Levich [1942] or Ruschak [1981] expressions can be used to relate the final film thickness to the radius of curvature. The meniscus can then be approximated by the arc of a circle.

However, for many flows the above assumptions do not hold and one must resort to using a numerical method. Such methods require the continuum equations governing the flow to be written in an approximate, discrete form, resulting in a system of algebraic equations whose solution yields the physical quantities of interest, e.g. fluid velocity and pressure, streamfunction, vorticity, at points (or nodes) within the flow domain. There are five such methods available - namely *(i)* finite difference (FD), *(ii)* finite volume (FV), *(iii)* boundary element (BE), *(iv)* finite element (FE) and *(v)* spectral element (SE).

In the FV method the associated control volumes are designed to conserve fluid flux locally and globally and as such it has found favour with those interested in high Reynolds number flows. The FD method, however, is usually used to study medium and low Reynolds number flows. Both methods are well suited to problems involving regular, fixed domains (i.e. no free surfaces), and advances have been made in applying them to irregular and moving domains through using boundary-fitted coordinates (Ryskin and Leal [1984], Glaister [1995], Wang and Domoto [1994]) or a Volume-of-Fluid technique (Hirt and Nichols [1981], Hirt and Chen [1996]).

The BE method has been applied successfully to free surface flows (see Kelmanson [1983]). This method is very efficient as it requires only information on the boundary to be evaluated. Its major drawback is that it is not easily applied to non-linear problems (i.e. $Re \neq 0$), though progress is being made in this area, for example by Liao and Chwang [1996].

The FE method can be applied relatively easily to solve non-linear problems with ir-

regularly shaped domains. The fluid domain is divided into sub-regions called elements inside which an approximate, local solution for the governing equations is found. The solutions from all the individual elements are then assembled to generate an overall approximate solution. Although this method is generally more computationally expensive than the FD, FV and BE methods, it is topologically very flexible and well-suited to the solution of nonlinear free surface flow problems.

FE solutions of free surface problems were first presented by Nickell, Tanner and Caswell [1974] and Tanner, Nickell and Bilger [1975], although they were limited by the large amount of data storage required. The development of a frontal method by Irons [1970] and Hood [1976] dramatically reduced the storage requirements, but early work still suffered from slow convergence since the free surface locations were determined by successive approximations (see Silliman and Scriven [1980]). Improvements in the representation of the free surfaces were made by Ruschak [1980] who devised the *boundary support* method which evolved into the *spine method.* This method, together with the introduction of a Newton-Raphson iterative scheme (Saito and Scriven [1981]) then made it possible to solve for the free surface location and flow field conveniently and simultaneously. Since Kistler and Scriven's [1983] review of the method, the FE approach has been successfully applied to many coating geometries e.g. forward roll coating (Coyle [1984], Gaskell *et al* [1995]), reverse roll coating (Coyle *et al* [1990a], Richardson [1996]) and slide coating (Christodoulou [1990], Walker [1995]) to name but a few.

The SE method, developed by Patera [1984], has also proved to be highly successful for solving free surface flows. The method is similar to that of the FEM in that the domain is represented by a number of elements and locating free surfaces can be computationally intensive (see Grald *et al* [1994]). However, unlike the FEM, very few elements are required to tessellate the domain because the order of interpolation used is much higher (4th to 14th order Legendre polynomials). The SE method has been applied to numerous coating problems (see Grald *et al* [1994]) and results agree well with those obtained with the FEM.

In this study, a FEM is chosen. The following sections, 2.1.2-2.1.10, briefly describe the FE formulation for solving steady, two-dimensional flows which include free surfaces with attendant dynamic or static contact lines.

2.1.2 Governing differential equations

The steady isothermal flow of a Newtonian, incompressible fluid of constant density, ρ, and kinematic viscosity, ν, is governed by the equations,

$$\rho(\underline{U}.\nabla)\underline{U} = -\nabla P + \mu\nabla^2\underline{U} + \rho\underline{g}, \tag{2.1}$$

$$\nabla.\underline{U} = 0, \tag{2.2}$$

expressing the conservation of momentum (the Navier-Stokes equations) and fluid mass (the 'continuity' condition) respectively. Here, $\underline{g}$ is the acceleration due to gravity. The dimensionless form of the equations is

$$Re(\underline{u}.\nabla)\underline{u} = \nabla\underline{\underline{\sigma}} + St\hat{\underline{g}}, \tag{2.3}$$

$$\nabla.\underline{u} = 0, \tag{2.4}$$

where lengths have been scaled by an appropriate length scale, D, velocities by a characteristic velocity, U, and pressure and viscous stresses by $\nu U/D$. The Reynolds number and Stokes number are then given by $Re = \rho UD/\mu$ and $St = \rho gD^2/\mu U$ and indicate the relative importance of inertial to viscous and gravitational to viscous forces respectively. Here $\underline{u} = (u, v)$ is the dimensionless fluid velocity, $\hat{\underline{g}}$ is the unit vector in the direction in which gravity acts and $\underline{\underline{\sigma}}$ is the dimensionless stress tensor which, for a Newtonian fluid, is given by

$$\underline{\underline{\sigma}} = -p\underline{\underline{I}} + [\nabla\underline{u} + (\nabla\underline{u})^T], \tag{2.5}$$

where $\underline{\underline{I}}$ is the unit tensor and p the dimensionless fluid pressure.

The domain of interest is discretised by dividing it into a finite number of elements, see figure 2.1, each containing a number of nodal points at which the pressure and/or the velocity is either known or to be determined. These nodes determine the level of interpolation to be used in order to approximate the unknown flow variables, u, v and p over an element. It is now generally recognised that in the primitive variable, FEM formulation of the Navier-Stokes equations, 'mixed interpolation' should be used i.e. pressure should be interpolated at least one order of magnitude lower than that of velocities so as to satisfy the *Ladyzenskaya Babuska Brezzi* or LBB stability condition (see, for example, Babuska and Aziz [1972] or Lee, Gresho and Sani [1979]). Failure to adopt this approach may lead to an ill-conditioned or even singular global matrix resulting in an oscillating pressure solution or no solution at all.

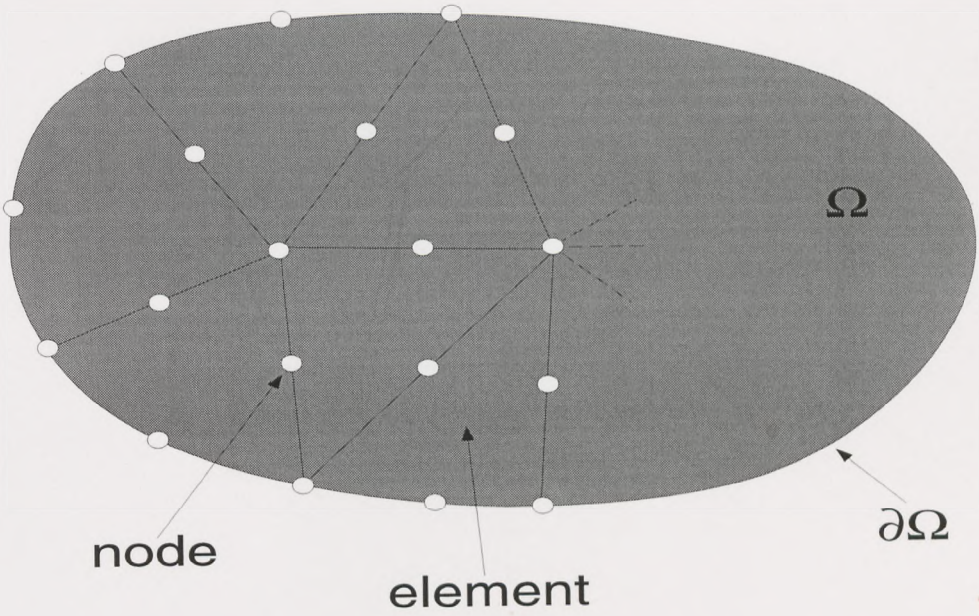

Figure 2.1: A fluid domain, Ω, with boundary $\partial\Omega$, as tessellated by finite elements.

The FE representations of velocity and pressure are defined as

$$\underline{u}(x,y) = \sum_{k=1}^{K} \underline{\bar{u}}_k N_k(x,y); \qquad p(x,y) = \sum_{l=1}^{L} \bar{p}_l \psi_l(x,y), \tag{2.6}$$

where $\underline{\bar{u}}_k = (\bar{u}_k, \bar{v}_k)$ is the velocity at the kth velocity node, p_l is the pressure at node l, and N_k and ψ_l are the interpolating functions satisfying

$$N_k = \begin{cases} 1 & \text{at node } k \\ \\ 0 & \text{at all other nodes} \end{cases} \qquad \psi_l = \begin{cases} 1 & \text{at the } l\text{th pressure node} \\ \\ 0 & \text{at all other corner nodes} \end{cases} \tag{2.7}$$

Although there are many different types of elements, in this study triangular V6/P3 ones are employed since they allow easier refinement into corners (see Thompson [1992]). Such elements have two velocity freedoms at each node and a pressure freedom at each corner node (see figure 2.2), giving fifteen unknowns. Thus the N_k are 6-node biquadratic functions and the ψ_l are 3-node bilinear functions.

2.1.3 Galerkin FE formulation

Galerkin's method is adopted in which values of (u_k, v_k) are sought which satisfy a weak form of the governing equations, generated by weighting (2.3) and (2.4) with the velocity and pressure interpolating functions, N_k and ψ_l respectively, integrating over the domain and setting them to zero. The momentum residuals are then

$$\underline{R}^k_m = \int_\Omega (ReN_k(\underline{u}.\nabla)\underline{u} - N_k \nabla.\underline{\underline{\sigma}} - N_k St\underline{\hat{g}})d\Omega = 0, \tag{2.8}$$

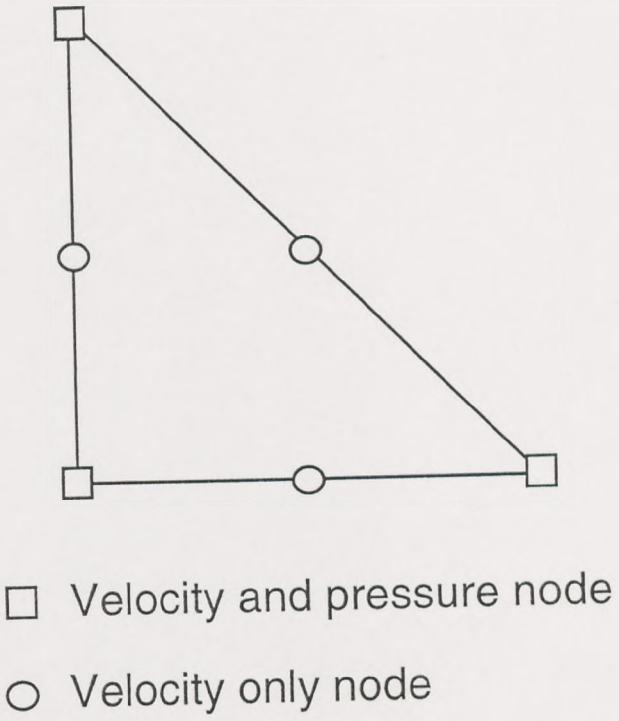

Figure 2.2: The V6/P3 element, satisfying the LBB stability condition.

and the continuity residuals are

$$R_c^l = \int_\Omega \psi_l \nabla . \underline{u} d\Omega = 0, \tag{2.9}$$

giving rise to $2K + L$, non-linear, algebraic equations for the $2K + L$ unknowns u_k, v_k and p_l. Using the identity

$$N_k \nabla . \underline{\underline{\sigma}} \;=\; \nabla . (N_k \underline{\underline{\sigma}}) - \nabla N_k . \underline{\underline{\sigma}} \tag{2.10}$$

and the divergence theorem, the momentum residuals then become

$$\underline{R}_m^k = \int_\Omega (Re N_k (\underline{u} . \nabla) \underline{u} + \nabla N_k . \underline{\underline{\sigma}} - N_k St \underline{\hat{g}}) d\Omega - \int_{\partial\Omega} N_k \underline{\underline{\sigma}} . \underline{\hat{n}} ds, \tag{2.11}$$

and are now seen to consist of contributions from the domain, Ω, and its boundary, $\partial\Omega$. At free surfaces, the boundary contribution will be non-zero and must therefore be evaluated. At fixed boundaries, the fluid is assumed to adhere to the surface and the 'no-slip' boundary condition is imposed such that the velocity is known at each of the relevant boundary nodes; thus the boundary contributions can be discarded there and need not be assembled.

2.1.4 Free surfaces

The presence of free surfaces introduces complications into the solution procedure since the shapes of these boundaries are unknown *a priori* and must be determined as part of the solution. The following non-linear boundary conditions are to be applied across each free surface:

(1) the normal velocity must vanish;

(2) the tangential (shear) stress must be continuous and is generally considered to be zero since air has a viscosity which is negligible compared to that of most fluids;

(3) the normal stresses and surface tension stresses must balance;

Condition (1), otherwise known as the kinematic condition, written as

$$\underline{u}.\hat{\underline{n}} = 0, \tag{2.12}$$

expresses the fact that no fluid may cross a steady interface. Following Kistler and Scriven [1983], conditions (2) and (3) may be expressed mathematically via the vector relation

$$\hat{\underline{n}}.\underline{\underline{\sigma}} = \frac{\kappa \hat{\underline{n}}}{Ca} - p_a \hat{\underline{n}}, \tag{2.13}$$

where p_a is the ambient air pressure and κ the dimensionless curvature of the free surface. A more convenient form is given by (Ruschak [1980])

$$\hat{\underline{n}}.\underline{\underline{\sigma}} = \frac{1}{Ca}\frac{d\underline{t}}{ds}, \tag{2.14}$$

where $\underline{t}$ is the unit tangent pointing in the direction of increasing arc length, s, along a free surface and pressures have been measured relative to the ambient pressure, p_a. Inserting (2.14) into (2.11) enables the boundary contributions of the momentum residual, $(R_m^k)_{\partial\Omega_{fs}}$, to be rewritten as

$$\begin{aligned}(R_m^k)_{\partial\Omega_{fs}} &= \frac{1}{Ca}\int_{\partial\Omega_{fs}} N_k \frac{d\hat{\underline{t}}}{ds} ds, \\ &= \frac{1}{Ca}\int_{\partial\Omega_{fs}} \hat{\underline{t}}\frac{dN_k}{ds} ds - \frac{1}{Ca}[N_k\hat{\underline{t}}_1 - N_k\hat{\underline{t}}_0],\end{aligned} \tag{2.15}$$

where $\hat{\underline{t}}_1$ and $\hat{\underline{t}}_0$ are the unit tangents to the beginning and end of the free surface respectively.

In this study, the position of a free surface is represented in terms of a set of conveniently placed spines, as defined by Kistler and Scriven [1983]. The spines, which are not necessarily independent, are typically straight lines; the spine 'height', h_i, is defined as the distance along a spine between its base node, $\underline{x}_i^b$, and a node which lies on the free surface.

Unlike the boundary support method (Ruschak [1980]), the representation of a free surface is independent of any reference surface, which requires the coordinates of base nodes and orientation of spines to be additional unknowns; they can be adjusted adaptively and automatically to the features of the flow during the iterative procedure. The

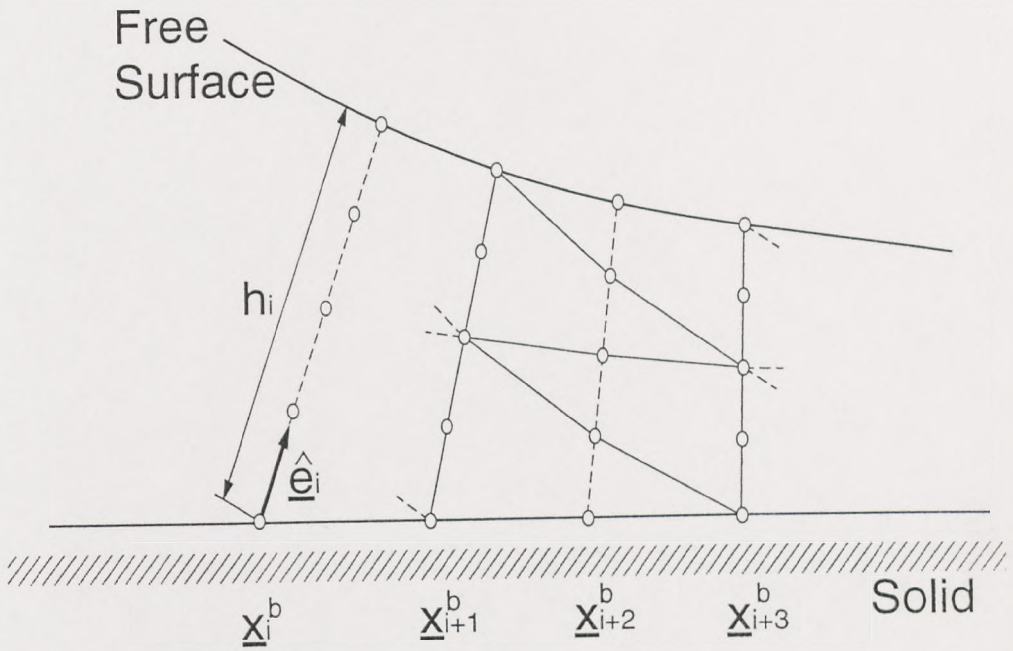

Figure 2.3: Parametrization of a free surface by the spine method.

coordinates of node k on the ith spine are given by the relation

$$\underline{x}_k = \underline{x}_i^b + w_k h_i \hat{\underline{e}}_i, \tag{2.16}$$

where w_k is a prescribed proportion of the spine height, h_i, and $\hat{\underline{e}}_i$ is a unit direction vector parallel to the spine.

To determine the magnitude of each spine height, h_i, the kinematic condition (2.12) is weighted with the shape functions associated with the free surface nodes. Since only

the shape functions defined on the free surface will be non-zero there, this leads to exactly as many equations as there are unknown spine heights. These additional equations are given by

$$R_K^i = \int_{\partial\Omega_{fs}} N_i \underline{u}.\underline{\hat{n}} ds = 0. \tag{2.17}$$

Note that the task of choosing a mesh generation algorithm is often complicated due to large variations in free surface shape as parameters vary. Similarly, it is important to avoid undue element distortion as this can have a serious detrimental effect on the accuracy of numerical solutions. It is thus often necessary to introduce what is known as an *inter-dependent* spine, where a spine contains nodes which are the base nodes for other spines. The coordinates of a free surface node, in a region containing inter-dependent spines, is given by $\underline{x}_j^{fs}$, where

$$\begin{aligned} \underline{x}_j^{fs} &= \underline{x}_j^b + h_j \underline{\hat{e}}_j \\ &= \underline{x}_0 + h_d \underline{\hat{e}}_d w_j + h_j \underline{\hat{e}}_j, \end{aligned} \tag{2.18}$$

where $\underline{x}_0$, h_d and $\underline{\hat{e}}_d$ are the location of the base node, height and direction vector of the inter-dependent spine respectively (see figure 2.4). The variable w_j represents the weight along the inter-dependent spine to the base node being described. Note that in figure 2.4, both $\underline{x}_i^b$ and $\underline{\hat{e}}_i$ $(i = 1, .., 3)$ are now dependent on h_d.

2.1.5 Dynamic contact angles

As discussed in Chapter 1, all practical coating processes contain at least one dynamic contact line. As the coating liquid displaces the air from the moving solid surface, both the liquid and the gas must move relative to the solid surface, and thus the no-slip boundary condition is violated (see Huh and Scriven [1971]). Applying conventional fluid dynamical theory along with the no-slip condition leads to an unbounded stress which has a non-integrable singularity. To eliminate this stress singularity, Dussan [1976] suggested the use of a small slip length over which slip occurs between the liquid and the solid surface, in the immediate vicinity of the wetting line. There are several alternative slip boundary conditions but Dussan [1976] showed that they have no effect on the global solution and so the choice of slip condition only matters close to the dynamic wetting line.

Here the slip length is defined over one element, where the velocity of the fluid is zero at the dynamic contact line, half the web velocity at the mid-side node located on

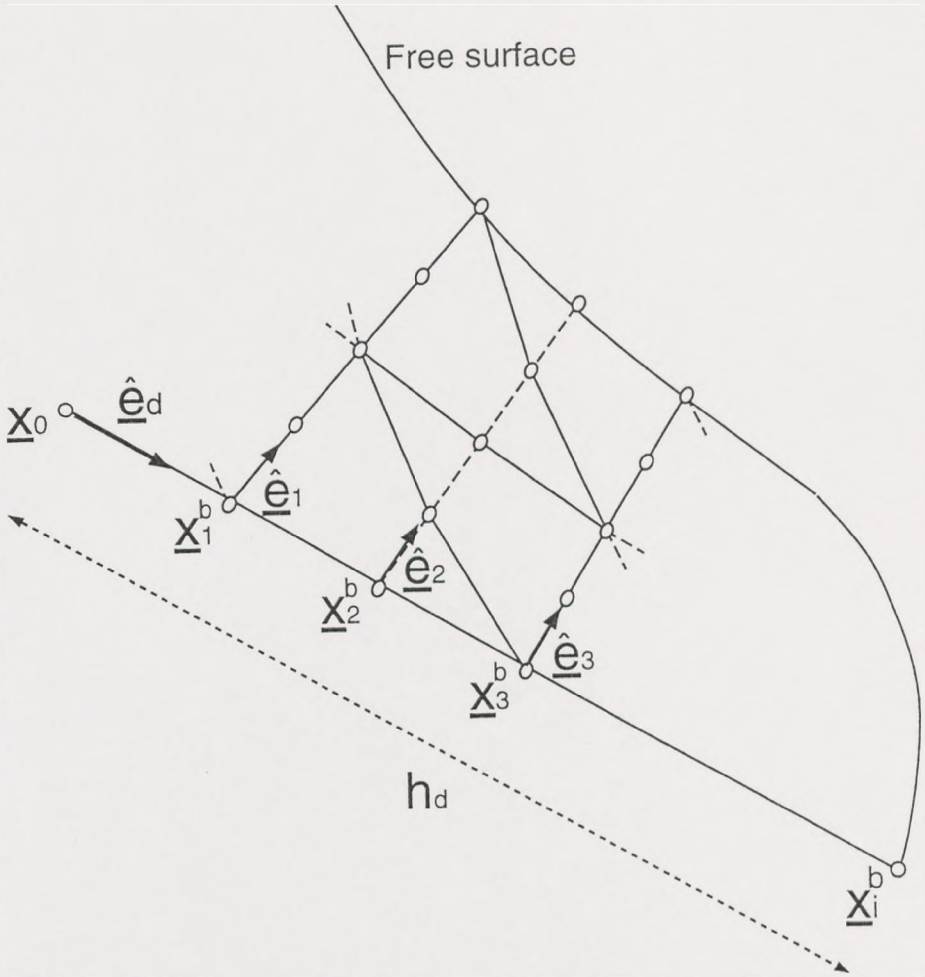

Figure 2.4: Parametrization of a free surface using inter-dependent spines.

the web, and equal to the web velocity at the final node.

As the location of the dynamic contact line is not known *a priori*, an additional boundary condition is required to find its position. A suitable condition is

$$\underline{t}_{fs} \cdot \underline{t}_{web} = \cos\theta_d, \tag{2.19}$$

where $\underline{t}_{fs}$ is the tangent to the free surface and $\underline{t}_{web}$ is the tangent to the web. Equation (2.19) is imposed in residual form by weighting with the shape function, N_k (see Kistler and Scriven [1983]). The dynamic contact angle, θ_d, is then imposed although it is recognised that a more rigorous treatment of the contact line is required. Recent advances have been made in this area by Shikhmurazev [1993,1994,1996], although, due to complexity of the theory, his analysis has yet to be incorporated fully into numerical algorithms for coating flows. Once the 'teething problems' are overcome, the concepts of Shikhmurazev may well become a powerful tool for dealing with the wetting line.

Work in this area is currently being carried out by Summers *et al* [1998].

2.1.6 Isoparametric mapping

By mapping a standard element defined in a local coordinate (ξ, η) space into each of the deformed elements in the flow domain, the calculation of the shape functions, N_k, may be simplified - they become too complicated when expressed in cartesian coordinates. The standard triangular element in local coordinate space, A_0, is shown in figure 2.5. The interpolating functions can then be expressed in a general form in terms of local

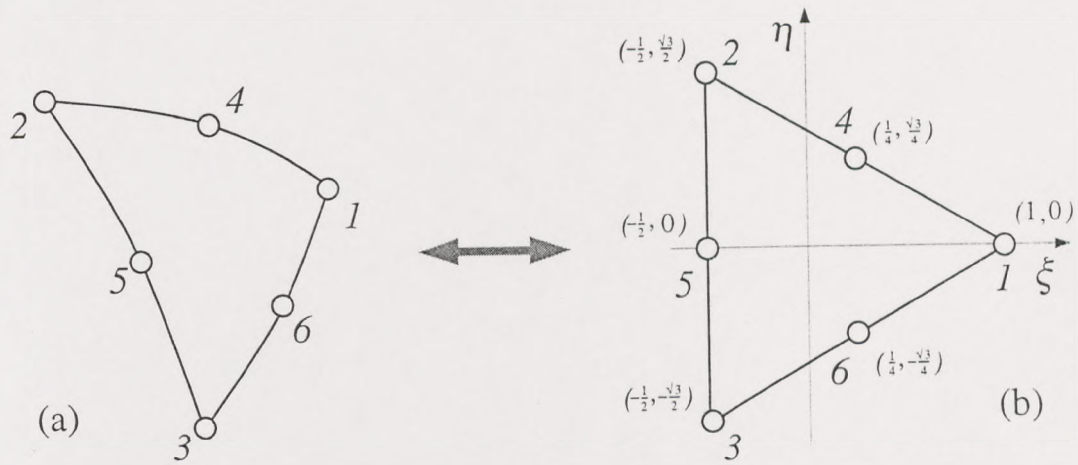

Figure 2.5: (a) A triangular element in global space. (b) The standard triangle, A_0, showing the local node numbering scheme and local coordinate system.

coordinates, L_1, L_2 and L_3, defined by

$$L_1 = \frac{A_1}{A}, \quad L_2 = \frac{A_2}{A}, \quad L_3 = \frac{A_3}{A}, \tag{2.20}$$

where A is the area of a triangular element and A_1, A_2 and A_3 are the areas of its subtriangles, as shown in figure 2.6. Since $A_1 + A_2 + A_3 = A$,

$$L_1 + L_2 + L_3 \;=\; 1. \tag{2.21}$$

Carter [1985] showed that in the local triangle, A_0,

$$L_1 = \frac{1}{3}(1 + 2\xi), \quad L_2 = \frac{1}{3}(1 - \xi + \sqrt{3}\eta), \quad L_3 = \frac{1}{3}(1 - \xi - \sqrt{3}\eta), \tag{2.22}$$

and it follows that

$$\begin{aligned} N_1 = L_1(2L_1 - 1), \quad N_2 = L_2(2L_2 - 1), \quad N_3 = L_3(2L_3 - 1), \\ N_4 = 4L_1L_2, \quad N_5 = 4L_2L_3, \quad N_6 = 4L_1L_3, \end{aligned} \tag{2.23}$$

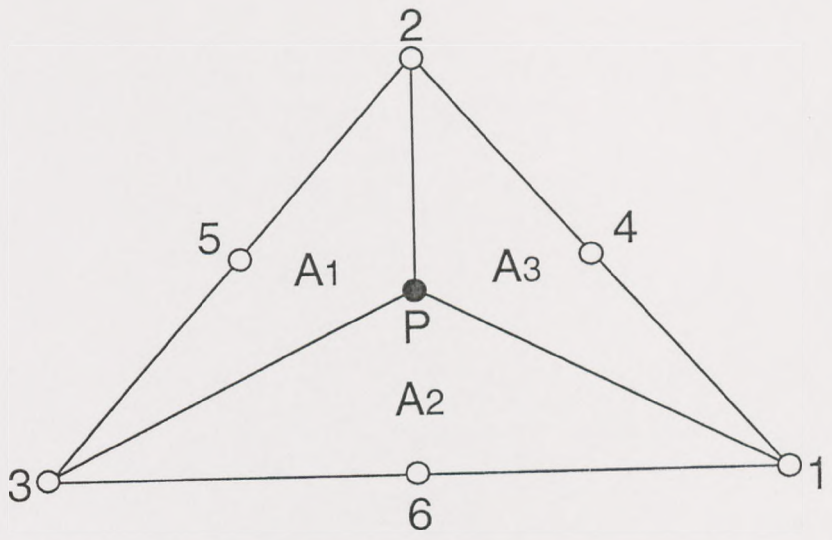

Figure 2.6: Subtriangles used to define the area coordinates, L_i, of an interior point P.

where N_k denotes the interpolating function associated with local node number k. The ψ_l interpolating functions associated with the lth corner node are

$$\psi_1 = L_1, \quad \psi_2 = L_2, \quad \psi_3 = L_3. \tag{2.24}$$

Note that at any point in the element, the interpolating functions sum to unity, i.e.

$$\sum_{k=1}^{6} N_k(\xi,\eta) = \sum_{l=1}^{3} \psi_l(\xi,\eta) = 1. \tag{2.25}$$

An element is said to be *isoparametric* if the global coordinates of any point in its interior can be found from the global coordinates of the element's nodes using the same interpolating functions as used for the dependent variables, i.e.

$$\underline{x} = \sum_{k=1}^{6} \underline{x}_k N_k(\xi,\eta), \tag{2.26}$$

where $\underline{x}_k$ are the global coordinates of the kth local node.

The residual equations require derivatives of the shape functions, N_k and ψ_l, with respect to the global coordinates. However, N_k and ψ_l are only defined in local coordinates and so the relation

$$\begin{pmatrix} \frac{\partial}{\partial \xi} \\ \frac{\partial}{\partial \eta} \end{pmatrix} = \begin{pmatrix} \frac{\partial x}{\partial \xi} & \frac{\partial y}{\partial \xi} \\ \frac{\partial x}{\partial \eta} & \frac{\partial y}{\partial \eta} \end{pmatrix} \begin{pmatrix} \frac{\partial}{\partial x} \\ \frac{\partial}{\partial y} \end{pmatrix} = J \begin{pmatrix} \frac{\partial}{\partial x} \\ \frac{\partial}{\partial y} \end{pmatrix}, \tag{2.27}$$

is required, where the entries of the Jacobian, J, are found using

$$\frac{\partial \underline{x}}{\partial \xi} = \sum_{k=1}^{6} \underline{x}_k \frac{\partial N_k}{\partial \xi}, \quad \frac{\partial \underline{x}}{\partial \eta} = \sum_{k=1}^{6} \underline{x}_k \frac{\partial N_k}{\partial \eta}. \tag{2.28}$$

Therefore, the residual integrals can be evaluated on an element-by-element basis where the integral over each element is determined by mapping the element to the standard triangle, A_0, and integrating over local space, i.e.

$$\int_\Omega f(\underline{x},\underline{\beta})dxdy = \sum_{elements} \left\{ \int_{A_0} f(\underline{x}(\xi,\eta),\underline{\beta})|J|d\xi d\eta \right\}, \tag{2.29}$$

where f is the relevant integrand and $\underline{\beta} = (\underline{\bar{u}}^T, \underline{\bar{v}}^T, \underline{\bar{p}}^T)$ is the vector of unknowns.

Free surface contributions to residuals are best evaluated in terms of local coordinates and since all free surface nodes lie along at least one side of an element, one of the three area coordinates must vanish. Without loss of generality, the global node numbering scheme can be chosen such that local nodes 1, 3, and 6 lie along the free surface, see figure 2.7. Then along this side $L_2 = (N_2 = N_4 = N_5) = 0$ and the remaining non-zero

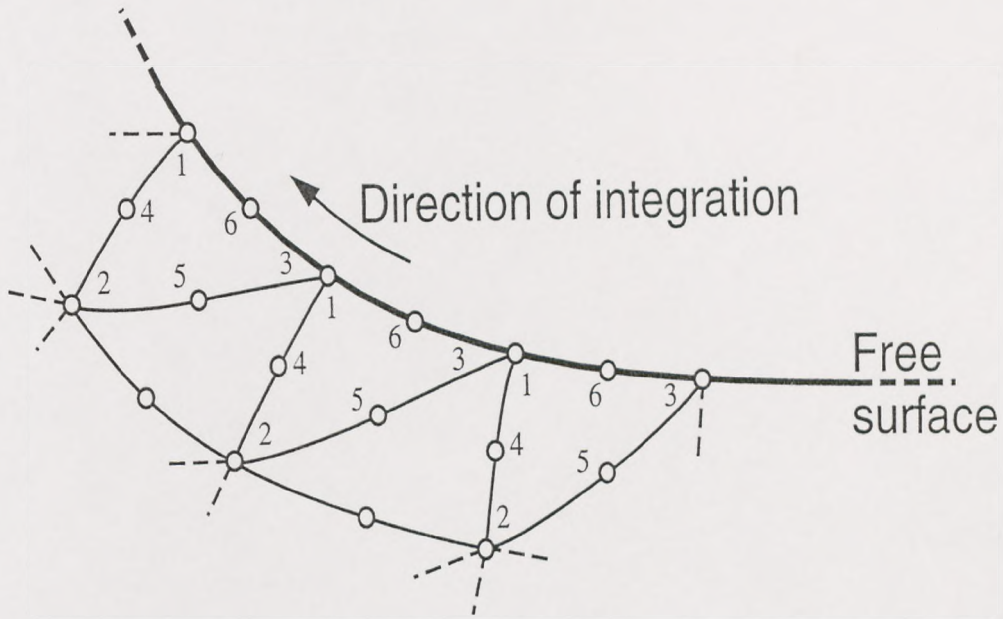

Figure 2.7: Local node numbering of elements which have one side lying on a free surface.

area coordinates satisfy

$$L_1 + L_3 = 1, \tag{2.30}$$

which allows the remaining interpolating functions to be written in terms of a single, independent variable:

$$N_1 = L_1(2L_1 - 1), \quad N_3 = 1 - 3L_1 + 2L_1^2, \quad N_6 = 4L_1(1 - L_1). \tag{2.31}$$

Note that for convenience L_1 has been used since it increases from 0 to 1 along the element side in the direction of integration (if the direction of integration is anti-clockwise). If $\underline{x}_1$, $\underline{x}_3$ and $\underline{x}_6$ are the global coordinates of local nodes 1, 3 and 6 respectively, the isoparametric map gives

$$\underline{x} = \underline{x}_1 N_1(L_1) + \underline{x}_3 N_3(L_1) + \underline{x}_6 N_6(L_1), \tag{2.32}$$

from which the unit tangent and normal,

$$\hat{\underline{t}} = \left(\frac{dx}{dL_1}\hat{\underline{i}} + \frac{dy}{dL_1}\hat{\underline{j}}\right) / \left(\frac{ds}{dL_1}\right), \quad \hat{\underline{n}} = \left(-\frac{dy}{dL_1}\hat{\underline{i}} + \frac{dx}{dL_1}\hat{\underline{j}}\right) / \left(\frac{ds}{dL_1}\right), \tag{2.33}$$

can be found, where

$$\frac{ds}{dL_1} = \sqrt{\left(\frac{dx}{dL_1}\right)^2 + \left(\frac{dy}{dL_1}\right)^2}. \tag{2.34}$$

In order to calculate dN_k/ds in (2.15) the identity (Kistler and Scriven [1983]),

$$\frac{dN_k}{ds} = \hat{\underline{t}}.\nabla N_k = \frac{\partial N_k}{\partial L_1}\frac{\partial L_1}{\partial s}, \tag{2.35}$$

is used, and now the boundary contributions can be expressed as

$$(\underline{R}^k_m)_{\partial\Omega_{fs}} = \sum_{sides}\left\{\int_{L_1=0}^{1} \frac{(dx/dL_1\hat{\underline{i}} + dy/dL_1\hat{\underline{j}})}{ds/dL_1}\frac{dN_k}{dL_1}dL_1\right\} - \frac{1}{Ca}[N_k\hat{\underline{t}}_1 - N_k\hat{\underline{t}}_0], \tag{2.36}$$

where summation is over all element sides lying along the free surface.

2.1.7 Numerical Integration

The element-level integrals discussed above are evaluated numerically by a Gauss quadrature scheme which replaces each integral by a sum of weighted values of the integrand at n specific points, i.e.

$$\int_{A_0} f(\xi,\eta)|J|d\xi d\eta = \sum_{i=1}^{n} f(\xi_i,\eta_i)w_i, \tag{2.37}$$

where w_i are the weights corresponding to the n Gauss points, (ξ_i, η_i). Boundary integrals can be determined from

$$\int_{L_1=0}^{L_1=1} g(\xi)\frac{ds}{d\xi}d\xi = \sum_{i=1}^{n} g(\xi_i)w_i, \tag{2.38}$$

where ξ_i and w_i are the n respective Gauss points and weights for a one-dimensional integral.

The Gaussian quadrature formulae are derived by approximating the integrand by a

polynomial, whose order dictates the number of Gauss points required for exactness. Thompson [1992] investigated the effect of using different numbers of Gauss points and concluded that a 4-point scheme was sufficient for the area integrals arising here. Figure 2.8 shows the positions of the quadrature points and the associated weights, together with the 3-point scheme used for the boundary integrals.

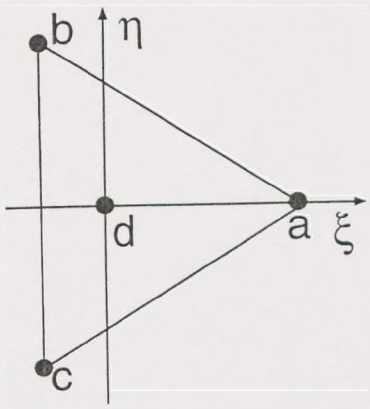

(a)

	ξ	η	ω
a	1	0	$\sqrt{3}/16$
b	-1/2	$\sqrt{3}/2$	$\sqrt{3}/16$
c	-1/2	$-\sqrt{3}/2$	$\sqrt{3}/16$
d	0	0	$9\sqrt{3}/16$

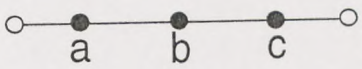

(b)

	L_1	ω
a	0.1127	5/18
b	0.5	4/9
c	0.8873	5/18

Figure 2.8: Gauss points and corresponding weights in (a) a 4-point quadrature scheme for domain integrals, and (b) a 3-point scheme for boundary (line) integrals.

2.1.8 Iterative technique

Even if $Re = 0$, the presence of a free surface makes the system of equations highly non-linear and an iterative method is necessary for their solution. In this study a Newton iteration scheme, first used by Saito and Scriven [1981], is employed due to its rapid convergence rate as the solution is approached. The system to be solved can be written as

$$\underline{R}(\underline{\alpha}) = \underline{0} \tag{2.39}$$

where

$$\underline{R} = \begin{Bmatrix} R^1_{mx} \\ R^1_{my} \\ \vdots \\ R^k_{mx} \\ R^k_{my} \\ R^1_c \\ \vdots \\ R^L_c \\ R^1_K \\ \vdots \\ R^S_K \end{Bmatrix}, \qquad \text{and} \qquad \underline{\alpha} = \begin{Bmatrix} \bar{u}_1 \\ \bar{v}_1 \\ \vdots \\ \bar{u}_k \\ \bar{v}_k \\ \bar{p}_1 \\ \vdots \\ \bar{p}_L \\ h_1 \\ \vdots \\ h_S \end{Bmatrix}, \tag{2.40}$$

are the vectors of residuals and unknowns respectively, and S represents the total number of spines throughout the domain. The iterative scheme is obtained from a Taylor expansion of (2.39) which gives, to first order,

$$\underline{R}(\underline{\alpha}_{n+1}) \approx \underline{R}(\underline{\alpha}_n) + \left[\frac{\partial \underline{R}}{\partial \underline{\alpha}}\right]_{\underline{\alpha}=\underline{\alpha}_n} \Delta\underline{\alpha}_n = \underline{0}, \tag{2.41}$$

where $\underline{\alpha}_n$ represents the vector of unknowns after n iterations and $\Delta\underline{\alpha}_n = \underline{\alpha}_{n+1} - \underline{\alpha}_n$. Hence at each iteration the matrix equation

$$\underline{\underline{J}}\Delta\underline{\alpha}_n = \left[\frac{\partial \underline{R}}{\partial \underline{\alpha}}\right]_{\underline{\alpha}=\underline{\alpha}_n} \Delta\underline{\alpha}_n = -\underline{R}(\underline{\alpha}_n), \tag{2.42}$$

must be solved for the increments $\Delta\underline{\alpha}_n$. Construction of the Jacobian matrix, $\underline{\underline{J}}$, requires the evaluation of the derivative of each residual with respect to each of the FE coefficients, and the element-level Jacobian takes the form

$$\underline{\underline{J}} = \begin{pmatrix} \frac{\partial R^i_{mx}}{\partial \bar{u}_j} & \frac{\partial R^i_{mx}}{\partial \bar{v}_j} & \frac{\partial R^i_{mx}}{\partial \bar{p}_k} & \frac{\partial R^i_{mx}}{\partial h_k} \\ \frac{\partial R^i_{my}}{\partial \bar{u}_j} & \frac{\partial R^i_{my}}{\partial \bar{v}_j} & \frac{\partial R^i_{my}}{\partial \bar{p}_k} & \frac{\partial R^i_{my}}{\partial h_k} \\ \frac{\partial R^l_c}{\partial \bar{u}_j} & \frac{\partial R^l_c}{\partial \bar{v}_j} & \underline{0} & \frac{\partial R^l_c}{\partial h_k} \\ \frac{\partial R^l_K}{\partial \bar{u}_j} & \frac{\partial R^l_K}{\partial \bar{v}_j} & \underline{0} & \frac{\partial R^l_K}{\partial h_k} \end{pmatrix}, \tag{2.43}$$

where $i, j = 1, .., 6$ and $k, l = 1, .., 3$. Once again the isoparametric mapping is used to simplify calculations.

It can be shown that the Newton iteration method gives quadratic convergence as the solution is approached (see, for example, Isaacson and Keller [1966]). This provides a useful check on the accuracy of the solution, for quadratic convergence would not be

achieved if there was a 'problem' (such as an incorrectly calculated Jacobian or excessive grid distortion). The process is stopped when the maximum increment is less than 10^{-10}. Solutions obtained must also be tested for accuracy by comparing solutions obtained on progressively finer grids. When there is a negligible difference between the solution on two grids, the coarser of the two can be viewed as guaranteeing grid independent solutions.

Note that the iterative method needs a starting point i.e. an initial estimate for $\underline{\alpha}$, say $\underline{\alpha}_0$. This $\underline{\alpha}_0$ is of crucial importance since convergence will not be achieved if it is not within a certain range of the converged solution. For viscous free surface flows the domain of convergence depends more on the free surface shape and position than it does on the velocity and pressure values (see Kistler and Scriven [1983]). A good estimate for this information can be obtained from experimental data or numerical results from previous authors. The domain of convergence can also be moderately improved by the use of relaxation factors (see Thompson [1992]), whereby only fractions of the updated changes called for by (2.42) are applied. Once a solution has been obtained, it can used as an initial guess to generate another, corresponding to a set of parameters in the neighbourhood of the first. This method, termed *Zeroth Order Continuation*, may be used to proceed through parameter space.

2.1.9 The frontal solution method

For problems with a large number of unknowns, the storage requirements for the matrix $\underline{\underline{J}}$ can become excessive, even if advantage is taken of any banded structure. When this is the case, a frontal method is employed.

The technique, developed by Irons [1970] and Hood [1976], is an adaptation of Gaussian elimination ideally suited to many finite element problems. The principle of the method is as follows: Each element level matrix is sequentially added into a larger 'global' matrix until that matrix is full. A pivotal search is made to determine the largest entry from those rows and columns to which there will be no further contribution from subsequent element assembly. Gaussian elimination is then used (with the pivotal row) to eliminate all the coefficients in the pivotal column. The pivotal row is then stored in an external file. The elimination process is repeated until enough space has been created for the assembly of further element-level matrices. When all elements have been assembled and the remaining coefficients eliminated, the increments $\Delta\underline{\alpha}_n$ can be determined by back substitution into the stored matrix rows.

The minimum size of the global matrix is dictated by the critical frontwidth, corresponding to the minimum number of elements which must be assembled to ensure that the matrix contains enough fully summed rows for the elimination-and-assembly process to continue. The numbering scheme for the elements is therefore crucial in determining the critical frontwidth. Generally, minimizing the range of element numbers surrounding each node will keep storage requirements to a minimum. The implementation of the frontal method used in this study was developed by Gaskell [1990] and subsequently refined by Thompson [1992].

Typical execution time:

For all the finite element base flows described in this thesis, the iteration time is approximately 35 c.p.u. seconds using a Silicon Graphics Indy workstation with a 150MHz, MIPS R5000 processor.

2.1.10 Post-processing

Determining the streamfunction:

Coyle [1984] showed how the streamfunction, ψ, can be found by solving the Poisson equation

$$\nabla^2\psi = \frac{\partial u}{\partial y} - \frac{\partial v}{\partial x} \tag{2.44}$$

over the domain Ω. The Galerkin weighted residual approach is again used, giving,

$$\int_\Omega N_k \left[\nabla^2\psi - \left(\frac{\partial u}{\partial y} - \frac{\partial v}{\partial x}\right)\right] d\Omega = 0, \tag{2.45}$$

which, after applying the vector identity

$$N_k\nabla.(\nabla\psi) \;=\; \nabla.(N_k\nabla\psi) - \nabla N_k.\nabla\psi \tag{2.46}$$

and the divergence theorem, becomes

$$\int_\Omega N_k\nabla^2\psi d\Omega \;=\; -\int_\Omega (\nabla N_k.\nabla\psi)d\Omega + \int_{\partial\Omega} N_k\frac{\partial\psi}{\partial n}ds. \tag{2.47}$$

With ψ specified as an essential condition at all boundaries, the boundary integral term need not be evaluated and the equation can be written in the linear form,

$$k_{ij}\psi_j \;=\; f_i, \tag{2.48}$$

where ψ is expanded in terms of the biquadratic shape functions, N_i, and

$$k_{ij} = \int_\Omega \left(\frac{\partial N_i}{\partial x}\frac{\partial N_j}{\partial x} + \frac{\partial N_i}{\partial y}\frac{\partial N_j}{\partial y} \right) d\Omega, \tag{2.49}$$

$$f_i = -\int_\Omega \left(\frac{\partial u}{\partial y} - \frac{\partial v}{\partial x} \right) d\Omega. \tag{2.50}$$

Calculations for the streamfunction were calculated using an algorithm written by Walker [1992].

Locating stagnation points:

Stagnation points in viscous flow structures are key features since any separation of the flow involves one or more of these. The initial step in locating them is to use linear interpolation of the velocity field to determine which elements contain a stagnation point; the FE representation for $\underline{u}$ can then be used to search for its position. The type of stagnation point can be inferred from the sign of

$$\left(\frac{\partial^2 \psi}{\partial x^2}\bigg|_{\underline{x}_0} \right) \left(\frac{\partial^2 \psi}{\partial y^2}\bigg|_{\underline{x}_0} \right) - \left(\frac{\partial^2 \psi}{\partial x \partial y}\bigg|_{\underline{x}_0} \right)^2, \tag{2.51}$$

where $\underline{x}_0$ is the position of the stagnation point. If expresssion (2.51) is negative in sign then the stagnation point is of hyperbolic type i.e. a saddle point. Otherwise, if (2.51) is positive is sign, the saddle point is of elliptic type i.e. a centre. The location and classification of stagnation points was determined using an algorithm written by Summers [1995].

2.2 Linear stability analysis based on the FEM

2.2.1 Introduction

For a specified flow domain, the finite element method produces a unique, steady solution. However, an important question concerning such solutions is whether or not the flow state predicted is stable to small disturbances, which are ever present in real systems.

Stability with respect to disturbances small enough to be regarded as infinitesimal is the subject of classical linear stability analysis, which proceeds as follows: a given solution to the governing equations and boundary conditions is subjected to a basis set of disturbance modes of infinitesimal amplitude from which any such disturbance could be composed. If all disturbances in the basis set decay in time, the steady state is, by definition, asymptotically stable; that is, once the source of the disturbance is removed the system eventually restores itself to the original flow state. If one or more of the basic disturbances grows in time, the steady state is unstable. The condition that divides these two classes of behaviour, where the disturbance neither grows nor decays in time, is termed *neutral stability*.

This section describes a rigorous way of analyzing stability by a combination of linear stability theory and the Galerkin finite element technique. This type of three dimensional stability analysis was first applied to coating flows by Bixler [1982] and Ruschak [1983], where a base flow was perturbed with an infinitesimal disturbance, represented by a series of Fourier modes in the transverse direction. Subsequently, Coyle [1984] and Coyle *et al* [1990] investigated the onset of ribbing in a symmetric, fully flooded, forward roll coater. They solved the steady 2-dimensional base flow, ignoring inertia and gravity, by the finite element method using a similar scheme to that presented in section 2.1. The stability was then tested for varying values of wave and capillary number and these results showed areas of parameter space where the system was stable. Christodoulou [1989] included the inertia terms (i.e. the $Re \neq 0$ case) and investigated the stability of slide coating as various geometrical parameters were varied.

2.2.2 Formulation of the equations

The first step in linear stability analysis is to perturb the steady state flow with an infinitesimal disturbance represented by a set of normal modes in the transverse (z)

direction, so this step is written as

$$\underline{u}(x,y,z,t) = \underline{u}^0(x,y) + \epsilon\underline{u}'(x,y)\underline{\underline{D}}(Nz)e^{\sigma t}, \tag{2.52}$$

$$p(x,y,z,t) = p^0(x,y) + \epsilon p'(x,y)cos(Nz)e^{\sigma t}, \tag{2.53}$$

$$h_i(z,t) = h_i^0 + \epsilon h_i' cos(Nz)e^{\sigma t}, \tag{2.54}$$

where

$$\underline{\underline{D}}(Nz) = \begin{pmatrix} cos(Nz) & 0 & 0 \\ 0 & cos(Nz) & 0 \\ 0 & 0 & sin(Nz) \end{pmatrix}, \tag{2.55}$$

N being the transverse wavenumber and σ is the growth rate of the perturbation. As $\epsilon \to 0$, $(u,v,w,p,h) \to (u^0,v^0,0,p^0,h^0)$ i.e. we reobtain the steady, 2-dimensional flow field.

The next step is to require that the 3-dimensional unsteady flow field satisfy the equations of motion throughout the domain, being the Navier-Stokes equation, the continuity condition and the kinematic condition (for free surfaces) i.e.

$$Re\frac{\partial \underline{u}}{\partial t} = -Re(\underline{u}.\nabla)\underline{u} + \nabla p + \mu\nabla^2\underline{u} + St\underline{f}, \tag{2.56}$$

$$0 = \nabla.\underline{u}, \tag{2.57}$$

$$\underline{n}.\frac{\partial \underline{x}}{\partial t} = \underline{n}.\underline{u}. \tag{2.58}$$

Note that, as before, the stress condition (equation (2.14)) is incorporated naturally into the momentum residuals on the free surface. After forming the Galerkin weighted residuals, using $N_i(x,y)\underline{\underline{D}}(Nz)$ (the basis functions) as the weighting functions, the equations are then linearised with respect to ϵ and the flow field expanded in finite element basis functions i.e.

$$\begin{aligned} \underline{u}^0 &= \Sigma\underline{u}_i^0 N_i(x,y), & \underline{u}' &= \Sigma\underline{u}_i' N_i(x,y), \\ p^0 &= \Sigma p_i^0 \psi_i(x,y), & p' &= \Sigma p_i' \psi_i(x,y), \\ h^0 &= \Sigma h_i^0 N_i(x,y), & h' &= \Sigma h_i' N_i(x,y). \end{aligned} \tag{2.59}$$

Differentiating both sides of the weighted residual equations with respect to the finite element coefficients of the perturbations $(\underline{u}', p', h')$ allows the equation set to be written as a generalized unsymmetric eigenproblem

$$\underline{\underline{J}}\underline{x} = \sigma\underline{\underline{M}}\underline{x}, \tag{2.60}$$

where $\underline{x}$ is the column vector $[u', v', w', p', h']^T$, $\underline{\underline{M}}$ is the mass matrix (arising from the time dependence) and $\underline{\underline{J}}$ is the Jacobian matrix. Here the Jacobian is the same as

that derived for the Newton iteration method calculation of the steady flow, with some additional terms stemming from the fact that the stability analysis is 3-dimensional. The construction of the Jacobian and mass matrices is shown below:

2.2.3 Derivation of the Jacobian matrix

The three basic parts of the Jacobian arise from the right-hand-sides of the momentum equation (2.56), continuity condition (2.57) and kinematic condition (2.58), the structure of which is

$$\underline{\underline{J}} = \begin{pmatrix} \frac{\partial R^i_{mx}}{\partial u'_j} & \frac{\partial R^i_{mx}}{\partial v'_j} & \frac{\partial R^i_{mx}}{\partial w'_j} & \frac{\partial R^i_{mx}}{\partial p'_k} & \frac{\partial R^i_{mx}}{\partial h'_k} \\ \frac{\partial R^i_{my}}{\partial u'_j} & \frac{\partial R^i_{my}}{\partial v'_j} & \frac{\partial R^i_{my}}{\partial w'_j} & \frac{\partial R^i_{my}}{\partial p'_k} & \frac{\partial R^i_{my}}{\partial h'_k} \\ \frac{\partial R^i_{mz}}{\partial u'_j} & \frac{\partial R^i_{mz}}{\partial v'_j} & \frac{\partial R^i_{mz}}{\partial w'_j} & \frac{\partial R^i_{mz}}{\partial p'_k} & \frac{\partial R^i_{mz}}{\partial h'_k} \\ \frac{\partial R^l_c}{\partial u'_j} & \frac{\partial R^l_c}{\partial v'_j} & \frac{\partial R^l_c}{\partial w'_j} & 0 & \frac{\partial R^l_c}{\partial h'_k} \\ \frac{\partial R^l_K}{\partial u'_j} & \frac{\partial R^l_K}{\partial v'_j} & 0 & 0 & \frac{\partial R^l_K}{\partial h'_k} \end{pmatrix}, \tag{2.61}$$

where $i, j = 1, .., 6$ and $k, l = 1, .., 3$. The method of deriving these quantities is as follows. The expressions for the flow field, (2.59), are inserted into the Jacobian weighted residuals. The resultant expression is linearised with respect to ϵ and the result is differentiated with respect to the primed finite element coefficients. The only z-dependence remains in factors of $\cos^2(Nz)$ or $\sin^2(Nz)$, either of which integrates analytically to produce a common factor of π/N. There is also a common factor of $e^{\sigma t}$ - it too can be cancelled across all of the equations.

Thus, the terms from the Jacobian become:

Kinematic equation:

$$\frac{\partial R^i_K}{\partial u'_j} = \int -y_\xi N_i N_j d\xi \tag{2.62}$$

$$\frac{\partial R^i_K}{\partial v'_j} = \int -x_\xi N_i N_j d\xi \tag{2.63}$$

$$\frac{\partial R^i_K}{\partial h'_j} = \int \left(-u \frac{\partial y_\xi}{\partial h_j} + v \frac{\partial x_\xi}{\partial h_j} \right) N_i d\xi \tag{2.64}$$

Continuity equation:

$$\frac{\partial R^i_c}{\partial u'_j} = \int \psi_i N_{j,x} |J| d\xi d\eta \tag{2.65}$$

$$\frac{\partial R_c^i}{\partial v_j'} = \int \psi_i N_{j,y} |J| d\xi d\eta \tag{2.66}$$

$$\frac{\partial R_c^i}{\partial w_j'} = N \int \psi_i N_j |J| d\xi d\eta \tag{2.67}$$

$$\frac{\partial R_c^i}{\partial h_j'} = \int\int \left(u_\xi \frac{\partial y_\eta}{\partial h_j} - u_\eta \frac{\partial y_\xi}{\partial h_j} - v_\xi \frac{\partial x_\eta}{\partial h_j} + v_\eta \frac{\partial x_\xi}{\partial h_j} \right) \psi_i d\xi d\eta \tag{2.68}$$

x-momemtum equation:

$$\frac{\partial R_{mx}^i}{\partial u_j'} = \int\int \Big[2N_{i,x}N_{j,x} + N_{i,y}N_{j,y} + N^2 N_i N_j$$

$$+ \; ReN_i(u_x N_j + uN_{j,x} + vN_{j,y})] \, |J| d\xi d\eta \tag{2.69}$$

$$\frac{\partial R_{mx}^i}{\partial v_j'} = \int\int [N_{i,y}N_{j,x} + Reu_y N_i N_j] |J| d\xi d\eta \tag{2.70}$$

$$\frac{\partial R_{mx}^i}{\partial w_j'} = -N \int\int N_i N_{j,x} |J| d\xi d\eta \tag{2.71}$$

$$\frac{\partial R_{mx}^i}{\partial p_j'} = -\int\int N_{i,x} \psi_j |J| d\xi d\eta \tag{2.72}$$

y-momemtum equation:

$$\frac{\partial R_{my}^i}{\partial u_j'} = \int\int [N_{i,x}N_{j,y} + Rev_x N_i N_j] |J| d\xi d\eta \tag{2.73}$$

$$\frac{\partial R_{my}^i}{\partial v_j'} = \int\int \Big[N_{i,x}N_{j,x} + 2N_{i,y}N_{j,y} + N^2 N_i N_j$$

$$+ \; ReN_i(v_y N_j + uN_{j,x} + vN_{j,y})] \, |J| d\xi d\eta \tag{2.74}$$

$$\frac{\partial R_{my}^i}{\partial w_j'} = -N \int\int N_i N_{j,y} |J| d\xi d\eta \tag{2.75}$$

$$\frac{\partial R_{my}^i}{\partial p_j'} = -\int\int N_{j,y} \psi_j |J| d\xi d\eta \tag{2.76}$$

z-momemtum equation:

$$\frac{\partial R_{mz}^i}{\partial u_j'} = -N \int\int N_{i,x} N_j |J| d\xi d\eta \tag{2.77}$$

$$\frac{\partial R^i_{mz}}{\partial v'_j} = -N \int\int N_{i,y} N_j |J| d\xi d\eta \tag{2.78}$$

$$\frac{\partial R^i_{mz}}{\partial w'_j} = \int\int \Big[N_{i,x} N_{j,x} + N_{i,y} N_{j,y} + 2N^2 N_i N_j$$

$$+ \; ReN_i(uN_{j,x} + vN_{j,y})\Big] |J| d\xi d\eta \tag{2.79}$$

$$\frac{\partial R^i_{mz}}{\partial p'_j} = -N \int\int N_i \psi_j |J| d\xi d\eta \tag{2.80}$$

Momentum equations - free surface derivatives:

$$\frac{\partial R^i_{mx}}{\partial h'_j} = \int\int \Bigg[(-p + 2u_x) \frac{\partial N_{i,x}|J|}{\partial h_j} + (u_y + v_x) \frac{\partial N_{i,y}|J|}{\partial h_j}$$

$$+ \; 2N_{i,x} \frac{\partial T_{xx}}{\partial h_j} + N_{i,y} \frac{\partial T_{xy}}{\partial h_j}$$

$$+ \; ReN_i u \left(u_\xi \frac{\partial y_\eta}{\partial h_j} - u_\eta \frac{\partial y_\xi}{\partial h_j} \right)$$

$$+ \; ReN_i v \left(-u_\xi \frac{\partial x_\eta}{\partial h_j} + u_\eta \frac{\partial x_\xi}{\partial h_j} \right)$$

$$+ \; StN_i \frac{\partial |J|}{\partial h_j} - N^2 \left(u_x \frac{\partial x}{\partial h_j} + u_y \frac{\partial y}{\partial h_j} \right) N_i |J| \Bigg] d\xi d\eta \tag{2.81}$$

$$\frac{\partial R^i_{my}}{\partial h'_j} = \int\int \Bigg[(u_y + v_x) \frac{\partial N_{i,x}|J|}{\partial h_j} + (-p + 2v_y) \frac{\partial N_{i,y}|J|}{\partial h_j}$$

$$+ \; N_{i,x} \frac{\partial T_{xy}}{\partial h_j} + 2N_{i,y} \frac{\partial T_{yy}}{\partial h_j}$$

$$+ \; ReN_i u \left(v_\xi \frac{\partial y_\eta}{\partial h_j} - v_\eta \frac{\partial y_\xi}{\partial h_j} \right)$$

$$+ \; ReN_i v \left(-v_\xi \frac{\partial x_\eta}{\partial h_j} + v_\eta \frac{\partial x_\xi}{\partial h_j} \right)$$

$$- \; N^2 \left(v_x \frac{\partial x}{\partial h_j} + v_y \frac{\partial y}{\partial h_j} \right) N_i |J| \Bigg] d\xi d\eta \tag{2.82}$$

$$\frac{\partial R^i_{mz}}{\partial h'_j} = N \int\int \left[-p \frac{\partial |J|}{\partial h_j} N_i / |J| - p \left(N_{i,x} \frac{\partial x}{\partial h_j} + N_{i,y} \frac{\partial y}{\partial h_j} \right) \right.$$

$$+ \quad N_{i,x}\left(u_x\frac{\partial x}{\partial h_j}+u_y\frac{\partial y}{\partial h_j}\right)$$

$$+ \quad N_{i,y}\left(v_x\frac{\partial x}{\partial h_j}+v_y\frac{\partial y}{\partial h_j}\right)\Bigg]|J|d\xi d\eta \tag{2.83}$$

where,

$$\begin{aligned}
\frac{\partial T_{xx}}{\partial h_j} &= \left(u_\xi\frac{\partial \xi_x}{\partial h_j}+u_\eta\frac{\partial \eta_x}{\partial h_j}\right)|J| \\
\frac{\partial T_{yy}}{\partial h_j} &= \left(v_\xi\frac{\partial \xi_y}{\partial h_j}+v_\eta\frac{\partial \eta_y}{\partial h_j}\right)|J| \\
\frac{\partial T_{xy}}{\partial h_j} &= \left(u_\xi\frac{\partial \xi_y}{\partial h_j}+u_\eta\frac{\partial \eta_y}{\partial h_j}+v_\xi\frac{\partial \xi_x}{\partial h_j}+v_\eta\frac{\partial \eta_x}{\partial h_j}\right)|J|
\end{aligned}$$

Momentum boundary integral over free surface:

$$\begin{aligned}
\frac{\partial R^i_{mx}}{\partial h'_j} &= \frac{1}{Ca}\int\int\left[\frac{1}{g^{1/2}}\frac{\partial x_\xi}{\partial h_j}N_{i,\xi}-\frac{x_\xi}{g^{3/2}}\left(x_\xi\frac{\partial x_\xi}{\partial h_j}+y_\xi\frac{\partial y_\xi}{\partial h_j}\right)N_{i,\xi}\right. \\
&\quad - \left. N^2\frac{y_\xi}{g^{1/2}}\left(x_\xi\frac{\partial y_z}{\partial h_j}-y_\xi\frac{\partial x_z}{\partial h_j}\right)N_i\right]d\xi \qquad (2.84) \\
\frac{\partial R^i_{my}}{\partial h'_j} &= \frac{1}{Ca}\int\int\left[\frac{1}{g^{1/2}}\frac{\partial y_\xi}{\partial h_j}N_{i,\xi}-\frac{y_\xi}{g^{3/2}}\left(x_\xi\frac{\partial x_\xi}{\partial h_j}+y_\xi\frac{\partial y_\xi}{\partial h_j}\right)N_{i,\xi}\right. \\
&\quad + \left. N^2\frac{x_\xi}{g^{1/2}}\left(x_\xi\frac{\partial y_z}{\partial h_j}-y_\xi\frac{\partial x_z}{\partial h_j}\right)N_i\right]d\xi \qquad (2.85) \\
\frac{\partial R^i_{mz}}{\partial h'_j} &= \frac{N}{Ca}\int\int\left[\frac{1}{g^{1/2}}\left(x_\xi\frac{\partial x_\xi}{\partial h_j}+y_\xi\frac{\partial y_\xi}{\partial h_j}\right)N_i\right. \\
&\quad + \left.\left(x_\xi\frac{\partial x_z}{\partial h_j}+y_\xi\frac{\partial y_z}{\partial h_j}\right)N_{i,\xi}\right]d\xi \qquad (2.86)
\end{aligned}$$

where g is defined by

$$g = x_\xi^2+y_\xi^2.$$

These free surface derivatives are computed by the chain rule and the isoparametric mapping e.g.

$$\begin{aligned}
x_\xi &= \Sigma x_i N_{i,\xi}, \\
|J| &= x_\xi y_\eta - x_\eta y_\xi,
\end{aligned}$$

and so

$$\begin{aligned}\frac{\partial N_{i,x}|J|}{\partial h_j} &= N_{i,\xi}\frac{\partial y_\eta}{\partial h_j} - N_{i,\eta}\frac{\partial y_\xi}{\partial h_j},\\ \frac{\partial N_{i,y}|J|}{\partial h_j} &= -N_{i,\xi}\frac{\partial x_\eta}{\partial h_j} + N_{i,\eta}\frac{\partial x_\xi}{\partial h_j}.\end{aligned}$$

2.2.4 Derivation of the mass matrix

The mass matrix arises from the time dependent terms in the governing equations. Those terms arising from the momentum equations that are proportional to Re are detailed by Bixler [1982]. They are not shown here because they are neglected, an approximation that is discussed in section 2.2.6. Thus, the mass matrix takes the form

$$\underline{\underline{M}} = \begin{pmatrix} 0 & 0 & 0 & 0 & 0 \\ 0 & 0 & 0 & 0 & 0 \\ 0 & 0 & 0 & 0 & 0 \\ 0 & 0 & 0 & 0 & 0 \\ 0 & 0 & 0 & 0 & M_{ij}^K \end{pmatrix}, \tag{2.87}$$

the only remaining time derivatives, M_{ij}^K, arising from the kinematic boundary condition (i.e. the elements directly on the free surface). Assuming no inter-dependent spines are present this is simply

$$M_{ij}^K = \int \left(-y_\xi \frac{\partial x_j}{\partial h_j} + x_\xi \frac{\partial y_j}{\partial h_j} \right) N_i N_j d\xi, \tag{2.88}$$

$(i, j = 1, .., 3)$ as reported by Coyle [1984].

Effect of inter-dependent spines:

The presence of inter-dependent spines only has an effect on the time-dependent portion of the kinematic boundary condition. The Galerkin weighted residual of this equation is

$$\int_{fs} \underline{n}.\frac{\partial \underline{x}^{fs}}{\partial t} N_i cos(Nz) ds = \int_{fs} \underline{n}.\underline{u} N_i cos(Nz) ds. \tag{2.89}$$

Because $\frac{\partial \underline{x}^{fs}}{\partial t}$, $\underline{n}$ and $\underline{u}$ are of order ϵ in the z-direction and dot products are being formed, the z-dimension enters first at $O(\epsilon^2)$. Thus only two-dimensional forms need to be considered.

Thus, after substituting (2.54) into (2.18) and differentiating with respect to time, the following equation is obtained:

$$\begin{aligned}\frac{\partial \underline{x}_j^{fs}}{\partial t} &= \epsilon\sigma e^{\sigma t} h'_d cos(Nz)\underline{\hat{e}}_d w_j \\ &+ \epsilon\sigma e^{\sigma t} h'_j cos(Nz)\underline{\hat{e}}_j \\ &+ h_j \frac{\partial \underline{\hat{e}}_j}{\partial t}. \end{aligned} \tag{2.90}$$

Inserting this into the left hand side of equation (2.89) and cancelling the common factor of $e^{\sigma t}\pi/N$ gives, to order ϵ,

$$\begin{aligned} LHS &= \int (\underline{n}.\underline{\hat{e}}_j) h'_j N_j N_i d\xi \\ &+ \int (\underline{n}.\underline{\hat{e}}_d) h'_d w_j N_j N_i d\xi \\ &+ \int (\underline{n}.\frac{\partial \underline{\hat{e}}_j}{\partial h_d^0}) h'_d h_j^0 N_j N_i d\xi. \end{aligned} \tag{2.91}$$

The ij-component of the mass matrix is $\frac{1}{\sigma}\frac{\partial(LHS)}{\partial h'_j}$, and so

$$\begin{aligned} M_{ij}^K &= \int (\underline{n}.\underline{\hat{e}}_j) N_j N_i d\xi \\ &+ \delta_{j4} \int (\underline{n}.\underline{\hat{e}}_d) w_j N_j N_i d\xi \\ &+ \delta_{j4} \int (\underline{n}.\frac{\partial \underline{\hat{e}}_j}{\partial h_d^0}) h_j^0 N_j N_i d\xi. \end{aligned} \tag{2.92}$$

The first term on the right hand side of equation (2.92) is identical to equation (2.88) i.e. the case where no inter-spine dependencies are present. The second and third terms are due to the inter-spine dependency and are only non-zero when the free surface node is dependent on the extra (4th) spine. Because any element can now depend on four spines, the local matrix is now of size (3×4) (as opposed to (3×3) with no extra spine dependencies).

2.2.5 Inclusion of a dynamic contact line

When a dynamic contact line is present in the geometry, an extra equation is necessary to solve for its location (see section 2.1.5); this equation forms an extra residual in the finite element analysis. On inclusion into the finite element stability analysis, the z-dimension enters first at $O(\epsilon^2)$ and so only two-dimensional forms need to be considered.

The structure of the Jacobian is thus,

$$\underline{\underline{J}} = \begin{pmatrix} \frac{\partial R^l_{\varrho}}{\partial u'_j} & \frac{\partial R^l_{\varrho}}{\partial v'_j} & \frac{\partial R^l_{\varrho}}{\partial w'_j} & \frac{\partial R^l_{\varrho}}{\partial p'_k} & \frac{\partial R^l_{\varrho}}{\partial h'_k} \\ \frac{\partial R^i_{mx}}{\partial u'_j} & \frac{\partial R^i_{mx}}{\partial v'_j} & \frac{\partial R^i_{mx}}{\partial w'_j} & \frac{\partial R^i_{mx}}{\partial p'_k} & \frac{\partial R^i_{mx}}{\partial h'_k} \\ \frac{\partial R^i_{my}}{\partial u'_j} & \frac{\partial R^i_{my}}{\partial v'_j} & \frac{\partial R^i_{my}}{\partial w'_j} & \frac{\partial R^i_{my}}{\partial p'_k} & \frac{\partial R^i_{my}}{\partial h'_k} \\ \frac{\partial R^i_{mz}}{\partial u'_j} & \frac{\partial R^i_{mz}}{\partial v'_j} & \frac{\partial R^i_{mz}}{\partial w'_j} & \frac{\partial R^i_{mz}}{\partial p'_k} & \frac{\partial R^i_{mz}}{\partial h'_k} \\ \frac{\partial R^l_c}{\partial u'_j} & \frac{\partial R^l_c}{\partial v'_j} & \frac{\partial R^l_c}{\partial w'_j} & 0 & \frac{\partial R^l_c}{\partial h'_k} \\ \frac{\partial R^i_K}{\partial u'_j} & \frac{\partial R^i_K}{\partial v'_j} & 0 & 0 & \frac{\partial R^i_K}{\partial h'_k} \end{pmatrix}, \tag{2.93}$$

where $i, j = 1, ..6$ and $k, l = 1, .., 3$.

2.2.6 Method of solution

Once the Jacobian and mass matrix are both evaluated, the generalised unsymmetric eigenproblem, (2.60), should ideally be solved for all the eigenvalues (and associated eigenvectors). If all the eigenvalues are negative the disturbances decay in time and the system would be 3-dimensionally stable. If at least one eigenvalue is positive the disturbance grows in time and the system is unstable. If the largest eigenvalue is zero then the system is neutrally stable, the disturbance neither growing nor decaying. However, because the continuity condition contains no time derivatives, $\underline{\underline{M}}$ is singular and so (2.60) has fewer eigenvalues than its dimension (see Stewart [1973], Golub and Van Loan [1983]). It is common to refer to the missing eigenvalues as "infinite eigenvalues" because if $\underline{\underline{M}}$ is perturbed slightly so that it is no longer singular, very large eigenvalues appear that grow unboundedly as the perturbation is reduced to zero. Before any attempt to solve (2.60) (to compute the eigenvalues/eigenvectors), the infinite eigenvalues have to be eliminated - otherwise they will be calculated before any of the ones that govern the stability of the flow. This can be achieved by means of the "shift and invert" transformation in which (2.60) is rewritten as

$$[(\underline{\underline{J}} - \lambda\underline{\underline{M}}] - (\sigma - \lambda)\underline{\underline{M}}]\underline{x} \;=\; 0, \tag{2.94}$$

where λ is termed the shift, allowing it to be transformed into the simple eigenproblem

$$\begin{aligned} \underline{\underline{A}}\,\underline{x} &= \mu\underline{x}, \\ \underline{\underline{A}} &= [\underline{\underline{J}} - \lambda\underline{\underline{M}}]^{-1}\underline{\underline{M}}, \\ \mu &= \frac{1}{\sigma - \lambda}. \end{aligned} \tag{2.95}$$

Using (2.94), the infinite eigenvalues of (2.60) become zero eigenvalues of (2.95). As Bixler [1982] and Christodoulou [1989] noted though, since the rank of $\underline{\underline{M}}$ is typ-

ically of the order 1000-2000, standard algorithms which compute all the eigenvalues/eigenvectors cannot be used for they would be too computationally expensive. However, the stability of the flow is dictated by the eigenvalues with the largest real parts, termed the "leading eigenvalues" and so it is then necessary only to calculate the eigenvalues that are, or are candidates to become, the leading ones. Unfortunately, the Arnoldi method, which can then be used to solve (2.95), favours the eigenvalues closest to the shift, λ, whereas the eigenvalues with algebraically largest real parts are wanted. Hence, another transformation which amplifies the leading part of the spectrum of (2.60) is required (see Christodoulou and Scriven [1990]).

Carvalho [1995], using this method, later analyzed the stability of flow in forward roll coating with one of the rolls covered by a layer of elastomer. He showed that for free surface flows the perturbations of nodes in the interior of the domain are not relevant to the stability of the flow. Hence, by not including the perturbation of the finite element interior nodes, the size of the eigenproblem and thereby the computational cost can be substantially reduced.

An alternative way to solve (2.60), and the one adopted in this thesis, is to follow the approach of Ruschak [1983], Coyle [1984] and Coyle *et al* [1990]. They considered the case when the Reynolds number was equal to zero for which the problem is greatly simplified - the only time dependent contributions to the equation set come from the kinematic boundary condition which is associated with the number of free surface nodes, F. Hence there are now only F eigenvalues that need to be evaluated. The remaining entries in the Jacobian and mass matrix can be eliminated using the frontal solver leaving a much smaller problem to be solved. The problem is now of a size that can be tackled by traditional methods and in this form the mass matrix is not singular. We can now rewrite (2.60) in a more conventional eigenvalue form as

$$\underline{\underline{M^*}}^{-1}\underline{\underline{J^*}}\underline{x} = \sigma \underline{\underline{I}}\underline{x}, \tag{2.96}$$

where $\underline{\underline{I}}$ is the identity matrix and $\underline{\underline{J^*}}$ and $\underline{\underline{M^*}}$ are the modified Jacobian and mass matrices respectively. Matrix inversion and multiplication are performed using NAG routines F07ADF, F07AJF and F01CKF. All the eigenvalues of (2.96) are then calculated using NAG routine F02AFF, from which the largest is taken to ascertain the stability.

Chapter 3

Onset of the Ribbing Instability in Inlet Flooded Reverse Roll Coating

Contents

3.1 Introduction 57

3.1.1 Outline of this chapter 60

3.2 Analysis based on lubrication theory **62**

3.2.1 Mathematical model 62

3.2.2 Method of solution 70

3.2.3 Discussion of Results 72

3.2.4 Comparison with the Stability Hypothesis (S.H.) 75

3.3 A computational approach **83**

3.3.1 Numerical solution of the base flow 83

3.3.2 Stability of the FE base flow 87

3.4 The effect of a hydrostatic head **89**

3.4.1 Mathematical model 90

3.4.2 Discussion of results 96

3.5 An improved model of the contact line region **101**

3.5.1 A general model for the dynamic contact line region 101

3.5.2 Small capillary number asymptotics for the contact line 103

3.5.3 Effect of Shikhmurzaev's asymptotic theory on the base flow . 106

3.5.4 Effect of Shikhmurzaev's asymptotic theory on the onset of ribbing 106

3.6 Conclusions **109**

3.1 Introduction

The origins of reverse roll coating date back over 65 years (Munch [1932]), since when it has become an important coating method due to its versatility, speed and precision. Indeed, it is capable of producing uniform films of thickness less than $25\mu m$ at speeds of 0.5-$9m/s$, using liquids ranging in viscosity from 0.001 to 50 Pas. Consequently, it has become a widely used technique for the manufacture of products such as magnetic and adhesive tapes, films, foils and paper (see Booth [1974], Higgins [1965] and Satas [1984]). The main drawbacks of using such a device are that it is unable to simultaneously coat multi-layer films while the final film thickness is dependent on the minimum gap separation (see Coyle [1984]). The method is also highly susceptible to instabilities such as ribbing (where lines of crests and troughs are observed in the direction of the moving web) and cascade (where the flow becomes time-dependent). It is thus clear that a full theoretical description of the process would be of great value to industry in order to determine parameter ranges where these instabilities are encountered and the desired steady 2-dimensional flow is achieved.

Reverse roll coating, in which fluid flows in the narrow gap between two co-rotating cylinders (see figure 3.1), has not received quite the same attention as the forward case. Broughton, Egan and Sturken [1950] established experimentally an empirical, linear relationship between the final film thickness and both speed ratio, S, and minimum gap separation (where $S = U_1/U_2$ is the ratio of the upper roll speed to the lower roll speed). They also noted the importance of U_2 as an additional control parameter. Ho and Holland [1978], Benkreira *et al* [1981] and Greener and Middleman [1981] presented lubrication type models which predicted that the coating thickness reduced as S is increased, although the results are only valid over a limited, but useful range of parameter space.

Coyle [1984] and then later Fukazawa *et al* [1992] solved the full steady state Navier-Stokes equations by a finite element method for the reverse roll, half problem consisting of a domain that extends from the downstream meniscus to a plane, close to the nip, on which lubrication conditions are imposed. Their results show that as S increases from zero, the dimensionless final film thickness, H_2, decreases initially and then, at some higher value of S, H_2 reaches a minimum beyond which it increases sharply. Coyle's results, later confirmed by Kang and Liu [1991] show that the minimum film thickness, H_2^{min}, corresponds to the point at which the wetting line penetrates the minimum gap and the sharp upturn in film thickness follows once the wetting line moves upstream of

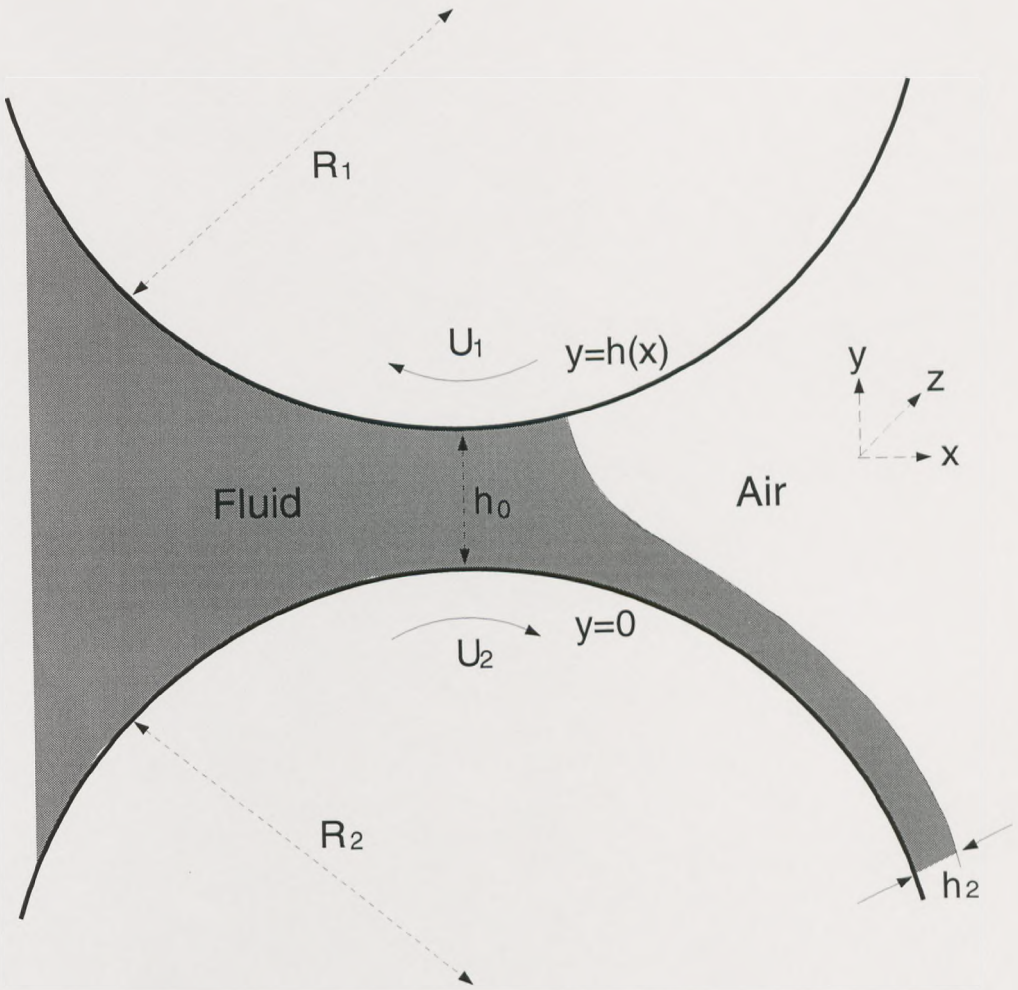

Figure 3.1: Schematic of an inlet flooded reverse roll coater.

the nip. In addition, Coyle showed that decreasing Ca (where $Ca = \mu U_2/T$) has little effect on H_2 at low values of S. However, H_2^{min} was shifted to a higher value of S and thus thinner coatings can be produced at lower Ca since a higher S can be achieved before the sharp upturn in film thickness occurs.

Fukazawa [1992] realised that by extending the lubrication model to incorporate more realistic boundary conditions at the downstream meniscus, the film thickness prediction could be improved. By modelling the meniscus using the arc of a circle and applying the Landau-Levich [1942] expression at the downstream outlet, the final film thickness, H_2, was predicted allowing for capillary and viscous effects at the downstream free surface. However, their analytical results are only valid for very small Ca, $Ca \leq 10^{-2}$.

Coyle [1984] considered the two free surface problem and found that for a dimensionless

inlet film thickness $H_i > 1$ the solution downstream of the nip is virtually identical to that obtained via the inlet flooded model. Richardson [1996] investigated the reverse roll coating process under different degrees of inlet starvation (including $H_i < 1$) for which various flow structures were established and their evolution followed as parameters varied. He determined the velocity and pressure fields, and the downstream film thickness and found that, contrary to the assertion made by Coyle *et al* [1990b], lubrication theory predictions are in close accord with those obtained numerically provided the wetting line is located downstream of the nip. For larger values of S, when the wetting line passes through the nip, his FEM results showed that thinner films could be obtained by either reducing h_0/R (the ratio of minimum gap width between the rolls to the average radius of the rolls) or Ca, results which are in accord with Coyle [1984].

The stability of the 2-dimensional flow in reverse roll coating was considered experimentally by Greener and Middleman [1981] who noted that it is more robust and less prone to the ribbing instability than forward roll coating. At sufficiently low values of Ca, Coyle [1984] showed experimentally that the flow of a Newtonian fluid is stable for all values of speed ratio, S. For higher values of Ca instabilities may occur, but Booth [1970] identified a stable window of operation i.e. a range of S for which the flow is stable and a defect free film is produced - see figure 3.2. Ribbing arises when S is below this range and an instability known as Cascade (see Coyle [1984], Coyle *et al* [1990a]) arises when S lies above this range. Coyle [1984] showed that the stable operating region can be enlarged, shifted or even eliminated when the gap ratio, h_0/R is varied. Further, it was shown that for particular values of S there are two ranges of Ca in which the base flow is stable (separated by an unstable range), see figure 3.2. For each Ca there is also a speed ratio beyond which no ribs occur (and a particular value of S, S^{min}, such that no ribbing occurs if $S > S^{min}$ for any Ca). This is unlike forward roll coating where the speed ratio has no such stabilising effect. This was also confirmed experimentally by Adachi *et al* [1988] who concluded that controlling the dynamic contact angle is the key to the control of this instability and this could be achieved easily by altering the various operating parameters.

In the case of inlet starved, reverse roll coating, the downstream free surface region will clearly exhibit the same type of instabilities as for a flooded inlet (ribbing, cascade etc). However, unlike the inlet flooded case, experiments show that the cascade instability causes the entire coating bead to oscillate at the same frequency as the cross web bars on the downtream film (Coyle [1984]). Recent experiments by Kapur [1998]

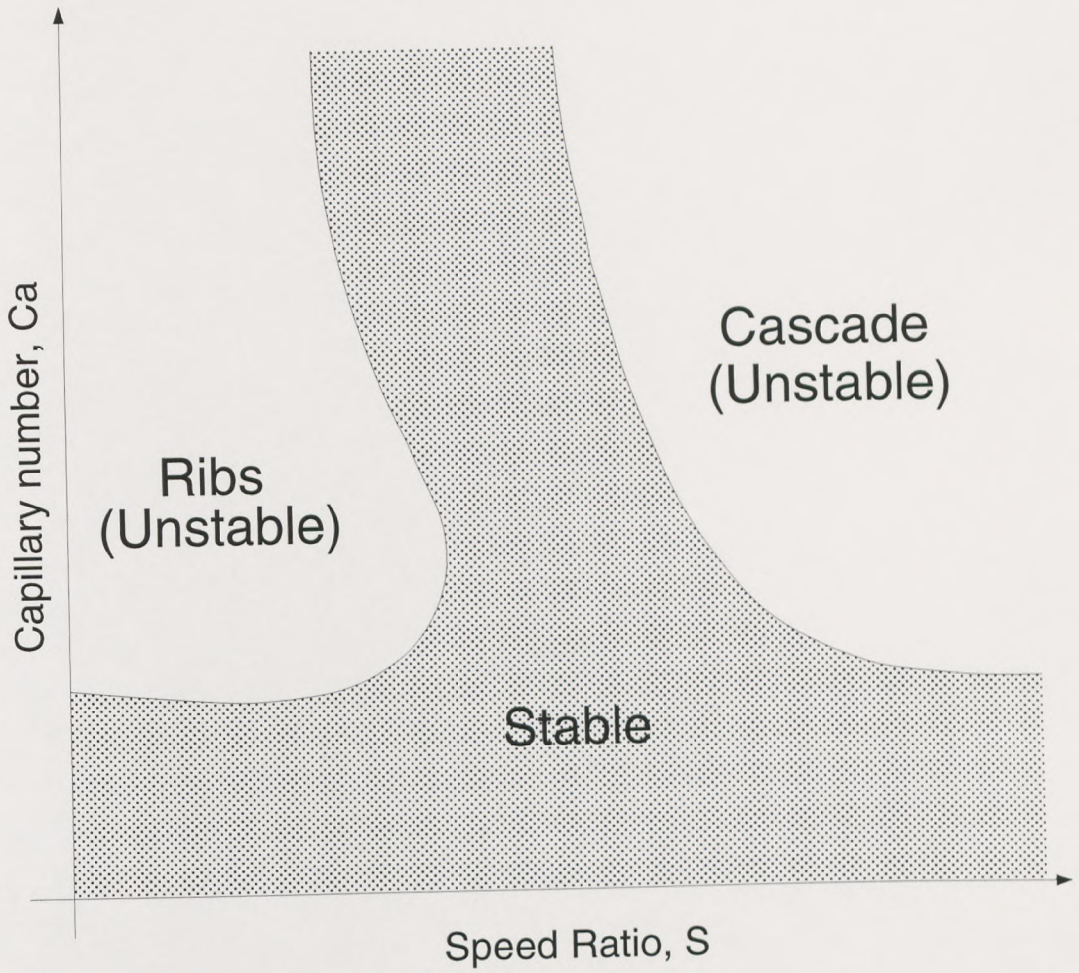

Figure 3.2: Typical $Ca - S$ operability diagram for a given value of h_0/R showing a stable window of operation.

have also shown that a two dimensional instability known as *bead break* (see chapter 4) may also manifest itself - the downstream free surface becomes unstable under certain operating conditions and the entire coating bead collapses.

3.1.1 Outline of this chapter

The aim of this chapter is to analyse the ribbing instability in inlet flooded, reverse roll coating. This is first investigated in section 3.2 by considering a 3-dimensional perturbation to a 2-dimensional base flow in the absence of gravity, from which regions of instability in the $Ca-S$ control space are established which are in qualitative agreement

with experimental observations. Results from this linear stability analysis are then compared with predictions obtained using a stability hypothesis; Pitts and Greiller [1960] and Savage [1977] independently formulated such a hypothesis for the onset of ribbing and derived a stability criterion by considering a force balance at the fluid-air interface. It was shown that the downstream interface would remain stable to small disturbances provided

$$\frac{d}{dx}\left(p + T/r\right) \leq 0,$$

where r represents the radius of curvature of the meniscus and p the pressure.

In section 3.3, results from the linear stability analysis carried out in section 3.2 are compared with those obtained numerically by applying linear stability theory to the finite element method (see chapter 2).

The effect of gravity on the ribbing instability has, to date, not been discussed in the literature and is investigated in section 3.4. This is a problem of practical interest (see Gaskell, Kapur, Thompson, Savage and Abbott [1998]) where the nip is fed from above by a large reservoir of fluid (i.e. a hydrostatic head). Hence an inlet flooded model is considered which introduces two extra operating parameters namely the *Stokes number* and non-dimensional height of the head, both of which are seen to have an influence on the base flow and stability.

For convenience, a constant dynamic contact angle, θ_d, is imposed in sections 3.2-3.4. However, in section 3.5 a more accurate representation of the wetting line, recently developed by Shikhmurzaev [1993,1994,1996], is incorporated where θ_d is related to several geometrical and hydrodynamic parameters.

3.2 Analysis based on lubrication theory

3.2.1 Mathematical model

An analytical model, based on lubrication theory, is presented from which the effects of Ca, S and h_0/R on the velocity and pressure field, together with the meniscus location, are determined. After applying linear stability theory to this base flow, the the onset of the ribbing instability is then investigated by obtaining critical curves in the $Ca - S$ control space.

3.2.1.1 Base flow

Neglecting body forces, transient and inertia terms, the Navier-Stokes equations reduce to

$$0 = -\nabla p + \mu \nabla^2 \underline{u}. \tag{3.1}$$

Assuming unidirectional flow through the nip and that velocity gradients across the bead are negligible i.e. $\partial u/\partial x << \partial u/\partial y$ then (3.1) becomes

$$\frac{\partial p}{\partial x} = \mu \frac{\partial^2 u}{\partial y^2} \tag{3.2}$$

and

$$\frac{\partial p}{\partial y} = 0. \tag{3.3}$$

Hence $p = p(x)$ and therefore integrating (3.2) twice and imposing the no slip boundary conditions on the rolls i.e.

$$\begin{aligned} u &= U_2 \text{ at } y = 0 \\ u &= -U_1 \text{ at } y = h(x) \end{aligned} \tag{3.4}$$

gives

$$u = \frac{1}{2\mu}\frac{dp}{dx} y(y-h) - (U_1 + U_2)\frac{y}{h} + U_2, \tag{3.5}$$

where $h(x)$ is the gap width between the two rolls. This is estimated by a parabolic approximation for the gap thickness,

$$h(x) \simeq h_0 + \frac{x^2}{R}, \tag{3.6}$$

where R is an average roll radius given by

$$\frac{2}{R} = \frac{1}{R_1} + \frac{1}{R_2}, \tag{3.7}$$

R_1 and R_2 being the radii of the upper and lower roll respectively. The flux Q is given by

$$Q = \int_0^{h(x)} u dy \tag{3.8}$$

which, using (3.5), becomes

$$Q = -\frac{1}{12\mu}\frac{dp}{dx}h^3 + (U_2 - U_1)\frac{h}{2}. \tag{3.9}$$

In equilibrium, the flux past any station x is constant and equal to the flux in the uniform film of thickness h_2 attached to the lower roll,

$$Q = h_2 U_2. \tag{3.10}$$

Therefore,

$$\frac{dp}{dx} = \frac{12\mu}{h^2}\left(\frac{(U_2 - U_1)}{2} - U_2\frac{h_2}{h}\right). \tag{3.11}$$

Boundary conditions on pressure are i) the flooded inlet condition - that the pressure far upstream of the nip is atmospheric i.e.

$$p(-\infty) = 0, \tag{3.12}$$

and ii) a balance of fluid pressure and surface tension pressure at the meniscus,

$$p(x_d) = \frac{-T}{r_d}, \tag{3.13}$$

where r_d is the radius of curvature of the meniscus. The meniscus is approximated by a circular arc which meets the film tangentially and intersects the upper roll surface at an angle θ_d, corresponding to the dynamic contact angle. Hence, at the downstream meniscus, $x = x_d$, the width of the gap can be approximated by (Fukazawa [1992])

$$h_d = r_d(1 + \cos(\theta_d)) + h_2. \tag{3.14}$$

Although the contact angle is dependent on several hydrodynamic parameters (see chapter 1), it is, for convenience, given a constant value of 90° in the first instance. Subsequently, a model developed by Shikhmurzaev [1993a] which relates the variation of contact angle to several geometrical and hydrodynamic parameters is incorporated, see section 3.5. Since x_d is unknown a third boundary condition is required which, for $Ca < 0.01$, is provided by the Landau-Levich [1942] relationship for the ratio of the asymptotic film thickness, h_2, to the radius of curvature, r_d,

$$\frac{h_2}{r_d} = 1.34Ca^{2/3}. \tag{3.15}$$

For higher values of Ca, i.e. $0.01 \leq Ca \leq 0.1$, Ruschak [1981] proposed a relationship of the form

$$\frac{h_2}{r_d} = 0.56Ca^{1/2}. \tag{3.16}$$

Using (3.14), together with $\theta_d = 90°$, the following expressions are obtained:

$$\alpha_d = \frac{h_2}{h_d} = \begin{cases} \frac{0.56Ca^{1/2}}{1+0.56Ca^{1/2}} & 10^{-2} \leq Ca \leq 10^{-1} \\ \\ \frac{1.34Ca^{2/3}}{1+1.34Ca^{2/3}} & Ca < 10^{-2}, \end{cases} \tag{3.17}$$

$$\beta_d = \frac{h_d}{r_d} = \begin{cases} 1 + 0.56Ca^{1/2} & 10^{-2} \leq Ca \leq 10^{-1} \\ \\ 1 + 1.34Ca^{2/3} & Ca < 10^{-2}. \end{cases} \tag{3.18}$$

Introducing non-dimensional variables defined by

$$\begin{aligned} H &= \frac{h}{h_0}, \\ H_2 &= \frac{h_2}{h_0}, \\ X &= \frac{x}{\sqrt{Rh_0}}, \\ S &= \frac{U_1}{U_2}, \\ P &= \frac{h_0}{\mu U_2}\sqrt{\frac{h_0}{R}}p, \end{aligned}$$

and writing $X = \tan(\gamma)$ (so $h(\gamma) = h_0 \sec^2\gamma$), then Reynolds equation, (3.11), becomes

$$\frac{dP}{d\gamma} = 6(1-S)\cos^2\gamma - 12H_2\cos^4\gamma. \tag{3.19}$$

If (3.19) is integrated between the limits $-\pi/2$ and $\bar{\gamma}$, where $\bar{\gamma}$ marks the position of the meniscus ($X_D = \tan(\bar{\gamma})$) and $\gamma \to -\pi/2$ as $X \to -\infty$, then, using (3.12),

$$\begin{aligned} P(\bar{\gamma}) &= 3(1-S)\left[\frac{\sin 2\bar{\gamma}}{2} + \bar{\gamma} + \frac{\pi}{2}\right] \\ \\ &- \frac{3H_2}{2}\left[\frac{sin4\bar{\gamma}}{4} + 2\sin 2\bar{\gamma} + 3\bar{\gamma} + \frac{3\pi}{2}\right]. \end{aligned} \tag{3.20}$$

Also, from (3.13),

$$p(\bar{\gamma}) = -\frac{T}{r_d}. \tag{3.21}$$

This, using (3.14) and (3.18), gives

$$p(\bar{\gamma}) = -\frac{\beta_d \mu U_2}{Ca h_0 \sec^2 \bar{\gamma}}, \tag{3.22}$$

which when non-dimensionalised becomes

$$P(\bar{\gamma}) = -\frac{\beta_d}{Ca \sec^2 \bar{\gamma}} \sqrt{\frac{h_0}{R}}. \tag{3.23}$$

Equating (3.20) and (3.23) yields the following equation for $\bar{\gamma}$ which is then solved once h_0/R, S and Ca are specified:

$$-\sqrt{\frac{h_0}{R}} \frac{\beta_d}{Ca \sec^2 \bar{\gamma}} = 3(1-S)\left[\frac{\sin 2\bar{\gamma}}{2} + \bar{\gamma} + \frac{\pi}{2}\right]$$

$$- \frac{3\alpha_d}{2} \sec^2 \bar{\gamma} \left[\frac{sin4\bar{\gamma}}{4} + 2\sin 2\bar{\gamma} + 3\bar{\gamma} + \frac{3\pi}{2}\right]. \tag{3.24}$$

The pressure distribution is then obtained by integrating (3.19) between the limits $-\pi/2$ and γ, giving

$$P(\gamma) = 3(1-S)\left[\frac{\sin 2\gamma}{2} + \gamma + \frac{\pi}{2}\right]$$

$$- \frac{3H_2}{2}\left[\frac{sin4\gamma}{4} + 2\sin 2\gamma + 3\gamma + \frac{3\pi}{2}\right], \tag{3.25}$$

where $H_2 = \alpha_d \sec^2 \bar{\gamma}$.

Figure 3.3 shows pressure profiles for $Ca = 0.1$ and $h_0/R = 0.01$ for four values of S. The pressure distributions for $S = 0.5$ and $S = 0.7$ each exhibit two turning points (one a maximum, the other a minimum). As S increases, the magnitude of the maximum pressure decreases and the sub-ambient loop disappears (e.g. pressure curves for $S = 0.9$ and $S = 1.0$). Also, as S is increased the dynamic wetting line moves further towards the nip (as expected).

Figure 3.4 shows pressure profiles for $S = 0.5$ and $h_0/R = 0.01$ for four values of Ca. As Ca increases, the height of the maximum increases slightly whereas the magnitude of the minimum pressure decreases sharply. The position of the meniscus moves inwards a little and in each case the subambient loop remains.

Figure 3.5 shows pressure plots for $Ca = 0.1$ and $S = 0.5$ for three values of h_0/R.

As h_0/R is decreased, again the height of the maximum increases slightly whereas the magnitude of the minimum pressure decreases more sharply and the subambient loop remains. It is thus evident that decreasing h_0/R and increasing Ca have a similar effect on fluid pressures downstream of the nip, namely to reduce the magnitude of the negative fluid pressure. Note that this could have been predicted using the expression for the pressure at the downstream free surface, equation (3.23). The figures also suggest that the presence of a sub-ambient loop in the pressure distribution depends on the value of S.

There is a limiting value of S (where $S = S^{lim}$) for which the wetting line is situated at the nip. In this case $\bar{\gamma} = 0$ and (3.24) yields

$$S^{lim} = \left(\frac{2\beta_d}{3\pi Ca} \sqrt{\frac{h_0}{R}} - \frac{3\alpha_d}{2} \right) + 1. \tag{3.26}$$

Figure 3.6 is a plot of film thickness distribution (H_2) for varying S (i.e. for $0 < S < S^{lim}$) for two values of Ca, $Ca = 0.03$ and $Ca = 0.1$, with gap ratio $h_0/R = 0.01$. For $Ca = 0.1$, the curve is effectively linear over the interval $0 < S < 0.8$, beyond which it reaches a minimum film thickness, $H_2 = 0.15$, at $S = S^{lim} = 1.02$. The curve for $Ca = 0.03$ is effectively linear over the interval $0 < S < 1.0$, after which it reaches a minimum film thickness, $H_2 = 0.088$, at $S = S^{lim} = 1.64$. It can be seen (via (3.26)) that S^{lim} is greater for a lower capillary number. This suggests that thinner films can be produced at a lower capillary numbers since a higher value of S can be used before the wetting line passes through the nip.

3.2.1.2 Perturbed flow

Following Pearson [1960], the base flow is perturbed such that the new location of the meniscus, x'_d, is given by

$$x'_d = x_d + \epsilon e^{\sigma t} sin(2\pi nz), \tag{3.27}$$

and the pressure by

$$p'(x,z,t) = p(x) + \epsilon G(x) e^{\sigma t} sin(2\pi nz), \tag{3.28}$$

where n is a wavenumber, z measures distance along the roll axis, ϵ a small amplitude, $G(x)$ is an unknown function of x and σ is a growth rate. For stability, this perturbation must tend to zero (with time) i.e. $\sigma < 0$. Substituting (3.28) into the 2-dimensional Reynolds equation,

$$\frac{\partial}{\partial x}\left(h^3 \frac{\partial p'}{\partial x}\right) + \frac{\partial}{\partial z}\left(h^3 \frac{\partial p'}{\partial z}\right) = 12\mu \frac{(U_2 - U_1)}{2}\left(\frac{dh}{dx}\right), \tag{3.29}$$

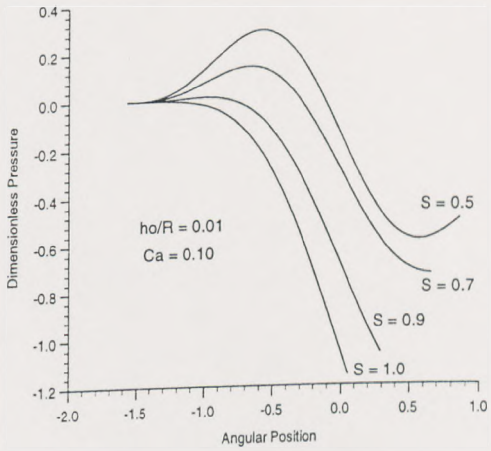

Figure 3.3: Pressure profiles for $Ca = 0.1$, $h_0/R = 0.01$ and various speed ratios.

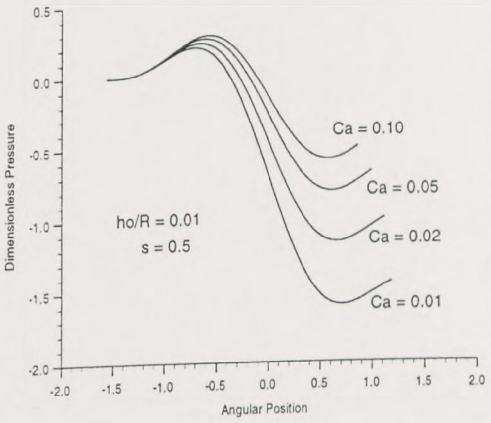

Figure 3.4: Pressure profiles for $S = 0.5$, $h_0/R = 0.01$ and various capillary numbers.

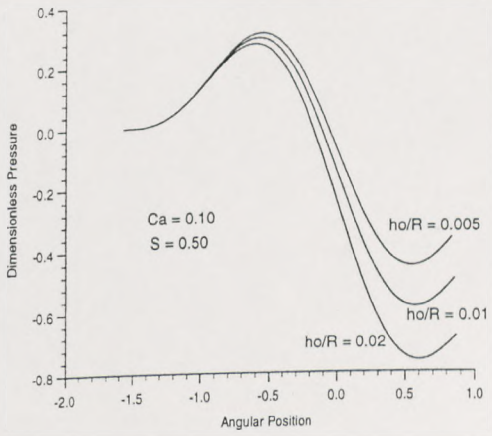

Figure 3.5: Pressure profiles for $S = 0.5$, $Ca = 0.1$ and various h_0/R.

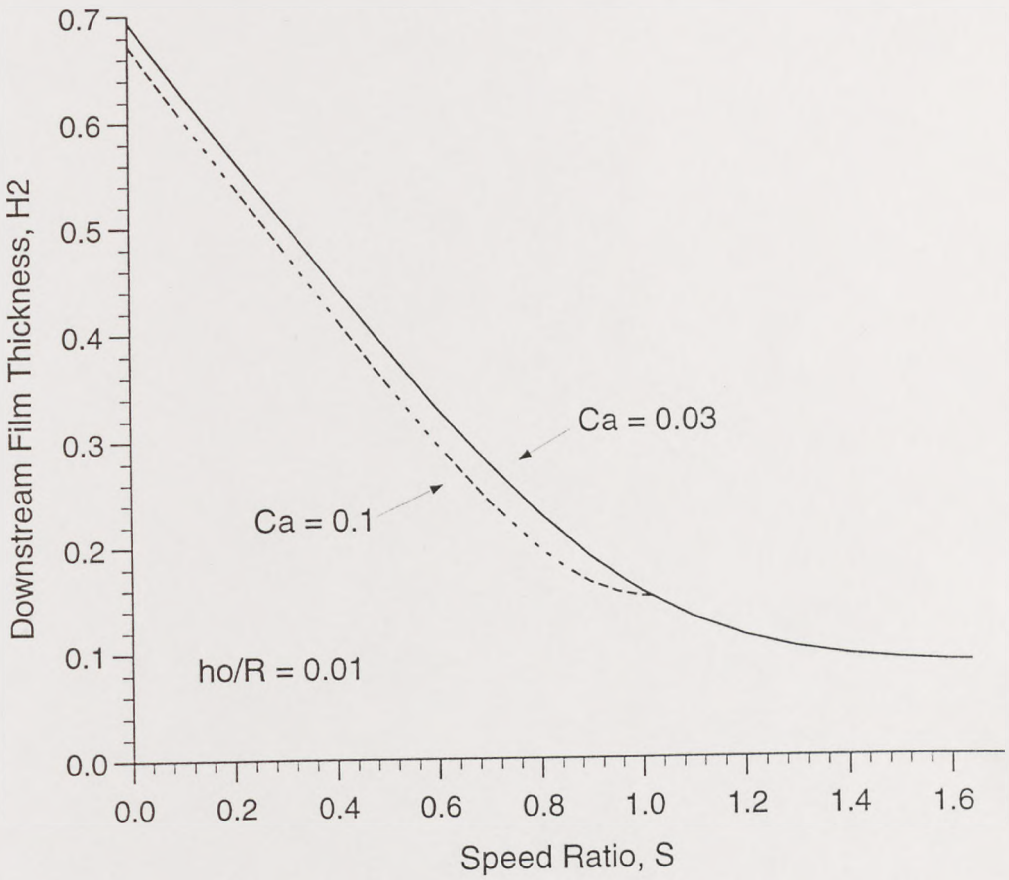

Figure 3.6: Film thickness predictions (H_2) against Speed ratio (S) for $h_0/R = 0.01$ with $Ca = 0.03$, 0.1. Note that both curves terminate at S^{lim} i.e. when the wetting line reaches the nip.

yields a second order equation for the unknown function $G(x)$,

$$\frac{d^2G}{dx^2} + \frac{3}{h}\frac{dh}{dx}\frac{dG}{dx} - 4\pi^2 n^2 G = 0. \tag{3.30}$$

The balance of surface tension forces and fluid pressure at the interface gives

$$p'(x'_d) = -\frac{\beta_d T}{h(x'_d)} + 4\pi^2 n^2 T \epsilon e^{\sigma t} sin(2\pi n z), \tag{3.31}$$

the additional surface tension term arising from curvature of the interface in the $x - z$ plane. A continuity of flow argument (see figure 3.7) states that the flux past station x''_d (i.e. $Q(x''_d)$) must equal that at the outlet i.e.

$$Q(x''_d) \;=\; h'_2\left(U_2 - \frac{dx'_d}{dt}\right). \tag{3.32}$$

However, the flux past station x''_d can be related to the flux past station x'_d by the equation

$$Q(x''_d) \;=\; Q(x'_d) - h(x'_d)\frac{dx'_d}{dt} \tag{3.33}$$

and so

$$h(x'_d)\left(\frac{U_2 - U_1}{2}\right) - \frac{h^3(x'_d)}{12\mu}\left(\frac{\partial p'}{\partial x}\right)_{x'_d} - h(x'_d)\frac{dx'_d}{dt} \;=\; h'_2\left(U_2 - \frac{dx'_d}{dt}\right). \tag{3.34}$$

Expressions (3.31) and (3.34) are linearised (by expanding about x_d and using (3.11),

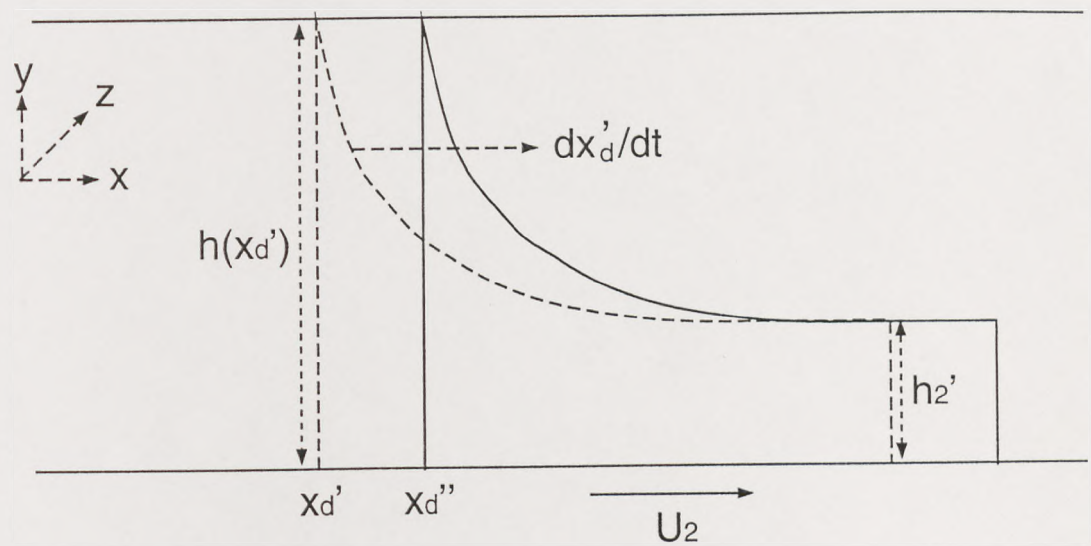

Figure 3.7: Schematic of the perturbed outflow region of an inlet flooded reverse roll coater.

(3.27), (3.28)) to give boundary conditions for $(\frac{dG}{dx})_d$ and $G(x_d)$. These, together with

the condition $G(-\infty) = 0$ (perturbation pressure tends to zero far upstream of the nip), give the following $o(\epsilon)$ problem for $G(x)$:

$$\frac{d^2G}{dx^2} + \frac{3}{h}\frac{dh}{dx}\frac{dG}{dx} - 4\pi^2 n^2 G = 0, \tag{3.35}$$

$$\left(\frac{dG}{dx}\right)_d = \frac{-12\mu U_2 \alpha_d}{h_d^3}\left(\frac{dh}{dx}\right)_d + \frac{12\mu\sigma}{h_d^2}(\alpha_d - 1), \tag{3.36}$$

$$G(x_d) = \frac{\beta_d T}{h_d^2}\left(\frac{dh}{dx}\right)_d - \frac{12\mu}{h_d^2}\left(\frac{U_2 - U_1}{2} - U_2\alpha_d\right) + 4\pi^2 n^2 T, \tag{3.37}$$

$$G(-\infty) = 0. \tag{3.38}$$

By introducing the following non-dimensional variables

$$\begin{aligned} X &= \frac{x}{\sqrt{Rh_0}}, \\ N &= n\sqrt{Rh_0}, \\ \Sigma &= \frac{\sqrt{Rh_0}}{U}\sigma, \\ g(X) &= \frac{h_d^2}{12\mu U_2}G(x), \end{aligned}$$

the boundary value problem for $g(x)$ becomes

$$\frac{d^2g}{dX^2} + \frac{6X}{1+X^2}\frac{dg}{dX} - 4\pi^2 N^2 g(X) = 0, \tag{3.39}$$

$$g(D) = \frac{\beta_d D}{6Ca}\sqrt{\frac{h_0}{R}} + \frac{\pi^2 N^2}{3Ca}\left(\frac{h_0}{R}\right)(1+D^2)^2 - \frac{1-S}{2} + \alpha_d, \tag{3.40}$$

$$\left(\frac{dg}{dX}\right)_D = \frac{-2\alpha_d D}{1+D^2} + \Sigma(\alpha_d - 1), \tag{3.41}$$

$$g(-\infty) = 0. \tag{3.42}$$

3.2.2 Method of solution

Before solving equations (3.39)-(3.42) numerically, an approximate analytical solution is obtained which is later used to give insight into the effect of the various parameters.

3.2.2.1 Analytical solution (approximate)

If the term $\frac{6X}{1+X^2}$ (in (3.39)) is replaced by its local value at the film split location where the disturbance arises then (3.39) has the form

$$\frac{d^2g}{dX^2} + \frac{6D}{1+D^2}\frac{dg}{dX} - 4\pi^2N^2g(X) = 0. \tag{3.43}$$

The justification for this is that experimentally perturbations to the downstream meniscus decay rapidly over a distance $\sqrt{Rh_0}$ such that at the position of minimum gap thickness ($X = 0$), there is virtually no trace of the perturbed flow (see Savage [1977], Carvalho and Scriven [1995]). Mathematically, equation (3.43) has an analytical solution satisfying (3.42) given by

$$g(X) = g(D)e^{w(X-D)}, \tag{3.44}$$

where

$$w = -k + \sqrt{k^2 + 4\pi^2N^2}, \tag{3.45}$$

$$k = \frac{3D}{1+D^2}. \tag{3.46}$$

Therefore,

$$\left(\frac{dg}{dX}\right)_D = wg(D). \tag{3.47}$$

Substituting (3.40) and (3.41) into (3.47) yields the following equation for the non-dimensional growth rate, Σ (as a function of N, given Ca, S and h_0/R):

$$\Sigma(N) = \frac{1}{\alpha_d - 1}\left[\frac{2\alpha_d D}{1+D^2} + \frac{w\beta_d D}{6Ca}\sqrt{\frac{h_0}{R}} - w\frac{(1-S)}{2} + w\alpha_d + \frac{w\pi^2N^2}{3Ca}\left(\frac{h_0}{R}\right)(1+D^2)^2\right]. \tag{3.48}$$

Hence, once h_0/R, Ca and S are specified and D is calculated from the base flow, graphs of $\Sigma(N)$ can be plotted using equation (3.48).

3.2.2.2 Numerical solution

The accuracy of the approximate analytical solution can be assessed by means of a numerical solution of the boundary value problem (3.39)-(3.42). This is achieved by using the NAG routine D02NBF (used generally to integrate an initial value problem for a stiff system of explicit ODE's). The boundary value problem is first converted to an initial value problem and then Newton iteration is carried out until the 3rd boundary condition is satisfied i.e. for each N, Σ is guessed and Newton iteration is carried out until (3.42) is satisfied. There is a maximum difference of 3% between the analytical and numerical solutions (for $\Sigma(N)$).

3.2.3 Discussion of Results

Since there are three independent parameters, one way of displaying results is to fix two (h_0/R and S) and plot Σ against N for various values of the third (Ca).

Fixed h_0/R

This section discusses results for a fixed gap ratio, $h_0/R = 10^{-4}$, and 4 fixed values of speed ratio, $S = 0.500$, 0.595, 0.597 and 0.610.

- $S = 0.50$

Figure 3.8 shows plots of $\Sigma(N)$ for $S = 0.5$ and various Ca. It can be observed that for both $Ca = 0.01$ and $Ca = 0.02$, $\Sigma < 0$ for all N and so the disturbance decays and the base flow is stable. A critical capillary number, $Ca*$, exists ($Ca* = 0.0342$) for which $\frac{d\Sigma}{dN} = \Sigma = 0$ for a particular value of N (and $\Sigma < 0$ for all other N). The base flow is therefore 'neutrally stable' and all flows for which $Ca > Ca*$ are unstable. $Ca = 0.05$ is an example of an unstable base flow since $\Sigma > 0$ for N in the range $0.38 < N < 1.09$. The base flow is stable to disturbances with wavenumber $N < 0.38$ and $N > 1.09$ (as $\Sigma < 0$ for all such values of N).

- $S = 0.595$

Figure 3.9 shows plots of $\Sigma(N)$ for $S = 0.595$ and various Ca. For this speed ratio there are now two critical capillary numbers, $Ca* = 0.064$ and $Ca* = 0.086$, for which the flow is neutrally stable. For $Ca < 0.064$ and $Ca > 0.086$, $\Sigma < 0$ for all N and the flows are stable. The base flow is unstable for capillary numbers in the range $0.064 < Ca < 0.086$.

- $S = 0.597$

As S is gradually increased, the two critical capillary numbers approach one another and coincide when $S = 0.597$. In this case, there is only one critical capillary number, $Ca* = 0.073$. Figure 3.10 shows plots of $\Sigma(N)$ for $S = 0.597$ and various Ca. For $Ca = 0.073$ the base flow is neutrally stable and for all other capillary numbers the flow is stable.

- $S = 0.61$

For $S > 0.597$ (e.g. $S = 0.61$ - see figure (3.11)), all the curves lie below $\Sigma(N) = 0$. There are no longer any critical capillary numbers present and therefore all flows are stable.

Figure 3.12 shows, for $h_0/R = 10^{-4}$, a plot of critical capillary number, $Ca*$, against S. Above the curve, ribs occur whereas below and to the right of the curve the base flow is stable. Corresponding to each Ca, there is clearly a minimum S beyond which no ribbing occurs. Moreover, there is an overall minimum value of speed ratio, S^{min} (corresponding to the vertical dotted line in figure 3.12) above which no ribs occur for any Ca. S^{min} is dependent on gap ratio, h_0/R, and for $h_0/R = 10^{-4}$, $S^{min} = 0.597$ (see figure 3.10). There is also an overall maximum value of capillary number, Ca^{max} (corresponding to the horizontal dotted line in figure 3.12) below which no ribs occur - for $h_0/R = 10^{-4}$ this value is $Ca^{max} = 0.0178$ and corresponds to the $Ca*$ at $S = 0$.

In section 3.2.4 an explanation will be given for the curve in figure 3.12 'turning back to the left' near $S = 0.6$.

Variable h_0/R

The effect of varying the gap ratio, h_0/R, is illustrated in figure 3.13 by means of critical curves in the $Ca - S$ plane for the onset of instability. It is observed that the region of stability increases as h_0/R increases such that for any S the critical capillary number increases with h_0/R. Further, for any h_0/R, a rough guide (underestimate) to the extent of the stability region can be gained by identifying, as in figure 3.12, a maximum capillary number Ca^{max} (and a minimum speed ratio S^{min}) below which (above which) the flow is always stable. For a given h_0/R, Ca^{max} is that value of critical capillary number corresponding to $S = 0$ and the graph of Ca^{max} against h_0/R is shown in figure 3.14. Ca^{max} increases as h_0/R increases and for $h_0/R > 2\times10^{-4}$ the curve is effectively linear.

For a given h_0/R, S^{min} can be found numerically by solving the following set of simultaneous equations

$$f(Ca, S, \bar{\gamma}) = 0, \tag{3.49}$$

$$\Sigma(Ca, S, \bar{\gamma}, N) = 0, \tag{3.50}$$

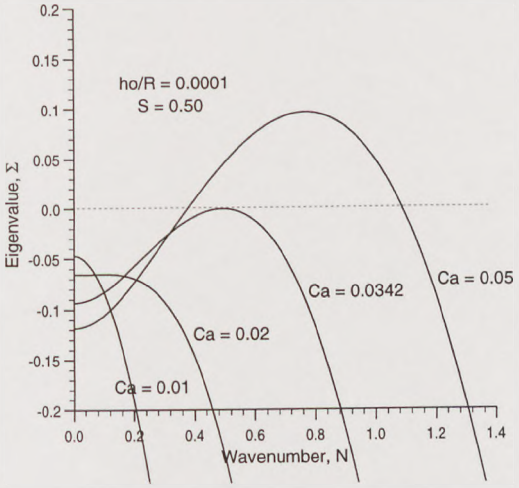

Figure 3.8: Growth rate (Σ) against wavenumber (N) for various Ca with $h_0/R = 10^{-4}$ and $S = 0.5$.

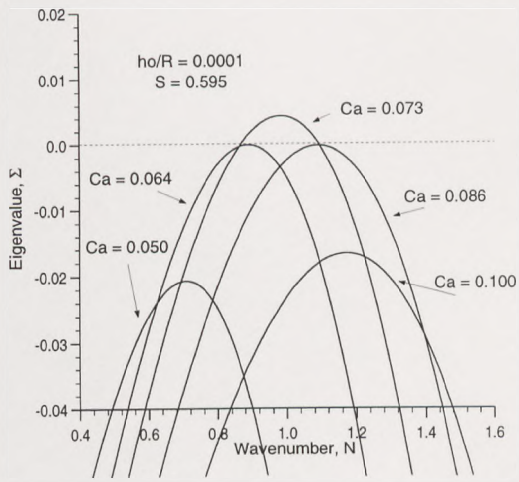

Figure 3.9: Growth rate (Σ) against wavenumber (N) for various Ca with $h_0/R = 10^{-4}$ and $S = 0.595$.

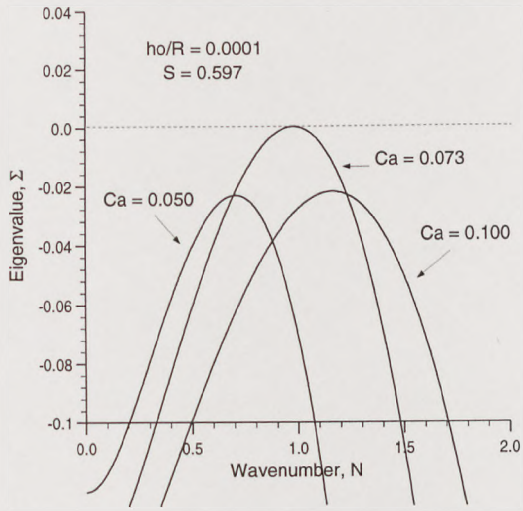

Figure 3.10: Growth rate (Σ) against wavenumber (N) for various Ca with $h_0/R = 10^{-4}$ and $S = 0.597$.

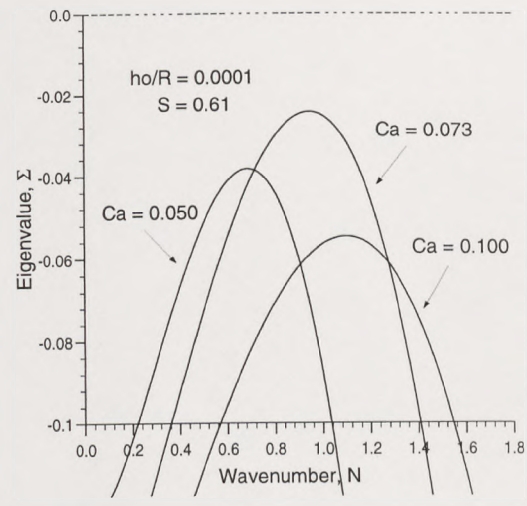

Figure 3.11: Growth rate (Σ) against wavenumber (N) for various Ca with $h_0/R = 10^{-4}$ and $S = 0.61$.

$$\frac{\partial \Sigma}{\partial N} = 0, \tag{3.51}$$

$$\frac{\partial \Sigma}{\partial Ca} + \frac{\partial \Sigma}{\partial \bar{\gamma}} \frac{\partial \bar{\gamma}}{\partial Ca} = 0, \tag{3.52}$$

where (3.49) represents the base flow equation (3.24) for $\bar{\gamma}$ in terms of Ca, S and h_0/R. Equations (3.50) and (3.51) determine, for a given h_0/R and any S, the critical capillary numbers for neutral stability and (3.52) is a condition to then select the minimum speed ratio, S^{min} (illustrated in figure 3.10), such that no critical capillary numbers exist for $S > S^{min}$. Note that equations (3.50), (3.51) and (3.52) could be more simply expressed together by $\frac{\partial S}{\partial Ca*} = 0$ (see figure 3.12). The above equations were solved using NAG routine C05NBF (a modification of the Powell hybrid method) and the graph of S^{min} against h_0/R is shown in figure 3.15, where it is seen to decrease as h_0/R is increased.

Various θ_d

The effect of varying the dynamic contact angle, θ_d, is illustrated in figure 3.16 by means of critical curves in the $Ca - S$ plane for the onset of instability. It is observed that decreasing (increasing) θ_d increases (decreases) Ca^{max} and S^{min}.

3.2.4 Comparison with the Stability Hypothesis (S.H.)

The stability hypothesis provides a simple criterion for predicting the stability of a meniscus of radius r when its location is perturbed from x_d to $x_d + \epsilon$ (see Savage [1977]). The net force acting on a unit area of the downstream interface (in the x-direction) is given by

$$F = p(x_d + \epsilon) + \frac{T}{r(x_d + \epsilon)} \tag{3.53}$$

and so using (3.13) and linearising, (3.53) becomes

$$F = \epsilon \left(\frac{dp}{dx} - \frac{T}{r^2} \frac{dr}{dx} \right)_{x=d}. \tag{3.54}$$

If the meniscus is stable, it will return to its original position and so, assuming $\epsilon > 0$, $F < 0$ which yields the following condition for stability:

$$\frac{\beta_d T}{h_d^2} \left(\frac{dh}{dx} \right)_d > \left(\frac{dp}{dx} \right)_d. \tag{3.55}$$

Note that at an upstream free surface this inequality is reversed (see chapter 4).

Hence we see (via the S.H.) that surface tension has a stabilising influence, whereas

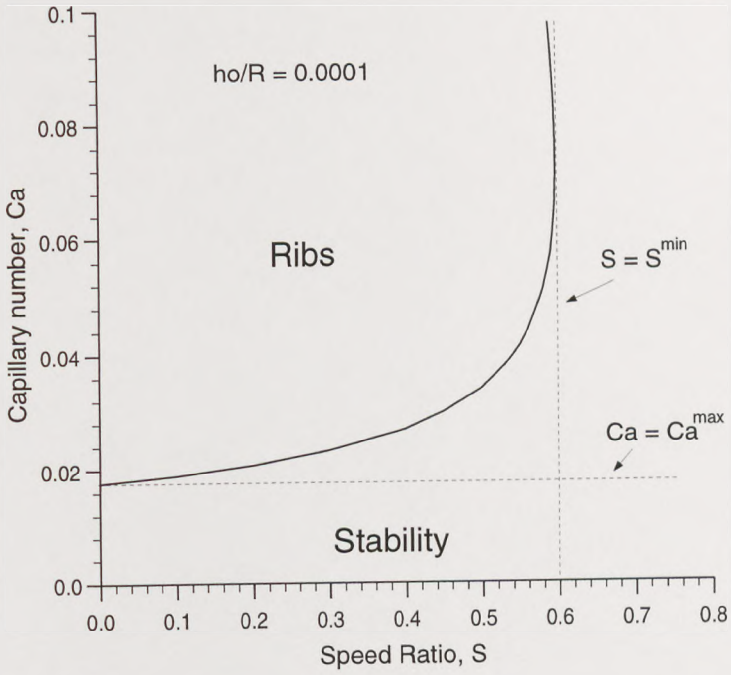

Figure 3.12: Operability diagram in the $Ca - S$ plane for $h_0/R = 10^{-4}$.

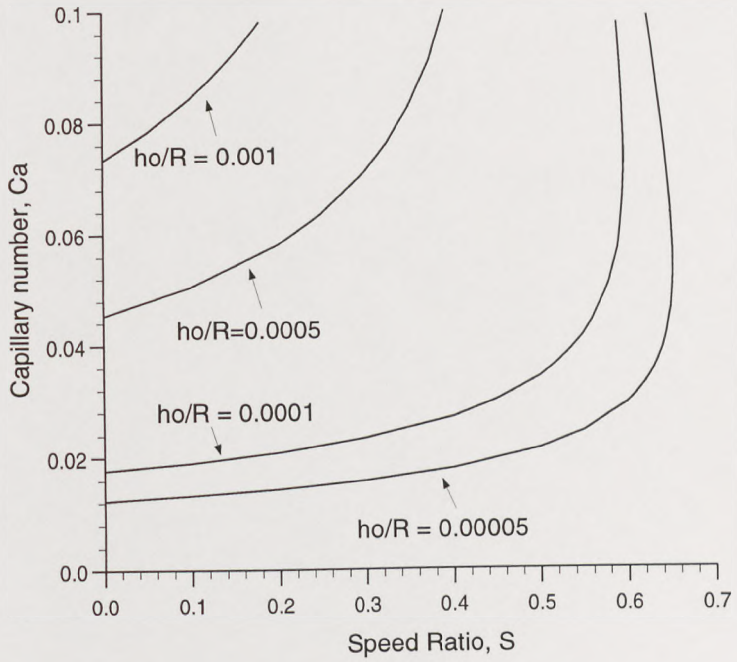

Figure 3.13: Operability diagrams in the $Ca - S$ plane with varying h_0/R.

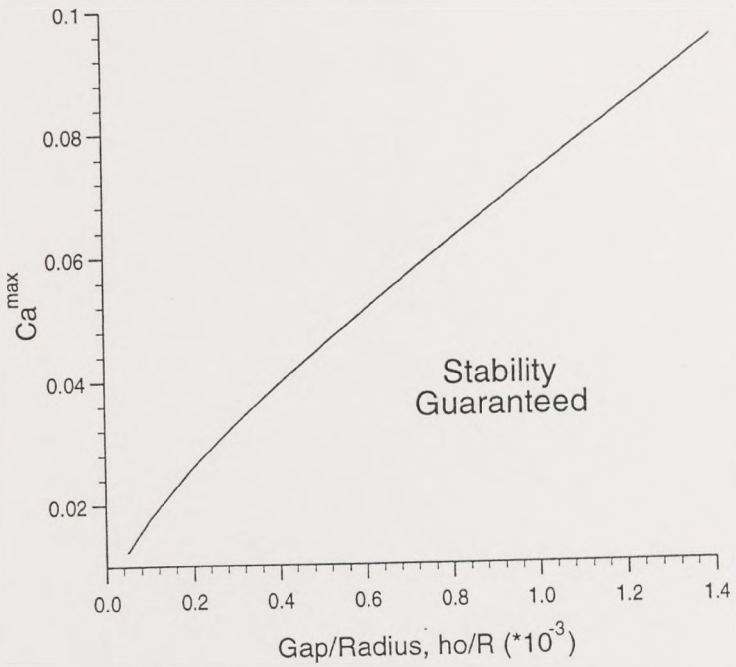

Figure 3.14: Graph of Ca^{max} against h_0/R, where stability is ensured if $Ca < Ca^{max}$.

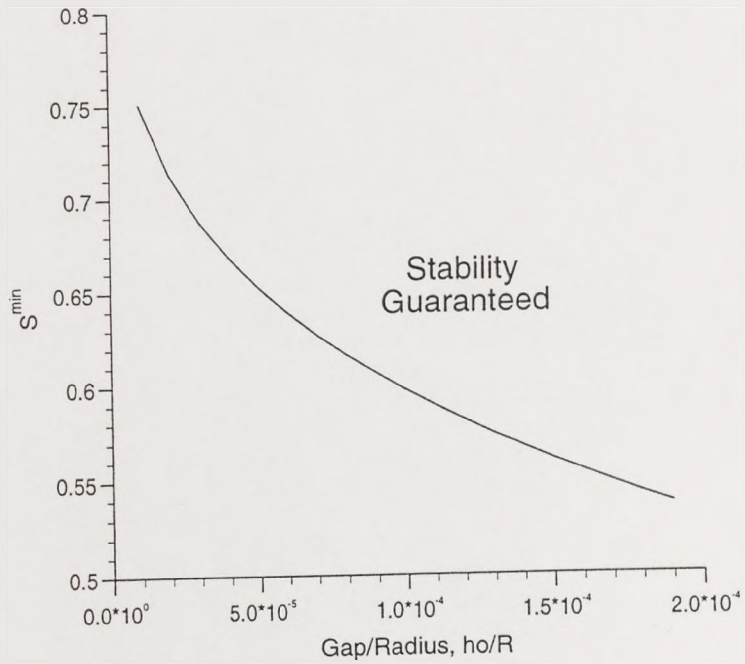

Figure 3.15: Graph of S^{min} against h_0/R, where stability is ensured for $S > S^{min}$.

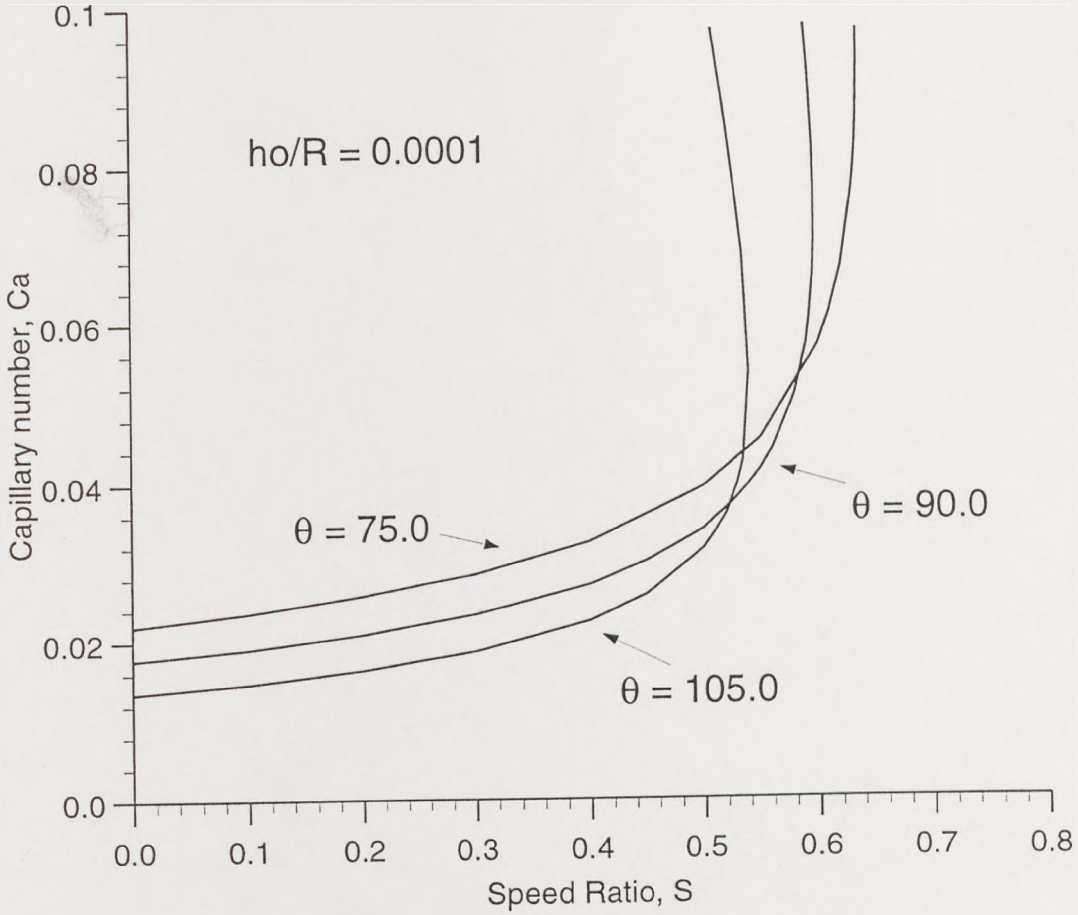

Figure 3.16: Operability diagram in the $Ca - S$ plane for $h_0/R = 10^{-4}$ and various θ_d values.

the pressure gradient (at x_d) has a destabilising effect.

If figure 3.3 is now re-examined, it is seen that as the speed ratio (S) is increased, the pressure gradient (at x_d) decreases. In fact, for $S = 0.5$ the pressure gradient at x_d is positive and as S increases to $S = 1.0$ it becomes negative. It can therefore be concluded (using (3.55)) that increasing S has a stabilising effect. Hence the presence of an S^{min}, as in figure 3.12, is to be expected.

Clearly the stability criterion is a very useful guide for understanding stability mechanisms and predicting instability. The question is "how accurate is it?":

Once (3.55) is non-dimensionalised, it is equivalent to

$$g(D, N = 0) \;>\; 0, \tag{3.56}$$

where $g(D, N)$ is given by equation (3.40). Figure 3.17 shows a plot of $g(D, N = 0)$ against Ca for $S = 0.5$ and $h_0/R = 10^{-4}$. For $Ca < 0.0193$, $g(D, N = 0) > 0$ and the base flow is stable whereas for $Ca > 0.0193$, $g(D, N = 0) < 0$ and the base flow is unstable. Hence the critical capillary predicted is $Ca* = 0.0193$ which is an underestimate of the critical value $Ca* = 0.034$ as given by linear stability analysis.

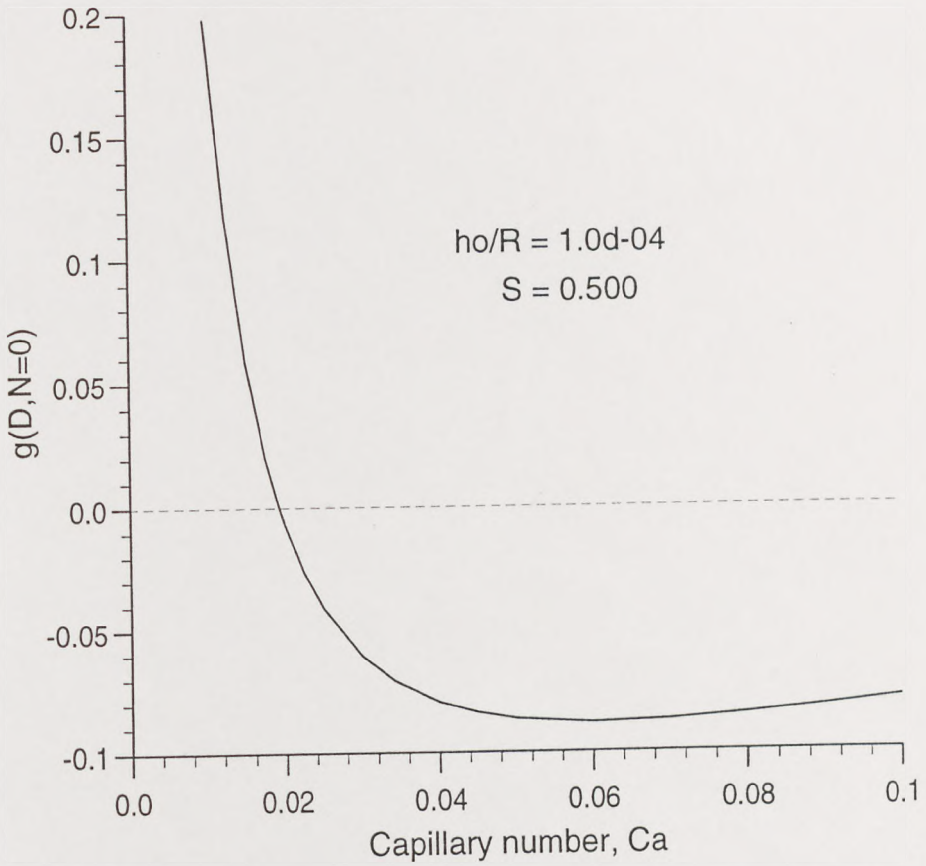

Figure 3.17: Graph of $g(D, N = 0)$ against Ca for $h_0/R = 10^{-4}$ and $S = 0.500$. Stability is ensured (via the S.H.) if $g(D, N = 0) > 0$.

Figure 3.18 shows, for $h_0/R = 10^{-4}$, a plot of critical capillary number, $Ca*$, against S for both the S.H. (the full line) and linear stability analysis (the dotted line). It can be seen that the two curves are qualitatively similar and that the approximate stability hypothesis gives a 'strong condition' which consistently underpredicts the critical capillary number for any S. This suggests that the S.H. is sufficient for predicting stability (but not for instability), a result which will now be proved for any h_0/R:

Proof:

It has already been shown, via figure 3.18, that the S.H. is not sufficient for predicting instability. It therefore only remains to be proved that the S.H. is sufficient for predicting stability. More precisely, when $Ca < Ca**$, *where* $Ca**$ *is the critical capillary number predicted via the S.H., it must be proved that the base flow is stable (via the linear stability analysis) i.e. that* $\Sigma(N)$ *is always negative:*

For $Ca < Ca**$, $g(D, N = 0) > 0$. *Therefore, because* $g(D, N)$ *is a monotonically increasing function (with* N*),* $g(D, N) > 0$ *(see equation (3.40)). However,* $g(D, N)$ *and* $\left(\frac{dg}{dX}\right)_d(N)$ *must have the same sign (see appendix A) and so* $\left(\frac{dg}{dX}\right)_d(N) > 0$. *Therefore, using (3.41),*

$$\Sigma < \frac{-2\alpha_d D}{(1+D^2)(1-\alpha_d)}. \tag{3.57}$$

Hence, since $0 < \alpha_d < 1$,

$$\Sigma < 0. \tag{3.58}$$

□

Figure 3.19 shows further operability diagrams (in the $Ca - S$ plane) for four different values of h_0/R. As with the linear stability analysis, it is clear that as h_0/R is increased, the minimum speed ratio for stability decreases and the maximum capillary number for stability increases. It is also clear that as h_0/R is decreased, the agreement between the linear stability analysis and S.H. improves.

Finally, the 'turning back to the left' of the critical curve in figure 3.12 is considered (i.e. for each h_0/R, there is a small range of S values near S^{min} for which there are two ranges of Ca in which the base flow is stable, separated by an unstable range). Because the stability hypothesis gives a qualitatively similar curve (see figure 3.18), this effect is clearly 2-dimensional and can be explained by examining equation (3.56), where

$$g(D, N = 0) = \frac{\beta_d D}{6Ca}\sqrt{\frac{h_0}{R}} - \left(\frac{1-S}{2} - \alpha_d\right). \tag{3.59}$$

The first term in (3.59) represents the surface tension term and the second term represents the pressure gradient term. However one component of this pressure gradient term (α_d) has a stabilising influence i.e. as α_d increases, so does $g(D, N = 0)$. Hence if a value of S is now considered where stability exists for both low and high Ca values,

it is evident that for low Ca the surface tension term dominates (as expected), but for high Ca the stabilising component of the pressure gradient dominates to ensure stability.

Note that in developing the above stability hypothesis the curvature of the meniscus in the $x - z$ plane was neglected. The effect of including this extra contribution to the surface tension is examined in Appendix A, although it is seen to be no more accurate than the 2-dimensional stability hypothesis for determining the onset of instability.

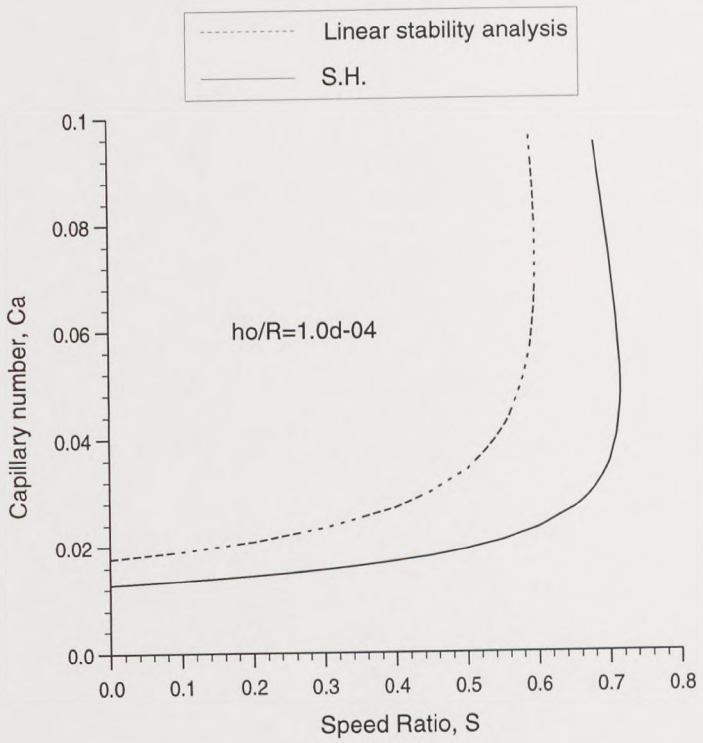

Figure 3.18: Operability diagram in the $Ca - S$ plane for $h_0/R = 10^{-4}$ for both the S.H. and ribbing analysis.

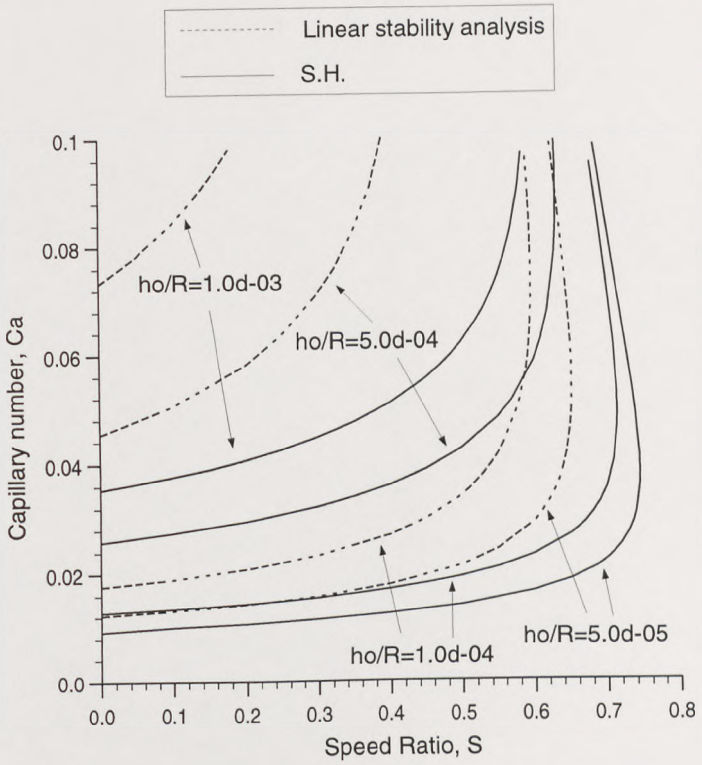

Figure 3.19: Operability diagram in the $Ca - S$ plane with varying h_0/R for both the S.H. and ribbing analysis.

3.3 A computational approach

In the previous section, inlet flooded reverse roll coating was analysed using the lubrication approximation to model the flow with suitable boundary conditions applied far upstream and at the downstream meniscus. The model predicted the pressure profile and final film thickness as a function of three operating parameters, namely S, Ca and h_0/R. The ribbing instability was then examined by applying linear stability theory to this base flow. However, lubrication models are only valid when the contact line is located downstream of the nip and even then only span a small region of parameter space (small Ca). Furthermore, it is necessary to model the downstream meniscus using the arc of a circle approximation.

The FE method does not suffer these drawbacks and so the aim of this section is to apply the linear stability theory (described in chapter 2) to FE solutions of an inlet flooded reverse roll coater in order to examine the accuracy of the previously obtained analytical results and to enable the stability of the flow to be examined over a much larger region of parameter space. The steady, two-dimensional FE code used in this study was written by Richardson [1996] and is described in section 3.3.1, the stability of which is examined computationally in section 3.3.2.

3.3.1 Numerical solution of the base flow

Boundary conditions:

The boundary conditions, summarised in figure 3.20, are as follows:

1. At the downstream free surface, the usual kinematic and stress boundary conditions are imposed (see chapter 2).

2. A zero traction condition is imposed at the downstream outlet.

3. At the dynamic wetting line, the apparent contact angle, θ_d, is specified. Further, as discussed in chapters 1 and 2, slip is applied over the element next to the wetting line (on the roll surface) to avoid the stress singularity.

4. At the inflow boundary (OC in figure 3.20), the lubrication approximation provides an accurate description of the flow. In order to contend with the wetting line passing through the nip, this boundary condition must be applied sufficiently far upstream of the nip. This requires expressions for the two-dimensional velocity field correct to $O(h_o/R)^{1/2}$, as derived by Savage [1992] and Gaskell, Savage

and Thompson [1998] for counter-rotating rolls. A zero inlet pressure condition (corresponding to $p(-\infty) = 0$) is also applied.

5. No-slip conditions are applied on the roll surfaces.

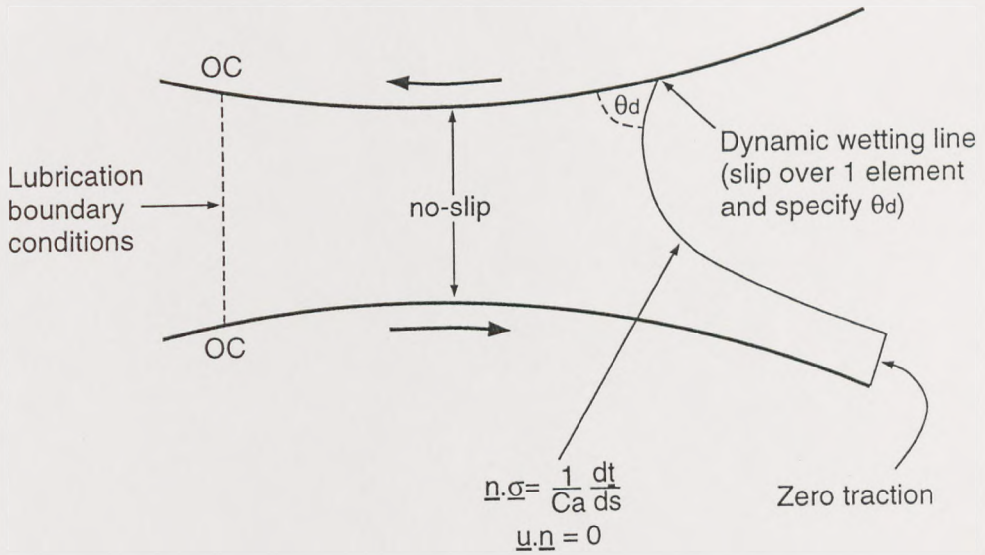

Figure 3.20: Computational boundary conditions for the inlet flooded reverse roll coater.

Computational mesh:

A schematic of the computational grid used is shown in figure 3.21 although for clarity of presentation, the mid-spines have been omitted and the y-axis has been scaled. As described by Richardson [1996], all nodes (except those that lie at the inflow plane) are parametrised by an unknown variable, XM_d (Coyle [1984], Thompson [1992]), whose x-coordinate is given by x_m^d. This allows the entire grid to move with the free surface. To avoid element distortion, nodes in region 1 undergo a concertina type motion as the value of x_m^d changes, and the x-coordinates of nodes in this region are

$$x_i = O_c + (x_m^d - O_c)\frac{i}{n_d}, \tag{3.60}$$

where n_d is the number of vertical spines in the region.

In region 2 the nodal positions are parametrised by the base line x_m^d and a series of i free surface spines of height h_i^d. The free surface region is tesselated by a combination of three polar origins, as shown in figure 3.21. Each spine which has a base point located on XM_d and lies between $y = 0$ and $y = h(x)$, has a direction vector which passes through the polar origin, O_2, whose position is a fixed (specified) distance from XM_d

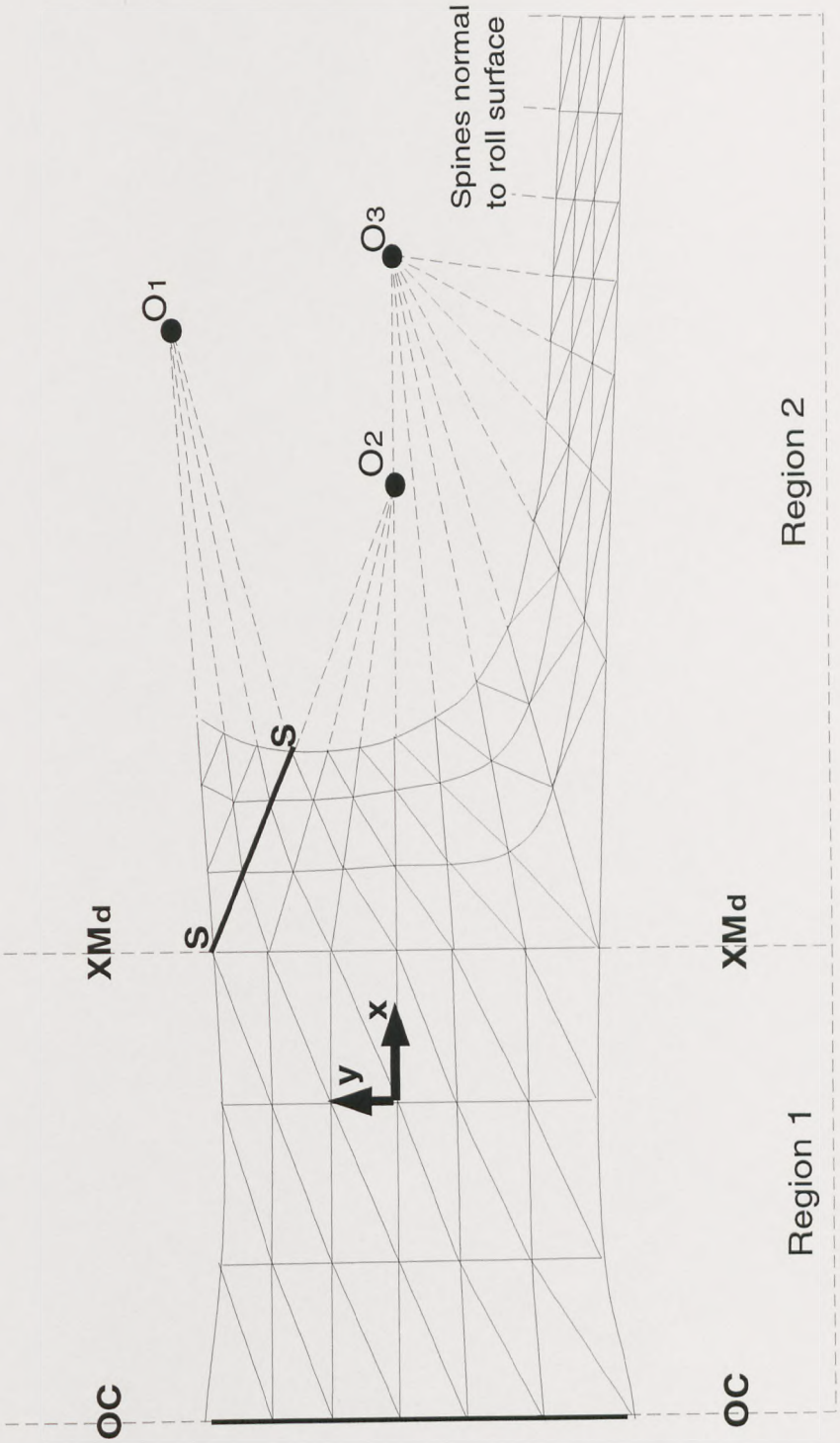

Figure 3.21: Schematic of the grid used to tesselate the downstream region. Note that for clarity of presentation, the y-axis has been scaled and the mid-spines have been omitted.

and lies on the line, $y = 0$. The remaining spines which have base points located on XM_d have direction vectors which pass through the polar origin, O_3, which again lies on the line $y = 0$ and is a fixed (specified) distance from XM_d. Note that O_3 is located further downstream than O_2.

The next set of spines have base points located on the lower roll surface and have direction vectors which also pass through O_3. Furthermore, the x-coordinates of all base points located on the roll surfaces are fixed increments of the current value of x_m^d, and are specified as part of the algorithm. The remaining spines with base points situated along the lower roll surface have direction vectors which are perpendicular to the roll. The spines in the neighbourhood of the dynamic wetting line have base nodes evenly distributed along the spine SS, and are classified as inter-dependent spines (see chapter 2). Their direction vectors pass through the polar origin O_1, which is situated a fixed distance along the tangent to the upper roll at the dynamic wetting line. Consequently, refinement of the wetting line region is relatively simple and avoids the unnecessary costs inherent in techniques employing elliptic mesh generation (see, for example Christodoulou and Scriven [1992]).

The downstream variable x_m^d is calculated using the contact angle equation, as summarized in chapter 2 (and the freedom of a spine height is removed).

The computational mesh used in this study contains 447 elements, 994 nodes and 2094 degrees of freedom which Richardson [1996] showed was suitable for producing grid independent solutions. A typical solution, together with corresponding streamlines is shown in figure 3.22.

In figure 3.23, predictions for H_2 from the lubrication model are compared with numerical results for $Ca = 0.06$, $R/h_0 = 85$ and varying S. Note that, unlike the FE method, lubrication theory can only model the flow if the wetting line is located downstream of the nip and so predictions are only plotted in the range $0 < S < S^{lim}$, where $S^{lim} = 1.20$ is the value of S for which the wetting line is situated at the nip and H_2 reaches its minimum value, $H_2 = 0.121$. The lubrication theory predictions are in good agreement with the finite element results at low S but, as expected, at higher values of S the predictions become inaccurate because the wetting line approaches the nip and so the assumptions which lubrication theory are based on are no longer appropriate. The finite element solutions reach a minimum film thickness, $H_2 = 0.146$, again when the

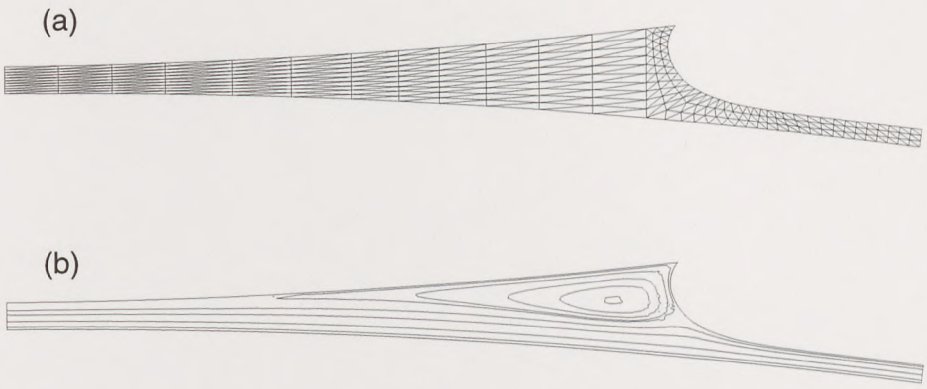

Figure 3.22: Typical finite element solution showing (a) the grid with (b) corresponding streamlines.

wetting line is situated at the nip i.e at $S = 1.35$. For $S > 1.35$, the wetting line moves upstream of the nip and H_2 increases.

3.3.2 Stability of the FE base flow

The finite element stability analysis described in chapter 2 is now applied to this inlet flooded, reverse roll coating problem. Using the grid described above there are now 2955 degrees of freedom (as opposed to 2094 freedoms with the 2-dimensional base flow). For a given wavenumber, N, (and set of base flow fluid and geometry parameters) an eigenvalue, Σ, is produced to indicate the stability — using a Silicon Graphics Indy workstation with a 150MHz, MIPS R5000 processor each such calculation takes 25 c.p.u. seconds. If, for a given base flow, the eigenvalue is negative for each wavenumber the base flow is stable. If one or more of the eigenvalues is positive then the base flow is unstable and ribbing appears.

For $S = 0.10$ and $h_0/R = 10^{-3}$ this numerical approach produced a critical capillary number of $Ca* = 0.070$, in comparison to $Ca* = 0.083$ via the analytical approach. In fact, the analytical approach consistently overpredicts the critical capillary number (for all S and h_0/R). It is the author's opinion that this discrepancy is due to the lack of a slip region at the dynamic wetting line in the analytical approach, a matter which will be discussed in chapter 4.

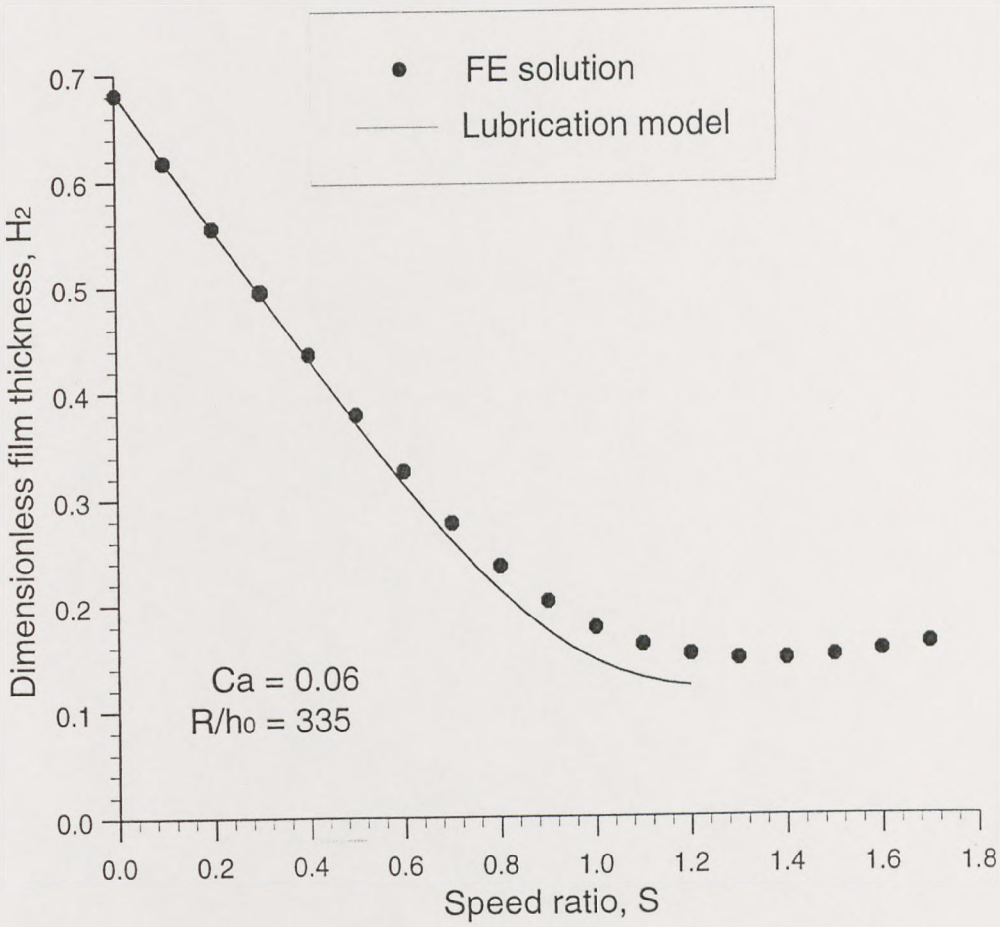

Figure 3.23: A comparison of film thickness predictions (H_2) against speed ratio (S) obtained via the finite element method and lubrication theory for $Ca = 0.06$ and $R/h_0 = 85$.

3.4 The effect of a hydrostatic head

In the past, the effects of gravity in forward and reverse roll coating have generally been assumed to be negligible (see, for example, Pitts and Greiller [1961], Greener and Middleman [1981], Coyle [1984] and Thompson [1992]). Its influence was first investigated by Ho and Holland [1978] who developed a mathematical model based on lubrication theory which included a term due to gravity for rolls positioned side by side, operating in the reverse mode with the web moving vertically upwards. However, they found experimentally that the gravity term was negligible and so ignored it in their analysis. Coyle *et al* [1990b] used experimental and numerical techniques to examine the flow in the special case of two half-submerged rolls (with the rolls again positioned side by side). They showed that gravity effects can become significant at low values of speed ratio and tended to increase the flow down through the gap. Coyle attributed the lack of effect of gravity in Ho and Holland's experiments to their use of large rolls and a small gap setting, thus giving a small *Stokes number* (the Stokes number being the ratio of gravity to viscous forces, a term which will be defined later). The excessively large flow rates measured by Greener *et al* [1981] were also, in part, attributed to gravity effects. This is because they used small rolls and a large gap setting, thus giving a much larger Stokes number. Due to a lack of appropriate boundary conditions at the free surface, Coyle *et al* [1990b] also found that lubrication theory did not accurately describe the base flow.

More recently, Walker [1995] investigated the effect of gravity on the flow structure, film split ratio and free surface location in various configurations of a fully flooded forward roll coater. For rolls positioned side by side, he developed an analytical model to predict the amount of flux passing through the nip and the location of the free surface. This model was also shown to have good agreement with computational results and experiment. For rolls located one above the other, experiments performed by Rees [1995] show that under certain operating conditions, a weak asymmetric jet can develop close to the downstream meniscus, transferring fluid from the upper to lower roll, even when $S = 1$. The existence of such a jet was attributed to gravity and was verified numerically by Walker [1995]. Walker hence showed that, with the rolls operating in this mode, gravity can have a significant effect on the film split ratio at low speeds. The behaviour of flows with unequal roll radii was also examined.

This section is concerned with investigating the reverse roll coating process in which the nip is fed from above by a large reservoir of fluid (i.e. a hydrostatic head), as shown in figure 3.24. An analytical, inlet flooded model based on lubrication theory, is presented

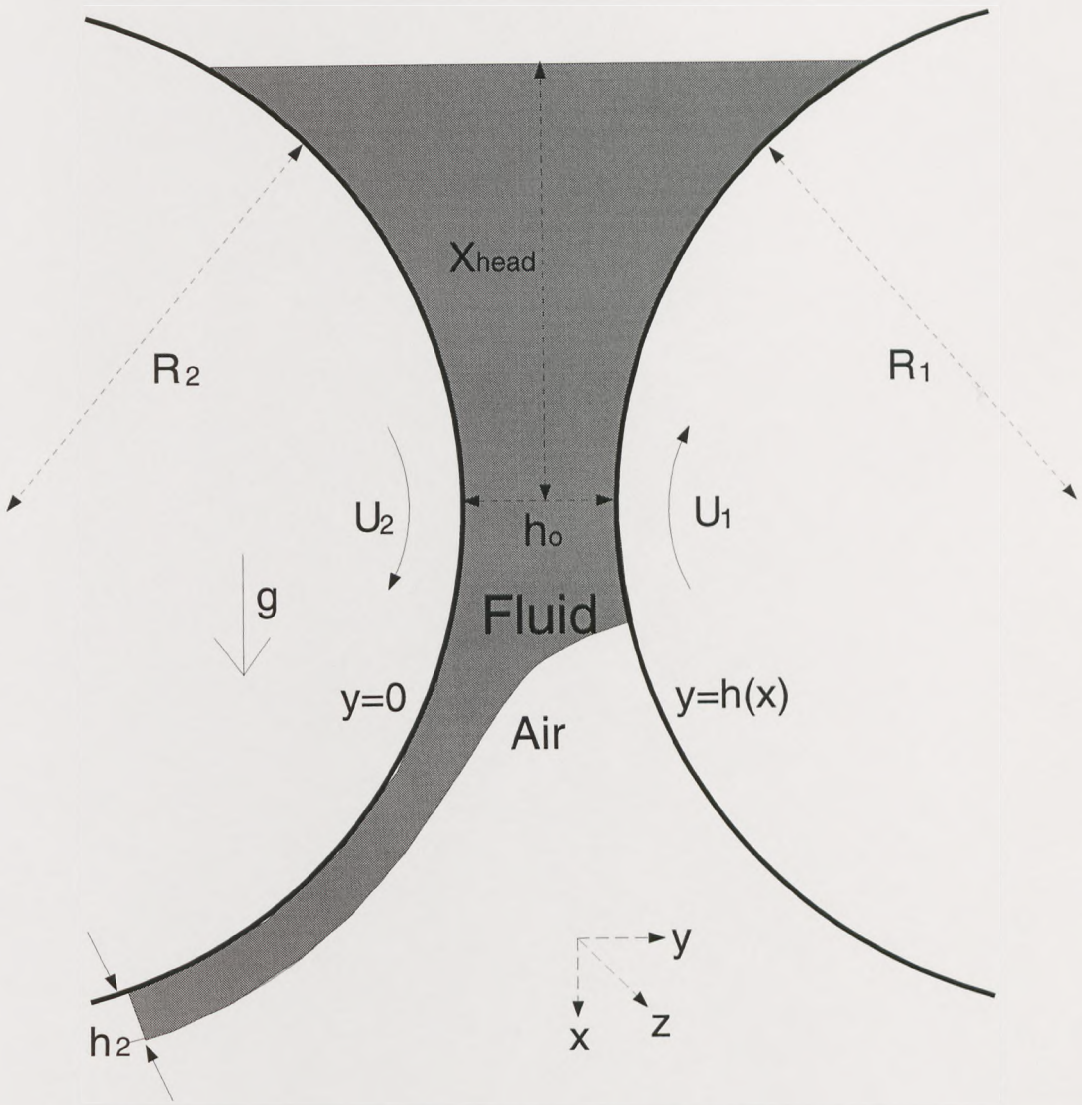

Figure 3.24: Schematic of a reverse roll coater fed by a hydrostatic head.

from which the effect of the hydrostatic head on the meniscus location and pressure profile is examined. After applying linear stability theory to the base flow, the influence of gravity on the ribbing instability is then determined by means of critical curves in the $Ca - S$ control space.

3.4.1 Mathematical model

3.4.1.1 Base flow

In this section the aim is to develop a model based on the lubrication approximation so as to determine the velocity and pressure fields, together with the location of the meniscus.

Neglecting transient and inertia terms, the Navier-Stokes equations reduce to

$$0 = -\nabla p + \mu \nabla^2 \underline{u} + \rho \underline{g}. \tag{3.61}$$

Assuming unidirectional flow through the nip and that velocity gradients across the bead are negligible i.e. $\partial u/\partial x << \partial u/\partial y$ then (3.61) becomes

$$\frac{\partial p}{\partial x} = \mu \frac{\partial^2 u}{\partial^2 y} + \rho g \tag{3.62}$$

and

$$\frac{\partial p}{\partial y} = 0. \tag{3.63}$$

Therefore $p = p(x)$ and so, using the no slip boundary conditions, (3.62) can be integrated twice to give

$$u = \frac{1}{2\mu}\left(\frac{dp}{dx} - \rho g\right) y(y-h) - (U_1 + U_2)\frac{y}{h} + U_2. \tag{3.64}$$

Using (3.8), equation (3.64) can be integrated to obtain the flux,

$$Q = -\frac{1}{12\mu}\left(\frac{dp}{dx} - \rho g\right) h^3 + (U_2 - U_1)\frac{h}{2}, \tag{3.65}$$

which, after equating to the flux in the downstream film (equation 3.10), gives the following expression for the pressure gradient:

$$\frac{dp}{dx} = \frac{12\mu}{h^2}\left(\frac{(U_2 - U_1)}{2} - U_2\frac{h_2}{h}\right) + \rho g. \tag{3.66}$$

However, the pressure field may be expressed as the sum of its hydrostatic, p_{HS}, and hydrodynamic, p_{HD}, components i.e.

$$p = p_{HS} + p_{HD}, \tag{3.67}$$

so the hydrostatic and hydrodynamic components of the pressure gradient are given by

$$\frac{dp_{HS}}{dx} = \rho g, \tag{3.68}$$

and

$$\frac{dp_{HD}}{dx} = \frac{12\mu}{h^2}\left(\frac{(U_2 - U_1)}{2} - U_2\frac{h_2}{h}\right), \tag{3.69}$$

respectively.

Introducing non-dimensional variables defined by

$$\begin{aligned} H &= \frac{h}{h_0}, \\ H_2 &= \frac{h_2}{h_0}, \\ X_{HS} &= \frac{x_{HS}}{R}, \\ X_{HD} &= \frac{x_{HD}}{\sqrt{Rh_0}}, \\ S &= \frac{U_1}{U_2}, \\ P &= \frac{h_0}{\mu U_2}\sqrt{\frac{h_0}{R}}p, \end{aligned}$$

and writing $X_{HD} = \tan(\gamma)$ (so $h(\gamma) = h_0 \sec^2\gamma$), then equations (3.68) and (3.69) become

$$\frac{dP_{HS}}{dX_{HS}} = St\sqrt{\frac{R}{h_0}}, \tag{3.70}$$

$$\frac{dP_{HD}}{d\gamma} = 6(1-S)\cos^2\gamma - 12H_2\cos^4\gamma, \tag{3.71}$$

respectively, where $St = \rho g h_0^2/\mu U_2$ is the Stokes number. Note that the hydrodynamic and hydrostatic lengthscales are different - this is due to the fact that the height of the head is of the same lengthscale as the radius of the rollers as opposed to the minimum gap width.

Boundary conditions:

The boundary condition on the hydrostatic pressure is that

$$p_{HS} \to 0 \text{ as } x_{HS} \to -x_{head}, \tag{3.72}$$

where x_{head} is the dimensional height of the hydrostatic head. Upon non-dimensionalisation, this becomes

$$P_{HS} \to 0 \text{ as } x_{HS} \to -X_{head}, \tag{3.73}$$

where $X_{head} = x_{head}/R$ is the non-dimensional height of the head. Boundary conditions on the hydrodynamic pressure are identical to those where gravity is neglected i.e.

$$p_{HD} \to 0 \text{ as } x_{HD} \to -\infty. \tag{3.74}$$

Note that, because the lubrication approximation has been used to calculate the hydrodynamic pressure, this *infinity* is but a few typical lengths $\sqrt{Rh_0}$ upstream of the nip. The fluid pressure at the downstream meniscus is again given by

$$p(\bar{\gamma}) = -\frac{T}{r_d}, \tag{3.75}$$

and the meniscus is, as before, approximated by a circular arc such that

$$h_d = r_d(1+\cos(\theta_d)) + h_2. \tag{3.76}$$

Since x_d is unknown a third boundary condition is required which, for $Ca < 0.01$, is provided by the Bretherton [1962] expression which relates the ratio of the asymptotic film thickness, h_2, to the radius of curvature, r_d, by

$$\frac{h_2}{r_d} = 1.34Ca^{2/3}\left(1+\frac{2}{3}Bo\, r_d^2\right), \tag{3.77}$$

where $Bo = St\ Ca$ is the Bond number which is constant for any given fluid. However, $Bo \ll 1$ for the purpose of most practical situations and so is assumed to be negligible. Hence, the Bretherton expression is now equivalent to the Landau-Levich [1942] expression which was previously used for this range of Ca. For higher values of Ca, i.e. $0.01 \leq Ca \leq 0.1$, Ruschak's [1981] suggested relationship,

$$\frac{h_2}{r_d} = 0.56Ca^{1/2}, \tag{3.78}$$

is again used - note that equation (3.78) does not explicitly involve a gravity term. Equation (3.75) then becomes

$$p(\bar{\gamma}) = -\frac{\beta_d \mu U_2}{Cah_0 \sec^2\bar{\gamma}}, \tag{3.79}$$

where $\beta_d = h_d/r_d$, as used in the previous case where gravity was neglected. Upon non-dimensionalisation this becomes

$$P(\bar{\gamma}) = -\frac{\beta_d}{Ca\sec^2\bar{\gamma}}\sqrt{\frac{h_0}{R}}. \tag{3.80}$$

Solution:

Now that suitable boundary conditions have been specified, equations (3.70) and (3.71) can be integrated to solve for the hydrostatic and hydrodynamic pressures which are required in order to determine the downstream meniscus location and film thickness. Using (3.73), equation (3.70) is thus integrated to determine the hydrostatic pressure,

$$P_{HS}(X_{HS}) = St\sqrt{\frac{R}{h_0}}(X_{HS}+X_{head}). \tag{3.81}$$

The hydrodynamic pressure, P_{HD}, is ascertained by integrating (3.71) between the limits $-\pi/2$ and $\bar{\gamma}$, where $\bar{\gamma}$ marks the position of the meniscus ($X_D = \tan(\bar{\gamma})$) and $\gamma \to -\pi/2$ as $X_{HD} \to -\infty$ (i.e. using (3.74)). Therefore,

$$P_{HD}(\bar{\gamma}) = 3(1-S)\left[\frac{\sin 2\bar{\gamma}}{2} + \bar{\gamma} + \frac{\pi}{2}\right]$$

$$- \frac{3H_2}{2}\left[\frac{sin4\bar{\gamma}}{4} + 2\sin 2\bar{\gamma} + 3\bar{\gamma} + \frac{3\pi}{2}\right]. \tag{3.82}$$

The total pressure at the meniscus is thus given by,

$$P(\bar{\gamma}) = 3(1-S)\left[\frac{\sin 2\bar{\gamma}}{2} + \bar{\gamma} + \frac{\pi}{2}\right]$$

$$- \frac{3\alpha_d}{2}\sec^2\bar{\gamma}\left[\frac{sin4\bar{\gamma}}{4} + 2\sin 2\bar{\gamma} + 3\bar{\gamma} + \frac{3\pi}{2}\right]$$

$$+ St\sqrt{\frac{R}{h_0}}\left[\sqrt{\frac{h_0}{R}}\tan(\bar{\gamma}) + X_{head}\right]. \tag{3.83}$$

Equations (3.80) and (3.83) can together be solved for the location of the meniscus, $\bar{\gamma}$, after which (3.70) and (3.71) can be integrated to find the pressure profile, $P(\gamma)$. Note that the pressure profiles obtained are only plotted on the hydrodynamic length scale and so do not extend to the top of the hydrostatic head (where the pressure is zero).

Figure 3.25 shows pressure profiles for $X_{head} = 0.50$, $Ca = 0.03$, $S = 0.50$ and $h_0/R = 10^{-4}$ for four values of Stokes number, St (including the dotted line representing $St = 0$ i.e. the case without gravity). As St increases the magnitude of the maximum pressure increases while the pressure gradient at the outlet increases only marginally.

Pressure profiles for $St = 0.02$, $Ca = 0.03$, $S = 0.50$ and $h_0/R = 10^{-4}$ for four values of X_{head} are shown in figure 3.26. As X_{head} increases, the magnitude of the maximum pressure increases and the pressure gradient at the outlet increases only marginally.

A plot of the location of the dynamic wetting line against X_{head} is shown in figure 3.27 for $Ca = 0.03$, $S = 0.50$, $h_0/R = 10^{-4}$ and four values of St. As expected, if $St = 0.00$ the height of the hydrostatic head has no influence on the wetting line position. However, as either St or X_{head} increase the wetting line location moves further downstream.

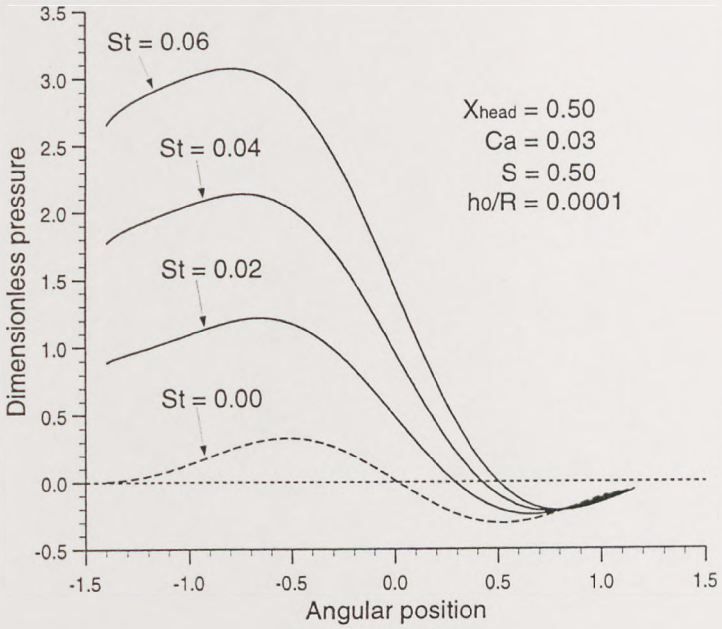

Figure 3.25: Pressure profiles for $X_{head} = 0.50$, $Ca = 0.03$, $S = 0.50$, $h_0/R = 10^{-4}$ and various Stokes numbers.

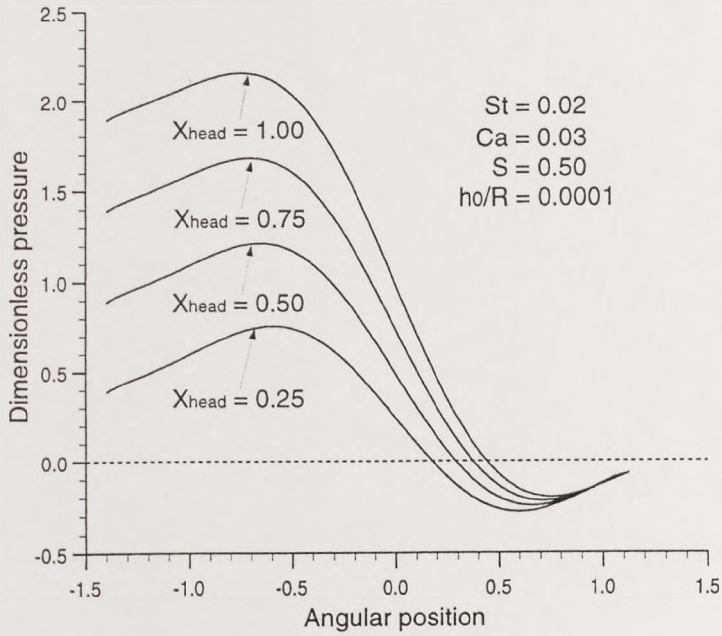

Figure 3.26: Pressure profiles for $St = 0.02$, $Ca = 0.03$, $S = 0.50$, $h_0/R = 10^{-4}$ and various hydrostatic head heights.

Figure 3.28 is a plot of film thickness distribution (H_2) against X_{head} for $Ca = 0.03$, $S = 0.50$ and $h_0/R = 10^{-4}$ for four values of St. Again, as expected, if $St = 0$ then X_{head} has no effect on H_2. If $St \neq 0$, then H_2 increases with both X_{head} and St i.e. as expected, the hydrostatic head causes the flux through the nip to increase.

3.4.1.2 Perturbed flow

The base flow is perturbed in an identical way to the previous case where gravity was neglected (following Pearson [1960]), which results in the following boundary value problem for $g(X)$

$$\frac{d^2g}{dX^2} + \frac{6X}{1+X^2}\frac{dg}{dX} - 4\pi^2N^2g(X) = 0, \tag{3.84}$$

$$g(D) = \frac{\beta_d D}{6Ca}\sqrt{\frac{h_0}{R}} + \frac{\pi^2N^2}{3Ca}\left(\frac{h_0}{R}\right)(1+D^2)^2 - \frac{1-S}{2} + \alpha_d - \frac{StH_D^2}{2}, \tag{3.85}$$

$$\left(\frac{dg}{dX}\right)_D = \frac{-2\alpha_d D}{1+D^2} + \Sigma(\alpha_d - 1), \tag{3.86}$$

$$g(-X_{head}\sqrt{\frac{R}{h_0}}) = 0. \tag{3.87}$$

For each base flow solution, equations (3.84)-(3.87) can then be solved numerically (using the NAG routine D02NBF) for the growth rate (Σ) as a function of wavenumber (N).

3.4.2 Discussion of results

Once Σ is obtained (given Ca, S, h_0/R, St and X_{head}), the critical conditions to produce neutral stability can be ascertained, from which operability diagrams in the $Ca-S$ plane can be drawn to illustrate regions of stability. As in section 3.1, above (and to the left of) each curve ribs occur whereas below (and to the right of) each curve the base flow is stable.

Figure 3.29 shows such an operability diagram for $X_{head} = 0.50$ and $h_0/R = 0.0005$ for four values of Stokes number. As St increases from 0.00 to 0.06, the region of instability increases (i.e. Ca^{max} decreases and S^{min} increases). It is thus clear that increasing St has a destabilising effect.

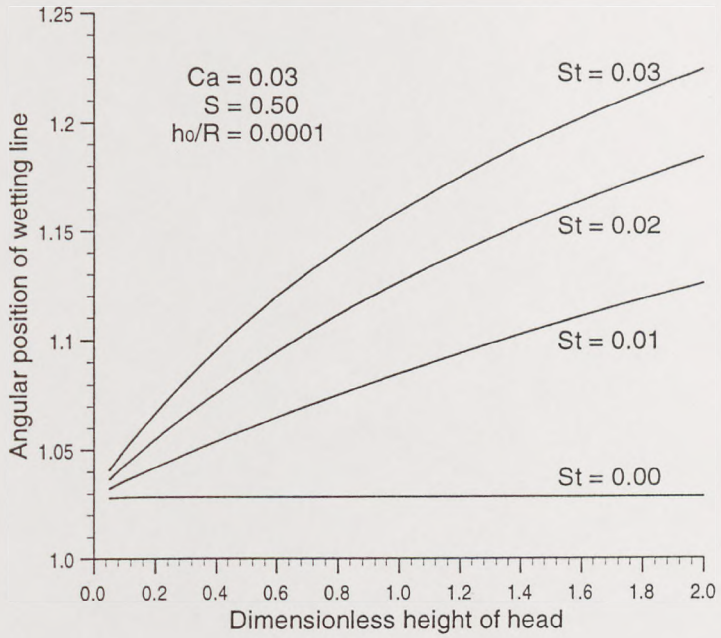

Figure 3.27: Angular position of the wetting line, $\bar{\gamma}$, against X_{head} for $Ca = 0.03$, $S = 0.50$ and $h_0/R = 10^{-4}$ for four values of St.

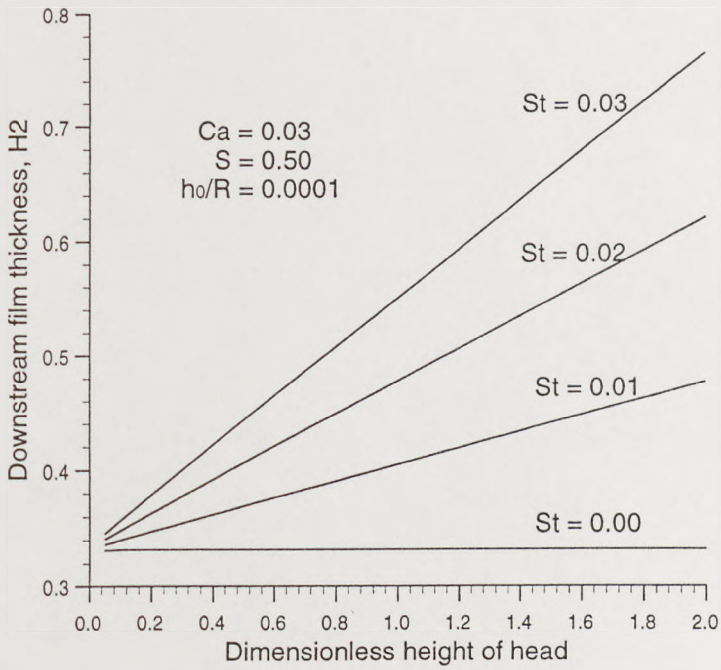

Figure 3.28: Film thickness predictions (H_2) against X_{head} for $Ca = 0.03$, $S = 0.50$ and $h_0/R = 10^{-4}$ for four values of St.

The effect of the non-dimensional height of the head is not so straightforward and is in fact dependent on the magnitude of the Stokes number, as shown by figures 3.30-3.32. Figure 3.30 shows an operability diagram for $St = 0.02$ and $h_0/R = 0.0005$ for four values of X_{head}. As X_{head} increases, the region of instability decreases (i.e. Ca^{max} increases and S^{min} decreases). However, for $St = 0.04$ and $h_0/R = 0.0005$ (as in figure 3.31) increasing X_{head} decreases Ca^{max} (promoting instability) but also decreases S^{min} (promoting stability). If St is increased still further to $St = 0.06$ (as in figure 3.32) then as X_{head} increases, the region of instability now increases (i.e. Ca^{max} decreases and S^{min} increases), the opposite effect to that at $St = 0.02$. Consequently, at small values of Stokes number increasing X_{head} has a stabilising effect, whereas at larger values, increasing X_{head} has a destabilising effect.

The above results can be explained via the S.H. for which it was previously noted that for 2-dimensional stability, $g(D, N = 0) > 0$, where

$$g(D, N = 0) = \frac{\beta_d D}{6Ca}\sqrt{\frac{h_0}{R}} - \left(\frac{1 - S}{2} - \alpha_d + \frac{StH_D^2}{2}\right). \tag{3.88}$$

The first term in (3.88), arising from the surface tension, is stabilising whereas the second term, arising from the pressure gradient at the outlet, is destabilising. Now, as seen from figure 3.27, increasing either St or X_{head} moves the meniscus further away from the nip, increasing D and so increasing the surface tension term. However, increasing St or X_{head} also increases the pressure gradient (at the outlet) and so it is clear that the overall effect on the stability comes from a balance of these two effects. Hence, as St increases (see figure 3.29), the increase in the pressure gradient term overrides the increase in the surface tension term to give an overall destabilising effect. At low St (e.g. $St = 0.02$ - see figure 3.30), increasing X_{head} has a stabilising effect because the increase in the surface tension term dominates. Conversely, at high St (e.g. $St = 0.06$ - see figure 3.32), increasing X_{head} has a destabilising effect because the increase in the pressure gradient term dominates.

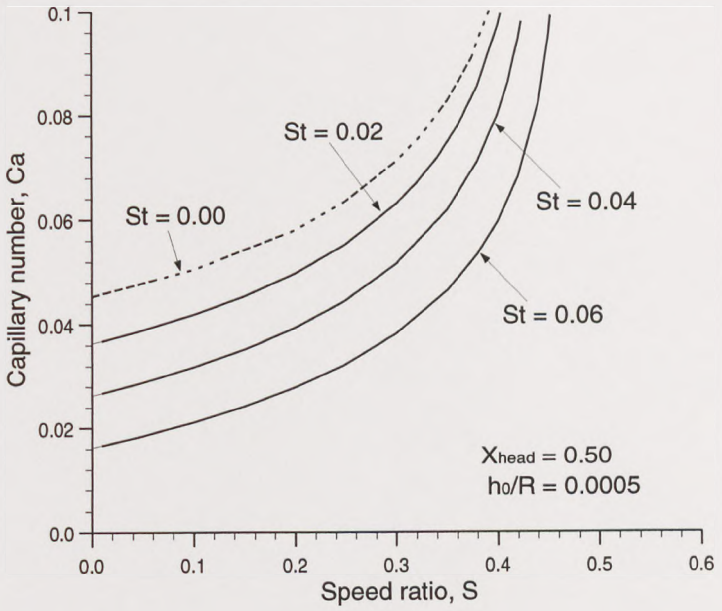

Figure 3.29: Operability diagram in the $Ca - S$ plane showing the effect of increasing St for $X_{head} = 0.50$ and $h_0/R = 0.0005$.

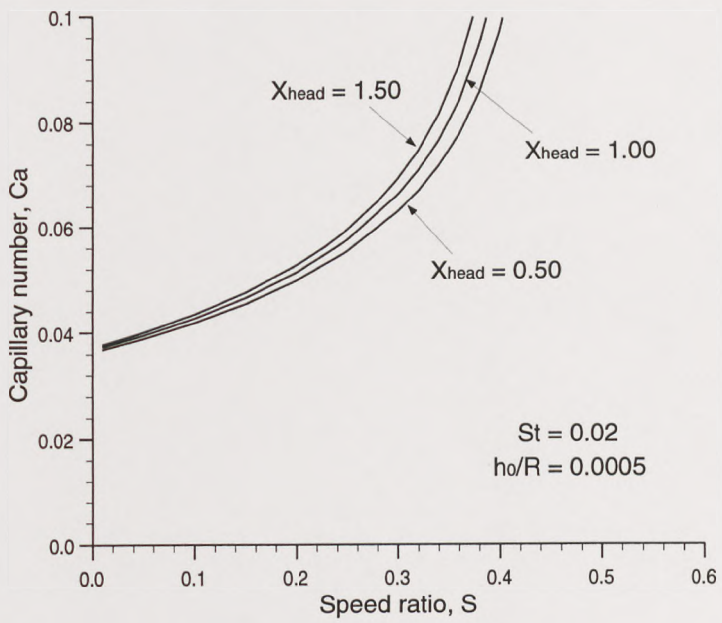

Figure 3.30: Operability diagram in the $Ca - S$ plane showing the effect of varying X_{head} for $St = 0.02$ and $h_0/R = 0.0005$.

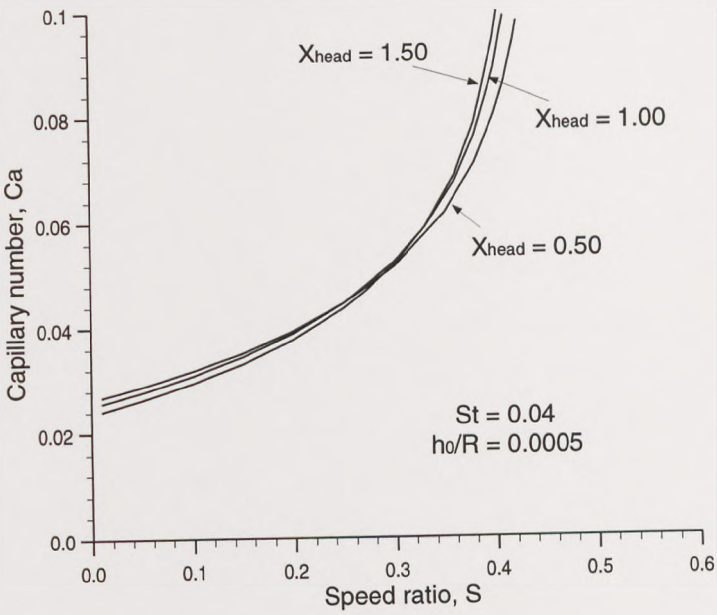

Figure 3.31: Operability diagram in the $Ca - S$ plane showing the effect of varying X_{head} for $St = 0.04$ and $h_0/R = 0.0005$.

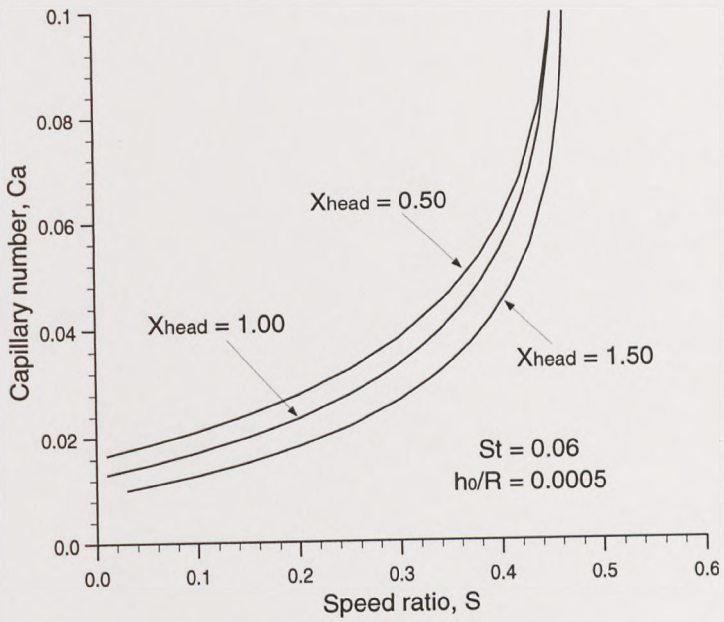

Figure 3.32: Operability diagram in the $Ca - S$ plane showing the effect of varying X_{head} for $St = 0.06$ and $h_0/R = 0.0005$.

3.5 An improved model of the contact line region

In the the previous model for the flow in a reverse roll coater the dynamic contact angle, θ_d, needed to be prescribed; it was chosen that $\theta_d = constant$. However, as experiments have shown (see Zhou and Sheng [1990] and Shikhmurzaev [1993a]), such models are insufficient and it would be greatly more beneficial for the mathematical model to produce θ_d once all the hydrodynamic parameters have been prescribed. The aim of this section is to apply such a model, recently proposed by Shikhmurzaev [1993a], to the inlet flooded reverse roll coater and examine its effect on the base flow and prediction for the onset of ribbing (in the form of operability diagrams). The main idea of the model is as follows: since in the advancing contact line motion material elements come from the gas-liquid interface to the solid-liquid interface, their properties change asymptoting to the equilibrium properties of the elements of the liquid-solid interface. Hence, the flow causes a surface tension gradient along the liquid-solid interface which influences the dynamic contact angle and the force between the liquid and the solid in the vicinity of the contact line.

3.5.1 A general model for the dynamic contact line region

The model uses the concept of two surface phases, labelled 1 and 2 for the liquid-gas and liquid-solid interfaces respectively. Each of these surfaces have their own equilibrium surface density, ρ^s_{1e} and ρ^s_{2e}, and unknown average dimensional interfacial velocities, V^s_1 and V^s_2, and pressures, P^s_1 and P^s_2.

To solve for the unknown surface velocities and pressure a set of boundary conditions are derived (Shikhmurzaev [1993a,1994]) based on balancing the forces across the two interfaces, continuity of surface mass and properties of the interface. The first boundary condition eliminates the shear stress singularity inherent in the classical formulation and is similar to that which has been documented as the Navier condition, but for the inclusion of the extra term which introduces a surface tension gradient. The full boundary condition is thus written as,

$$T_{nt} + \frac{1}{2}\nabla\sigma \;=\; \beta(\underline{U} - U_1\hat{\underline{t}}), \tag{3.89}$$

where T_{nt} is the dimensional tangential shear stress component of the stress tensor, $\underline{\underline{T}}$, $\hat{\underline{t}}$ is the positive oriented tangent to the roller, β is the coefficient of sliding friction and $\underline{U}$ is the bulk fluid velocity. Note that the first term on the left-hand-side of (3.89) only becomes important in the immediate vicinity of the contact line, while in the major part of the slip region, slip is determined by the surface tension gradient (see Shikhmurzaev

[1993a]). The equations which describe the surface parameters along the liquid-solid interface are,

$$\frac{\partial \rho^s}{\partial t} + \nabla.(\rho^s \underline{V}^s) = -\frac{\rho^s - \rho^s_{2e}}{\tau}, \tag{3.90}$$

$$\underline{V}^s = \frac{1}{2}(\underline{U} + U_1\hat{\underline{t}}) + \alpha\nabla\sigma, \tag{3.91}$$

$$(\underline{U} - U_1\hat{\underline{t}}).\hat{\underline{n}} = 0, \tag{3.92}$$

$$\sigma = \gamma(\rho^s_0 - \rho^s), \tag{3.93}$$

where τ represents the relaxation time of the liquid (see Kochurova *et al* [1974]), $\underline{U}$ and $U_1\hat{\underline{t}}$ are the velocities of the liquid and the solid on opposite sides of the interface, ρ^s is the surface density, ρ^s_0 is the surface density corresponding to zero surface pressure, and γ and α are phenomenological coefficients. The right-hand-side of the continuity condition, equation (3.90), represents the relaxation of the surface density due to mass exchange between the liquid-solid interface and bulk fluid and is neglected in the boundary conditions for the bulk velocity. The equation for the velocity of the interface, (3.91), is derived thermodynamically (see Shikhmurzaev [1993a],[1994]), although it can be thought of as an average of the bulk and roll velocities. Equation (3.92) represents the kinematic condition and (3.93) is the equation of state for the liquid-solid interfacial layer.

The dimensional boundary conditions on the free surface are derived in the same way (Shikhmurzaev [1993a,1994]) and are given as

$$T_{nn} - \sigma\kappa + P_g = 0 \quad \left[cf \quad \underline{\underline{T}}.\hat{\underline{n}} - \sigma\frac{d\hat{\underline{t}}}{ds} + P_g\hat{\underline{n}} = 0 \right], \tag{3.94}$$

$$T_{tn} + \nabla\sigma = 0, \tag{3.95}$$

$$\frac{\partial \rho^s}{\partial t} + \nabla.(\rho^s \underline{V}^s) = -\frac{\rho^s - \rho^s_{1e}}{\tau}, \tag{3.96}$$

$$(1 + 4\alpha\beta)\nabla\sigma = 4\beta(\underline{V}^s - \underline{U}), \tag{3.97}$$

$$\sigma = \gamma(\rho^s_0 - \rho^s). \tag{3.98}$$

In the equation for the normal stress balance (3.94), P_g is the dimensional pressure of the gas (assumed to be zero for the remainder of this study) and κ is the curvature of the liquid-gas interface. Equation (3.95) represents the non-zero tangential shear stress condition due to the non-zero surface tension gradient.

To resolve the dynamic contact angle and slip region, matching conditions are required at the contact line to relate the liquid-solid properties to the liquid-gas properties,

namely the surface mass balance equation (which guarantees that the liquid motion is rolling) and Young equation (see Young [1805]), being

$$(\rho_1^s \underline{v}_1^s).\underline{e} \;=\; (\rho_2^s \underline{v}_2^s).\hat{\underline{t}}, \tag{3.99}$$

and

$$\sigma_1 \cos\theta_d \;=\; -\sigma_2, \tag{3.100}$$

respectively. Here $\underline{e}$ is the tangent to the free surface at the wetting line.

Incorporating such a complex model into the full finite element formulation forms a subject in its own right and is beyond the scope of this research. In fact, to the authors knowledge, the model has yet to be incorporated into any numerical code although, it is possible to use the asymptotic theory for small Ca (Shikhmurzaev [1993a,1994,1996]) which is the topic of the following section.

3.5.2 Small capillary number asymptotics for the contact line

Shikhmurzaev [1993a,1994] applied the technique of matched asymptotic expansions for small $U_1\tau/h_0$ and Ca in order to more simply obtain the dynamic contact angle. The assumption that the free surface is planar in the vicinity of the contact line enables one to identify three asymptotic regions (see figure 3.33):

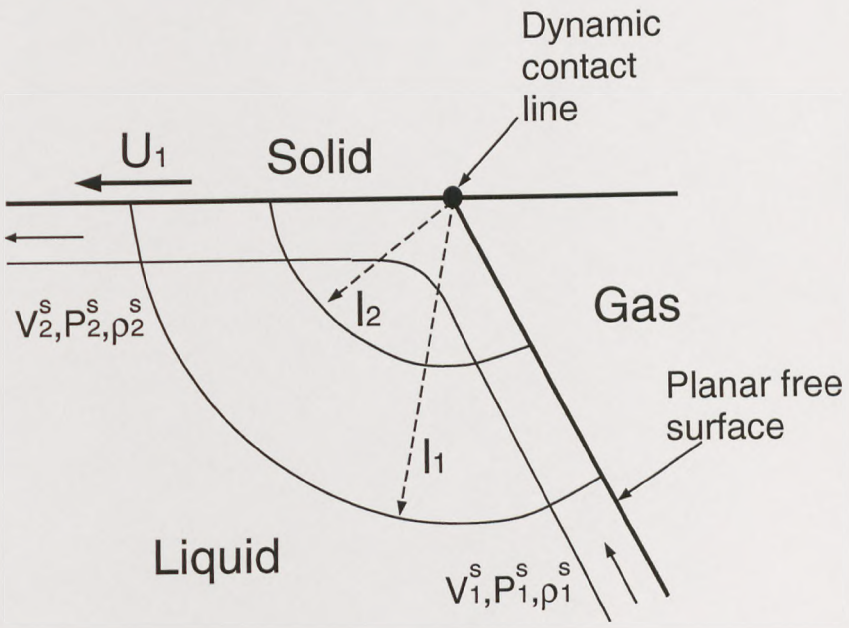

Figure 3.33: Schematic of the region of flow near the contact line.

1. The *outer* region is associated with length scale h_0 and is located far from the contact line. The classical solution of the Stokes equation with the no-slip boundary condition on the solid surface and zero tangential stress on the free surface is valid here and so the radial and transverse components of velocity and the streamfunction are given by (see Moffatt [1964])

$$\begin{aligned} U_r &= \frac{1}{r}\frac{\partial \psi}{\partial \theta}, \\ U_\theta &= -\frac{\partial \psi}{\partial r}, \\ \psi &= \frac{r}{\sin\theta_d \cos\theta_d - \theta_d}\left[(\theta - \theta_d)\sin\theta - \theta\cos\theta_d \sin(\theta - \theta_d)\right]. \end{aligned} \tag{3.101}$$

2. The *intermediate* region has a characteristic non-dimensional length of order $l_1 = U_1\tau/h_0$ and is where properties of surface phases can considerably change and surface tension gradients along the liquid-solid interface appear. The gradient induces apparent slip between the liquid and the solid.

3. The *inner* or *viscous* region with dimensions of the order $l_2 = l_1 Ca$, where $Ca \ll 1$, includes the three-phase interaction zone (contact line). In this region viscous stress become comparable with the surface tension gradients and as $Ca \to 0$ this inner region may be neglected.

Following Shikhmurzaev [1993a] the *dimensionless contact line speed* is related to the capillary number by,

$$\nu = SCaYu, \tag{3.102}$$

where Yu is the yet unknown parameter, but is related to the properties of the bulk fluid. Here, it is broken down into the form

$$Yu = \sqrt{\left(\frac{\sigma\tau}{\mu h_0}\right)\left(\frac{\beta h_0}{\mu}\right)\left(\frac{1-\rho_{1e}^s}{1+4\alpha\beta}\right)}, \tag{3.103}$$

which is fixed for a particular fluid. The term $\frac{\sigma\tau}{\mu h_0}$ is used to determine the length of the intermediate region, l_1, so that it is a function of Ca,

$$l_1 = SCa\left(\frac{\sigma\tau}{\mu h_0}\right). \tag{3.104}$$

To determine the dynamic contact angle, θ_d, the velocity of the fluid in the liquid-gas interface needs to be calculated which, from (3.101), is given by

$$U_r(\theta_d) = \frac{\sin\theta_d - \theta_d\cos\theta_d}{\sin\theta_d\cos\theta_d - \theta_d}. \tag{3.105}$$

Applying the technique of matched asymptotic expansions to (3.90) and (3.91) as $(1-\rho_{1e}^s) \to 0$ (i.e. for fluids of low compressibility) and using the static Young equation,

$$\rho_{2e}^s = 1 + (1-\rho_{1e}^s)\cos(\theta_s), \tag{3.106}$$

together with (3.99) and (3.100) then leads to the following equation for θ_d which can be solved once the fluid properties, θ_s, Ca and S are specified (see Shikhmurzaev [1993a,1994,1996]):

$$(\cos\theta_s - \cos\theta_d)\left[1 + \frac{\sqrt{\nu^2+1}-\nu}{2\nu}\right] = \frac{1+\rho_{1e}^s U_r(\theta_d)}{1-\rho_{1e}^s} + \cos\theta_s. \tag{3.107}$$

For the rest of this section, the physical parameters have been set to,

$$\begin{aligned} \tau = 1.0\times10^{-4}, \quad \sigma = 4.0\times10^{-2}, \quad \rho_{1e}^s = 0.98, \\ \mu = 2.0\times10^{-2}, \quad \beta = 1.0\times10^{4}, \quad \alpha = 1.0\times10^{-4}, \end{aligned} \tag{3.108}$$

giving $Yu = 0.632$. The above theory enables the contact angle to be calculated before

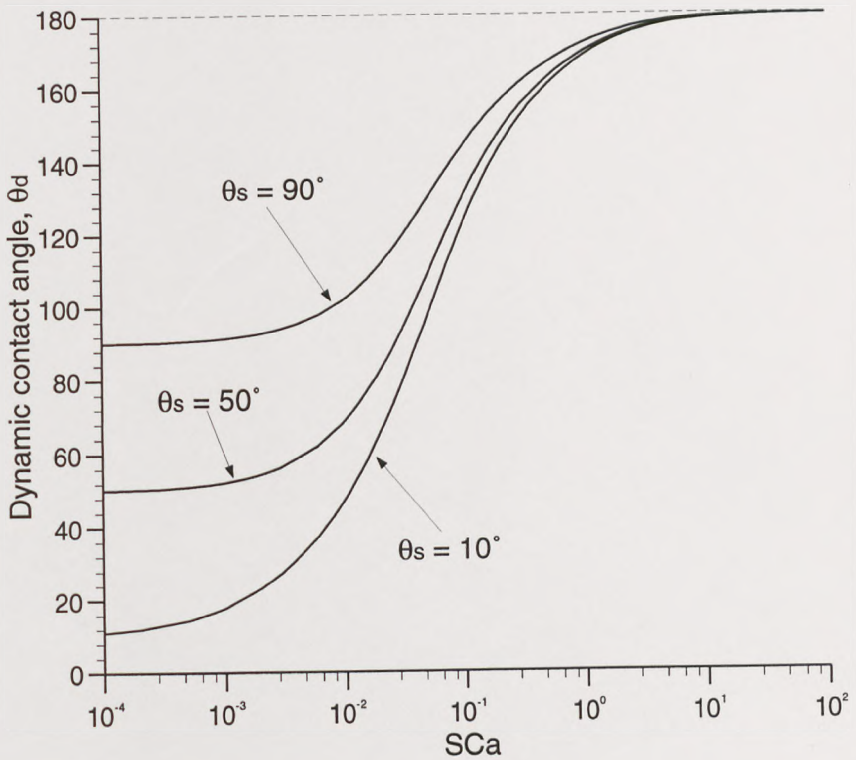

Figure 3.34: Dependence of the dynamic contact angle, θ_d, with the capillary number based on the upper roll speed, SCa for $\theta_s = 10°, 50°, 90°$.

the 2-dimensional flow field is calculated. This, in effect, means that the dynamic contact angle is only a function of Ca and S. A plot of θ_d against $log(SCa)$ for three values

of θ_s is shown in figure 3.34. The three curves are qualitatively similar with $\theta_d \rightarrow \theta_s$ as $SCa \rightarrow 0$. Further, θ_d increases with SCa (as predicted by experiment) and, for the set of parameters chosen (see (3.108)), θ_d asymptotes to 180°.

Shikhmurzaev [1993a] found that analytical predictions for θ_d compared well with results obtained experimentally by Hoffman [1975] and Strom *et al* [1990]. The numerical coupling of the asymptotics to the 2-dimensional flow field is currently being investigated by Summers *et al* [1998] for inlet starved forward roll coating using the FE method.

Note that recent experimental evidence by Savelski *et al* [1995] suggests that the rolling motion assumed in Shikhmurzaev's [1993a] model is not always present but, for small θ_d and certain viscosity ratios (between the displaced and displacing liquids), a *splitting streamline* is present.

3.5.3 Effect of Shikhmurzaev's asymptotic theory on the base flow

Figure 3.35 shows pressure profiles for $Ca = 0.05$, $S = 0.50$ and $h_0/R = 0.01$ for three values of θ_s. As θ_s increases, the dynamic wetting line moves further towards the nip and the magnitude of the minimum pressure decreases.

Again, there is a limiting value of S (where $S = S^{lim}$) for which the wetting line is situated at the nip (i.e. so $\bar{\gamma} = 0$). Figure 3.36 is a plot of film thickness, H_2, for varying S (i.e. for $0 < S < S^{lim}$) for $Ca = 0.03$, $h_0/R = 0.01$ and three values of θ_s (the full lines). Recall that using Shikhmurzaev's asymptotic theory, θ_d varies with θ_s, S and Ca and is calculated using equation (3.107). For comparison, the graph also shows (via the dotted line) the variation of H_2 with S using the previous model where $\theta_d = 90° = constant$. It can be seen that increasing θ_s reduces S^{lim}. This suggests that thinner films can be produced by using fluids which have smaller static contact angles because a higher value of S can be used before the wetting line passes through the nip.

3.5.4 Effect of Shikhmurzaev's asymptotic theory on the onset of ribbing

Figure 3.37 shows, for $h_0/R = 10^{-4}$, a plot of $Ca*$ against S for three different values of θ_s (the full lines) with comparison to the previous model where $\theta_d = 90° = constant$ (the dotted line). Increasing θ_s has two effects, the first of which is to reduce S^{min} thus increasing the prospect of stability. However, this is countered by the second

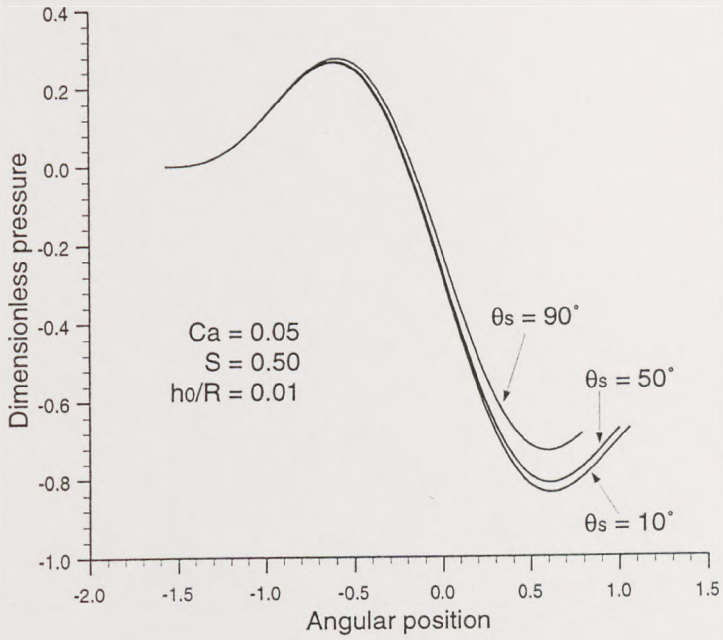

Figure 3.35: Pressure profiles for $Ca = 0.05$, $S = 0.50$, $h_0/R = 0.01$ and various static contact angles.

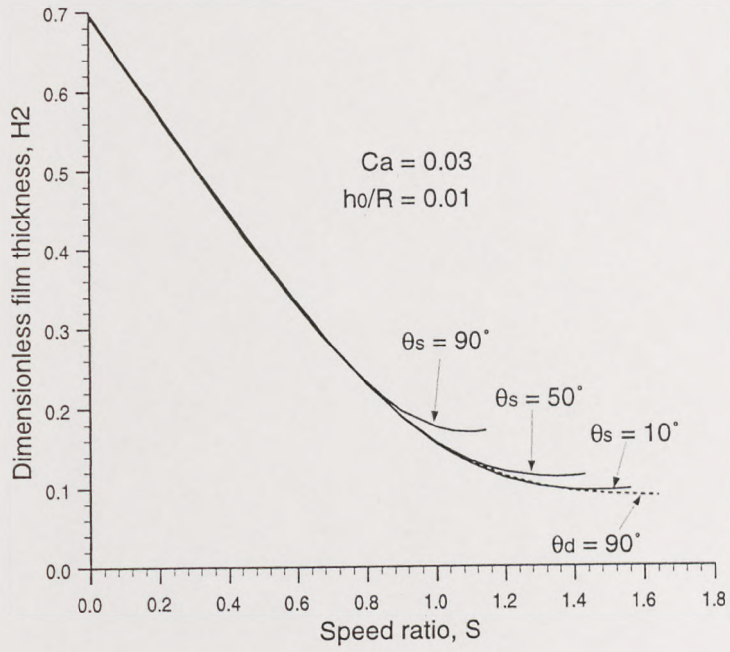

Figure 3.36: Film thickness predictions (H_2) against speed ratio (S) for $Ca = 0.03$, $h_0/R = 0.01$ with three values of θ_s (the full lines); A comparison is shown with the previous model, $\theta_d = 90° = constant$ (the dotted line). Note that all the curves terminate at S^{lim} i.e. when the wetting line reaches the nip.

effect which promotes the possibility of instability by reducing Ca^{max}. An operator of a reverse roll coater therefore needs to know in which part of the operability diagram he/she is operating, in order to determine whether increasing θ_s reduces the possibility of ribbing or not.

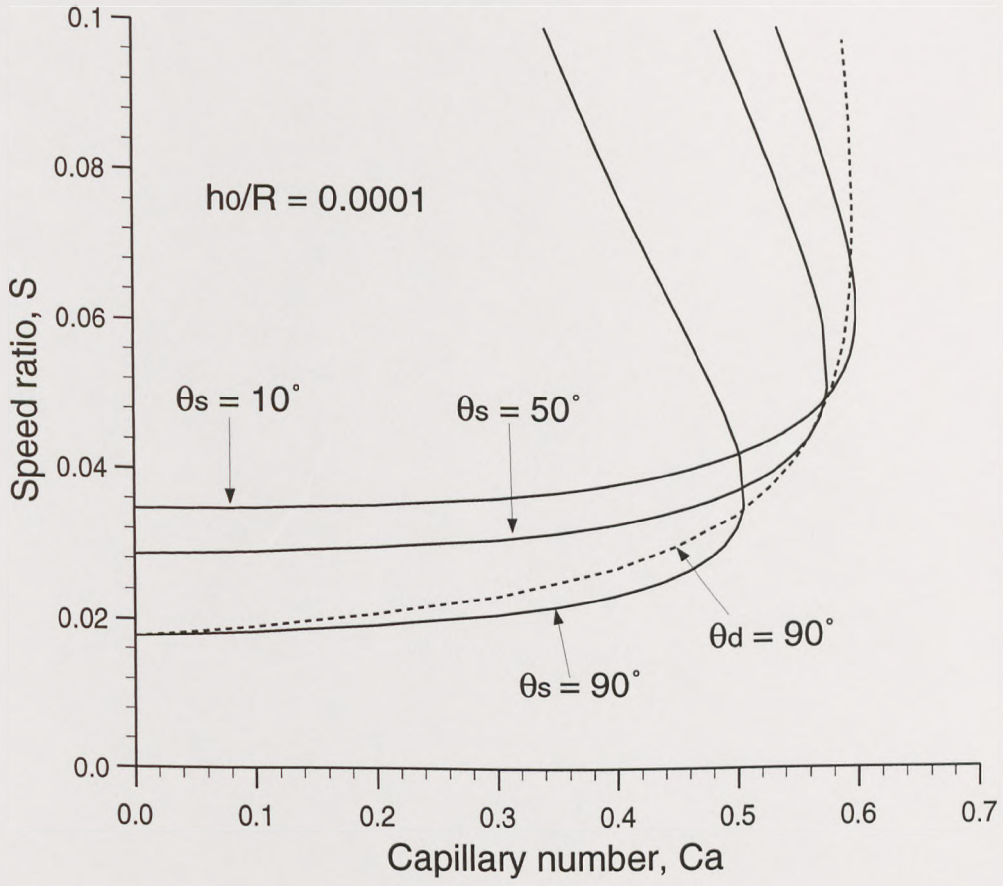

Figure 3.37: Operability diagram in the $Ca-S$ plane for $h_0/R = 10^{-4}$ and three values of θ_s (the full lines). A comparison is shown with the previous model, $\theta_d = 90^o = constant$ (the dotted line).

Note that the critical curves in the operability diagram can also be 'shifted' by altering other properties of the liquid used (apart from θ_s) i.e. by changing the parameters in (3.108).

3.6 Conclusions

In this chapter, the ribbing instability has been investigated in inlet flooded, reverse roll coating. By considering a 3-dimensional perturbation to a 2-dimensional base flow (based on lubrication theory), regions of instability in the $Ca - S$ control space were established which were in accordance with experimental observations. These diagrams have four key results:

- For each h_0/R, there is a Ca^{max} such that no ribbing occurs if $Ca < Ca^{max}$.
- For each Ca, there is a speed ratio beyond which no ribs occur (and a particular value of S, S^{min}, such that no ribbing occurs if $S > S^{min}$ for any Ca).
- Near S^{min}, there is a small range of S values for which there are two ranges of Ca in which the base flow is stable (separated by an unstable range).
- As h_0/R is increased, the region of stability increases (i.e. S^{min} decreases and Ca^{max} increases).

Results obtained using this linear stability analysis were then compared to predictions from a stability hypothesis, being a simple force argument to determine the stability of the flow which only take account of perturbations to the meniscus and pressure in the direction of the moving web. Using this criterion, it was shown that the effect of the various parameters on the stability of the downstream free surface can be ascertained by determining their effect on the pressure gradient and meniscus location. The S.H. was also shown to be sufficient for predicting stability (but not for instability), the agreement between the two theories improving as h_0/R is decreased.

Results from the linear stability analysis were also compared to those using a numerical approach based on the FE method, from which it was seen that the analytical approach overpredicts the critical capillary number for the onset of instability. This was attributed to the different contact line models in the two theories.

A variation of the inlet flooded model was then considered in which the nip was fed from above by a large reservoir of fluid (i.e. a hydrostatic head). It was seen that increasing both the height of the head and Stokes number moved the meniscus further downstream and enlarged the final film thickness. Increasing St also destabilises the flow (for all head heights). However, at low St, increasing the height of the head has a stabilising influence, whereas at high St it has the opposite effect.

Finally, an improved model of the dynamic contact line (developed by Shikhmurzaev [1993a]) was described in which the dynamic contact angle was no longer set to 90^0 but given a (constant) value related to various fluid and geometrical parameters. The limit of this theory for small Ca was then incorporated into the model and its effect on the base flow and its stability was examined.

Chapter 4

Instabilities in Forward Roll Coating

Contents

4.1 Introduction 112

4.1.1 Outline of this chapter 114

4.2 Inlet flooded case 119

4.2.1 Mathematical model 119

4.2.2 Method of solution 126

4.2.3 Discussion of results 127

4.2.4 Comparison with the Stability Hypothesis (S.H.) 129

4.2.5 Comparison with the computational approach 131

4.3 Inlet starved case 138

4.3.1 Mathematical Model 138

4.3.2 Discussion of results 147

4.3.3 Stability Hypothesis: downstream interface 152

4.3.4 Stability Hypothesis: upstream interface 153

4.3.5 Operability diagrams in the $Ca - H_i$ plane 155

4.4 Conclusions 161

4.1 Introduction

As described in chapter 1, there are three coating regimes in forward roll coating (see Malone [1992]), namely the *inlet flooded*, *moderately starved* and *meniscus* regimes.

The inlet flooded case has been thoroughly investigated using analytical, experimental and computational approaches. This includes measurement and prediction of the flux and final film thickness (see Pitts and Greiller [1961], Benkreira, Edwards and Wilkinson [1981], Coyle [1984], Ruschak [1985], Savage [1982] and Gaskell, Savage, Summers and Thompson [1995]). In this regime, not all the arriving liquid can pass through the nip and there is a 'rolling bank' of fluid far upstream where excess liquid runs back over the incoming film (Schneider [1962]). Therefore, mathematical models ignore the presence of the upstream free surface and consider the liquid to extend to "infinity" upstream of the nip.

In the moderately starved and meniscus regimes, the upstream free surface lies closer to the nip and therefore has an effect on the flow and must be included in the mathematical modelling. These two regimes are similar in that all the arriving liquid passes through the nip and so they will be referred to collectively as the *inlet starved* regime. Although used in industry for many years, this regime has not received quite the same attention as the inlet flooded case. Malone [1992] (see also Gaskell, Innes and Savage [1998]) demonstrated the differences between the regimes experimentally and subsequently Gaskell *et al* [1995], using lubrication theory, obtained predictions for the film split ratio, meniscus location and pressure profile and showed them to be in good agreement with results obtained numerically using the FE method.

The stability of forward roll coating has been the subject of much investigation for many years, particularly with regard to the ribbing instability in the inlet flooded case which has received considerable attention from both experimentalists and theoreticians. Pitts and Greiller [1961] presented experimental data for the case of equal speed, contra-rotating rolls of equal radii. To mark the onset of ribbing they correlated the critical capillary number, $Ca* = \mu U/T$ (where U is the speed of the rollers, μ the viscosity of the fluid and T its surface tension), and geometry parameter, h_0/R (the ratio of the minimum gap between the rolls to the radius of the rolls), by the linear relationship

$$Ca* = 31\left(\frac{h_0}{R}\right).$$

Mill and South [1967] and Greener *et al* [1980] (with rollers of equal size and speed) obtained further data which they correlated by

$$Ca* = 10.3\left(\frac{h_0}{R}\right)^{3/4} \text{ and } Ca* = 7500\left(\frac{h_0}{R}\right)^{2}$$

respectively. Cheng [1981] gave an explanation for these different functional relationships. He suggested that the form of the neutral stability curve may vary throughout parameter space so that each relationship approximates the curve over a particular range of h_0/R values.

Following Pearson [1960], Savage [1984] used a linearised stability analysis in order to determine the stability of the base flow in the equal speed, inlet flooded, forward roll coater. Subsequently, Carter and Savage [1987] examined the unequal speed case. Fall [1982] went on to consider the stability of the 2-dimensional flow between a roll and a flat plate in which he included the time dependent response so as to obtain growth rate as a function of wavenumber. Coyle [1984] and Coyle *et al* [1990] applied ideas from linear stability theory to the finite element method and this approach, first developed by Bixler [1982], enabled them to determine critical capillary numbers (for each h_0/R) above which ribbing occurs for the $S = 1$ case.

By comparison, the stability of the inlet starved case has received considerably less attention in the literature. A similar problem which has been studied involves flow in the partially filled, narrow gap between two rotating cylinders, placed eccentrically one inside the other. This has been investigated experimentally by Rabaud, Michalland and Couder [1990], Rabaud and Hakim [1991], Michalland [1992] and Pan and De Bruyn [1994]. For the relatively large volume of fluid used, they saw ribbing on the meniscus situated on the diverging side of the nip. Reinelt [1995] then theoretically analysed this problem using linear stability theory and showed that there are actually two possible instabilities for this geometry, which he described as follows:

- The *primary instability* occurs when the volume of fluid is large so that the upstream interface remains on the converging side of the nip. The downstream meniscus (on the diverging side of the nip) becomes unstable at a critical capillary number and ribbing occurs.
- The *inverse instability* occurs when the volume of fluid is small enough such that the upstream meniscus passes through the nip and becomes unstable.

Michalland, Rabaud and Couder [1996] then examined experimentally the stability of the upstream meniscus for different volumes of fluid and obtained qualitative agree-

ment with Reinelt's analytical predictions. They observed two types of instability: first a propagating wave then a steady state pattern of fingers separated by air columns.

In meniscus roll coating, Malone [1992] showed experimentally that, for the forward case, increasing the upper roll speed caused the upstream meniscus to move to the diverging side of the nip. At a critical speed ratio, the meniscus becomes unstable and the coating bead collapses due to an instability termed *bead break*. Gaskell *et al* [1998] later illustrated the manifestation of this instability with the aid of figures 4.1 and 4.2. Figure 4.1 shows a series of images taken at increasing S with H_i, Ca and h_0/R all constant. No manipulation of the image has been performed on the flow field itself, although dotted lines have been added to indicate the edge of the rolls and arrows used to indicate roll direction. The x-position of minimum gap between the rolls, x_0, has also been added in order to mark the positions of the menisci. As S is increased from $S = 0.0$ to $S = 1.05$ the downstream (upstream) meniscus moves further upstream (downstream). Further, for $S > 0.8$, the upstream meniscus lies on the same side of the nip as the downstream.

Figure 4.2 shows a series of images taken at $0.5s$ intervals once speed ratio is stepped from $S = 1.05$ to $S = 1.08$ at $t = 0$. The images show that as time elapses, the downstream meniscus remains stationary whilst the upstream meniscus accelerates rapidly and touches the downstream interface before the bead breaks (at $t = 2.5s$). Bead break thus represents the limit of operability for a meniscus roll coater. Note that when this instability occurs, the transmission of light along the bead is broken and so the entire bead is observed to go dark.

For large S and a small gap between the rolls, air entrainment can also arise which can manifest by an upstream travelling wave or bubble generation (see Malone [1992]).

4.1.1 Outline of this chapter

The first aim of this chapter is to analyse the ribbing instability in inlet flooded forward roll coating in the absence of gravity, see figure 4.3. As in the reverse case (in chapter 3), by considering a 3-dimensional perturbation to a 2-dimensional base flow, regions of instability in the $Ca - S$ plane will be established and compared to those obtained using a stability hypothesis (as described in chapter 3) and a numerical finite element stability approach (described in chapter 2).

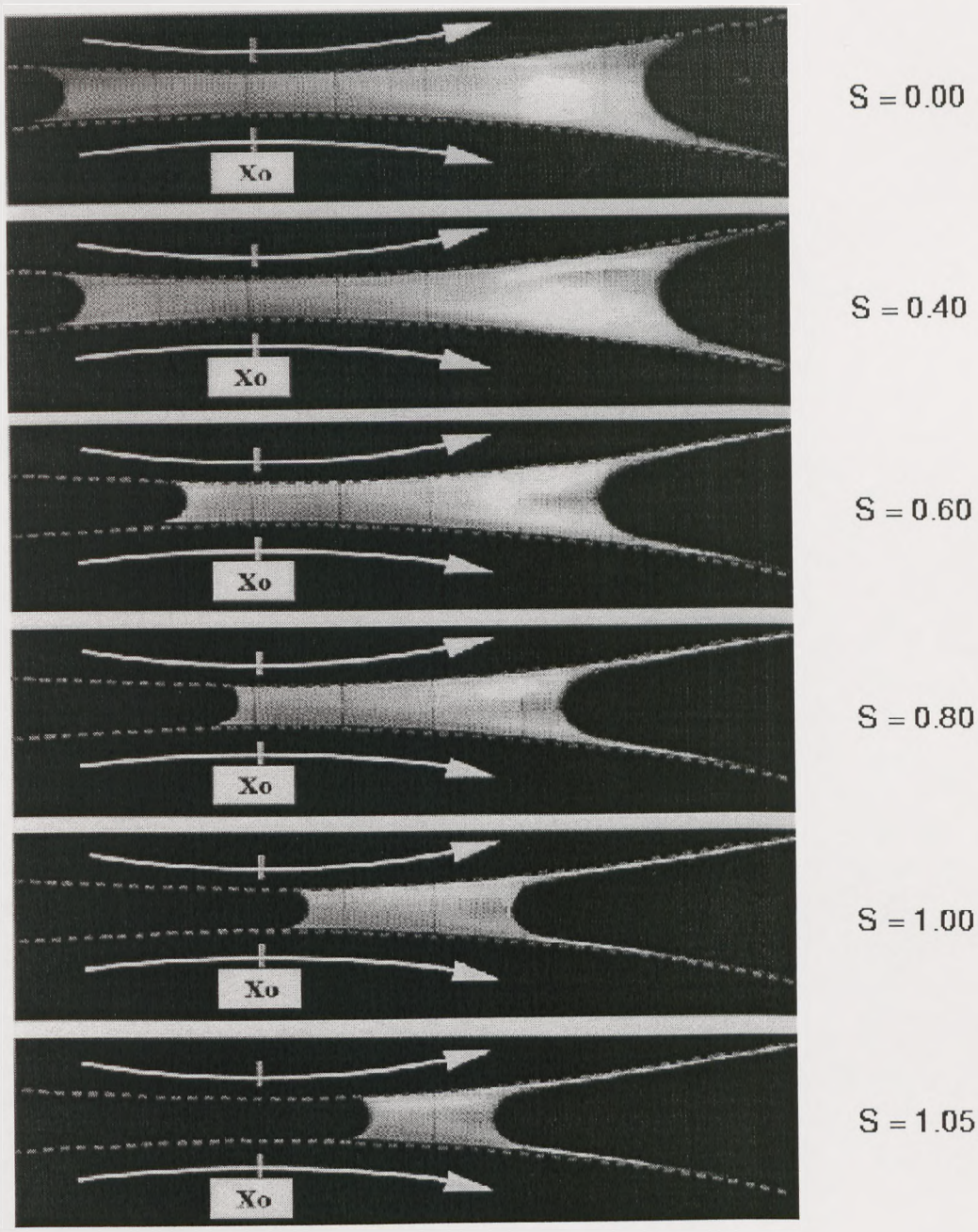

Figure 4.1: Pictures of the steady state bead in forward meniscus coating, obtained by Gaskell *et al* [1998].

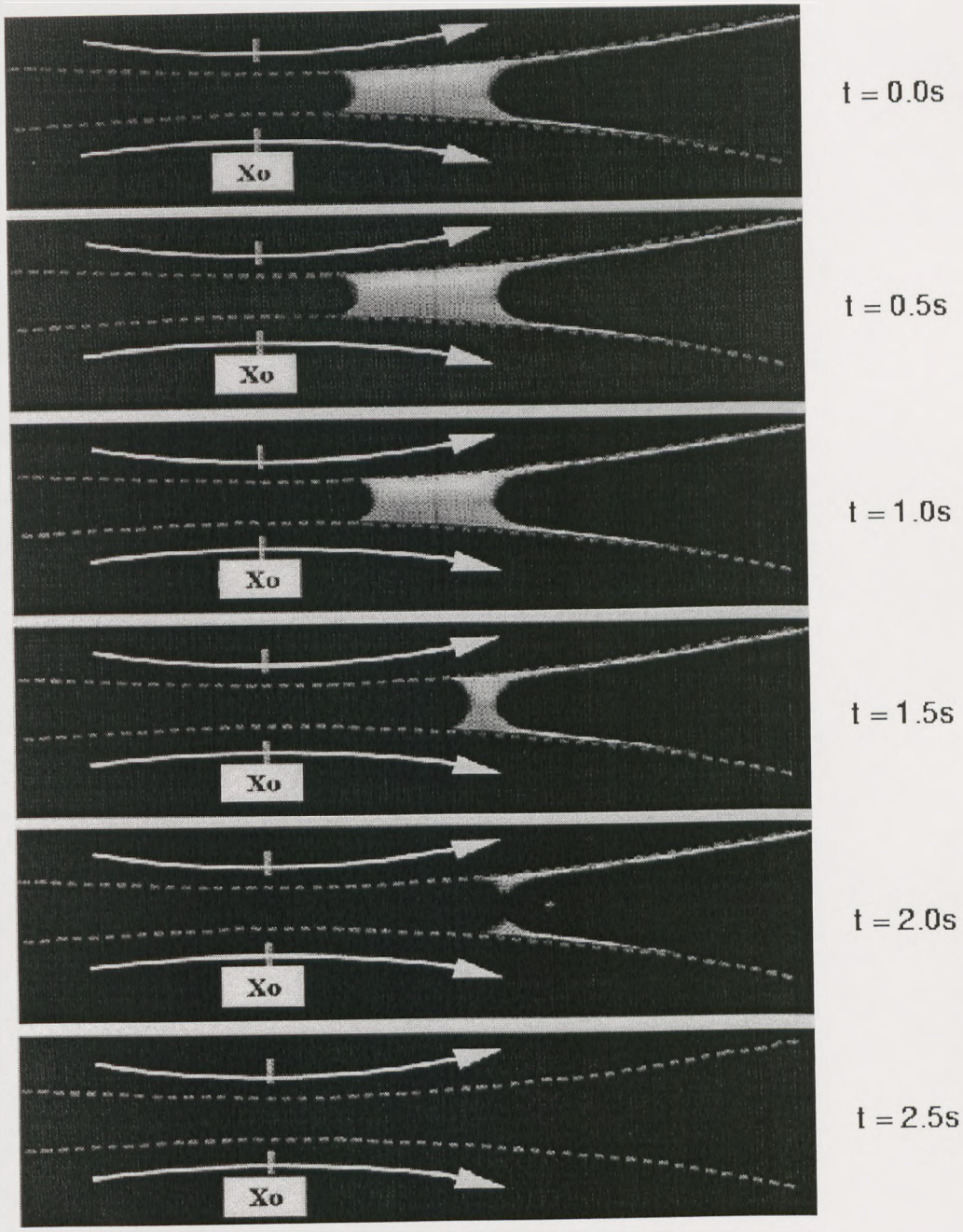

Figure 4.2: Bead break in forward meniscus coating, where S has been stepped from $S = 1.05$ to $S = 1.08$ at $t = 0.0s$; Gaskell *et al* [1998].

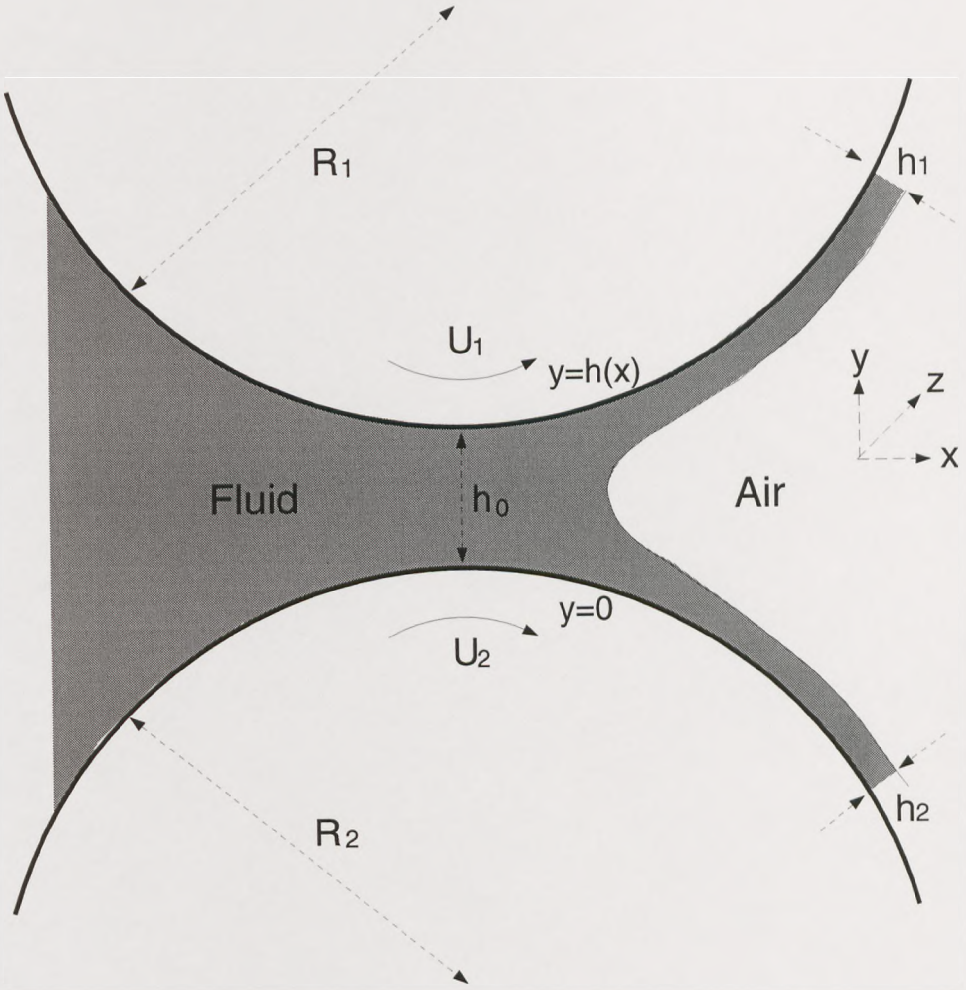

Figure 4.3: Schematic of an inlet flooded forward roll coater.

Instabilities in the two free surface case are then investigated, where the inlet is fed by an incoming film of prescribed thickness, see figure 4.4. An examination of the bead break phenomenon is performed and the effect of the upstream free surface on downstream ribbing examined. This is achieved again by considering a 3-dimensional perturbation to a 2-dimensional base flow, from which regions of instability in the $Ca - H_i$ plane are established (for each S, h_0/R). This linear stability theory is also compared to predictions obtained using a stability hypothesis on both the upstream and downstream free surfaces. Note that the upstream stability hypothesis and 2-dimensional stability analysis has already been examined by Gaskell *et al* [1998], although they did not consider the effect of the incoming film thickness which is included in the present model.

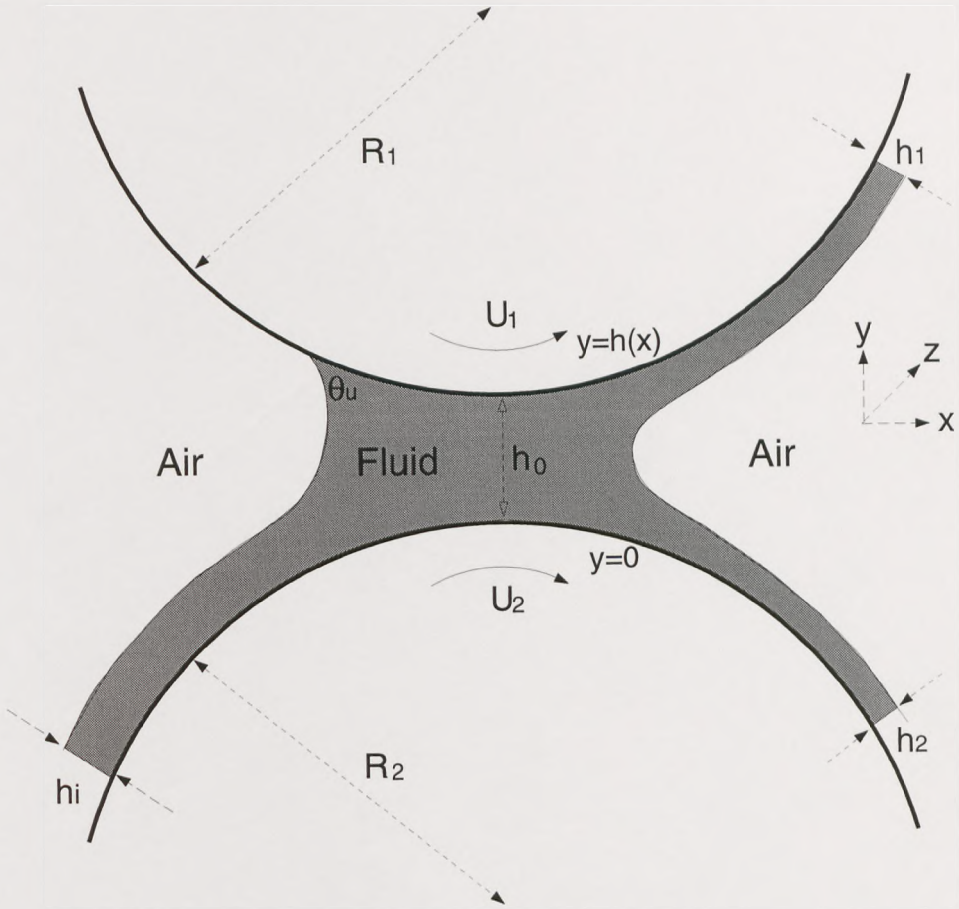

Figure 4.4: Schematic of an inlet starved forward roll coater.

4.2 Inlet flooded case

4.2.1 Mathematical model

4.2.1.1 Base flow

In this section, the aim is to determine the velocity and pressure fields together with the location of the meniscus (given h_0/R, S and and Ca) which are required in order to carry out the linear stability analysis.

Neglecting body forces, transient and inertia terms, the Navier-Stokes equations reduce to

$$0 = -\nabla p + \mu \nabla^2 \underline{u}. \tag{4.1}$$

Assuming unidirectional flow through the nip and that velocity gradients across the bead are negligible i.e. $\partial u/\partial x << \partial u/\partial y$ then (4.1) becomes

$$\frac{\partial p}{\partial x} = \mu \frac{\partial^2 u}{\partial y^2}, \tag{4.2}$$

and

$$\frac{\partial p}{\partial y} = 0. \tag{4.3}$$

Hence $p = p(x)$ and therefore integrating (4.2) twice and imposing the no slip boundary conditions on the rolls i.e.

$$\begin{aligned} u &= U_2 \text{ at } y = 0 \\ u &= U_1 \text{ at } y = h(x) \end{aligned} \tag{4.4}$$

gives

$$u = \frac{1}{2\mu}\frac{dp}{dx} y(y-h) + (U_1 - U_2)\frac{y}{h} + U_2, \tag{4.5}$$

where $h(x)$ is the gap width between the two rolls. This is approximated by a parabola,

$$h(x) \simeq h_0 + \frac{x^2}{R}, \tag{4.6}$$

where R is an average roll radius given by

$$\frac{2}{R} = \frac{1}{R_1} + \frac{1}{R_2}, \tag{4.7}$$

R_1 and R_2 being the radii of the upper and lower roll respectively. The flux, Q, is given by

$$Q = \int_0^{h(x)} u dy \tag{4.8}$$

which, using (4.5), becomes

$$Q = -\frac{1}{12\mu}\frac{dp}{dx}h^3 + (U_2 + U_1)\frac{h}{2}. \tag{4.9}$$

In equilibrium, the flux past any station x is constant and equal to the sum of the fluxes in the uniform films attached to the top and bottom rolls of thickness h_1 and h_2 respectively,

$$Q = h_1U_1 + h_2U_2. \tag{4.10}$$

Therefore,

$$\frac{dp}{dx} = \frac{12\mu}{h^2}\left(\frac{(U_2 + U_1)}{2} - h_1U_1 - h_2U_2\right). \tag{4.11}$$

Boundary conditions on pressure are i) a flooded inlet, so the pressure far upstream is zero i.e.

$$p(-\infty) = 0, \tag{4.12}$$

and ii) a balance of fluid and surface tension pressure at the meniscus,

$$p(x_d) = \frac{-T}{r_d}, \tag{4.13}$$

where r_d is the radius of curvature of the meniscus. The meniscus is approximated by a circular arc which meets the two films tangentially and so

$$h_d = 2r_d + h_1 + h_2, \tag{4.14}$$

where h_d is the width of the gap at $x = x_d$. Since x_d is unknown, another boundary condition is required which, for $Ca < 0.01$ (where $Ca = \mu U_2/T$), is provided by the Landau-Levich relationship for the ratios of the asymptotic film thicknesses, h_1 and h_2, to the radius of curvature, r_d,

$$\frac{h_1}{r_d} = 1.34(SCa)^{2/3}, \tag{4.15}$$

$$\frac{h_2}{r_d} = 1.34Ca^{2/3}.$$

For higher values of Ca, i.e. $0.01 \leq Ca \leq 0.1$, Ruschak [1981] suggested a relationship of the form

$$\frac{h_1}{r_d} = 0.56(SCa)^{1/2}, \tag{4.16}$$

$$\frac{h_2}{r_d} = 0.56Ca^{1/2}.$$

Using (4.14), the following expressions are obtained:

$$\alpha_{d1} = \frac{h_1}{h_d} = \begin{cases} \frac{0.56(SCa)^{1/2}}{2+0.56(1+S)Ca^{1/2}} & 10^{-2} \leq Ca \leq 10^{-1} \\ \\ \frac{1.34(SCa)^{2/3}}{2+1.34(1+S)Ca^{2/3}} & Ca < 10^{-2}, \end{cases} \tag{4.17}$$

$$\alpha_{d2} = \frac{h_2}{h_d} = \begin{cases} \frac{0.56Ca^{1/2}}{2+0.56(1+S)Ca^{1/2}} & 10^{-2} \leq Ca \leq 10^{-1} \\ \\ \frac{1.34Ca^{2/3}}{2+1.34(1+S)Ca^{2/3}} & Ca < 10^{-2}, \end{cases} \tag{4.18}$$

$$\beta_d = \frac{h_d}{r_d} = \begin{cases} 2 + 0.56(SCa)^{1/2} + 0.56Ca^{1/2} & 10^{-2} \leq Ca \leq 10^{-1} \\ \\ 2 + 1.34(SCa)^{2/3} + 1.34Ca^{2/3} & Ca < 10^{-2}. \end{cases} \tag{4.19}$$

Introducing non-dimensional variables defined by

$$\begin{aligned} H &= \frac{h}{h_0}, \\ H_2 &= \frac{h_2}{h_0}, \\ X &= \frac{x}{\sqrt{Rh_0}}, \\ S &= \frac{U_1}{U_2}, \\ P &= \frac{h_0}{\mu U_2}\sqrt{\frac{h_0}{R}}p, \end{aligned} \tag{4.20}$$

and writing $X = \tan(\gamma)$ (so $h(\gamma) = h_0 \sec^2\gamma$), Reynolds equation, (4.11), becomes

$$\frac{dP}{d\gamma} = 6(1+S)\cos^2\gamma - 12(H_2 + SH_1)\cos^4\gamma. \tag{4.21}$$

If (4.21) is integrated between the limits $-\pi/2$ (as $p(-\pi/2) = 0$) and $\bar{\gamma}$ (where $\bar{\gamma}$ marks the position of the film split - $X_D = \tan(\bar{\gamma})$) then

$$\begin{aligned} P(\bar{\gamma}) &= 3(1+S)\left[\frac{\sin 2\bar{\gamma}}{2}\bar{\gamma} + \frac{\pi}{2}\right] \\ &- \frac{3(H_2 + SH_1)}{2}\left[\frac{sin4\bar{\gamma}}{4} + 2\sin 2\bar{\gamma} + 3\bar{\gamma} + \frac{3\pi}{2}\right]. \end{aligned} \tag{4.22}$$

Also, from (4.13),

$$p(\bar{\gamma}) = -\frac{T}{r_d}. \tag{4.23}$$

This, using (4.14) and (4.19), gives

$$p(\bar{\gamma}) = -\frac{\beta_d \mu U_2}{Ca h_0 \sec^2 \bar{\gamma}}, \tag{4.24}$$

which when non-dimensionalised becomes

$$P(\bar{\gamma}) = -\frac{\beta_d}{Ca \sec^2 \bar{\gamma}} \sqrt{\frac{h_0}{R}}. \tag{4.25}$$

Equating (4.22) and (4.25) gives the following equation for $\bar{\gamma}$ which is solved once h_0/R, S and Ca are specified:

$$-\sqrt{\frac{h_0}{R}} \frac{\beta_d}{Ca \sec^2 \bar{\gamma}} = 3(1+S)\left[\frac{\sin 2\bar{\gamma}}{2} + \bar{\gamma} + \frac{\pi}{2}\right] - \frac{3(\alpha_{d2} + S\alpha_{d1})}{2} \sec^2 \bar{\gamma} \left[\frac{sin4\bar{\gamma}}{4} + 2\sin 2\bar{\gamma} + 3\bar{\gamma} + \frac{3\pi}{2}\right]. \tag{4.26}$$

Once $\bar{\gamma}$ has been calculated, the pressure distribution can be obtained by integrating (4.21) between the limits $-\pi/2$ and γ, giving

$$P(\gamma) = 3(1+S)\left[\frac{\sin 2\gamma}{2} + \gamma + \frac{\pi}{2}\right] - \frac{3(H_2 + SH_1)}{2} \left[\frac{sin4\gamma}{4} + 2\sin 2\gamma + 3\gamma + \frac{3\pi}{2}\right], \tag{4.27}$$

where $H_2 = \alpha_{d2} \sec^2 \bar{\gamma}$ and $H_1 = \alpha_{d1} \sec^2 \bar{\gamma}$.

Figure 4.5 shows resulting pressure profiles for $S = 1.00$ and $h_0/R = 0.001$ for three values of Ca. As Ca is increased, the location of the film split moves further towards the nip and the magnitude of the minimum pressure decreases. The pressure gradient at the film split location also decreases very slightly.

Pressure profiles for $Ca = 0.05$, $h_0/R = 0.001$ and three values of S are shown in figure 4.6. As S is increased, the magnitudes of the minimum and maximum pressures increase. The location of the film split changes only marginally.

Figure 4.7 shows pressure profiles for $Ca = 0.05$ and $S = 1.00$ for three values of h_0/R. As the gap ratio is increased the magnitude of the minimum pressure decreases, but the location of the film split remains the same.

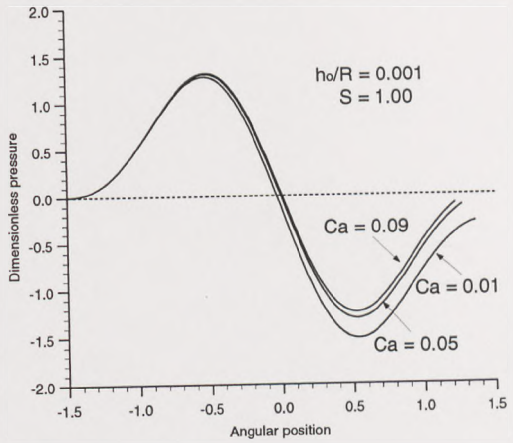

Figure 4.5: Pressure profiles for $S = 1.00$ and $h_0/R = 0.001$ and various capillary numbers.

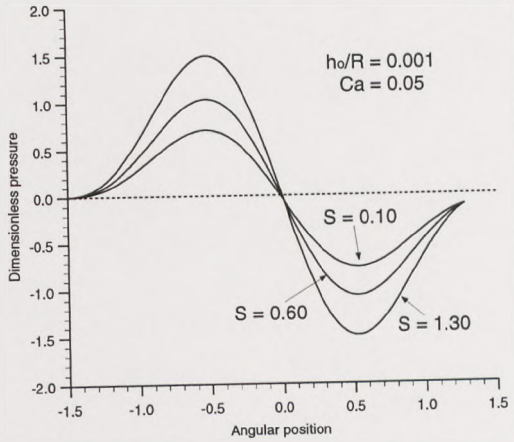

Figure 4.6: Pressure profiles for $Ca = 0.05$ and $h_0/R = 0.001$ and various speed ratios.

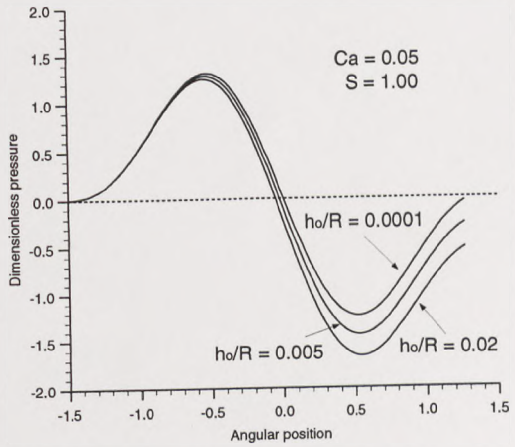

Figure 4.7: Pressure profiles for $S = 1.00$ and $Ca = 0.05$ and various h_0/R.

4.2.1.2 Perturbed flow

Following Pearson [1960], the base flow is perturbed such that the new location of the meniscus, x'_d, is given by

$$x'_d = x_d + \epsilon e^{\sigma t} sin(2\pi n z), \tag{4.28}$$

and the pressure is given by

$$p'(x,z,t) = p(x) + \epsilon G(x) e^{\sigma t} sin(2\pi n z), \tag{4.29}$$

where n represents the number of waves per unit width, ϵ a small amplitude, $G(x)$ is an unknown function of x and σ is a growth rate. For stability, this perturbation must tend to zero (with time) i.e. $\sigma < 0$. Substituting (4.29) into the 2-dimensional Reynolds equation,

$$\frac{\partial}{\partial x}\left(h^3 \frac{\partial p'}{\partial x}\right) + \frac{\partial}{\partial z}\left(h^3 \frac{\partial p'}{\partial z}\right) = 12\mu \frac{dh}{dx} \frac{(U_2 - U_1)}{2}, \tag{4.30}$$

yields a second order equation for the unknown function $G(x)$,

$$\frac{d^2G}{dx^2} + \frac{3}{h}\frac{dh}{dx}\frac{dG}{dx} - 4\pi^2 n^2 G = 0. \tag{4.31}$$

The balance of surface tension forces and fluid pressure at the interface gives

$$p'(x'_d) = -\frac{\beta_d T}{h(x'_d)} + 4\pi^2 n^2 T \epsilon e^{\sigma t} sin(2\pi n z), \tag{4.32}$$

the additional surface tension term arising from curvature of the interface in the $x - z$ plane. A continuity of flow argument (see figure 4.8) states that the flux past station x''_d (i.e. $Q(x''_d)$) must equal the amount of fluid flowing into the thin films i.e.

$$Q(x''_d) = h'_1\left(U_1 - \frac{dx'_d}{dt}\right) + h'_2\left(U_2 - \frac{dx'_d}{dt}\right). \tag{4.33}$$

However, the flux past station x''_d can be related to the flux past station x'_d by the equation

$$Q(x''_d) = Q(x'_d) - h(x'_d)\frac{dx'_d}{dt} \tag{4.34}$$

and so

$$h(x'_d)\frac{U_2 + U_1}{2} - \frac{h^3(x'_d)}{12\mu}\left(\frac{\partial p'}{\partial x}\right)_{x'_d} - h(x'_d)\frac{dx'_d}{dt} = h'_1\left(U_1 - \frac{dx'_d}{dt}\right) + h'_2\left(U_2 - \frac{dx'_d}{dt}\right). \tag{4.35}$$

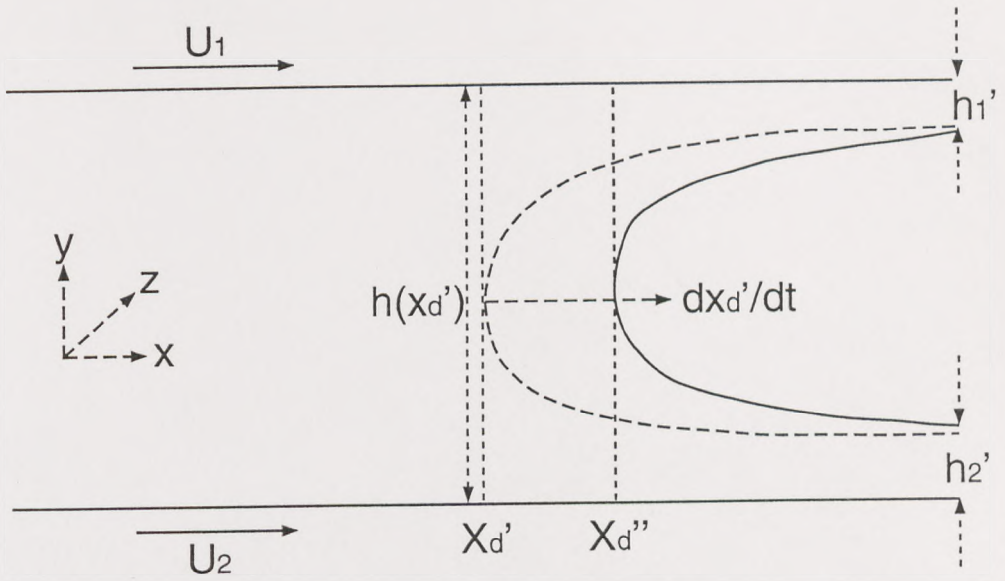

Figure 4.8: Schematic of the perturbed downstream meniscus region of the inlet flooded forward roll coater.

Equations (4.32) and (4.35) are then linearised (by expanding about x_d and using (4.11), (4.28) and (4.29)) to give boundary conditions for $(\frac{dG}{dx})_d$ and $G(x_d)$. These, together with the condition $G(-\infty) = 0$ (which states that the perturbation pressure tends to zero far upstream of the nip), give the following $o(\epsilon)$ problem for $G(x)$:

$$\frac{d^2G}{dx^2} + \frac{3}{h}\frac{dh}{dx}\frac{dG}{dx} - 4\pi^2 n^2 G = 0, \tag{4.36}$$

$$\left(\frac{dG}{dx}\right)_d = \frac{-12\mu U_2}{h_d^3}(\frac{dh}{dx})_d(\alpha_{d2} + S\alpha_{d1}) + \frac{12\mu\sigma}{h_d^2}(\alpha_{d2} + \alpha_{d1} - 1), \tag{4.37}$$

$$G(x_d) = \frac{\beta_d T}{h_d^2}(\frac{dh}{dx})_d - \frac{12\mu U_2}{h_d^3}\left(\frac{(1+S)h_d}{2} - h_2 - Sh_1\right) + 4\pi^2 n^2 T, \tag{4.38}$$

$$G(-\infty) = 0. \tag{4.39}$$

By introducing the following non-dimensional variables

$$\begin{aligned} X &= \frac{x}{\sqrt{Rh_0}}, \\ N &= n\sqrt{Rh_0}, \\ \Sigma &= \frac{\sqrt{Rh_0}}{U}\sigma, \\ g(X) &= \frac{h_d^2}{12\mu U_2}G(x), \end{aligned}$$

the boundary value problem for $g(x)$ becomes

$$\frac{d^2g}{dX^2} + \frac{6X}{1+X^2}\frac{dg}{dX} - 4\pi^2N^2g(X) = 0, \tag{4.40}$$

$$g(D) = \frac{\beta_d D}{6Ca}\sqrt{\frac{h_0}{R}} + \frac{\pi^2N^2}{3Ca}\left(\frac{h_0}{R}\right)(1+D^2)^2 - \frac{1+S}{2} + \alpha_{d2} + S\alpha_{d1}, \tag{4.41}$$

$$\left(\frac{dg}{dx}\right)_D = \frac{-2D}{1+D^2}(\alpha_{d2} + S\alpha_{d1}) + \Sigma(\alpha_{d2} + \alpha_{d1} - 1), \tag{4.42}$$

$$g(-\infty) = 0. \tag{4.43}$$

4.2.2 Method of solution

Before solving equations (4.40)-(4.43) numerically, an approximate analytical solution for Σ is first obtained, as in the reverse case.

Analytical solution (approximate):

The term $\frac{6X}{1+X^2}$ is again replaced by its local value at the film split location where the disturbance arises i.e. by $\frac{6D}{1+D^2}$, so equation (4.40) becomes

$$\frac{d^2g}{dX^2} + \frac{6D}{1+D^2}\frac{dg}{dX} - 4\pi^2N^2g(X) = 0. \tag{4.44}$$

Equation (4.44) then has a solution satisfying

$$g(X) = g(D)e^{w(X-D)}, \tag{4.45}$$

where

$$w = -k + \sqrt{k^2 + 4\pi^2N^2}, \tag{4.46}$$

$$k = \frac{3D}{1+D^2}. \tag{4.47}$$

Therefore,

$$\left(\frac{dg}{dX}\right)_D = wg(D). \tag{4.48}$$

Substituting (4.41) and (4.42) into (4.48) yields the following equation for the non-dimensional growth rate, Σ (as a function of N, given Ca, S and h_0/R):

$$\Sigma(N) = \frac{1}{(\alpha_{d1} + \alpha_{d2} - 1)}\left[\frac{2\alpha_d D}{1+D^2}(S\alpha_{d1} + \alpha_{d2}) + \frac{w\beta_d D}{6Ca}\sqrt{\frac{h_0}{R}}\right.$$

$$\left. + \frac{w\pi^2N^2}{3Ca}\left(\frac{h_0}{R}\right)(1+D^2)^2 - \frac{w(1+S)}{2} + w(S\alpha_{d1} + \alpha_{d2})\right] \tag{4.49}$$

Hence, once h_0/R, Ca and S are specified, then D is calculated from the base flow model and graphs of $\Sigma(N)$ can be plotted using equation (4.49).

Numerical solution:

A numerical solution to the first order problem is obtained by solving (4.40), (4.41), (4.42) and (4.43) directly. This is achieved using the NAG routine D02NBF (used generally to integrate an initial value problem for a stiff system of explicit ODE's. As this problem is a boundary value problem, it is converted to an initial value problem and then Newton iteration is carried out until the 3rd boundary condition is satisfied i.e. for each N, Σ is guessed and Newton iteration is carried out until (4.43) is satisfied). There is a maximum difference of 3% between the analytical and numerical solutions (for $\Sigma(N)$).

4.2.3 Discussion of results

Since there are three independent parameters, one way of displaying results is to fix two (h_0/R and S) and plot Σ against N for various values of the third (Ca). The critical Ca can then be determined and the effects of varying h_0/R and S seen by plotting the critical capillary number against speed ratio for various h_0/R.

4.2.3.1 Fixed h_0/R

In this section, results for a fixed and then variable speed ratio are discussed using a fixed gap ratio, $h_0/R = 10^{-3}$.

Fixed S

Figure 4.9 shows plots of $\Sigma(N)$ for $S = 1.00$, $h_0/R = 0.001$ and various Ca. It can be observed that for both $Ca = 0.03$ and $Ca = 0.05$, $\Sigma < 0$ for all N and so the disturbance decays and the base flow is stable. A critical capillary number, $Ca*$, exists ($Ca* = 0.0626$) for which $\frac{d\Sigma}{dN} = \Sigma = 0$ for a particular value of N (and $\Sigma < 0$ for all other N). The base flow is termed 'neutrally stable' and all flows for which $Ca > Ca*$ are unstable. $Ca = 0.08$ is an example of an unstable base flow since $\Sigma > 0$ for N in the range $0.11 < N < 0.32$. The base flow is stable to disturbances with wavenumber $N < 0.11$ and $N > 0.32$ (as $\Sigma < 0$ for all such values of N).

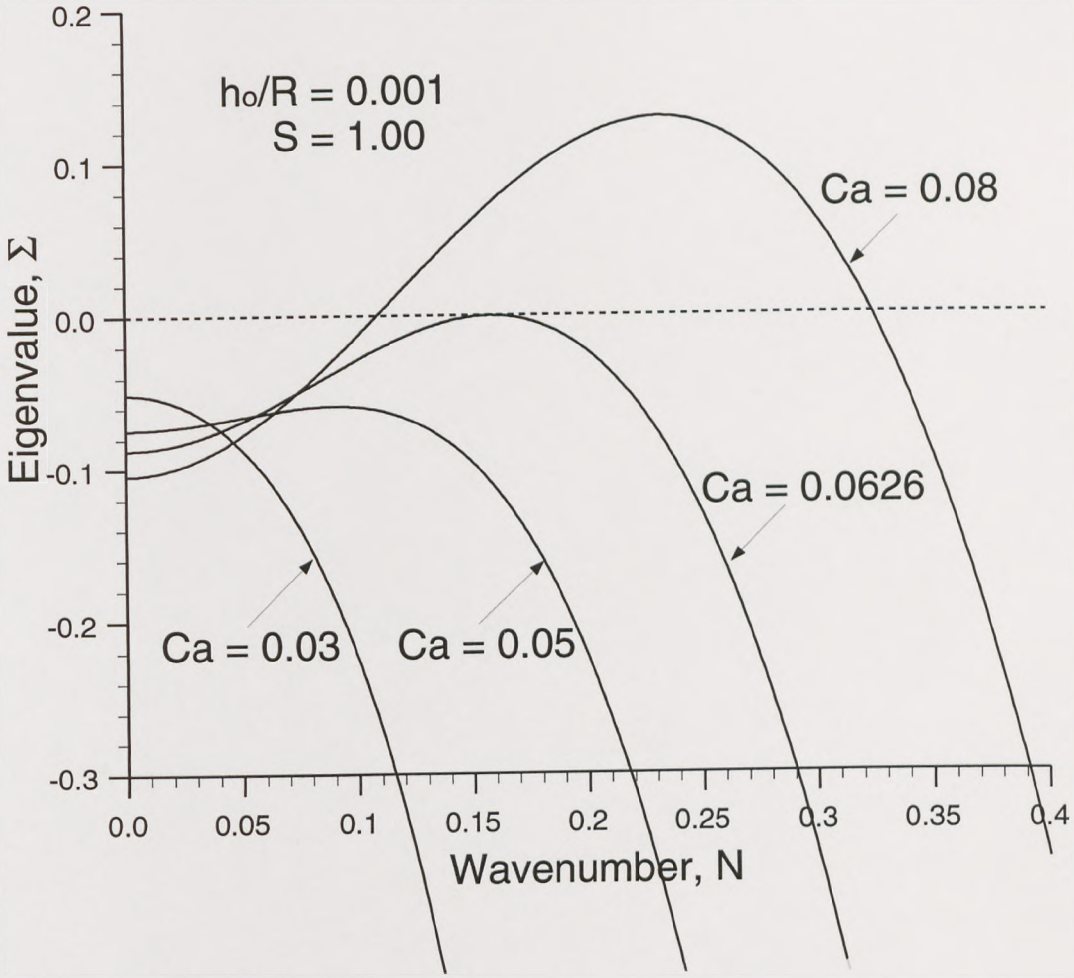

Figure 4.9: Growth rate (Σ) against wavenumber (N) for various Ca with $S = 1.00$ and $h_0/R = 0.001$.

Variable S

With $h_0/R = 0.001$ remaining fixed, the critical capillary number, $Ca*$, is determined for various values of speed ratio, S and a a plot of $Ca*$ against S is drawn - see figure 4.10. Above the curve ribs occur, whereas below it the base flow is stable. Corresponding to each Ca (S) there is clearly a minimum value of speed ratio, $S*$, (capillary number, $Ca*$) above which ribs occur. Hence it is clear that increasing either Ca or S has a destabilising effect unlike inlet flooded reverse roll coating, where S was found to have a stabilising effect.

4.2.3.2 Variable h_0/R

The effect of varying the gap ratio, h_0/R is illustrated in figure 4.11 by means of critical curves in the $Ca - S$ plane for the onset of instability. It is observed that the region of stability increases as h_0/R increases such that for any S (Ca) the critical capillary number (speed ratio) increases with h_0/R.

4.2.4 Comparison with the Stability Hypothesis (S.H.)

Recall that a stability hypothesis is an approximate means of determining the stability of an interface (see section 3.2.4). Applying a similar perturbation to the downstream of the current problem (see figure 4.12) results in the following condition for stability:

$$\frac{\beta_d T}{h_d^2}\left(\frac{dh}{dx}\right)_d > \left(\frac{dp}{dx}\right)_d. \tag{4.50}$$

Hence we see (via the S.H.) that at the downstream meniscus, surface tension has a stabilising influence, whereas the pressure gradient (at x_d) has a destabilising influence (as in the reverse case).

After non-dimensionalising (4.50) it can be seen that for stability (via the S.H.),

$$g(D, N = 0) \;>\; 0, \tag{4.51}$$

where $g(D, N)$ is given by equation (4.41). Using condition (4.51), a plot of $Ca*$ against S can be drawn (for this particular value of h_0/R i.e. $h_0/R = 10^{-3}$) - see figure 4.13. A comparison of the S.H. (the full line) is shown with the linear stability analysis (the dotted line). It can be seen that the two curves are qualitatively similar yet the approximate stability hypothesis consistently underpredicts the critical capillary number for any S. This implies that that the S.H. is sufficient for predicting stability only, the proof of which is identical to that for the inlet flooded, reverse roll coating case.

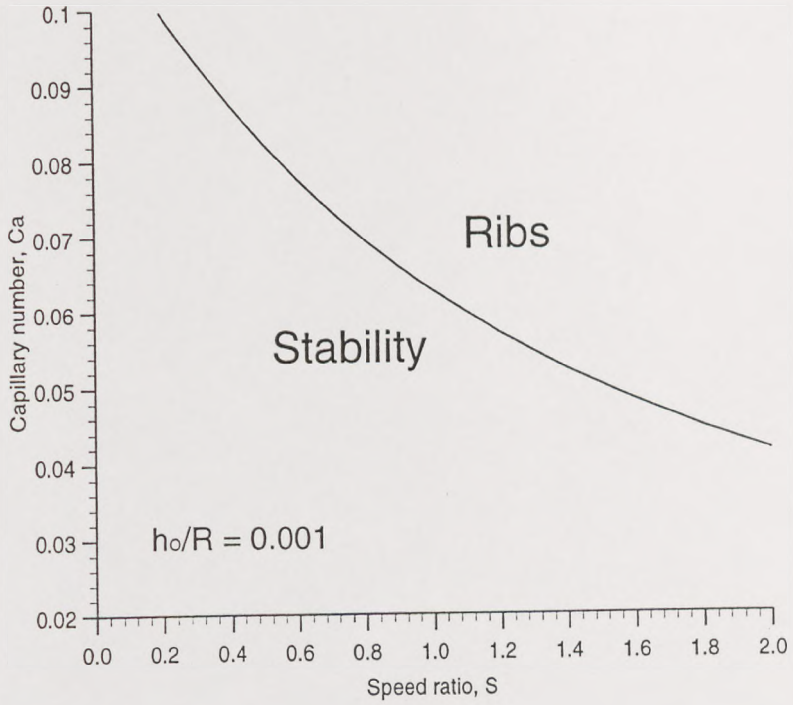

Figure 4.10: Operability diagram in the $Ca - S$ plane for $h_0/R = 10^{-3}$.

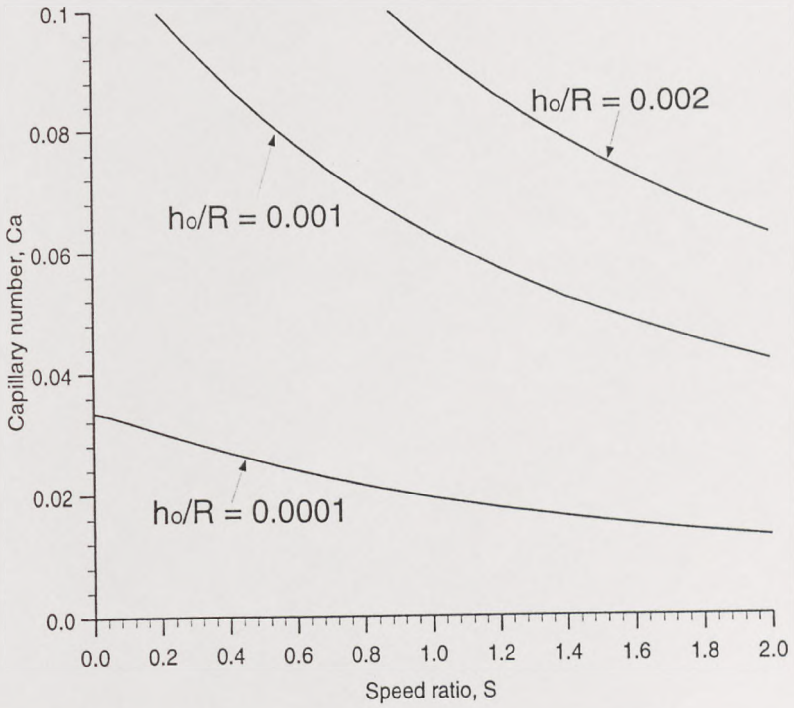

Figure 4.11: Operability diagrams in the $Ca - S$ plane with varying h_0/R.

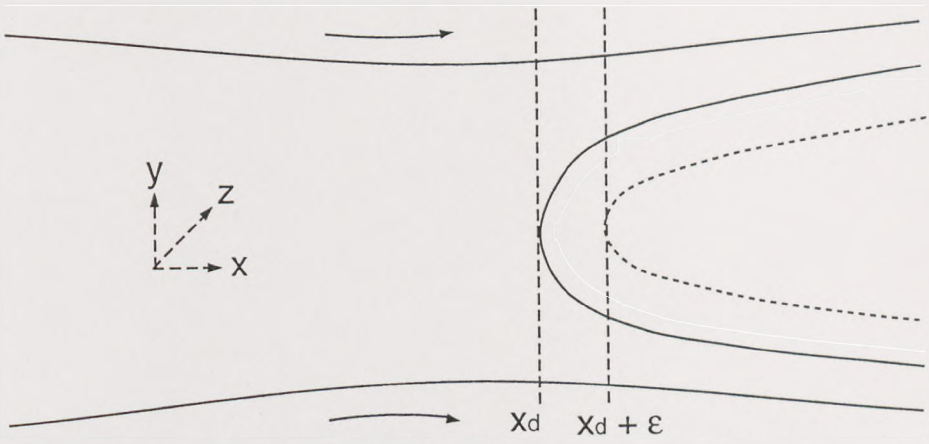

Figure 4.12: Schematic of the downstream meniscus region of an inlet flooded forward roll coater showing both the disturbed meniscus at $x = x_d + \epsilon$, and the original uniform meniscus at $x = x_d$.

Figure 4.14 shows further operability diagrams (in the $Ca - S$ plane) for three different values of h_0/R. It is clear that the agreement between the linear stability analysis and S.H. improves as h_0/R is reduced.

4.2.5 Comparison with the computational approach

In the previous section, inlet flooded forward roll coating was analysed using lubrication theory to model the flow from far upstream to the downstream meniscus region. The model predicted the pressure profiles and final film thicknesses as functions of three operating parameters, namely S, Ca and h_0/R. As with the reverse case, the ribbing instability was then examined by applying linear stability theory to the base flow. However, analytical models are only valid over a limited region of parameter space (small Ca for $S \neq 1$) and it is necessary to model the downstream meniscus by the arc of a circle.

The FE method does not suffer these drawbacks and so it is therefore the aim of this section to apply the linear stability theory (detailed in chapter 2) to FE solutions of an inlet flooded, forward roll coater in order to examine the accuracy of the previously obtained analytical results and to enable the stability of the flow to be examined over a much larger region of parameter space. The steady 2-dimensional FE code used in this study is based on the work of Thompson [1992], the boundary conditions and computational mesh associated with which are described below.

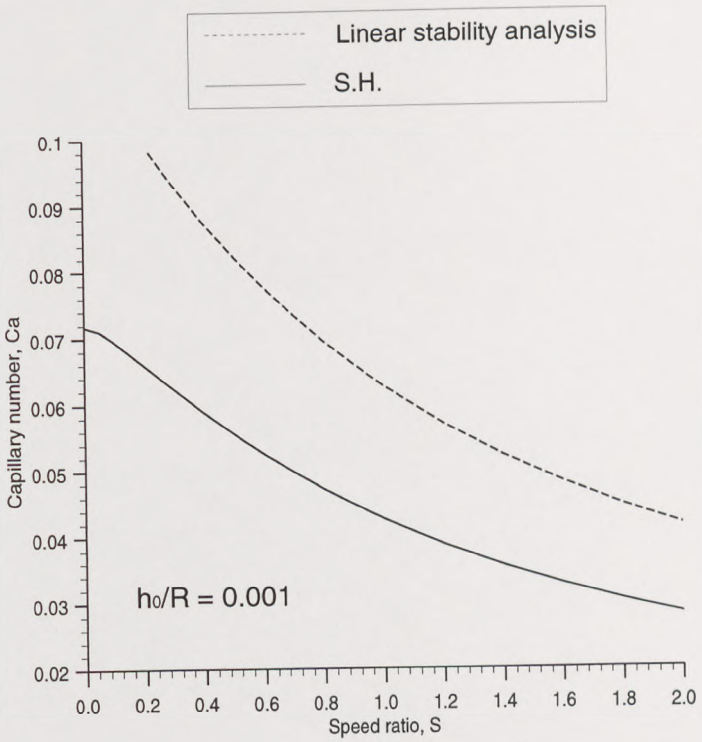

Figure 4.13: Operability diagram in the $Ca - S$ plane for $h_0/R = 10^{-4}$ for both the S.H. and linear stability analysis.

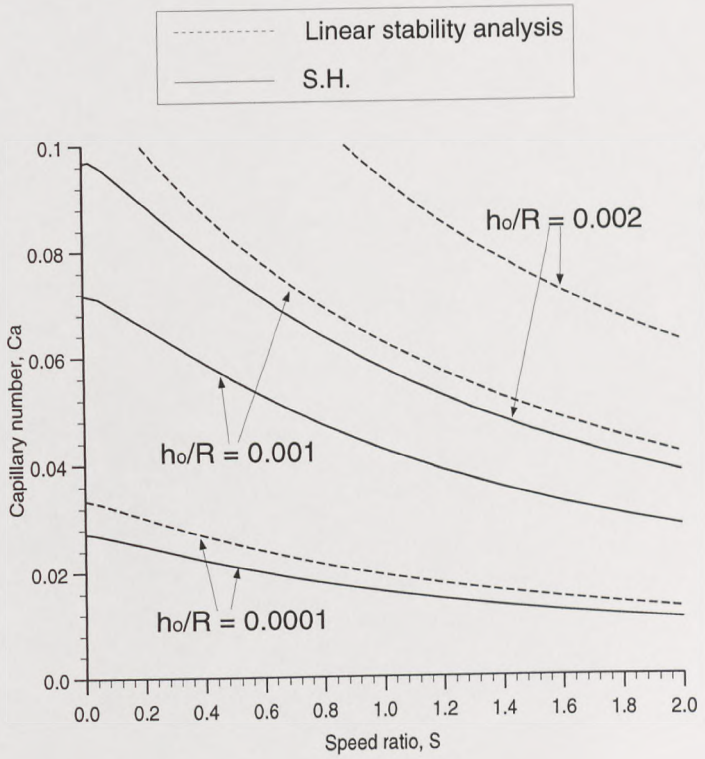

Figure 4.14: Operability diagram in the $Ca - S$ plane with varying h_0/R for both the S.H. and linear stability analysis.

Boundary conditions:

The boundary conditions, shown in figure 4.15, are as follows:

1. At the downstream free surface, the usual kinematic and stress boundary conditions are imposed (see chapter 2).

2. Zero traction conditions are imposed at both downstream outlets.

3. At the inflow boundary, situated at the nip, the lubrication approximation provides an accurate description of the flow. A zero inlet pressure condition (corresponding to $p(-\infty) = 0$) is also applied.

4. At the roll surfaces the no slip condition is applied.

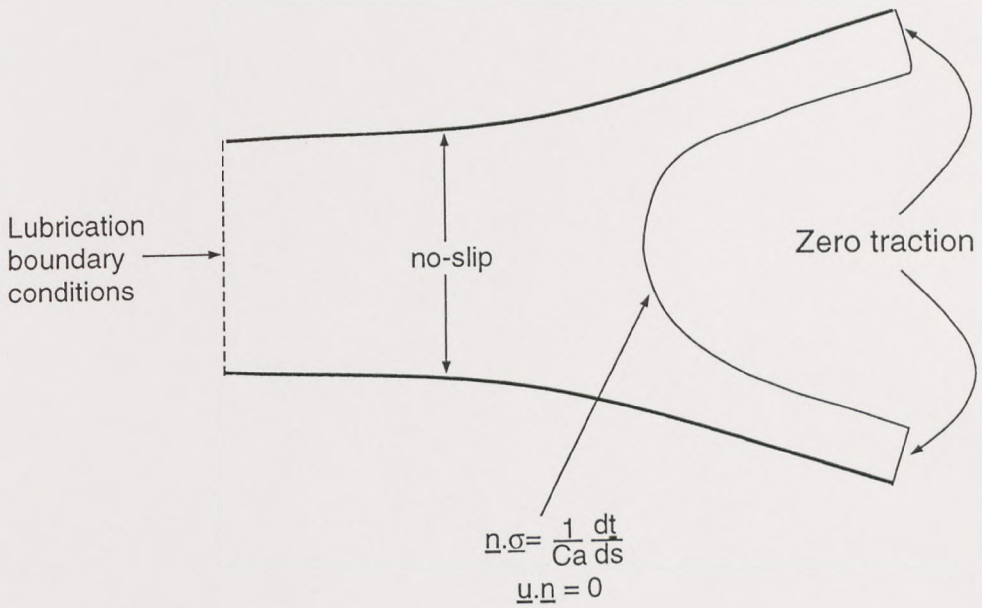

Figure 4.15: Computational boundary conditions for the downstream region of an inlet flooded forward roll coater.

Computational mesh:

The location of the free surface is highly sensitive to the values of Ca, S and h_0/R being considered (see Thompson [1992], Coyle *et al* [1986]) e.g. as Ca is reduced, the free surface moves further away from the nip. To accommodate this, the FE grid must be designed to cope with large variations in free surface location. Such an approach was initially developed by Coyle *et al* [1986] who split the grid into two regions, see 4.16.

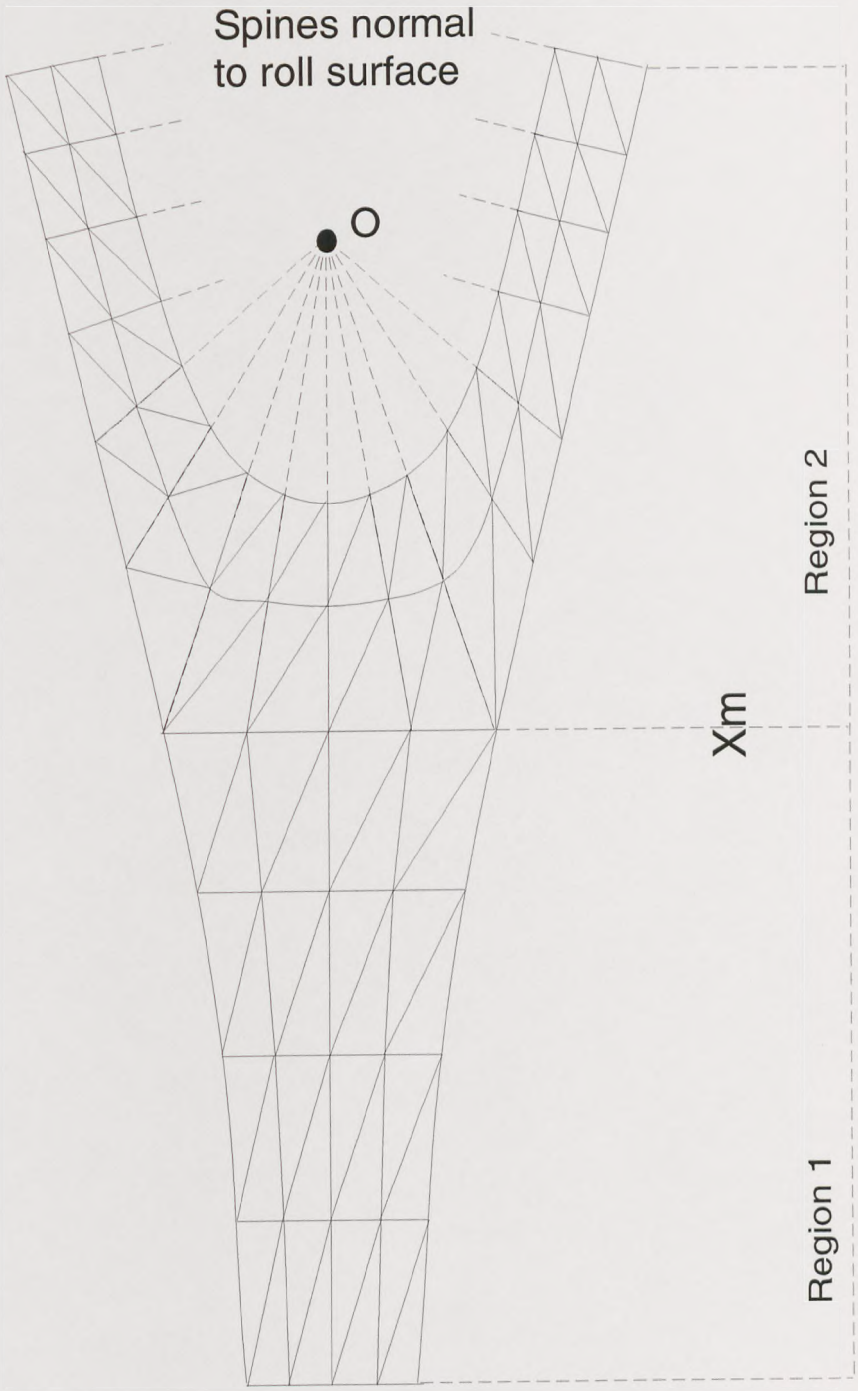

Figure 4.16: Schematic of the finite element grid used to tessellate the downstream region of an inlet flooded forward roll coater.

Region 1, the nip region, terminates at the variable x-location $x = x_m$ and nodes inside it undergo a concertina type motion as x_m varies. The nodes in the free surface region, region 2, are located on spines whose direction vectors either pass through a polar origin O, or are perpendicular to the roll surfaces. The base nodes of all the spines in this region either lie on one of the rolls or on the line $x = x_m$.

Since x_m is allowed to vary, another unknown is introduced into the problem and so the length of the central spine in the free surface region is fixed i.e. the kinematic boundary condition that would have been used to evaluate this height is instead used to calculate x_m. Since the position of every node in the grid now depends on x_m, the element-level Jacobian must now also include derivatives with respect to it.

Figure 4.17 shows the finite element grid used to calculate the base flow in this study. The grid contains 2016 elements, 4243 nodes and 9128 degrees of freedom. The figure also shows streamlines for a typical solution.

In figure 4.18, predictions for H_1/H_2 from the lubrication model are compared with numerical results for $Ca = 0.06$, h_0/R and varying S. As expected, the lubrication theory predictions are in good agreement with the finite element results, especially near $S = 1$ (see Gaskell, Savage and Thompson [1998]).

Stability of the FE base flow:

The finite element stability analysis described in chapter 2 is now applied to the above problem, and for the associated computational grid there are now 13066 degrees of freedom (as opposed to 9128 freedoms with the 2-dimensional base flow). As in the reverse case, for each wavenumber, N, (and set of base flow fluid and geometry parameters) an eigenvalue, Σ, is produced to indicate the stability. If, for a given base flow, the eigenvalue is negative for each wavenumber the base flow is stable. If one or more of the eigenvalues are positive then the base flow is unstable to the disturbance and ribbing appears.

It was found that this numerical approach is in good agreement with the analysis previously performed in this chapter. Indeed, there is a maximum difference of less than 1% for the $Ca*$ in the two methods. This ratifies the assumptions made in the analysis (e.g. the approximation of the free surface by the arc of a circle) and shows how

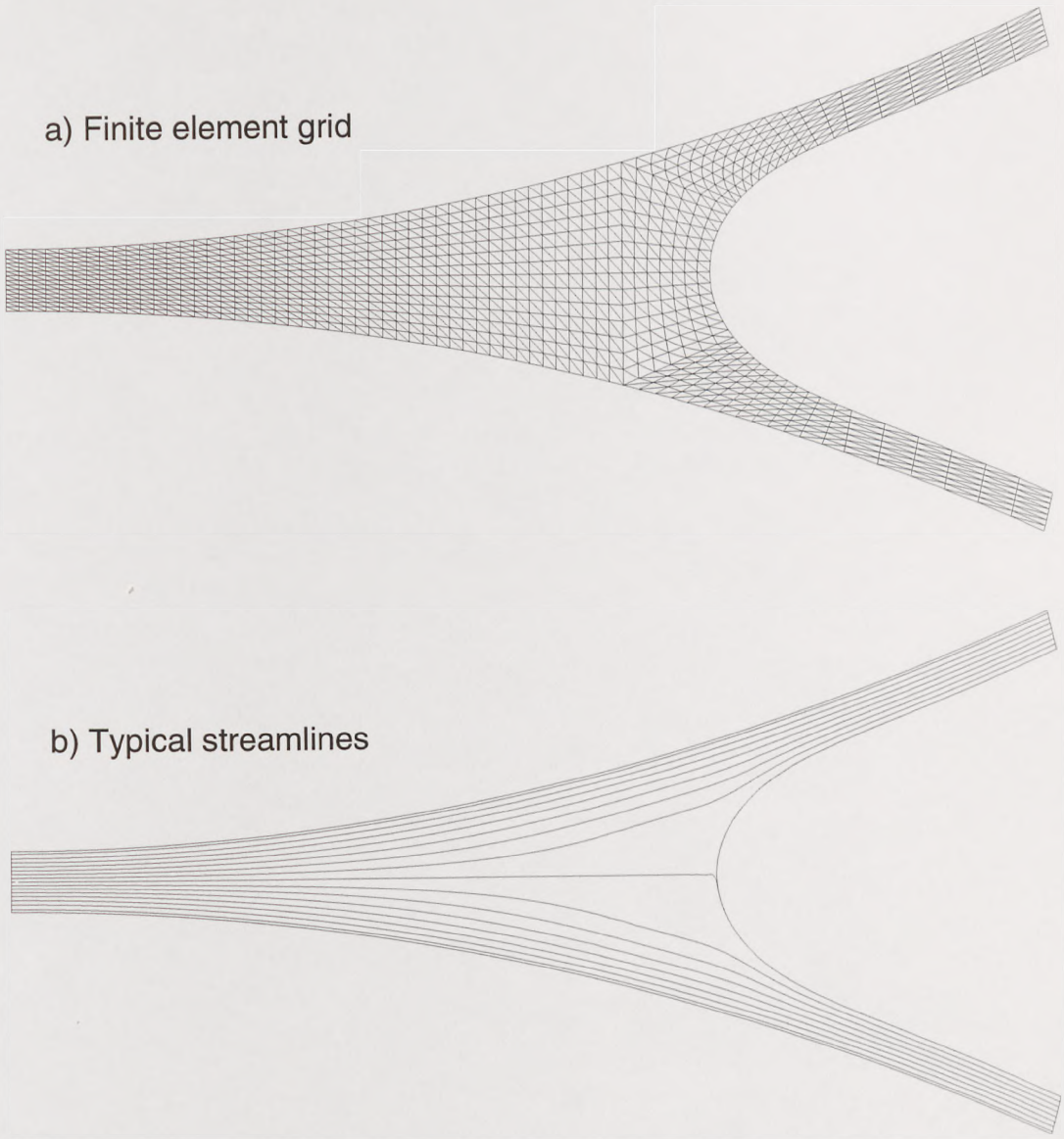

Figure 4.17: Finite element grid used to form a numerical description of the base flow, together with typical streamlines.

lubrication theory can be used to accurately determine stability for this range of Ca. The critical Ca (for each h_0/R) are also in agreement with Coyle's [1989] numerical results obtained for $S = 1$ - this is to be expected as the same methodology has been used.

Note that it can now be postulated that the discrepancy between the critical capillary number for the reverse case (in chapter 3) is due to the modelling of the contact line. In particular, the main difference between the analytical and numerical modelling of the base flow is that it is necessary to impose a slip condition in the latter to avoid a

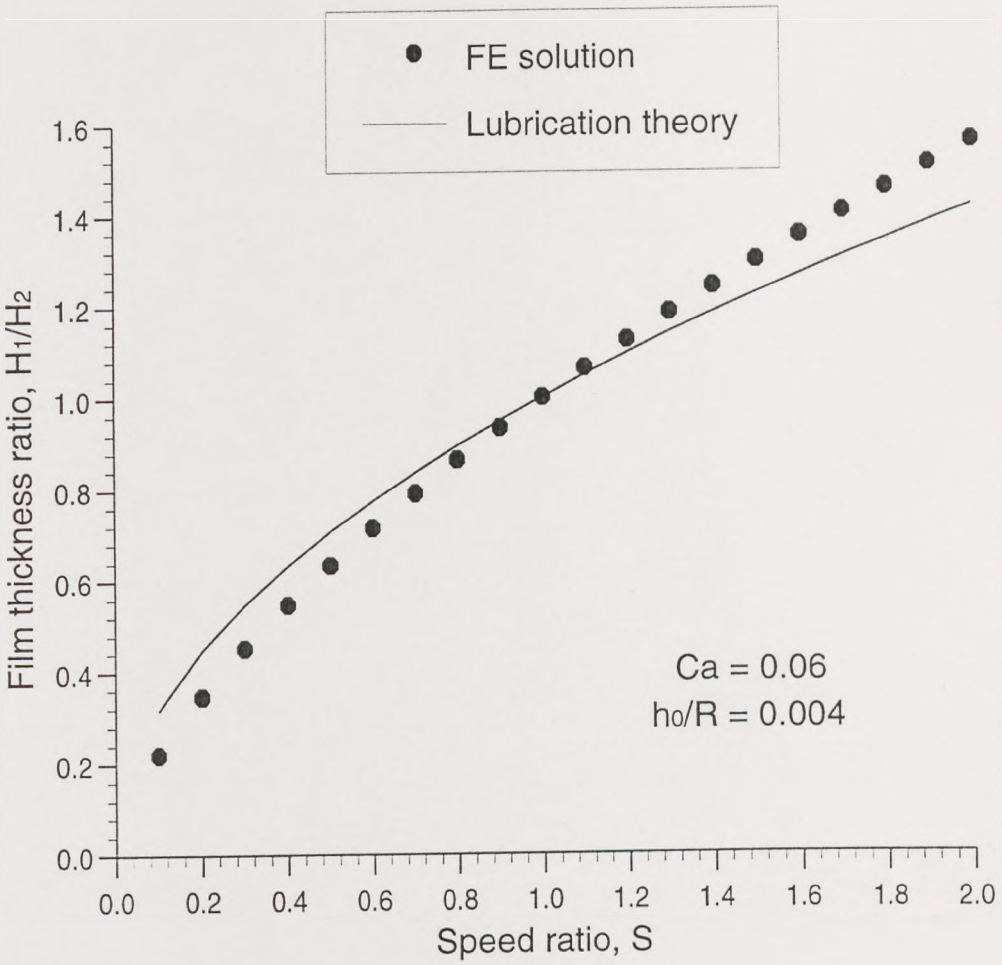

Figure 4.18: A comparison of film thickness ratio (H_1/H_2) against speed ratio (S) obtained via the finite element method and lubrication theory for $Ca = 0.06$ and $h_0/R = 0.004$.

stress singularity whereas the analytical approach does not include effects local to the wetting line, and so is less accurate.

4.3 Inlet starved case

In the above analysis of forward roll coating, the upstream inlet was assumed to be fully flooded in the sense that the fluid extends to 'infinity' upstream of the nip. If the supply of fluid upstream of the nip is reduced, the inlet becomes starved and a fluid bead appears which is finite in width and bounded by two free surfaces (see figure 4.4). The aim here is to formulate a 2-dimensional model for this flow, based on lubrication theory (see section 4.3.1.1), and use linear stability theory to determine its stability (see section 4.3.1.2). As before, a comparison is made with the stability hypothesis (on both the upstream and downstream free surfaces), see sections 4.3.3-4.3.5.

4.3.1 Mathematical Model

4.3.1.1 Base flow

In this section the aim is, again, to determine the velocity and pressure fields together with the location of the upstream and downstream menisci (given h_0/R, Ca, S and H_i) which are required in order to carry out the linear stability analysis.

A conservation of flow argument leads to the constraint that the flux in the incoming film (of thickness h_i) is equal to the sum of the fluxes in the two exiting films (of thickness h_1 and h_2),

$$h_i U_2 = h_1 U_1 + h_2 U_2. \tag{4.52}$$

When non-dimensionalised with respect to the variables defined in equation (4.20), together with

$$H_i = \frac{h_i}{h_0}, \tag{4.53}$$

this gives

$$H_i = S H_1 + H_2. \tag{4.54}$$

The downstream meniscus can be modelled as in the flooded case to give equations (4.17)-(4.19). Using (4.17) and (4.18), equation (4.54) becomes

$$H_i = H_d(S\alpha_{d1} + \alpha_{d2}), \tag{4.55}$$

giving

$$\sec^2 \bar{\gamma} = \frac{H_i}{(S\alpha_{d1} + \alpha_{d2})}, \tag{4.56}$$

where $X = \tan(\gamma)$ and $\bar{\gamma}$ marks the position of the downstream film split. Hence it is clear that after specifying Ca, S and H_i, $\bar{\gamma}$ can be determined by solving (4.56).

To ascertain the dimensionless location of the upstream free surface, $X_U = \tan\hat{\gamma}$, the lubrication theory developed for the inlet flooded case can be used, although not with the same pressure boundary conditions. Hence, the dimensionless pressure gradient is again

$$\frac{dP}{d\gamma} = 6(1+S)\cos^2\gamma - 12(H_2 + SH_1)\cos^4\gamma. \tag{4.57}$$

If (4.57) is integrated between the limits of $\hat{\gamma}$ and $\bar{\gamma}$ then

$$\begin{aligned} P(\bar{\gamma}) - P(\hat{\gamma}) &= 3(1+S)\left[\frac{\sin 2\gamma}{2} + \gamma\right]_{\hat{\gamma}}^{\bar{\gamma}} \\ &+ \frac{3(H_2 + SH_1)}{2}\left[\frac{\sin 4\gamma}{4} + 2\sin 2\gamma + 3\gamma\right]_{\hat{\gamma}}^{\bar{\gamma}}. \end{aligned} \tag{4.58}$$

The pressure boundary condition at the downstream meniscus is the same as in the flooded case,

$$p(x_d) = \frac{-T}{r_d}, \tag{4.59}$$

which, after non-dimensionalisation and using (4.19), becomes

$$P(\bar{\gamma}) = -\frac{\beta_d}{Ca\sec^2\bar{\gamma}}\sqrt{\frac{h_0}{R}}. \tag{4.60}$$

For the inlet flooded case, the fluid domain extended far upstream and so it was assumed that the pressure far upstream of the nip was zero. However, for the inlet starved case, the fluid domain no longer necessarily extends far upstream and so this upstream pressure boundary condition must be replaced by a balance of fluid and surface tension pressure at the upstream meniscus,

$$p(x_u) = \frac{-T}{r_u}, \tag{4.61}$$

where r_u is the radius of curvature of the upstream meniscus which is approximated by a circular arc meeting the film tangentially and intersecting the upper roll surface at an angle θ_u, corresponding to the dynamic contact angle. Hence, at the upstream meniscus,

$$h_u = r_u(1 + \cos(\theta_u)) + h_i, \tag{4.62}$$

and so

$$r_u = \frac{h_u - h_i}{1 + \cos(\theta_u)}, \tag{4.63}$$

giving

$$\beta_u = \frac{h_u}{r_u} = \frac{1 + \cos(\theta_u)}{1 - Hi\cos^2\hat{\gamma}}. \tag{4.64}$$

Equation (4.61), on non-dimensionalisation, becomes

$$P(\hat{\gamma}) = -\frac{\beta_u}{Ca\sec^2\hat{\gamma}}\sqrt{\frac{h_0}{R}}. \tag{4.65}$$

Hence, once Ca, S, H_i and h_0/R have been specified and $\bar{\gamma}$ found (using (4.56)), the location of the upstream free surface can be obtained by solving (4.58) together with (4.60) and (4.65). The pressure distribution is then obtained by integrating (4.57) between the limits of $\hat{\gamma}$ and γ, giving

$$\begin{aligned} P(\gamma) &= P(\hat{\gamma}) + 3(1+S)\left[\frac{\sin 2\gamma}{2} + \gamma\right]_{\hat{\gamma}}^{\gamma} \\ &+ \frac{3(H_2 + SH_1)}{2}\left[\frac{\sin 4\gamma}{4} + 2\sin 2\gamma + 3\gamma\right]_{\hat{\gamma}}^{\gamma}. \end{aligned} \tag{4.66}$$

The thickness of the inlet film has a pronounced effect on the pressure distribution, as shown in figure 4.19 where pressure profiles corresponding to various H_i are plotted with $h_0/R = 0.001$, $Ca = 0.10$ and $S = 1.00$. The dotted line indicates the pressure profile for the flooded case and corresponds to $H_i \simeq 1.33$. As the inlet film thickness is decreased, both the upstream and downstream menisci move towards the nip. In fact, for $H_i = 0.84$, the upstream meniscus lies on the same side of the nip as the downstream one. It can also be seen that as H_i is reduced, the turning points in the pressure gradient disappear and the pressure becomes entirely sub-ambient. The limit $H_i \to 0.84$ corresponds to the meniscus coating regime where the pressure gradient is positive and almost constant. Note that solutions to equation (4.58) could not be obtained for $H_i < 0.84$.

Figure 4.20 shows pressure profiles for $h_0/R = 0.001$, $S = 1.00$, $H_i = 1.20$ and four values of Ca. The downstream, as in the flooded case, and upstream menisci move towards the nip as Ca increases. The pressure gradient at the upstream meniscus remains the same and the maximum and minimum pressures across the nip increase. Further, as Ca is increased, a point is reached where solutions of (4.58) no longer exist.

Pressure profiles for $h_0/R = 0.001$, $Ca = 0.10$, $H_i = 1.20$ and five values of S are shown in figure 4.21. As S is increased, the downstream (as in the flooded case) and upstream menisci move towards the nip. Again, as S is increased, there is a point at which solutions of (4.58) no longer exist.

Figure 4.22 shows pressure profiles for $Ca = 0.10$, $S = 1.00$, $H_i = 1.20$ and three values of h_0/R. As h_0/R is increased the location of the downstream film split, along with its associated pressure gradient, remain the same (as in the flooded case). However, the upstream meniscus moves away from the nip, the pressure gradient there remaining about the same.

4.3.1.2 Perturbed flow

With the addition of the upstream free surface, the objective is to determine the stability characteristics of this free surface and also how its presence affects the stability of the downstream free surface.

The base flow is perturbed, following Pearson [1960] and Reinelt [1995], such that the new location of the downstream and upstream menisci, x'_d and x'_u respectively, are given by

$$x'_d = x_d + \epsilon_d e^{\sigma t} sin(2\pi n z), \tag{4.67}$$

$$x'_u = x_u + \epsilon_u e^{\sigma t} sin(2\pi n z), \tag{4.68}$$

and the pressure is given by

$$p'(x,y,t) = p(x) + [\epsilon_d G_d(x) + \epsilon_u G_u(x)] e^{\sigma t} sin(2\pi n z), \tag{4.69}$$

where n represents the number of waves per unit width, ϵ_d and ϵ_u are small amplitudes, $G_d(x)$ and $G_u(x)$ are unknown functions of x and σ is a growth rate. Note that equations (4.67) and (4.68) have identical growth rates and wavenumbers but different amplitudes. This is due to the fact that disturbances may arise on the downstream and affect the upstream or visa versa.

For each n, not only is σ required to determine the stability of the geometry, but if $\sigma > 0$, ϵ_u/ϵ_d is also required in order to identify which of the two free surfaces is unstable:

$$\left|\frac{\epsilon_u}{\epsilon_d}\right| > 1 \quad \text{upstream unstable if } \sigma > 0 \tag{4.70}$$

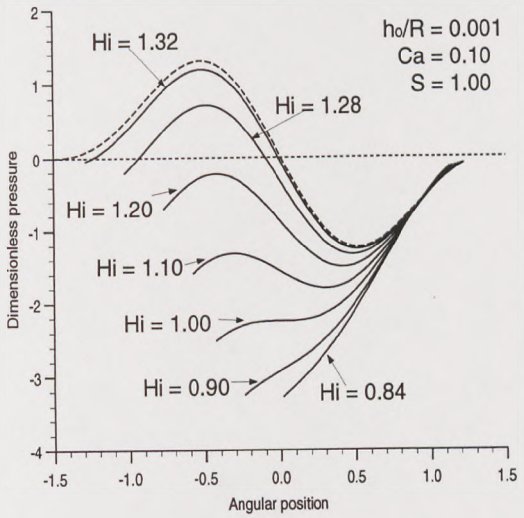

Figure 4.19: Pressure profiles for $h_0/R = 0.001$, $Ca = 0.10$, $S = 1.00$ and various H_i.

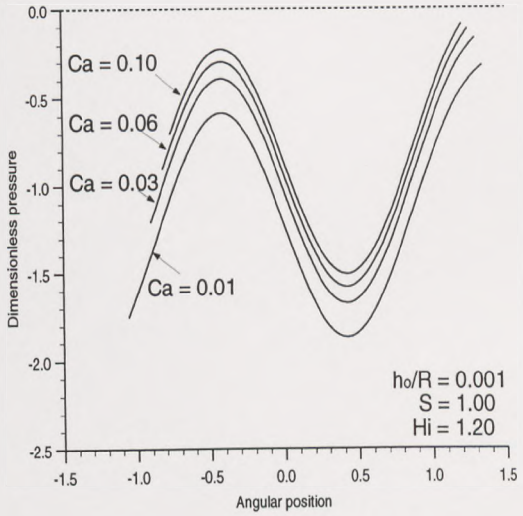

Figure 4.20: Pressure profiles for $h_0/R = 0.001$, $S = 1.00$, $H_i = 1.20$ and various Ca.

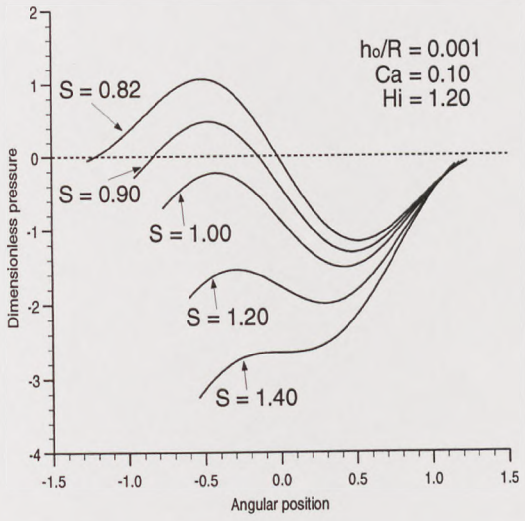

Figure 4.21: Pressure profiles for $h_0/R = 0.001$, $Ca = 0.10$, $H_i = 1.20$ and various S.

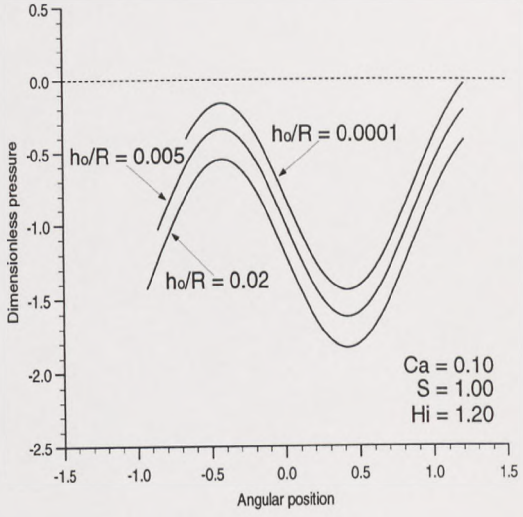

Figure 4.22: Pressure profiles for $Ca = 0.10$, $S = 1.00$, $H_i = 1.20$ and various h_0/R.

$$\left|\frac{\epsilon_u}{\epsilon_d}\right| < 1 \quad \text{downstream unstable if } \sigma > 0 \tag{4.71}$$

Substituting (4.69) into the 2-dimensional Reynolds equation, (4.30), and assuming that $G_d(x)$ and $G_u(x)$ are two linearly independent functions, yields two second order ordinary differential equations for the unknowns $G_d(x)$ and $G_u(x)$,

$$\frac{d^2G_d}{dx^2} + \frac{3}{h}\frac{dh}{dx}\frac{dG_d}{dx} - 4\pi^2n^2G_d = 0, \tag{4.72}$$

$$\frac{d^2G_u}{dx^2} + \frac{3}{h}\frac{dh}{dx}\frac{dG_u}{dx} - 4\pi^2n^2G_u = 0. \tag{4.73}$$

For convenience and without loss of generality, the linearly independent solutions are chosen to satisfy

$$G_d(x_u) = 0, \tag{4.74}$$

$$G_u(x_d) = 0. \tag{4.75}$$

The balance of surface tension pressure and fluid pressure at the downstream and upstream interfaces gives

$$p'(x'_d) = -\frac{\beta_d T}{h(x'_d)} + 4\pi^2n^2T\epsilon_d e^{\sigma t}sin(2\pi nz), \tag{4.76}$$

and

$$p'(x'_u) = -\frac{\beta_u T}{h(x'_u)} - 4\pi^2n^2T\epsilon_u e^{\sigma t}sin(2\pi nz), \tag{4.77}$$

respectively. The additional surface tension terms arise from curvature of the interfaces in the $x-z$ plane. Note the change in sign of the wavenumber term, which is due to the curvature of the upstream and downstream menisci (with respect to the liquid) being opposite in sign for each value of z, see figure 4.23.

The continuity of flow constraint at the downstream interface is identical to that in the flooded case, and so

$$h(x'_d)\frac{U_2+U_1}{2} - \frac{h^3(x'_d)}{12\mu}\left(\frac{\partial p'}{\partial x}\right)_{x'_d} - h(x'_d)\frac{dx'_d}{dt} = h'_1\left(U_1 - \frac{dx'_d}{dt}\right) + h'_2\left(U_2 - \frac{dx'_d}{dt}\right). \tag{4.78}$$

A similar constraint argument can be formulated at the upstream interface (see figure 4.24), whereby the flux past station x''_u (i.e. $Q(x''_u)$) must equal that at the inlet i.e.

$$Q(x''_u) = U_2h_i. \tag{4.79}$$

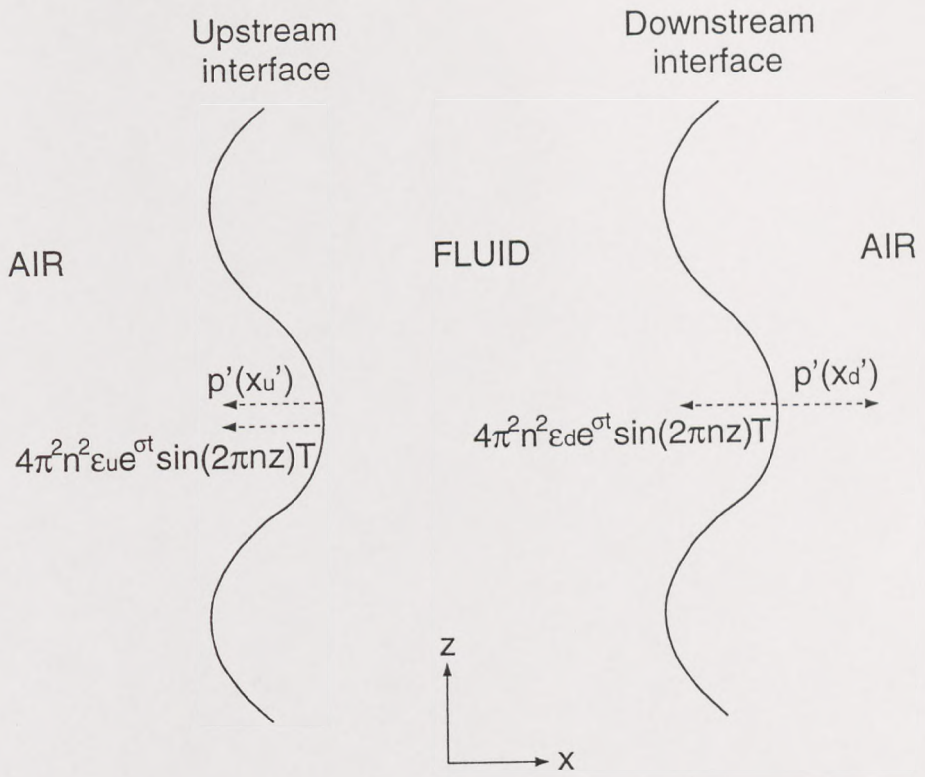

Figure 4.23: Schematic of the forces acting on the perturbed upstream and downstream menisci in the $x - z$ plane.

The flux past station x_u'' can be related to the flux past station x_u' via the equation

$$Q(x_u'') = Q(x_u') - h(x_u')\frac{dx_u'}{dt}, \tag{4.80}$$

and so

$$h(x_u')\frac{U_2 + U_1}{2} - \frac{h^3(x_u')}{12\mu}\left(\frac{\partial p'}{\partial x}\right)_{x_u'} - h(x_u')\frac{dx_u'}{dt} = h_i\left(U_2 - \frac{dx_u'}{dt}\right). \tag{4.81}$$

Equations (4.76), (4.77), (4.78) and (4.81) are then linearised by expanding about x_d, x_u and using (4.11), (4.67), (4.68) and (4.69). With equations (4.74) and (4.75), this gives the following $o(\epsilon)$ boundary value problems for $G_d(x)$ and $G_u(x)$:

$$\frac{d^2G_d}{dx^2} + \frac{3}{h}\frac{dh}{dx}\frac{dG_d}{dx} - 4\pi^2n^2G_d = 0, \tag{4.82}$$

$$\frac{d^2G_u}{dx^2} + \frac{3}{h}\frac{dh}{dx}\frac{dG_u}{dx} - 4\pi^2n^2G_u = 0, \tag{4.83}$$

$$\left(\frac{dG_d}{dx}\right)_d + \frac{\epsilon_u}{\epsilon_d}\left(\frac{dG_u}{dx}\right)_d = \frac{-12\mu U_2}{h_d^3}\left(\frac{dh}{dx}\right)_d(U_2\alpha_{d2} + U_1\alpha_{d1}) + \frac{12\mu\sigma}{h_d^2}(\alpha_{d2} + \alpha_{d1} - 1), \tag{4.84}$$

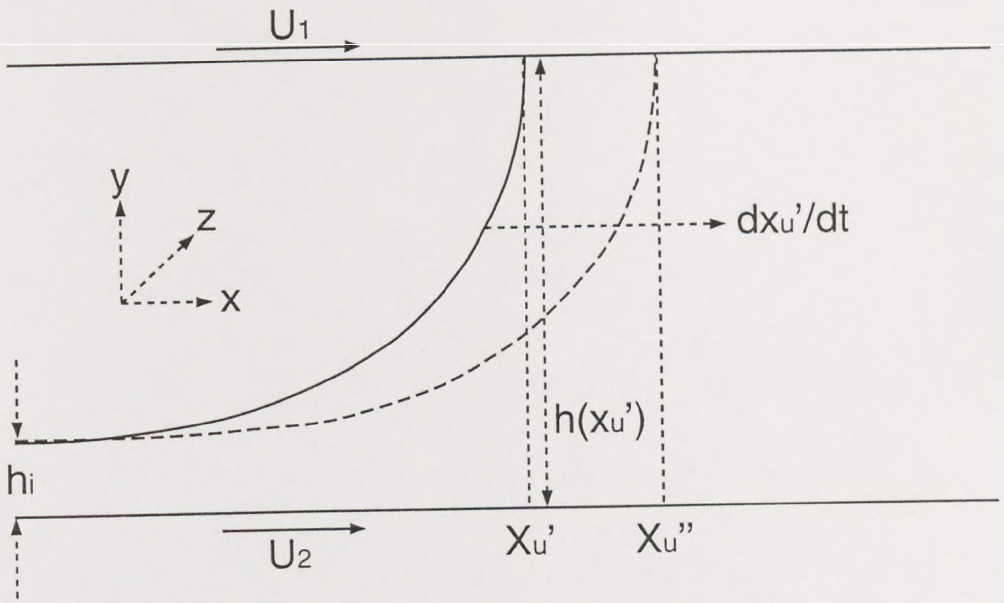

Figure 4.24: Schematic of the perturbed inlet region of a starved forward roll coater.

$$\left(\frac{dG_u}{dx}\right)_u + \frac{\epsilon_d}{\epsilon_u}\left(\frac{dG_d}{dx}\right)_u = \frac{12\mu\sigma}{h_u^2}(h_i - h_u), \tag{4.85}$$

$$G_d(x_d) = \frac{\beta_d T}{h_d^2}(\frac{dh}{dx})_d - \frac{12\mu}{h_d^3}\left(\frac{(U_1+U_2)h_d}{2} - h_2U_2 - h_1U_1\right) + 4\pi^2n^2T, \tag{4.86}$$

$$G_u(x_u) = \frac{\beta_u T}{h_u^2}(\frac{dh}{dx})_u - \frac{12\mu}{h_u^3}\left(\frac{(U_1+U_2)h_u}{2} - h_2U_2 - h_1U_1\right) - 4\pi^2n^2T, \tag{4.87}$$

$$G_d(x_u) = 0, \tag{4.88}$$

$$G_u(x_d) = 0. \tag{4.89}$$

By introducing the following non-dimensional variables

$$\begin{aligned} X &= \frac{x}{\sqrt{Rh_0}}, \\ N &= n\sqrt{Rh_0}, \\ \Sigma &= \frac{\sqrt{Rh_0}}{U}\sigma, \\ g_d(X) &= \frac{h_d^2}{12\mu U_2}G_d(x), \\ g_u(X) &= \frac{h_d^2}{12\mu U_2}G_u(x), \end{aligned} \tag{4.90}$$

the boundary value problems for $g_d(x)$ and $g_u(x)$ become

$$\frac{d^2 g_d}{dX^2} + \frac{6X}{1+X^2}\frac{dg_d}{dX} - 4\pi^2 N^2 g_d(X) = 0, \tag{4.91}$$

$$\frac{d^2 g_u}{dX^2} + \frac{6X}{1+X^2}\frac{dg_u}{dX} - 4\pi^2 N^2 g_u(X) = 0, \tag{4.92}$$

$$\left(\frac{dg_d}{dx}\right)_D + \frac{\epsilon_u}{\epsilon_d}\left(\frac{dg_u}{dx}\right)_D = \frac{-2D}{H_D}(\alpha_{d2} + S\alpha_{d1}) + \Sigma(\alpha_{d2} + \alpha_{d1} - 1), \tag{4.93}$$

$$\left(\frac{dg_u}{dx}\right)_U + \frac{\epsilon_d}{\epsilon_u}\left(\frac{dg_d}{dx}\right)_U = \frac{H_D^2}{H_U^3}\Sigma(H_i - H_U), \tag{4.94}$$

$$\begin{aligned} g_d(D) &= \frac{\beta_d D}{6Ca}\sqrt{\frac{h_0}{R}} - \frac{1}{H_D}\left[\frac{(1+S)H_D}{2} - H_2 - SH_1\right] \\ &+ \frac{\pi^2 N^2 H_D^2}{3Ca}\left(\frac{h_0}{R}\right), \end{aligned} \tag{4.95}$$

$$\begin{aligned} g_u(U) &= \frac{\beta_u U}{6Ca}\sqrt{\frac{h_0}{R}}\frac{H_D^2}{H_U^3} - \frac{H_D^2}{H_U^3}\left[\frac{(1+S)H_U}{2} - H_2 - SH_1\right] \\ &- \frac{\pi^2 N^2 H_D^2}{3Ca}\left(\frac{h_0}{R}\right), \end{aligned} \tag{4.96}$$

$$g_d(U) = 0, \tag{4.97}$$

$$g_u(D) = 0. \tag{4.98}$$

To obtain $\epsilon_u/\epsilon_d(N)$ and $\Sigma(N)$, the derivatives in equations (4.93) and (4.94) are first sought via solving the two boundary value problems for g_d ((4.91), (4.95) and (4.97)) and g_u ((4.92), (4.96) and (4.98)). Once g_d and g_u are known, their derivatives can be calculated numerically and equations (4.93) and (4.94) then reduce to a quadratic for one of the unknowns, $\epsilon_u/\epsilon_d(N)$ or $\Sigma(N)$. For each N, this quadratic will have two roots, of which the root with the largest growth rate is considered.

4.3.2 Discussion of results

From the flooded geometry, it was found that increasing S and Ca and decreasing the gap ratio, h_0/R, had a destabilising influence on the downstream interface and caused ribbing. These effects, as well as those of H_i, are now examined on both the downstream and upstream interfaces.

Instabilities on the downstream free surface:

Figure 4.25 shows a plot of Σ against N for $Ca = 0.05$, $S = 1.00$, $h_0/R = 0.001$ and six values of H_i. For $H_i > 0.84$, $\Sigma < 0$ for all N and the base flow is stable. For $H_i = 0.84$, $\Sigma = \frac{d\Sigma}{dN} = 0$ for $N = 0.185$ and $\Sigma < 0$ for all other N - the base flow is now neutrally stable. For $H_i < 0.84$, $\Sigma > 0$ for some N and so the base flow is unstable. Hence it is clear that increasing the inlet film thickness has a stabilising influence. An explanation for this will be shown later when the stability hypothesis is considered.

The corresponding plots of ϵ_u/ϵ_d against N are shown in figures 4.26 and 4.27. Figure 4.26 identifies the near inlet flooded regime, which has been shown to be stable (for the parameters used). Note that it is unnecessary to examine the $\epsilon_u/\epsilon_d(N)$ curve in this case because neither free surface becomes unstable, but it is included here for completeness. The cusp in the $\Sigma(N)$ curve, which is only present for large values of H_i, corresponds to a positive maximum in the $\epsilon_u/\epsilon_d(N)$ curve. Within a small region of N up to this maximum, $\Sigma(N)$ and $\epsilon_u/\epsilon_d(N)$ are imaginary whereas elsewhere they are always real. As N is further increased, ϵ_u/ϵ_d rapidly reduces to zero. Thus if the growth rate was positive in the inlet flooded regime, then $|\epsilon_u/\epsilon_d| < 1$ and so the upstream interface is stable and the downstream is unstable. Figure 4.27 shows a similar plot for smaller values of H_i. At values of N for which the growth rate is positive (e.g. for $H_i = 0.75$, $\Sigma(N) > 0$ for $0.14 < N < 0.28$), $|\epsilon_u/\epsilon_d| < 1$ and so the downstream interface is unstable.

The effect of increasing Ca or S is the same as with the inlet flooded case and is shown later in the form of control space diagrams.

Instabilities on the upstream free surface:

Figures 4.28 and 4.29 show the effect of decreasing H_i on the upstream free surface for $Ca = 0.01$, $S = 1.00$ and $h_0/R = 0.001$ in the form of $\Sigma(N)$ and $\frac{\epsilon_u}{\epsilon_d}(N)$ curves. It is clear that for each H_i, $\Sigma(N)$ is a monotonically decreasing function and so the onset

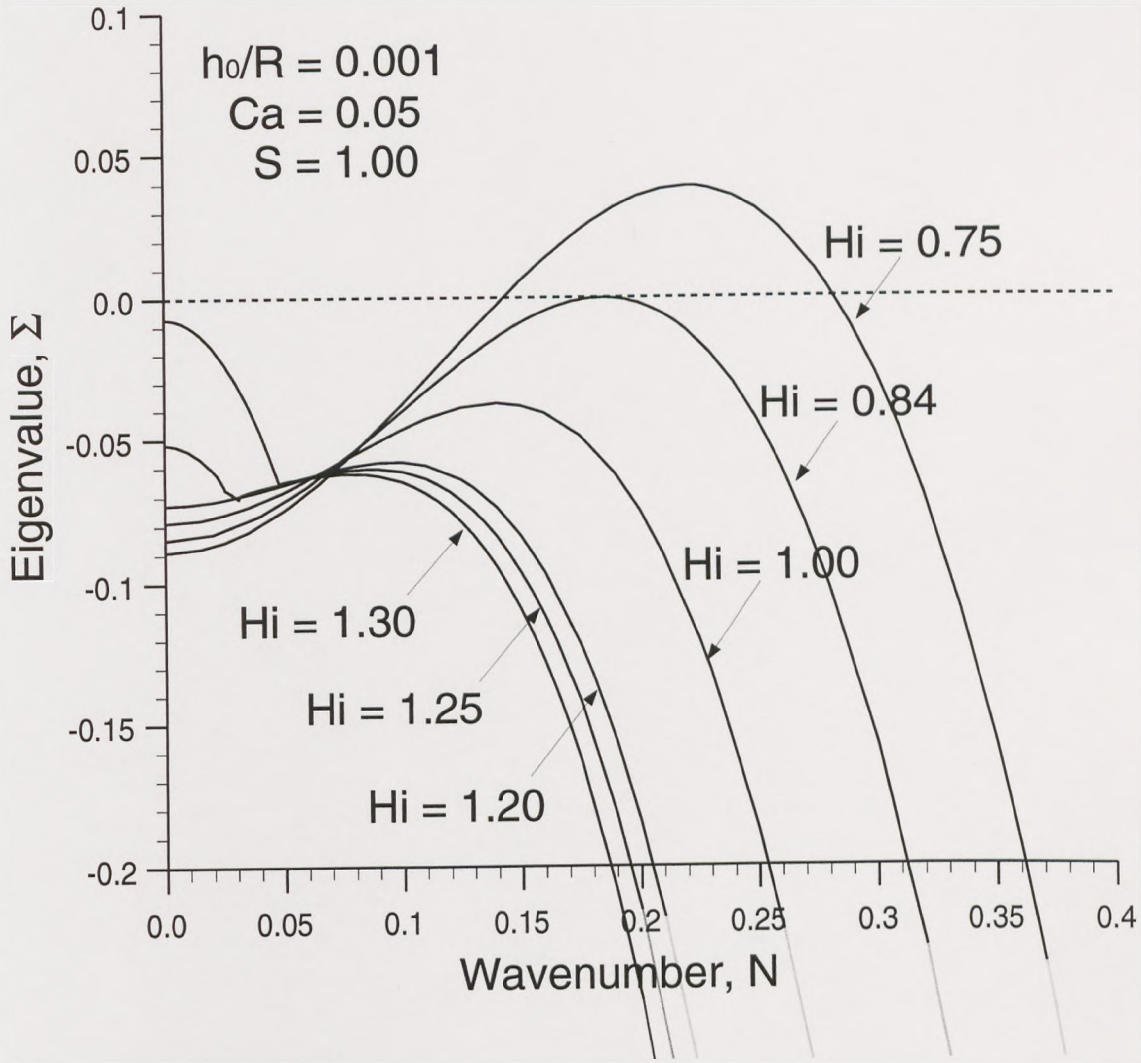

Figure 4.25: Growth rate (Σ) against wavenumber (N) for various H_i with $h_0/R = 10^{-3}$, $Ca = 0.05$ and $S = 1.00$.

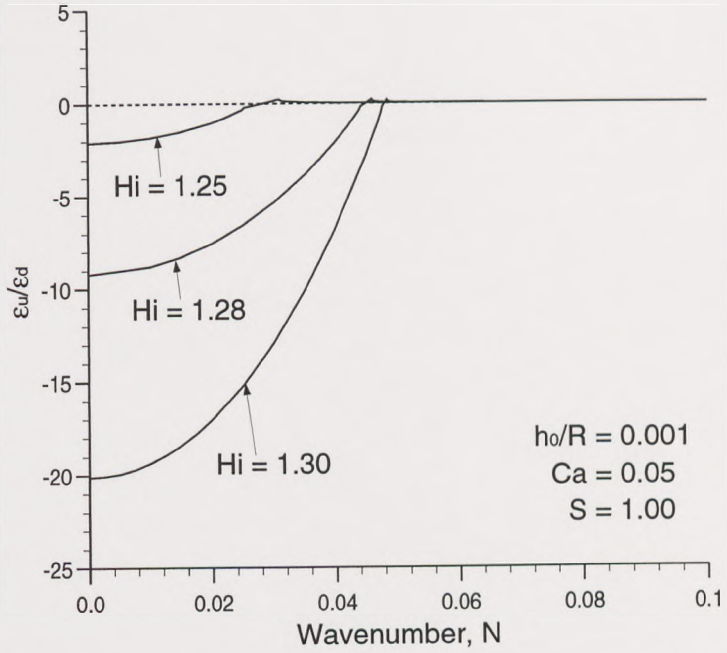

Figure 4.26: ϵ_u/ϵ_d against wavenumber (N) for various H_i with $h_0/R = 10^{-3}$, $Ca = 0.05$ and $S = 1.00$.

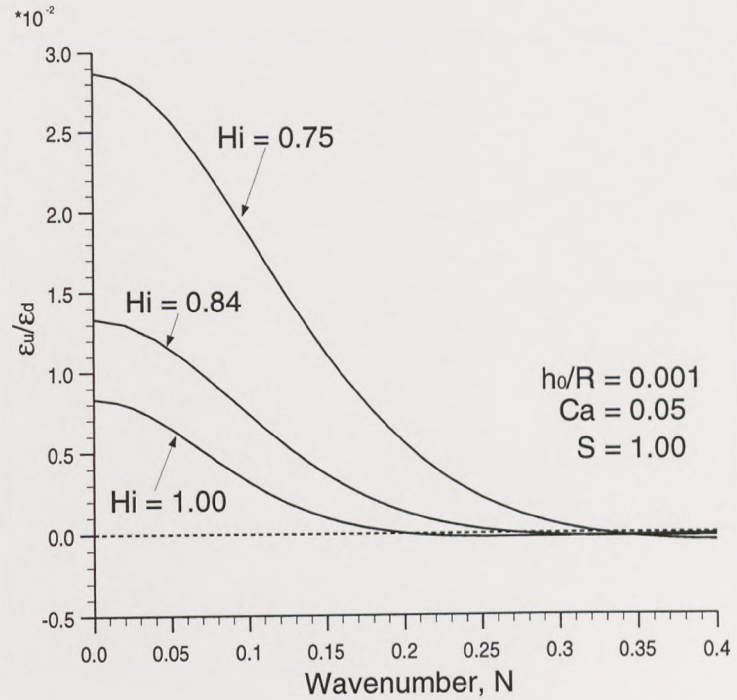

Figure 4.27: ϵ_u/ϵ_d against wavenumber (N) for further, various values of H_i with $h_0/R = 10^{-3}$, $Ca = 0.05$ and $S = 1.00$.

of instability is given by that value of H_i for which $\Sigma(N = 0) = 0$, H_i*. However, this point in parameter space could not be reached because a solution to the base flow equation, (4.58), could not be obtained. In fact, solutions could not be obtained for $H_i < 0.193$ and so the author has assumed that the onset of instability occurs at the same critical conditions for which a solution to the base flow equation no longer exists. The justification for this is that the rate of change of $\Sigma(N = 0)$ with H_i becomes very large as H_i approaches this critical value. Figure 4.29 verifies that this instability will occur on the upstream free surface since for $H_i = 0.193$, $|\epsilon_u/\epsilon_d| > 1$.

Note that increasing Ca or S was found to have a similar effect to that of decreasing H_i on the stability of the upstream free surface. This is shown later in the form of operability diagrams.

It is observed that the conditions for which $\Sigma(N = 0) = 0$ are the critical conditions for the onset of instability at the upstream free surface. This implies that instabilities arising at this upstream free surface are 2-dimensional, a result which can be proved:

Proof:

By examining equations (4.91)-(4.98) and assuming that the upstream perturbation is dominant (i.e. $\epsilon_u >> \epsilon_d$), equations (4.91)-(4.98) reduce to

$$\frac{d^2 g_u}{dX^2} + \frac{6X}{1+X^2}\frac{dg_u}{dX} - 4\pi^2 N^2 g_u(X) = 0, \tag{4.99}$$

$$\left(\frac{dg_u}{dx}\right)_U = \frac{H_D^2}{H_U^3}\Sigma(H_i - H_U), \tag{4.100}$$

$$g_u(U) = \frac{\beta_u U}{6Ca}\sqrt{\frac{h_0}{R}}\frac{H_D^2}{H_U^3} - \frac{H_D^2}{H_U^3}\left[\frac{(1+S)H_U}{2} - H_2 - SH_1\right]$$

$$- \frac{\pi^2 N^2 H_D^2}{3Ca}\left(\frac{h_0}{R}\right), \tag{4.101}$$

$$g_u(D) = 0. \tag{4.102}$$

For a positive radius of curvature at the upstream meniscus, (4.63) gives

$$H_i < H_U. \tag{4.103}$$

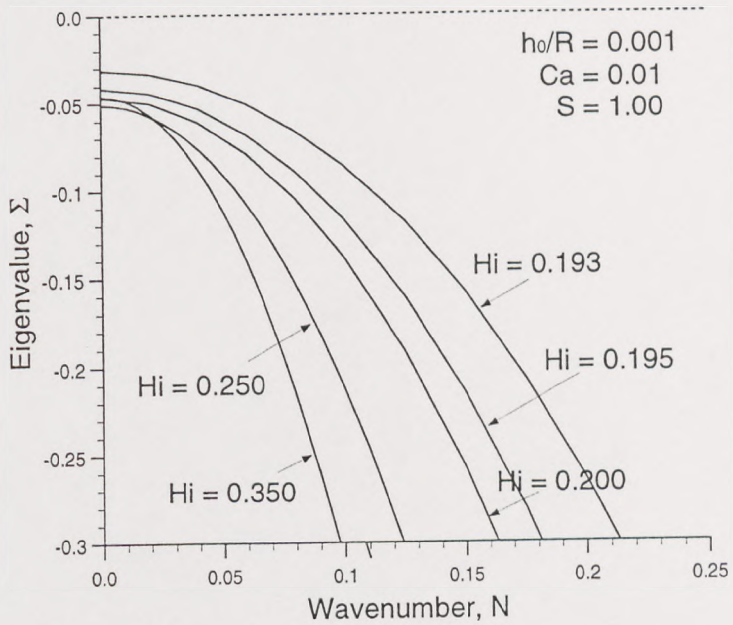

Figure 4.28: Growth rate (Σ) against wavenumber (N) for various H_i with $h_0/R = 10^{-3}$, $Ca = 0.01$ and $S = 1.00$.

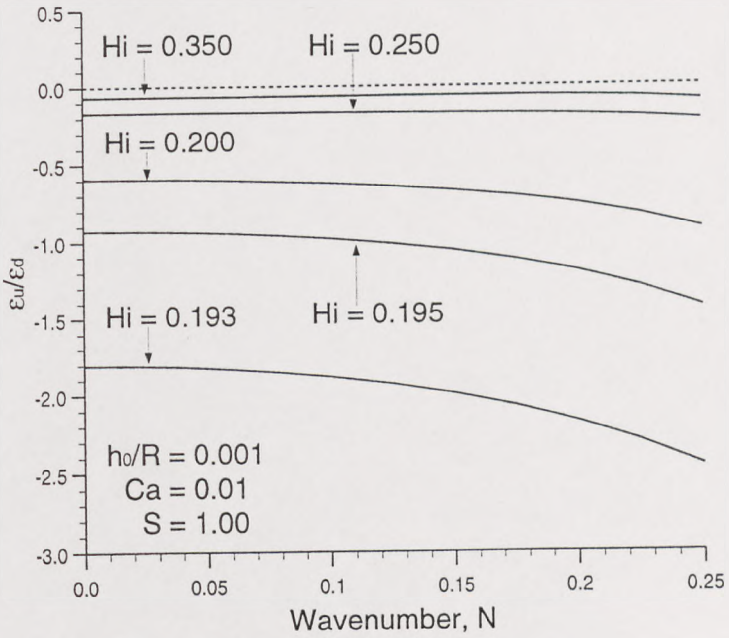

Figure 4.29: ϵ_u/ϵ_d against wavenumber (N) for various H_i with $h_0/R = 10^{-3}$, $Ca = 0.01$ and $S = 1.00$.

For instability, $\Sigma > 0$, and so, using (4.100), $g_u'(U) < 0$. However, $g_u(U)$ and $g_u'(U)$ must be opposite in sign in order that the disturbance should decay monotonically to zero (following an argument similar to that at the downstream interface where $g_d(D)$ and $g_d'(D)$ must have the same sign - see appendix A) and so $g_u(U) > 0$. Similarly, if $\Sigma < 0$ then $g_u(U) < 0$ and so Σ and $g_u(U)$ must have the same sign. Therefore, to determine the stability of the upstream free surface, it is sufficient to determine the sign of $g_u(U)$. However, because $g_u(U)$ is a monotonically decreasing function with N (see equation (4.101)), only the sign of $g_u(U, N = 0)$ is required and so instabilities which arise from the upstream free surface must be 2-dimensional.

□

This proof has two important consequences, namely

1. ribbing, being a 3-dimensional instability, can only occur at the downstream free surface, and

2. a simple 2-dimensional force balance argument (i.e. a stability hypothesis, see section 4.3.4) will give an accurate description of the stability at the upstream free surface.

Note that the above proof confirms the assertion by Gaskell *et al* [1998] that bead break is a 2-dimensional instability to the base flow.

4.3.3 Stability Hypothesis: downstream interface

The S.H. for the downstream interface follows the same argument as for the flooded case, i.e. the base flow is stable if

$$g_d(D, N = 0) \quad > \quad 0, \tag{4.104}$$

where $g_d(D, N = 0)$ is given by equation (4.95). Again, the S.H. only provides a sufficient condition for predicting stability and, as with the flooded case, increasing h_0/R and decreasing Ca and S all cause $g_d(D, N = 0)$ to increase and so have a stabilising effect on the downstream free surface. Thus, the remainder of this section only considers the effect of H_i on the stability of the downstream free surface via its effect on $g_d(D, N = 0)$.

Figure 4.30 shows a plot of $g_d(D, N = 0)$ against H_i for $h_0/R = 0.001$, $Ca = 0.05$ and $S = 1.00$. It is clear that increasing H_i causes $g_d(D, N = 0)$ to increase and therefore has a stabilising influence on the downstream interface (an effect already seen via the linear stability analysis). An explanation for this is given in the context of splitting

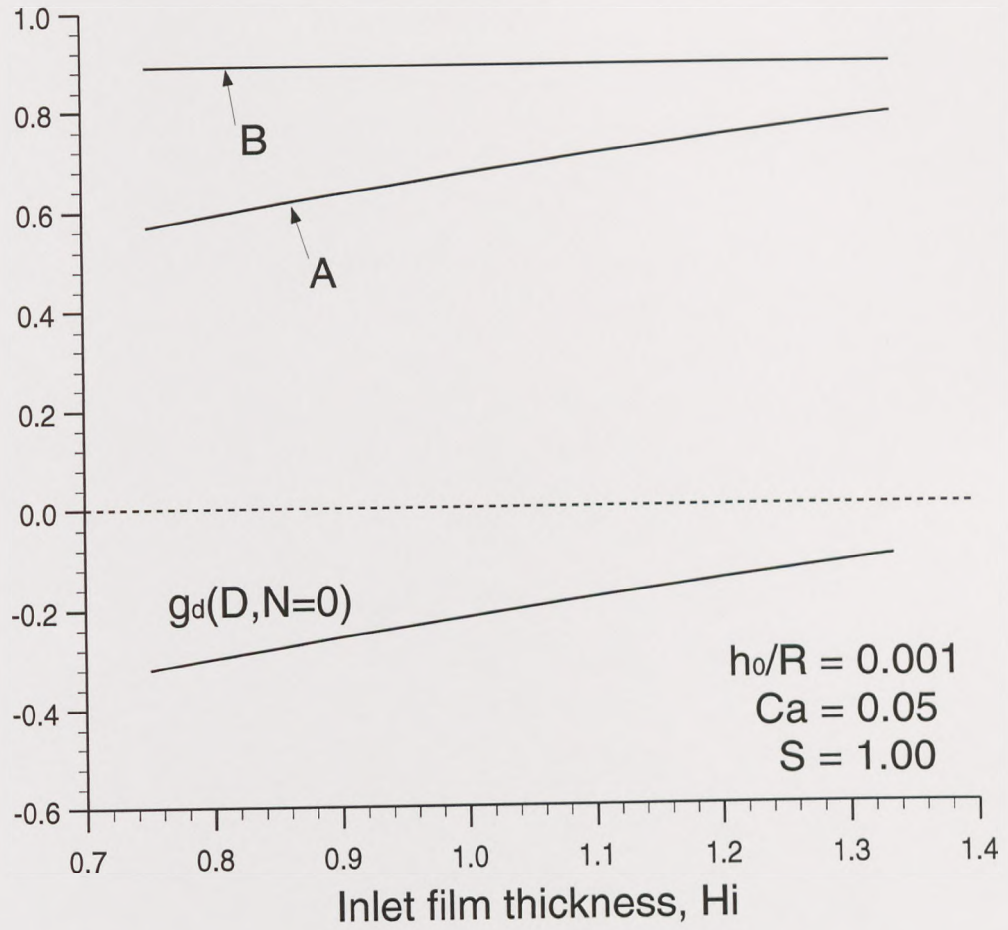

Figure 4.30: Graph of $g_d(D, N = 0)$ against H_i (with its surface tension (A) and pressure gradient (B) components) for $h_0/R = 10^{-3}$, $Ca = 0.05$ and $S = 1.00$.

$g_d(D, N = 0)$ into its two components, namely its surface tension and pressure gradient components (curves A and B respectively in figure 4.30). As H_i is increased, the downstream meniscus moves further away from the nip (see figure 4.19) causing the surface tension term to increase, thus having a stabilising effect. However, H_i does not affect the pressure gradient at the downstream free surface (represented by curve B) and so does not affect the destabilising term. Therefore, it is clear that increasing H_i has an overall stabilising influence on the downstream interface.

4.3.4 Stability Hypothesis: upstream interface

The simple force balance applied above to the downstream meniscus was considered in order to gain insight into the mechanism causing instability and develop a simple, approximate means of predicting stability there. On the upstream meniscus, however, a similar force balance argument gives more than just an approximate predition of sta-

bility. Indeed it was shown in section 4.3.2 that a 2-dimensional stability hypothesis will provide an accurate description of the stability there. Such an argument is now formulated in order to determine the stability of the upstream meniscus and explore the mechanism causing it to become unstable.

When the location of a meniscus of radius r is perturbed from an x-location x_u to $x_u + \epsilon$ the net force acting on a unit area of the interface (in the negative x-direction) is given by

$$F = p(x_u + \epsilon) + \frac{T}{r(x_u + \epsilon)} \tag{4.105}$$

and so using (4.61) and linearising, (4.105) becomes

$$F = \epsilon \left(\frac{dp}{dx} - \frac{T}{r^2} \frac{dr}{dx} \right)_{x=u}. \tag{4.106}$$

If the meniscus is stable, it will return to its original position, and so, assuming $\epsilon > 0$, $F > 0$. Therefore, for stability,

$$\frac{\beta_u T}{h_u^2} \left(\frac{dh}{dx} \right)_u < \left(\frac{dp}{dx} \right)_u. \tag{4.107}$$

It is thus clear that at the upstream meniscus, surface tension effects have a destabilising influence whereas the pressure gradient (at x_u) has a stabilising influence. These influences are opposite to those at the downstream interface. However, because the pressure gradient is always positive at the upstream free surface (see figures 4.19-4.22), for an unstable upstream interface the surface tension term must also be positive i.e. $\frac{\beta_u T}{h_u^2} \left(\frac{dh}{dx} \right)_u > 0$. Hence for instability $\left(\frac{dh}{dx} \right)_u > 0$ and so the upstream free surface must lie downstream of the nip.

After non-dimensionalising (4.107) it can be seen that for instability (via the S.H.),

$$g_u(U, N = 0) > 0, \tag{4.108}$$

where $g_u(U, N = 0)$ is given by equation (4.96). A plot of $g_u(U, N = 0)$ against H_i is shown in figure 4.31 for $Ca = 0.01$, $S = 1.00$ and $h_0/R = 0.001$. As H_i is decreased, $g_u(U, N = 0)$ increases and so decreasing H_i has a destabilising effect. However, solutions for the base flow break down before the point when $g_u(U, N = 0) = 0$, although the two events appear to be so close that they can be taken to occur at the same value of H_i. The graph is in accord with the linear stability analysis (as expected) and predicts a critical inlet film thickness, $H_i = 0.193$.

Plots of $g_u(U, N = 0)$ against Ca and S are shown in figures 4.32 and 4.33 respectively for $h_0/R = 0.001$ and $H_i = 0.35$. Increasing both S and Ca increases $g_u(U, N = 0)$ and therefore has a destabilising effect on the upstream free surface. Again, the conditions at which base flow solutions can no longer be obtained (which occur before the point when $g_u(U, N = 0) = 0$) are taken to be the conditions at which the instability arises. Therefore, the graphs show that for $S = 1.00$ (and the above conditions) a critical capillary number, $Ca = 0.0158$, exists above which the upstream free surface is unstable, and likewise for $Ca = 0.01$ there is a critical speed ratio, $S = 1.686$, above which the upstream free surface is unstable.

4.3.5 Operability diagrams in the $Ca - H_i$ plane

For specific S and h_0/R values, operability diagrams in the $Ca - H_i$ can be mapped out, see for example figure 4.35 for $S = 1.00$ and $h_0/R = 0.001$. The shaded region, which marks the region of stability, is bounded by three lines:

1. The height of this stable coating window is bounded above (i.e. as Ca is increased) by the onset of instability on the downstream interface (predicted by the S.H.). The critical capillary number to mark the onset of this instability increases as H_i increases (as predicted).

2. The coating window is bounded to the right (i.e. as H_i is increased) by the maximum inlet film thickness to give an inlet flooded, forward roll coater. This maximum H_i marginally decreases as Ca increases.

3. The coating window is bounded to the left (i.e. as H_i is decreased) by the onset of instability on the upstream free surface (predicted identically by the S.H. and linear stability analysis). As was shown earlier, as H_i is reduced, the critical capillary number marking the onset of this instability, more commonly known as bead break, reduces.

Figures 4.34-4.36 show operability diagrams for the cases $S = 0.50$, $S = 1.00$ and $S = 1.50$ with $h_0/R = 0.001$. This change in S can influence all three lines which bound the stable operating window and so has three effects:

1. As S is increased the critical capillary number which marks the onset of instability on the downstream interface decreases i.e. the height of the coating window decreases, as predicted by the analysis carried out for the inlet flooded forward roll coater.

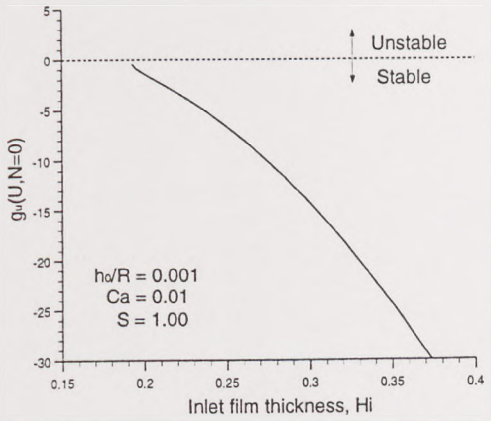

Figure 4.31: Graph of $g_u(U, N = 0)$ against H_i for $h_0/R = 10^{-3}$, $Ca = 0.01$ and $S = 1.00$, where stability is ensured (via the S.H.) if $g_u(U, N = 0) < 0$.

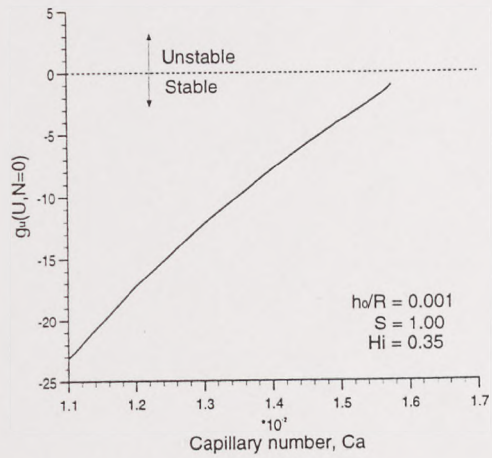

Figure 4.32: Graph of $g_u(U, N = 0)$ against Ca for $h_0/R = 10^{-3}$, $H_i = 0.35$ and $S = 1.00$, where stability is ensured (via the S.H.) if $g_u(U, N = 0) < 0$.

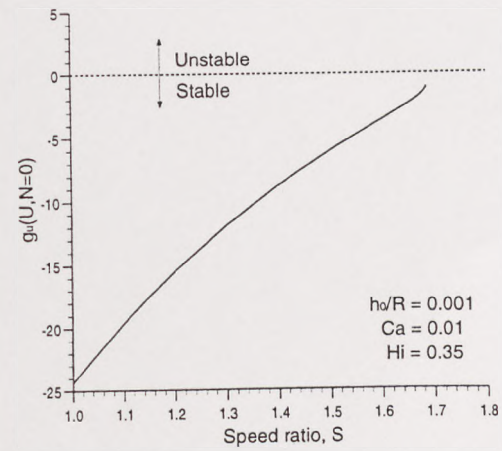

Figure 4.33: Graph of $g_u(U, N = 0)$ against S for $h_0/R = 10^{-3}$, $H_i = 0.35$ and $Ca = 0.01$, where stability is ensured (via the S.H.) if $g_u(U, N = 0) < 0$.

2. For a fixed H_i, as S is increased bead break occurs for a smaller value of Ca, so stable thinner films are more difficult to obtain.

3. For a fixed Ca, the maximum inlet film thickness to give a flooded inlet increases as S increases.

The effect of changing the value of h_0/R on the operability diagram is shown by figures 4.37-4.39 for $h_0/R = 0.005$, $h_0/R = 0.001$ and $h_0/R = 0.0002$ with $S = 1.00$. This change in gap ratio will also influence each line bounding the stable operating window and so has three effects:

1. Increasing h_0/R increases the critical capillary number marking the onset of instability on the downstream interface i.e. the height of the coating window increases, as predicted by the analysis carried out for the inlet flooded forward roll coater.

2. For fixed H_i, as h_0/R is increased bead break occurs for a larger value of Ca making stable thinner films easier to obtain.

3. The effect of h_0/R has a negligible effect on the maximum inlet film thickness to give a flooded inlet.

A comparison of the operability diagrams predicted by the linear stability analysis (L.S.A) and stability hypothesis is shown in figure 4.40 by means of critical curves in the $Ca - H_i$ plane for $S = 1.00$ and $h_0/R = 0.001$. The only difference in the predicted stable operating window is for instability at the downstream interface, where the S.H. underpredicts the critical capillary number for the onset of instability (as with inlet flooded, forward and reverse roll coating). As already shown, the S.H. at the upstream free surface accurately predicts the onset of instability (bead break).

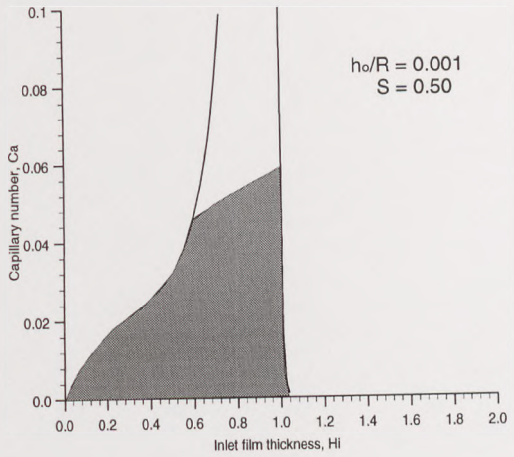

Figure 4.34: Operability diagram in the $Ca - H_i$ plane for $S = 0.50$ and $h_0/R = 0.001$.

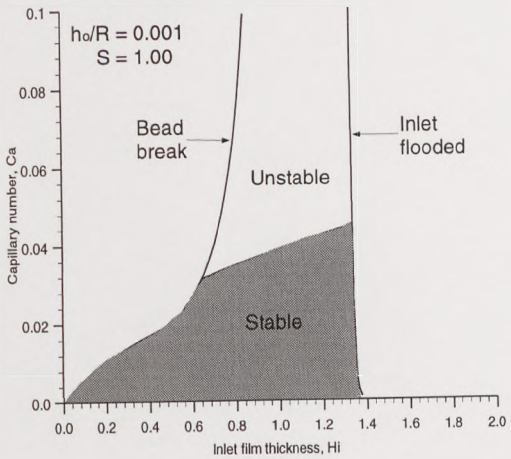

Figure 4.35: Operability diagram in the $Ca - H_i$ plane for $S = 1.00$ and $h_0/R = 0.001$.

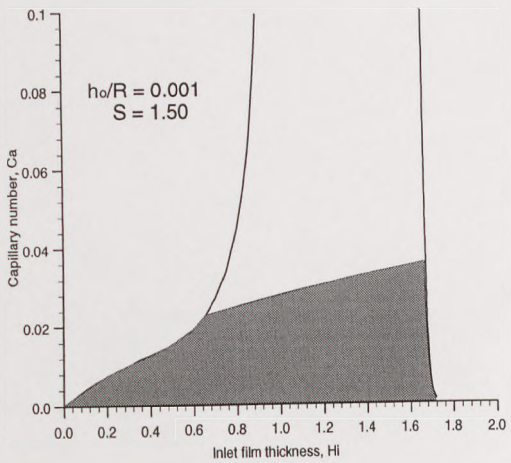

Figure 4.36: Operability diagram in the $Ca - H_i$ plane for $S = 1.50$ and $h_0/R = 0.001$.

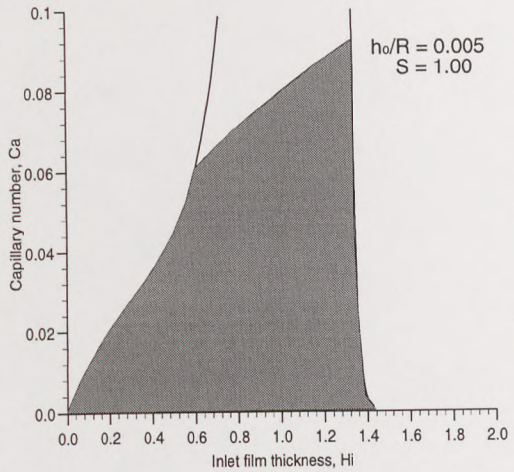

Figure 4.37: Operability diagram in the $Ca - H_i$ plane for $S = 1.00$ and $h_0/R = 0.005$.

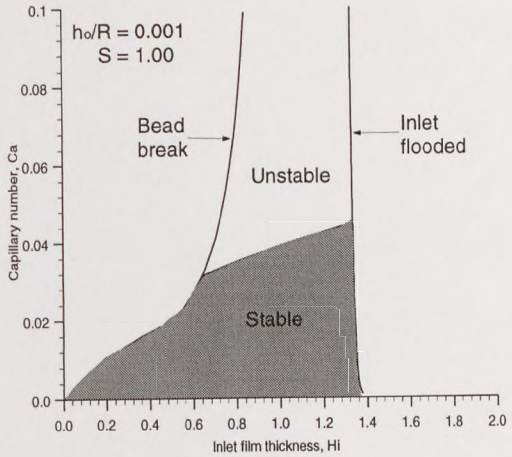

Figure 4.38: Operability diagram in the $Ca - H_i$ plane for $S = 1.00$ and $h_0/R = 0.001$.

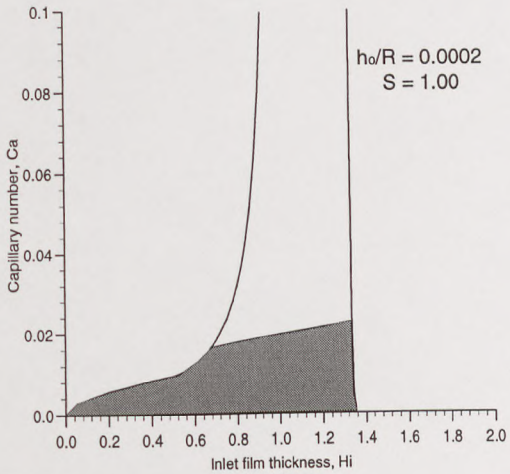

Figure 4.39: Operability diagram in the $Ca - H_i$ plane for $S = 1.00$ and $h_0/R = 0.0002$.

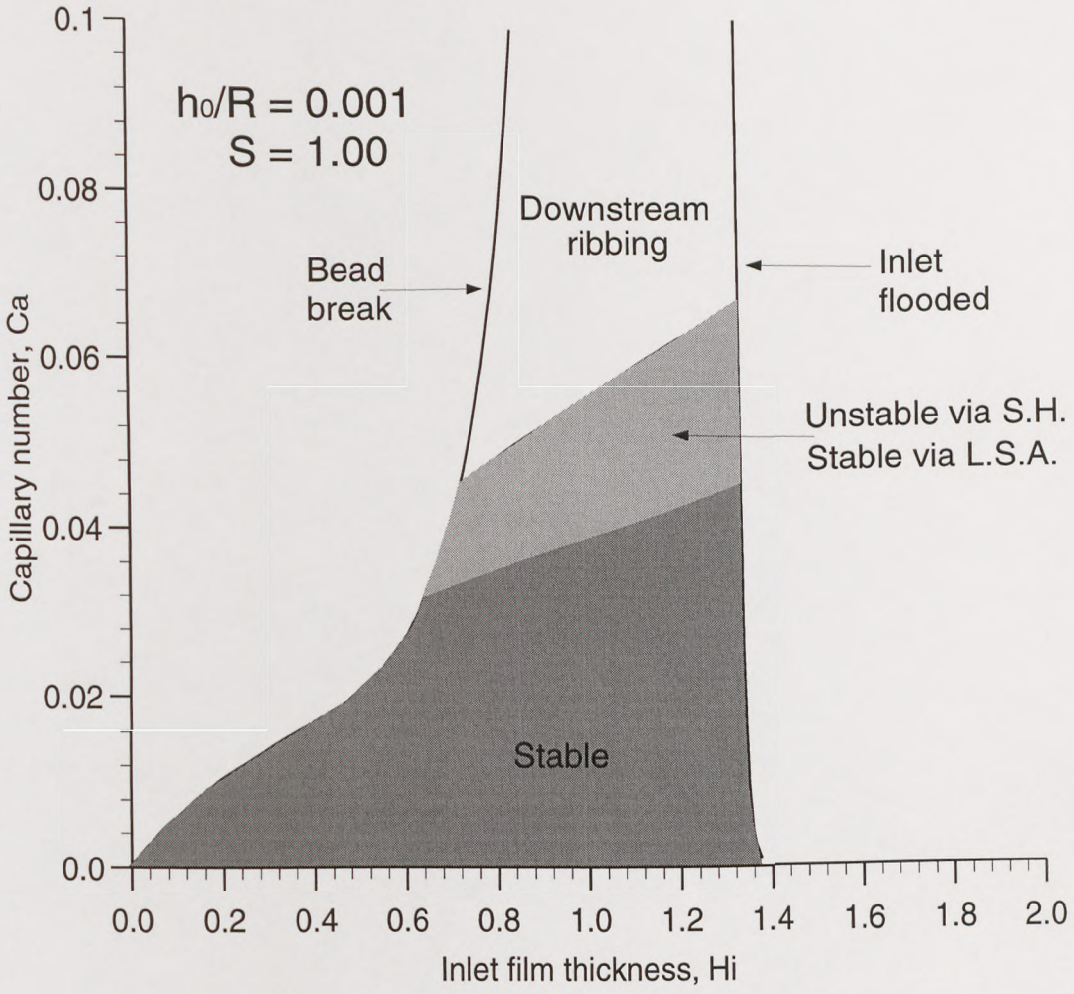

Figure 4.40: Operability diagram in the $Ca - H_i$ plane for $S = 1.00$ and $h_0/R = 0.001$ obtained using both a linear stability analysis (L.S.A.) and stability hypothesis (S.H.).

4.4 Conclusions

In this chapter, instabilities in forward roll coating have been investigated both analytically and numerically. The flooded case was examined using linear stability analysis, a stability hypothesis and a numerical technique based on the FE method. It was shown that decreasing Ca and S and increasing h_0/R has a stabilising effect. As in the reverse case, the S.H. is sufficient for predicting stability only and the agreement with the linear stability analysis improves with decreasing h_0/R. However, unlike the reverse case, the numerical approach has very good agreement with the linear stability theory. It is the author's opinion that this contrast is due to the absence of a dynamic contact line. In particular, the main difference between the analytical and numerical modelling of the base flow for the reverse roll coater arises in the need to impose a slip condition in the numerics to avoid a stress singularity. The analytical approach does not include effects local to the wetting line and so is less accurate.

Inlet starved, forward roll coating was then investigated, in which the coater was fed by a film of dimensionless thickness H_i. By using linear stability theory and the stability hypothesis it was shown that, as with the inlet flooded case, ribbing can appear on the downstream free surface and reducing H_i has the effect of destabilising the flow. The downstream stability hypothesis again underpredicted the critical capillary number for the onset of this instability.

Malone [1992] and Gaskell *et al* [1998] noted from experiment the presence of an instability arising from the upstream free surface which they termed *bead break*. They showed that increasing Ca or S moved the upstream meniscus to the same side of the nip as the downstream free surface and that a further increase caused it to accelerate rapidly towards the downstream meniscus, at which point the coating bead collapsed. This instability has been verified analytically in this chapter using 3-dimensional linear stability theory, from which it was also shown that decreasing H_i also gives bead break. It was then proved that an upstream stability hypothesis gives an accurate (i.e. identical to the linear stability analysis) description of the stability of the upstream free surface (unlike the downstream case), confirming the assertion by Gaskell *et al* that bead break is a 2-dimensional instability.

Chapter 5

Slot Coating

Contents

5.1 Introduction 163

5.2 Base flow 170

5.2.1 Downstream pinned: computational approach 175

5.2.2 Downstream pinned: analytical approach 178

5.2.3 Downstream unpinned: computational approach 184

5.3 Finite element stability analysis 187

5.4 Conclusions 191

5.1 Introduction

Slot coating, otherwise known as extrusion coating, is an extremely versatile premetered process for coating single or multiple layers of liquid onto a moving substrate. With a single external design, a very wide range of applications can be handled for liquids whose viscosity lies in the range from less than $1mPas$ to several thousand Pas. The substrate velocity can similarly cover a wide range of values, from less than $0.1ms^{-1}$ to in excess of $10ms^{-1}$. The minimum wet thickness achievable is of the order of $10\mu m$ with a realisation of less than $\pm 2.5\%$. Examples of liquids applied with a slot coater are photosensitive materials e.g. photoresist, magnetic suspensions, wax, inks, hot melt adhesives, silicon, rubber and foams (Aurin [1985], Campbell [1980], Lippert [1987]). Low viscosity melts of alloys, metals and organic materials can also be applied using a slot arrangement (Carpenter and Steen [1990]).

During the process, liquid is forced through a coating die and fed onto the substrate, see figure 5.1. Within this coating die, a distribution system, consisting of a distribution

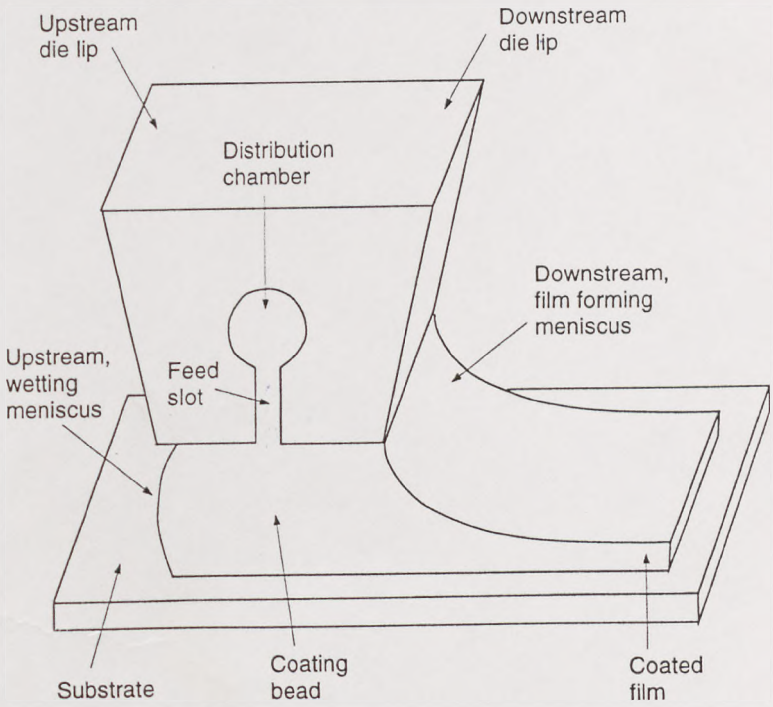

Figure 5.1: Main features of a slot coater.

chamber and a feed slot, provides a uniform liquid flow rate. Note that the different designs of this distribution system are not discussed here since they form a separate topic of interest in their own right (see, for example, Sartor [1990]) and play no role in the

subsequent investigations. The feed slot separates the downstream and upstream die lips. The region between the the die lips and substrate is known as the *coating gap* and is typically from 100 to 500μm across. During operation this space is filled partially or wholly by fluid - this liquid, termed the *coating bead*, is confined by the upstream and downstream menisci. The static contact line at the downstream meniscus can either be pinned at the lip edge (see figure 5.2(a)), regress into the coating gap (see figure 5.2(b)), or climb along the shoulder of the die (see figure 5.2(c)) - see Sartor [1990]. This is dependent on the fluid and geometrical parameters, including the angle δ, see figure 5.2 (see Gibbs [1961], Oliver, Huh and Mason [1977] and Schweizer [1988]). If the

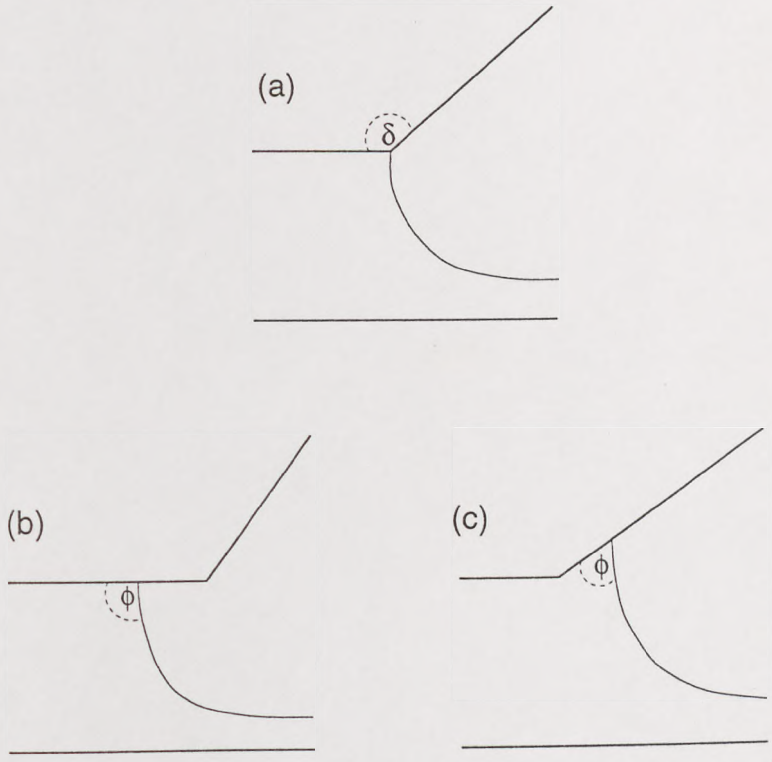

Figure 5.2: Various possible positions of the downstream static wetting line.

downstream static contact line is unpinned, it will meet the downstream lip or shoulder with a characteristic static contact angle, ϕ (see chapter 1). The upstream free surface meets the coating bead on the upstream lip at a static contact line. On the opposite side of the coating gap, the free surface meets the substrate at a dynamic contact line.

In order to maintain the coating bead, a vacuum is often applied behind the upstream meniscus (Beguin [1954]). This imposed potential counteracts the pressure drop across the bead due to capillary and viscous effects, enabling thinner films to be applied. The greater this *back pressure*, pb, the further upstream lies the upstream meniscus.

A qualitative description of the change in the coating bead due to variations of the feed flow rate with the web speed kept constant has been described by Durst and Wagner [1997] and is shown in figure 5.3. If the flow rate is too low, the liquid cannot

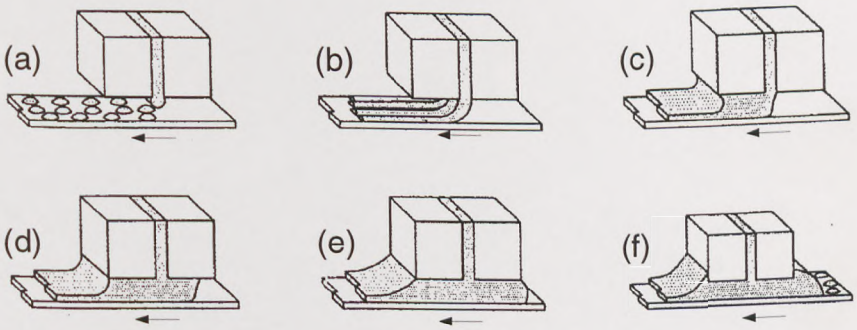

Figure 5.3: Influence of the flow rate on the shape of the coating bead. The flow rate is increasing from (a) to (f) (Durst and Wagner [1997]).

maintain a stable liquid bridge across the coating gap and single drops or rivulets will form on the substrate, as shown in figures 5.3(a) and 5.3(b) respectively. In (b), the dragging action of the moving substrate on the liquid is stronger than the stabilising effects of fluid inertia and capillary forces. Disturbances, present in any coating process, propagating faster than the liquid velocity, lead to a rupture of the liquid bridge and so several liquid bridges form in the cross web direction, each being stable, owing to a higher flow rate within it. Increasing the flow rate leads to a stable situation, as in 5.3(c). The liquid partially or completely fills the gap under the downstream lip and the upstream meniscus bridges the coating gap at the exit of the feed slot. The viscous forces caused by the moving web are balanced by a drop in capillary pressure between the free surfaces. Increasing the flow rate further increases the pressure drop within the downstream coating gap and so the pressure level at the feed slot increases. The fluid is pushed into the upstream region of the coating gap against the the direction of the web motion. The wetting meniscus moves into the rear gap and the upstream die lip wets as indicated in figures 5.3(d) and 5.3(e). Figure 5.3(f) shows the coating bead when the limit of stable coating conditions is reached after a further increase in the flow rate. The pressure drop within the downstream coating gap increases and the pressure at the feed slot is now so high that it cannot be reduced sufficiently by the viscous forces within the upstream region. The capillary forces at the upstream menis-

cus cannot compensate for the pressure difference between the liquid and the gas and so the upstream meniscus swells and fluid wets the upstream die shoulder. The wetting meniscus can no longer bridge the gap and the coating fluid spills onto the substrate, a phenomenon often termed *weeping* or *tears*. If the downstream meniscus does not pin at the edge of the downstream lip, the film forming meniscus climbs up the die shoulder.

Within the parameter space of web speed against upstream vacuum pressure a region exists for which the coated film is defect free. This region is termed the *coating window*, a typical example of which is shown in figure 5.4. Manufacturers have learnt that the

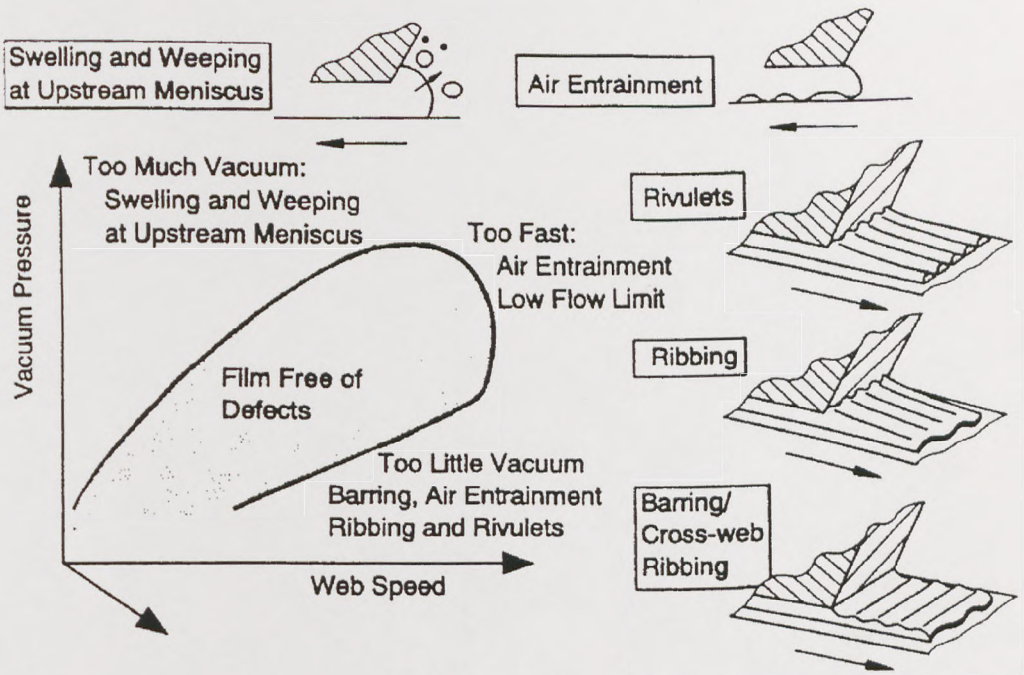

Figure 5.4: Coating window and flow instabilities for variable vacuum pressure, web speed and film thickness (Sartor [1990]).

breadth of the coating window is related to, amongst other things, the shape of the lips of the die and their distance from the substrate. Indeed, numerous patents have been granted for various slot geometries directed at enlarging the operating window, see figure 5.5. Clearly these geometrical parameters will have a significant effect on the meniscus locations as well as the velocity and pressure field within the coating bead.

Ruschak [1976] was the first to analyse the coating window of a slot coater. He neglected viscous effects so that the capillary pressure alone set the bounds on the coating bead operability. His model was valid for low flow rate, low web speed and small die

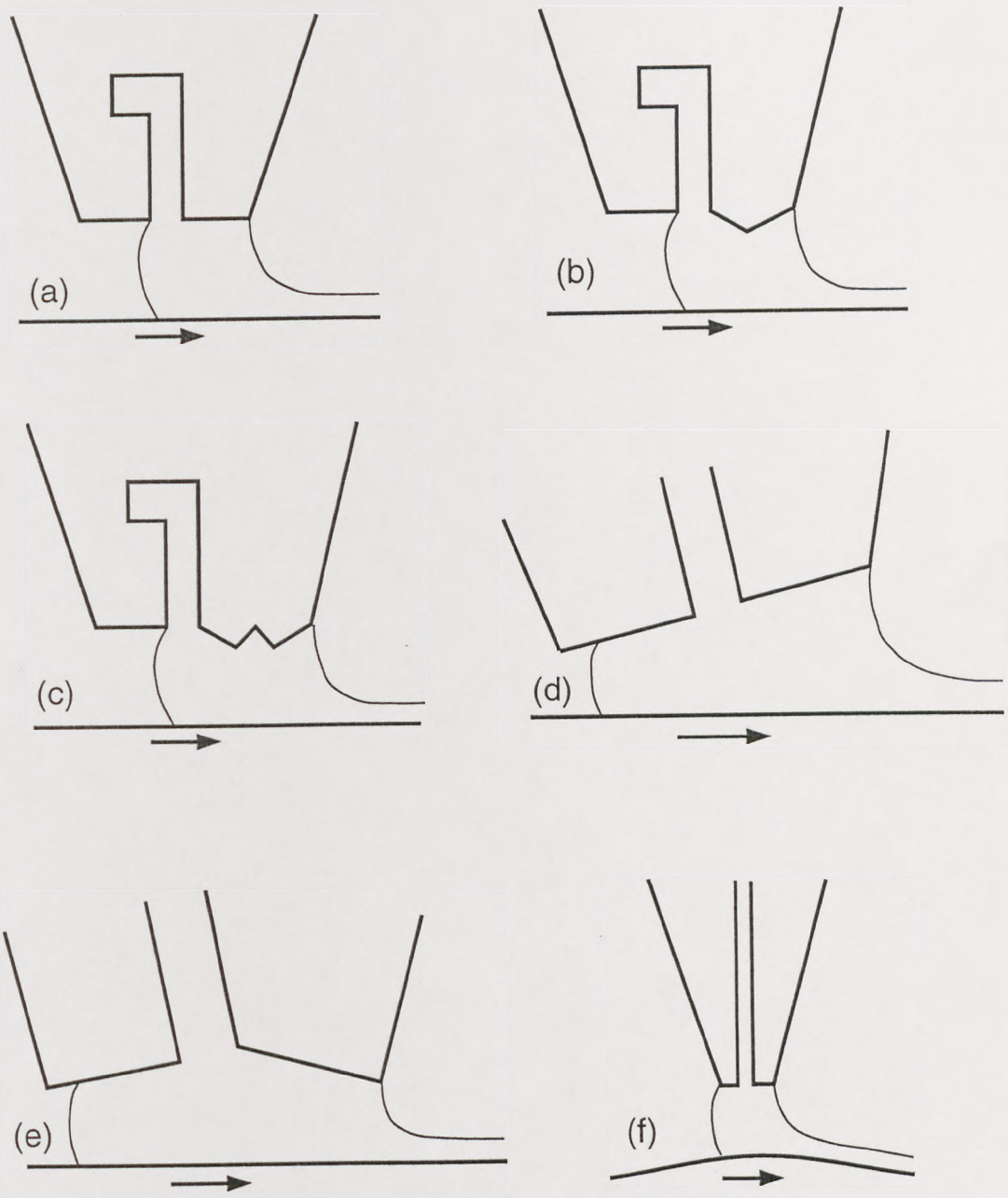

Figure 5.5: Various die designs of the slot coater. Figures (a), (b) and (c) are from Kageyama and Yoshida [1986]. Figures (d) and (e) are from O'Brien [1984] and figure (f) is from Aitken [1964].

lip lengths. Higgins and Scriven [1980] extended this work to include viscous effects, which might become important when the bead length and web speed are not exceedingly small. The case of an unpinned downstream meniscus was not examined since this was thought to be a rare occurrence. They did however investigate the effects of both a pinned and unpinned upstream meniscus. Although more accurate than Ruschak's model, their viscocapillary model retained approximations that are only valid when the web speed and flow rate are small. The menisci are considered as arcs of circles and the radius of curvature (and hence capillary pressure) at the downstream meniscus is estimated using the Landau-Levich [1942] boundary condition. In addition, the model assumes unidirectional flow, an approximation which breaks down where the flow is 2-dimensional, namely at the entrance flow region and the regions close to the free surfaces.

Giavedoni and Saita [1993] compared the predictions from Higgins and Scriven's [1980] viscocapillary model with results from a finite element analysis. They found that at high web speeds, the viscocapillary model overestimated the numerical predictions for the differential pressure along the coating bead, the error being largely due to the 2-dimensional zone near the upstream meniscus. This error was seen to increase as the flow rate increased. At low web speeds, the main source of error was found to be the effect of gravity on the downstream meniscus. Thus, they found that the viscocapillary model accurately predicted the differential pressure to be sustained by the coating bead provided small flow rates and low coating speeds were used and gravity effects could be neglected. Further, even if the operating conditions are far from those indicated above, the viscocapillary model would still be a useful guide because the differential pressure it predicts can be considered as an upper bound of the actual differential pressure to be applied between the ends of the coating device.

The operability diagrams predicted by Higgins and Scriven [1980] do not consider the growth of disturbances with time; only linear and non-linear stability analyses, of which there are few in the literature, can provide such information. An analysis of the sensitivity of the upstream meniscus to 3-dimensional disturbances was made by Higgins and Brown [1984], which confirmed the results of the static analysis previously undertaken by Higgins and Scriven [1980]. Instabilities have also been briefly examined experimentally by Sartor [1990] and Durst and Wagner [1997]. However, since the upstream vacuum pressure affects the instabilities, the author is of the opinion that the instability originates at the upstream free surface, a postulation that is later confirmed by using a linear stability analysis to investigate the effect of pb on the stability of the downstream

interface. Experiments by Kapur [1998] show that ribbing on the downstream meniscus only occurs when the static wetting line is not pinned but free to move along the downstream die lip (thus providing a plausible explanation for the use of the die designs in figures 5.5(b) and (c) - the *jagged* downstream lip allows the film forming meniscus to pin at more than one location). These experiments prompted the present investigation of the ribbing instability on the downstream free surface in terms of a finite element linear stability analysis (described in chapter 2) applied to the slot coating problem with an unpinned downstream wetting line. Firstly, a finite element base flow for the case of a pinned downstream meniscus is obtained and the effect of various fluid and geometrical parameters considered (see section 5.2.1). The resulting pressure profiles and upstream meniscus locations are compared to those predicted via a model based on lubrication theory, see section 5.2.2. In section 5.2.3, the finite element base flow is extended to include an unpinned downstream wetting line - the resulting pressure profiles and menisci locations are again compared to those in section 5.2.1 i.e. when a pinned downstream contact line was used. Finally, linear stability theory is applied to the unpinned case and the effect of various fluid and geometrical parameters on the stability of the flow examined (see section 5.3). Note that instabilities on the upstream free surface are not examined since a comprehensively different finite element mesh would be required - this is a topic for future work.

5.2 Base flow

A schematic of a slot coater with the downstream pinned at the edge of the downstream die lip is shown in figure 5.6. The origin and centre of roller are marked by the positions

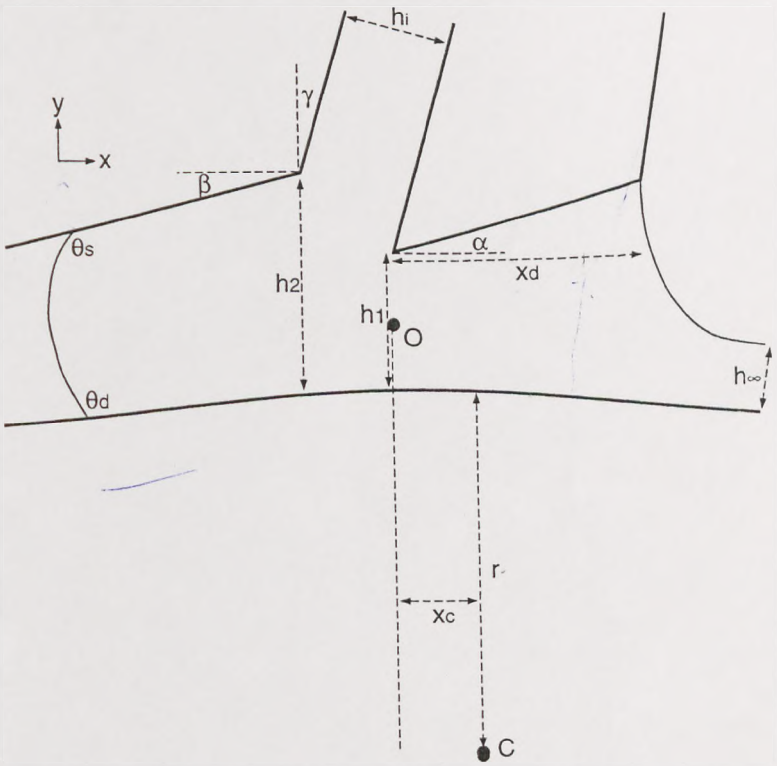

Figure 5.6: Schematic of a slot coater with variable geometry.

O and C respectively. All distances are non-dimensionalised with respect to h_1, so the non-dimensional flux is $\lambda = h_\infty/h_1$, $H_i = h_i/h_1$, $H_2 = h_2/h_1$, $X_d = x_d/h_1$, $X_c = x_c/h_1$ and $R = r/h_1$.

This problem is solved using the finite element method described in chapter 2 allowing for maximum flexibility in the associated geometry. The boundary conditions, shown in figure 5.7, are as follows:

1. At the upstream and downstream free surfaces, the usual kinematic and stress boundary conditions are imposed (see chapter 2).

2. A zero traction condition is imposed at the downstream outlet.

3. At the dynamic wetting line, the apparent contact angle, θ_d, is specified. In addition, as discussed in chapters 1 and 2, a linear slip distribution is specified

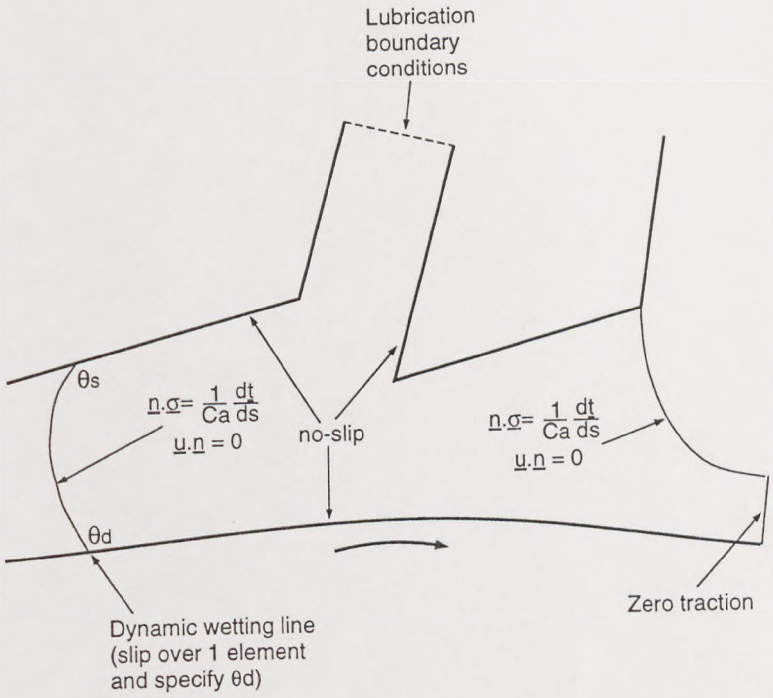

Figure 5.7: Computational boundary conditions for the slot coater.

over the element next to the wetting line (on the surface of the curved substrate) to avoid the stress singularity.

4. At the inflow boundary within the slot, lubrication theory is used to provide the velocity profile.

5. No-slip conditions are applied on the substrate and the upstream and downstream die lip surfaces.

The first FE solutions of a slot coater geometry were obtained by Silliman and Scriven [1980], who only simulated the downstream end of the problem. They used a mesh in which the downstream free surface is represented by a series of vertical spines, see figure 5.8. However, their solutions were restricted to a certain region of parameter space because decreasing the flux caused the curvature of the free surface to increase. This, in practice, results in the meniscus receding into the gap, a feature which vertical spines cannot contend with. Accordingly, in order to achieve greater flexibility, the computational grid employed here for the downstream is similar to that used by Saito and Scriven [1981], Carter [1985] and Thompson [1992], where the spines which capture the free surface position eminate from an origin P outside the flow domain - see figure 5.9.

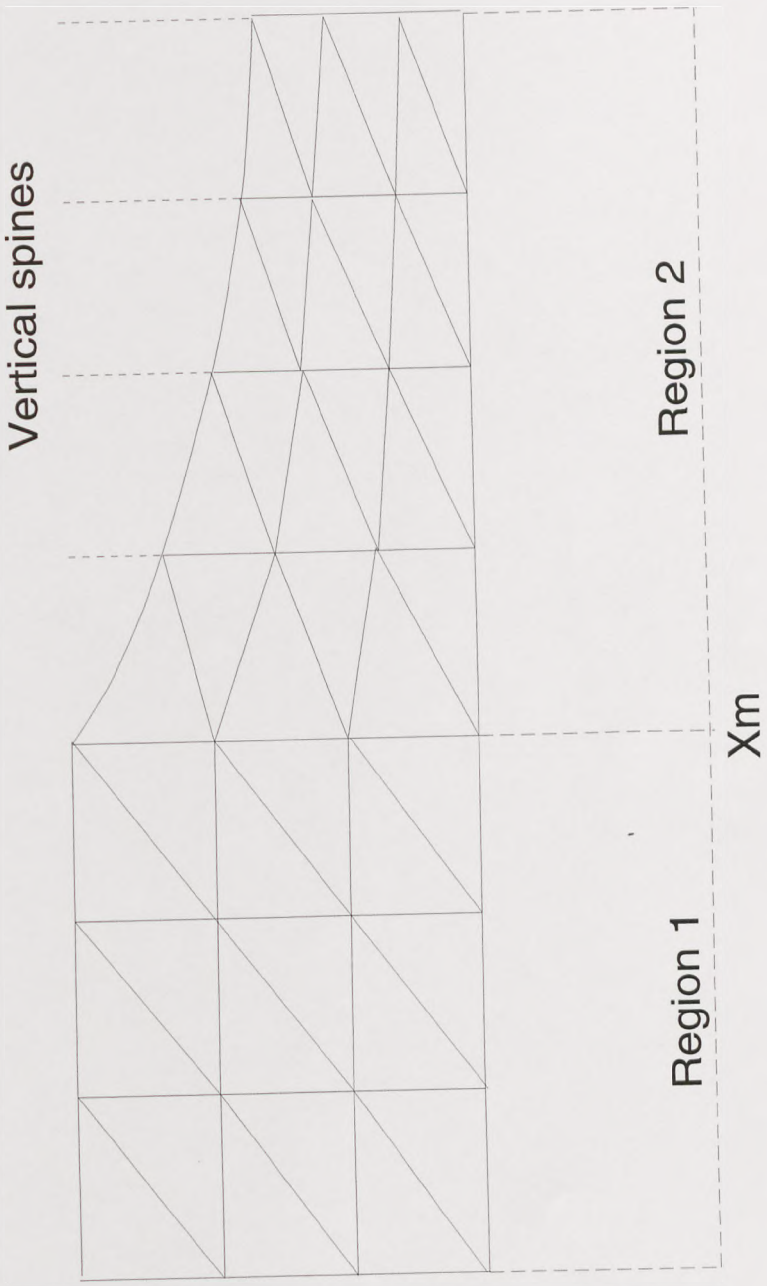

Figure 5.8: Schematic of the grid employed by Silliman and Scriven [1980] to tessellate the downstream region of a slot coater. Note that, for the sake of clarity, the mid-spines have been omitted.

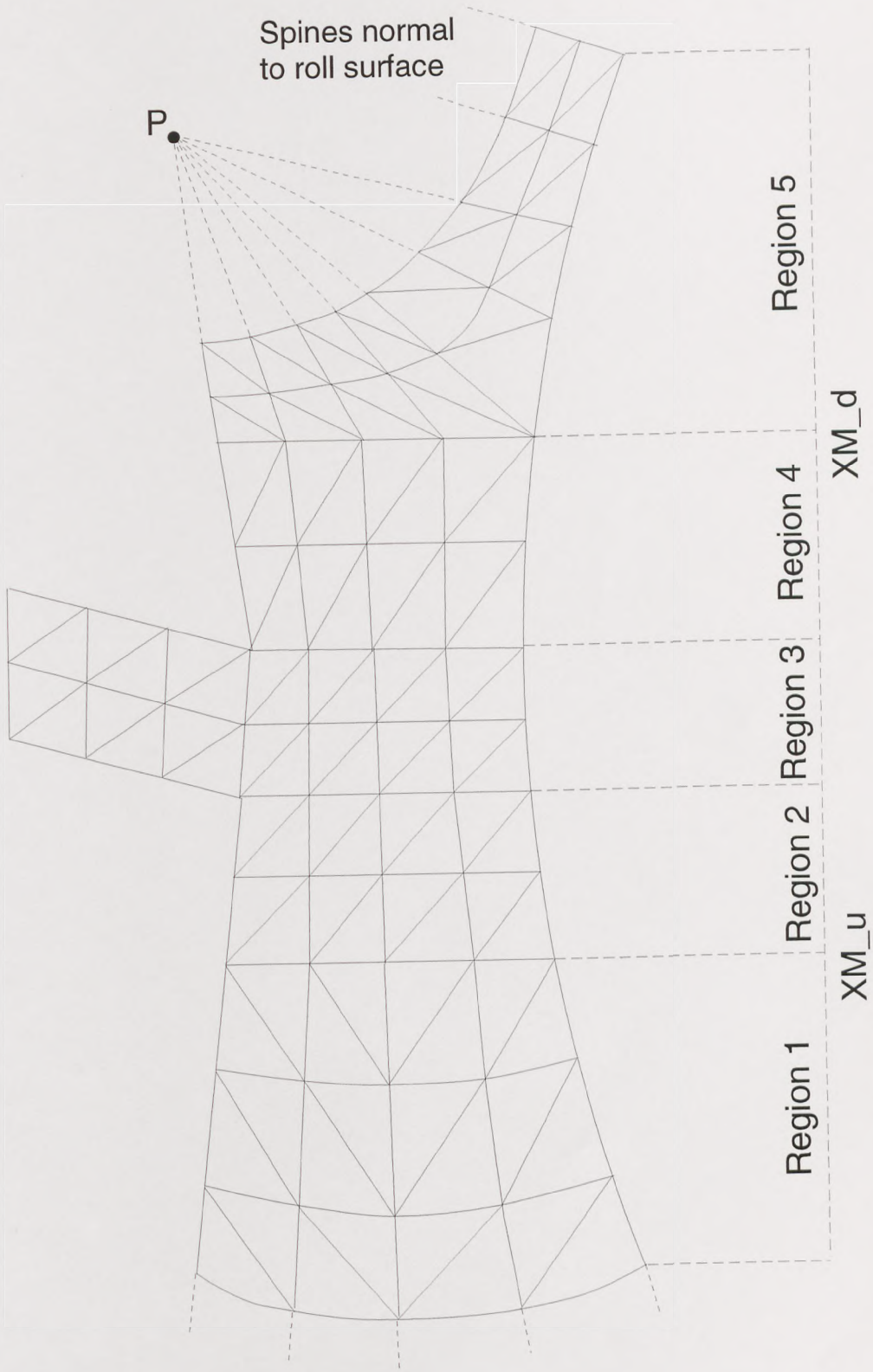

Figure 5.9: Schematic of the grid used to tessellate the slot coater. Note that for clarity the mid-spines have been omitted.

The full slot coating geometry divides naturally into five regions: In region 1, horizontal spines with base nodes on the line XM_u determine the location of the upstream free surface. The y-location of each node in this region is obtained by equally spacing the nodes between the upstream lip and the curved substrate. The parameter XM_u is an unknown; varying it allows the entire upstream grid to move in response to the upstream free surface. Indeed, as XM_u changes, nodes in region 2 undergo a concertina type motion. Nodes in the inlet region, region 3, remain fixed. The parametrisation of the nodes in the downstream region depends on the movement of the downstream wetting line. If stationary (i.e. pinned), the location of the nodes in region 4 remain fixed. Spines which describe the position of the downstream free surface in region 5 either have base points located on the fixed line XM_d or on the curved substrate. A specified number of these spines pass through a polar origin P, which lies at a fixed distance from the wetting line, and all others are perpendicular to the web. If the downstream wetting line is free to move along the lip, then XM_d becomes an unknown parameter and nodes in region 4 undergo a concertina type motion as it changes. The downstream static contact angle, ϕ, is specified in order to determine XM_d.

The computational mesh used in this study consists of 1711 nodes, 776 elements and 3411 unknowns (3412 unknowns if the downstream contact line is free to move), see figure 5.10. Solutions obtained using this grid were compared to those from a grid

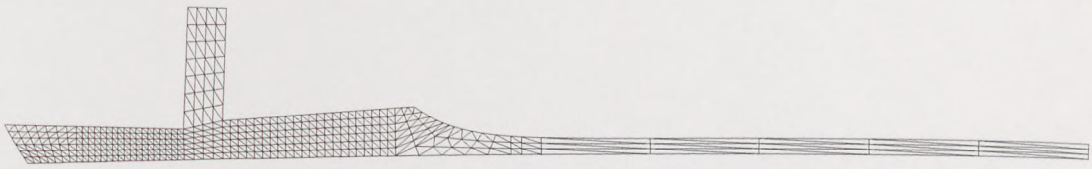

Figure 5.10: Finite element grid containing 1711 nodes and 776 elements.

containing 2147 nodes, 992 elements and 4388 unknowns to test the sensitivity of the solutions to grid refinement. It was observed that when using the two grids, the location of the upstream free surface changed by less than 0.0001%. This suggests that the grid containing 1711 nodes is refined enough to achieve accurate solutions. Tests were also made to ensure that inlet height and outlet film length were long enough so that they had no effect on the solution. Note that for the remainder of this study, $\theta_s = 60^0$, $\theta_d = 120^0$, $\beta = 0.0 = \gamma = 0.0$, $H_i = 1.0$ and a roll with an infinite radius of curvature (i.e. a flat substrate) is used unless otherwise specified.

5.2.1 Downstream pinned: computational approach

This case was considered by Sartor [1990], who examined the flow structure for various fluid and geometrical parameters, see figure 5.11. Figure 5.11 (1) represents the ideal

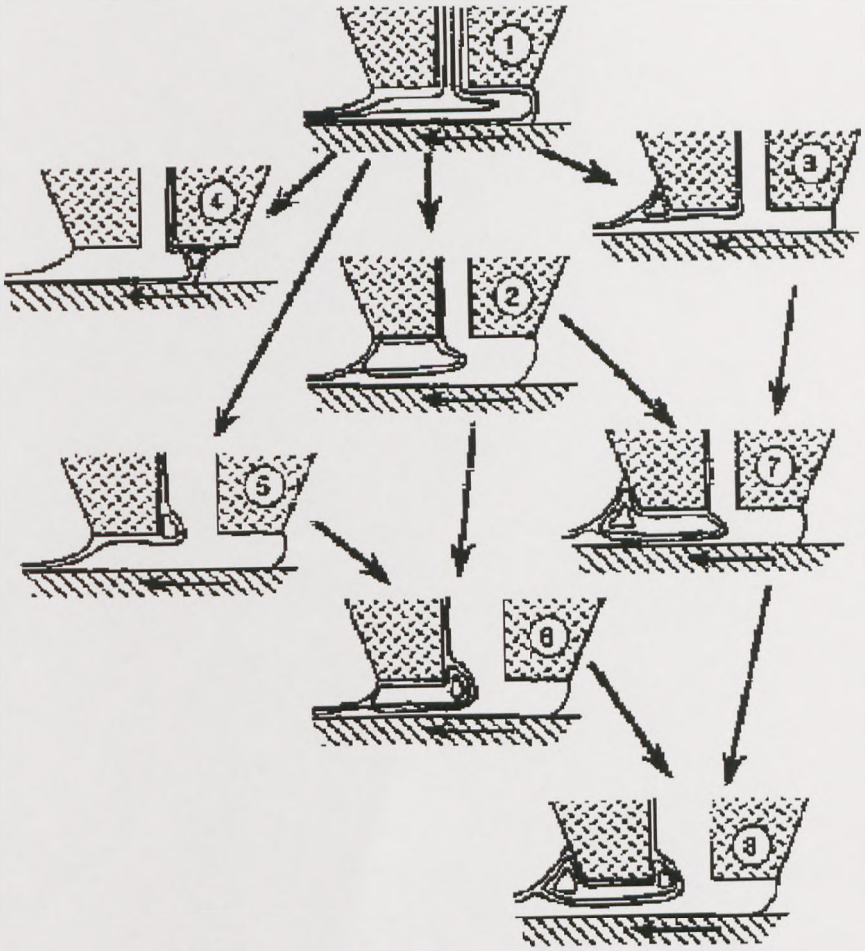

Figure 5.11: Possible flow structures in slot coating (Sartor [1990]).

vortexless bead. However, when the film thickness is less than one third of the coating gap, an eddy forms under the downstream die lip, as shown in (2). Also, from (1), if the downstream wetting line climbs the shoulder of the lip, then a vortex can form as in (3). Similarly, an eddy can form at the upstream static wetting line as in (4). The wetting of the shoulder in (3) is caused by too thick a film or too slow a coating speed for a particular coating gap. The eddy in (4) is caused by a low vacuum. If the feed slot width is larger than five times the final film thickness, a vortex can form at the mouth of the feed slot as in (5). Vortices can also combine (e.g. (2) and (5) give (6), (2) and

(3) give (7) and (6) and (7) give (8)) or coexist if they are too far apart (e.g. (3) and (4)).

Typical streamlines obtained using the grid described above (see figure 5.10) are shown in figure 5.12. Note that when the aspect ratio in the upstream region diminishes beyond a certain value, it has been found here that it is possible for a recirculation to form under the upstream die lip (as in free surface, cavity flows, see Thompson [1992], Gurcan [1996], Wilson [1997]). Above this critical aspect ratio, there is only *turn around* flow in the upstream region.

Figures 5.13-5.15 show pressure profiles obtained using this FE approach. Note that the pressure profile is taken from the upstream free surface to XM_d along the centre of the coating bead.

Figure 5.13 shows pressure profiles for $\alpha = 0.0$, $Ca = 0.05$, $XM_d = 4.50$, $pb = -50.0$, $H_2 = 1.0$ and various λ values. Whereas the pressure gradient in the upstream region retains the same positive value for each λ, the downstream pressure gradient decreases as λ increases. In fact, for the given conditions, if $\lambda < 0.50$ then $\frac{dP}{dX} > 0$, if $\lambda = 0.50$ then $\frac{dP}{dX} = 0$ and if $\lambda > 0.50$ then $\frac{dP}{dX} < 0$. Thus, if $\lambda < 0.50$ a back pressure is required in order to maintain the coating bead, as shown by Beguin [1954]. Note that increasing λ also moves the upstream free surface towards the inlet.

The effect of α on the pressure profiles is shown in figure 5.14 for $\lambda = 0.50$, $Ca = 0.05$, $XM_d = 4.50$, $pb = -50.0$ and $H_2 = 1.0$. Increasing α increases the pressure gradient in the downstream region and, if $\alpha > 0.00$ then $\frac{dP}{dX} > 0$, if $\alpha = 0.00$ then $\frac{dP}{dX} = 0$ and if $\alpha < 0.00$ then $\frac{dP}{dX} < 0$. Increasing α has no effect on the positive, constant, upstream pressure gradient although the wetting meniscus moves marginally towards the nip.

Figure 5.15 shows pressure profiles for $\alpha = 0.05$, $\lambda = 0.50$, $Ca = 0.05$, $pb = -50.0$, $H_2 = 1.0$ and various XM_d. Altering XM_d has no effect on the upstream pressure gradient, although the upstream meniscus moves towards the inlet as XM_d increases (for the above conditions). This movement is however significantly dependent on α and λ and under certain conditions the upstream free surface can move away from the inlet with increasing XM_d (e.g. for $\alpha = 0.00$ and $\lambda = 0.60$). Increasing XM_d also increases the pressure gradient at the downstream outlet.

The effects of Ca, pb and H_2 on the dynamic wetting line location are shown in fig-

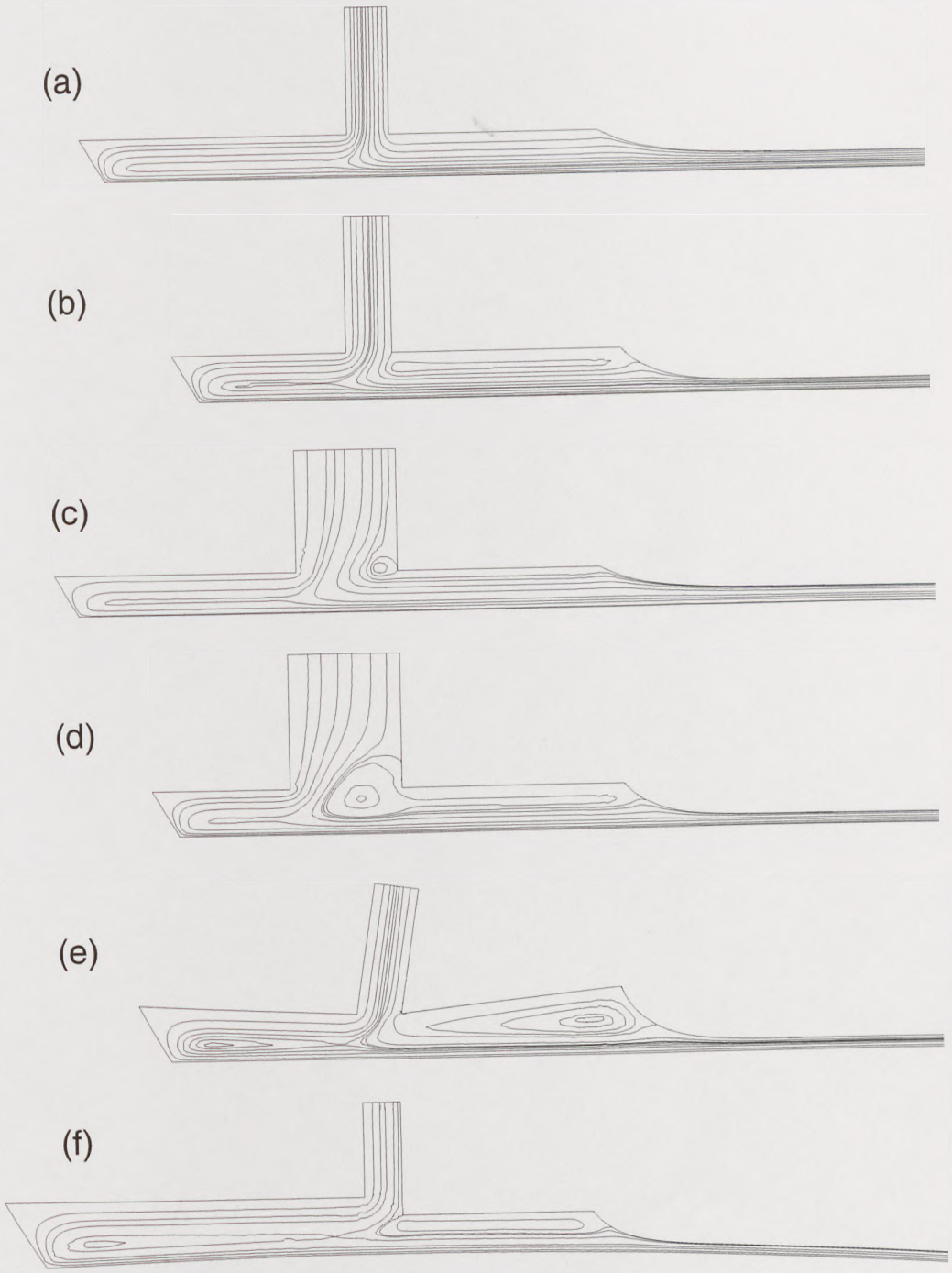

Figure 5.12: Typical streamlines obtained using an FE grid with 1711 nodes. Flow conditions: (a) $Ca = 0.05$, $\lambda = 0.40$, $pb = -50.0$, $\alpha = \beta = \gamma = 0.0$, $H_2 = 1.00$, $X_d = 5.00$, $H_i = 1.00$, $X_c = 0.00$ and $R = 10^8$; (b) as (a) with $\lambda = 0.25$; (c) as (a) with $H_i = 2.50$; (d) as (c) with $\lambda = 0.24$; (e) as (b) with $\alpha = 0.10$, $\beta = -0.05$ and $\gamma = 0.15$; (f) as (b) with $R = 200.0$ and $H_2 = 1.50$.

ures 5.16, 5.17 and 5.18 respectively. Note that their effect on the downstream region was found to be minimal. As Ca increases, the dynamic wetting line moves further away from the inlet (due to an increase in the capillary pressure at the downstream meniscus). However, this effect is only marginal unless Ca is very small ($Ca < 0.1$). For the the parameters shown (i.e. $\alpha = 0.00$, $\lambda = 0.50$, $XM_d = 4.50$, $pb = -50.0$ and $H_2 = 1.0$), there is a minimum Ca below which solutions could not be obtained because the upstream free surface moved so close to the inlet that meshing difficulties occurred. As the back pressure, pb, is increased in magnitude, the upstream meniscus moves further away from the inlet (the pressure gradient remaining the same). For the parameters shown, solutions could not be obtained for $pb > -14.8$, again because of meshing problems. The effect of increasing H_2 is to move the upstream free surface further away from the inlet (and reduce the pressure gradient in the upstream region). Meshing difficulties once again become a problem when the upstream free surface is too close to the inlet and for the conditions indicated in figure 5.18, solutions could not be obtained for $H_2 < 0.5$.

Note that the effect of increasing β on the upstream free surface location is similar to that of decreasing H_2 as the upstream coating gap is effectively narrowed. However, β does have an effect on the upstream pressure gradient, which is no longer constant for $\beta \neq 0.0$. In fact, as will be shown later using lubrication theory, the pressure gradient in the upstream region is inversely proportional to the square of the distance between the upstream lip and web. Similarly, the effect of including a more sizeable radius of curvature of the roller (and different roll centre positions) is qualitatively similar to certain values of H_2, β and α, the effects of which have already been noted.

5.2.2 Downstream pinned: analytical approach

Here, the aim is to develop a model for a slot coater (with a pinned downstream) based on the lubrication approximation, in order to predict the velocity and pressure field together with the location of the upstream meniscus. The predictions obtained will be compared to the results obtained using the finite element method in the above section.

Neglecting body forces, transient and inertia terms, the Navier-Stokes equations reduce to

$$0 = -\nabla p + \mu \nabla^2 \underline{u}. \tag{5.1}$$

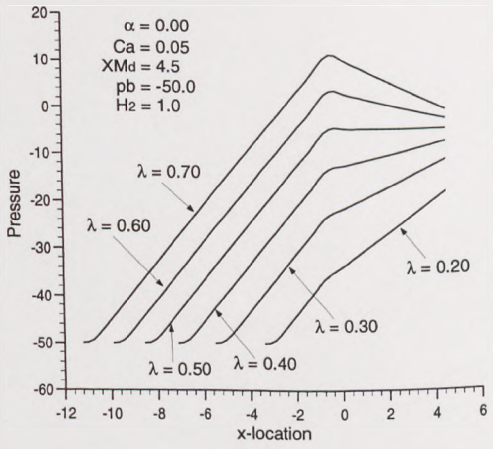

Figure 5.13: Pressure profiles for $\alpha = 0.00$, $Ca = 0.05$, $XM_d = 4.50$, $pb = -50.0$, $H_2 = 1.0$ and various λ.

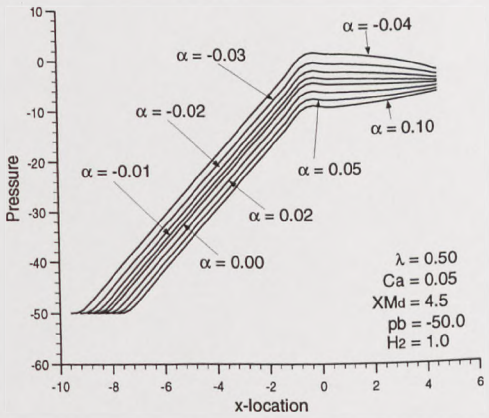

Figure 5.14: Pressure profiles for $\lambda = 0.50$, $Ca = 0.05$, $XM_d = 4.50$, $pb = -50.0$, $H_2 = 1.0$ and various α.

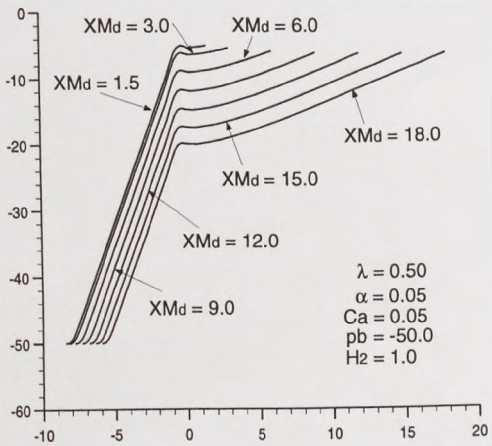

Figure 5.15: Pressure profiles for $\alpha = 0.05$, $\lambda = 0.50$, $Ca = 0.05$, $pb = -50.0$, $H_2 = 1.0$ and various XM_d.

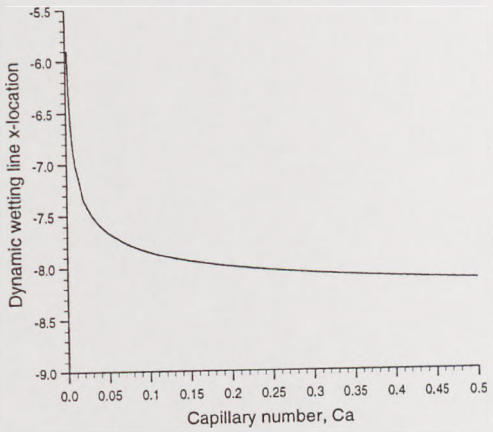

Figure 5.16: Dynamic wetting line x-location against capillary number (Ca) for $\alpha = 0.00$, $\lambda = 0.50$, $XM_d = 4.50$, $pb = -50.0$ and $H_2 = 1.0$.

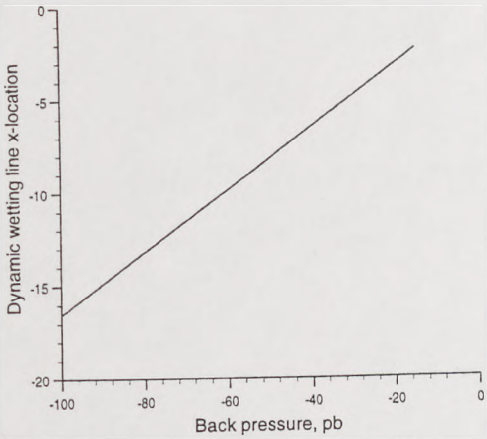

Figure 5.17: Dynamic wetting line x-location against back pressure (pb) for $\alpha = 0.00$, $\lambda = 0.50$, $Ca = 0.05$, $XM_d = 4.50$ and $H_2 = 1.0$.

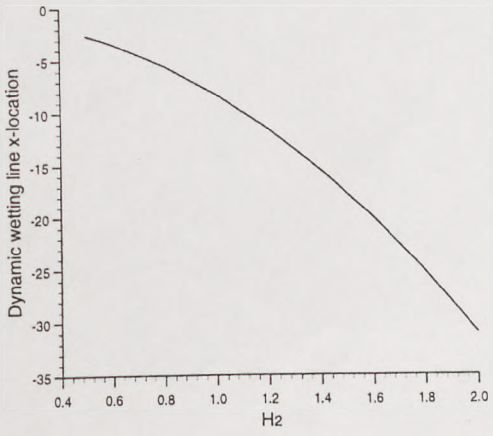

Figure 5.18: Dynamic wetting line x-location against H_2 for $\alpha = 0.00$, $\lambda = 0.50$, $Ca = 0.05$, $XM_d = 4.50$ and $pb = -50.0$.

Assuming unidirectional flow and that velocity gradients across the bead are negligible i.e. $\partial u/\partial x << \partial u/\partial y$ then (5.1) becomes

$$\frac{\partial p}{\partial x} = \mu \frac{\partial^2 u}{\partial y^2} \tag{5.2}$$

and

$$\frac{\partial p}{\partial y} = 0. \tag{5.3}$$

Hence $p = p(x)$ and therefore integrating (5.2) twice and imposing the no slip boundary conditions on the upstream and downstream lips (which are assumed to join up at the centre of the inlet) and roll i.e.

$$\begin{aligned} u &= U \text{ at } y = 0 \\ u &= 0 \text{ at } y = h(x) \end{aligned} \tag{5.4}$$

gives

$$u = \frac{1}{2\mu}\frac{dp}{dx}(y^2 - yh) - U\left(1 - \frac{y}{h}\right), \tag{5.5}$$

where $h(x)$ is the gap width between the roll and die lip. The flux Q is given by

$$Q = \int_0^{h(x)} u dy \tag{5.6}$$

which, using (5.5), becomes

$$Q = -\frac{h^3}{12\mu}\frac{dp}{dx} + \frac{Uh}{2}. \tag{5.7}$$

At this stage, the flow in the slot coater can be split up into two regions, separated by the centre of the inlet. In the downstream region the flux, Q^R, past any station x is constant and equal to the flux in the uniform film of thickness h_∞ attached to the roll,

$$Q^R = Uh_\infty. \tag{5.8}$$

Therefore, the pressure gradient in the downstream region, $(dp/dx)^R$, is

$$\left(\frac{dp}{dx}\right)^R = \frac{6\mu U}{h^2}\left(1 - \frac{2h_\infty}{h}\right). \tag{5.9}$$

In the upstream region there is no net flow i.e. so the the flux, Q^L, is given by

$$Q^L = 0, \tag{5.10}$$

and the pressure gradient in the upstream region, $(dp/dx)^L$, by

$$\left(\frac{dp}{dx}\right)^L = \frac{6\mu U}{h^2}. \tag{5.11}$$

As with finite element case (see figure 5.6), all distances are non-dimensionalised with respect to h_1. Hence, by introducing non-dimensional variables defined by

$$\begin{aligned} H &= \frac{h}{h_1}, \\ \lambda &= \frac{h_\infty}{h_1}, \\ X &= \frac{x}{h_1}, \\ P &= \frac{h_1}{\mu U} p, \end{aligned}$$

equations 5.9 and 5.11 become

$$\left(\frac{dP}{dX}\right)^R = \frac{6}{H^2}\left(1 - \frac{2\lambda}{H}\right) \tag{5.12}$$

and

$$\left(\frac{dP}{dX}\right)^L = \frac{6}{H^2} \tag{5.13}$$

respectively i.e. so the pressure gradient in the downstream region depends on the distance between the lip and roll together with the flux, whereas the pressure gradient in the upstream region is only related to the distance between the lip and curved substrate.

Boundary conditions:

At the downstream meniscus, a balance of fluid and surface tension pressure is used to describe the pressure, i.e.

$$p(x_d) = -\frac{T}{r_d}, \tag{5.14}$$

where x_d is the x-location of the downstream meniscus and r_d is its radius of curvature. The Landau-Levich [1942] and Ruschak [1981] conditions,

$$\frac{h_\infty}{h_d} = \begin{cases} 0.56 Ca^{1/2} & 10^{-2} \leq Ca \leq 10^{-1} \\ \\ 1.34 Ca^{2/3} & Ca < 10^{-2}, \end{cases} \tag{5.15}$$

are then used to determine r_d. Hence, the non-dimensional pressure at the downstream meniscus is

$$P(X_d) = -\frac{1}{CaR_d} = \begin{cases} -\frac{0.56 Ca^{-1/2}}{\lambda} & 10^{-2} \leq Ca \leq 10^{-1} \\ \\ -\frac{1.34 Ca^{-1/3}}{\lambda} & Ca < 10^{-2}, \end{cases} \tag{5.16}$$

where R_d is the non-dimensional r_d. The pressure at the upstream free surface is given by the surface tension and vacuum pressure i.e.

$$p(x_u) = -\frac{T}{r_u} + pb, \tag{5.17}$$

where r_u is the radius of curvature of the upstream meniscus which is located at x-location x_u. This upstream meniscus can be modelled by the arc of a circle, of which all possible radii (i.e. shapes) are given by the expression

$$r_u = \frac{h(x_u)}{\cos(\theta_s - \beta) + \cos(\theta_d)}. \tag{5.18}$$

Hence the non-dimensional pressure at the upstream meniscus is,

$$P(X_u) = -\frac{\cos(\theta_s - \beta) + \cos(\theta_d)}{H(X_u)Ca} + Pb. \tag{5.19}$$

Solution:

It only remains to specify the upstream and downstream die lip shapes and positions together with the roll radius and location. Equation (5.12) can then be integrated and the pressure (given by (5.16)) and location of the downstream meniscus used to calculate the pressure at the centre of the inlet. Equation (5.13) can then be integrated and solved for the upstream pressure and dimensionless meniscus location, X_u. Figure 5.19 shows a comparison of the pressure profiles predicted using the above lubrication theory with results obtained using the finite element method (for $\alpha = \beta = \gamma = 0.0$, $Pb = -50.0$, $H_2 = 1.0$, $X_d = 5.00$, $XM_d = 4.50$ and various λ). Note that the pressure profiles from the lubrication theory extend further than those from the FE method. This is because the pressure profiles obtained using the FE method end at XM_d whereas those obtained using the model based on lubrication theory end at X_d i.e. at the downstream contact line. Clearly lubrication theory accurately predicts the upstream and downstream pressure gradients as well as the upstream meniscus location. The main source of error arises from equation (5.16) (i.e. the approximation for the pressure at the downstream free surface) which underpredicts (overpredicts) $P(X_d)$ for large (small) λ.

Note that it is not possible to formulate a model based on lubrication theory for an unpinned downstream. This is because it is necessary to know X_d in order to determine the pressure at the centre of the inlet (which would then be used with (5.13) to determine the pressure and location of the upstream free surface). The following section therefore examines the slot coater with an unpinned downstream using the finite element method only.

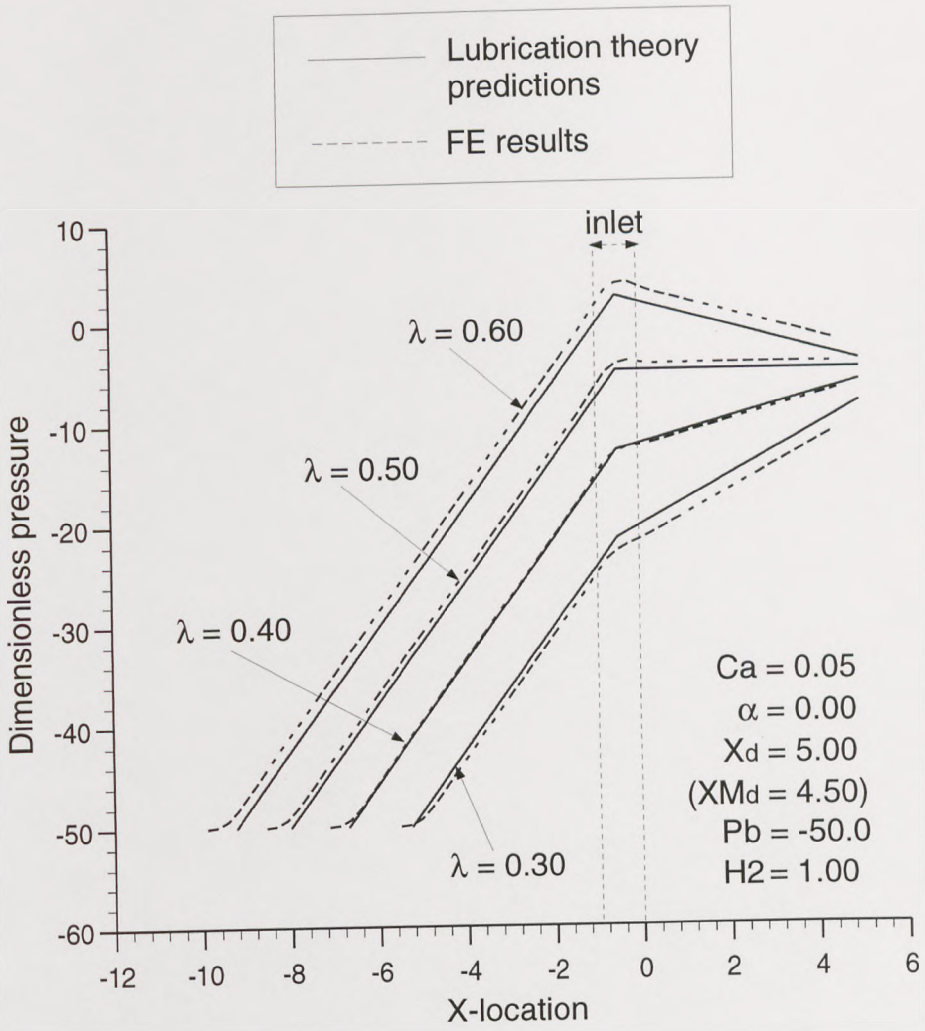

Figure 5.19: Comparison of pressure profiles predicted using lubrication theory with like results obtained using the FE method.

5.2.3 Downstream unpinned: computational approach

Sartor [1990] recognised that the downstream contact line did not necessarily pin at the edge of the downstream die lip, although he did not study this case. This has been experimentally confirmed by Kapur [1998], who also examined the flow numerically using the finite element method for the case when the wetting line climbed up the downstream die shoulder. Kapur further noted from experiment that ribs could only occur when operating in the unpinned regime. It is therefore the aim of this section to investigate slot coating with an unpinned, downstream, static wetting line. Again, the effects of the fluid and geometrical parameters will be considered, with particular attention given to the effect on the downstream contact line location and downstream pressure gradient since it has already been shown in chapters 3 and 4 that these are

crucial for ascertaining the stability of the downstream free surface. The same mesh is used as for the pinned case, although there are now 3412 unknowns - one more than for the pinned case because XM_d is now unknown.

Figure 5.20 shows resulting pressure profiles for the conditions $\alpha = 0.0575$, $Ca = 0.05$, $\phi = 145.0°$, $pb = -50.0$, $H_2 = 1.0$ and various λ. As with the downstream pinned case, as the flux is increased the upstream meniscus moves away from the inlet (the upstream pressure gradient remaining the same). The effect on the downstream region is to reduce the pressure gradient (at the outlet) and move the free surface further downstream.

Pressure profiles for the conditions $\lambda = 0.60$, $Ca = 0.05$, $\phi = 145.0°$, $pb = -50.0$, $H_2 = 1.0$ and various α are shown in figure 5.21. Increasing α moves the downstream meniscus further upstream and reduces the pressure gradient at the outlet. The upstream pressure gradient remains the same and the meniscus moves marginally towards the inlet.

Figure 5.22 shows pressure profiles for various Ca with $\alpha = 0.05$, $\lambda = 0.60$, $\phi = 145.0°$, $pb = -50.0$, $H_2 = 1.00$. Note that Ca has no effect on the pressure gradient in the upstream or downstream regions (as already shown using lubrication theory). However, decreasing Ca does move the downstream meniscus away from the inlet which, in turn, gives rise to an increased pressure gradient at the outlet. In fact, for $Ca = 2.00$ there is a negative pressure gradient at the outlet whereas for $Ca = 0.04$ the gradient is positive there. The effect of reducing Ca on the upstream region is to move the meniscus towards the inlet (due to a reduction in the capillary pressure at the downstream free surface, as in the pinned case).

The effect of the variation of ϕ on the pressure profile is shown in figure 5.23 for $\alpha = 0.05$, $\lambda = 0.60$, $Ca = 0.05$, $pb = -50.0$ and $H_2 = 1.00$. As with the capillary number, the downstream static contact angle, ϕ, has no effect on the pressure gradient in the upstream or downstream regions. However, decreasing ϕ causes the downstream meniscus to move further downstream (away from the inlet), thus again giving rise to an increased pressure gradient at the outlet. This change can be very significant e.g. for $\phi = 140.0°$ the pressure gradient at the outlet is positive, whereas for $\phi = 160.0°$ it is negative. The only effect of decreasing ϕ on the upstream region is to move the upstream meniscus marginally further towards the inlet. This is again due to a decrease in the capillary pressure at the downstream meniscus.

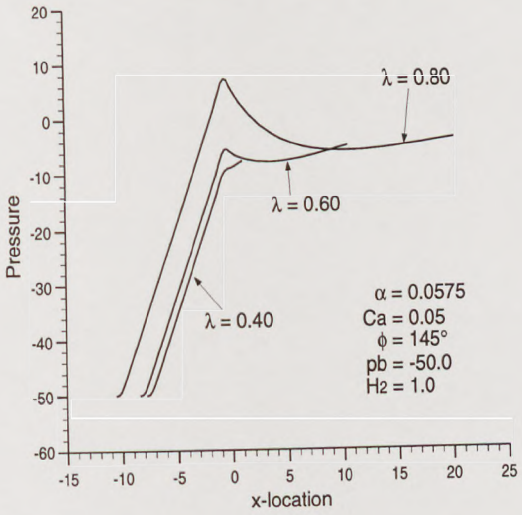

Figure 5.20: Pressure profiles for $\alpha = 0.0575$, $Ca = 0.05$, $\phi = 145.0°$, $pb = -50.0$, $H_2 = 1.00$ and various λ.

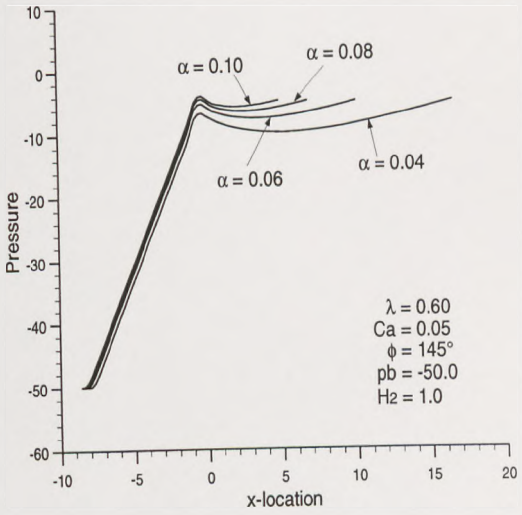

Figure 5.21: Pressure profiles for $\lambda = 0.60$, $Ca = 0.05$, $\phi = 145.0°$, $pb = -50.0$, $H_2 = 1.00$ and various α.

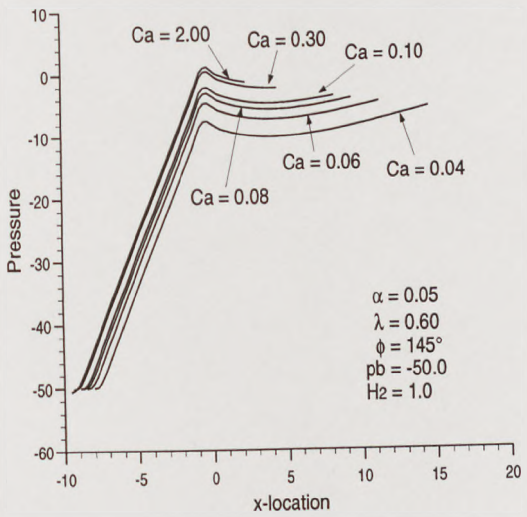

Figure 5.22: Pressure profiles for $\alpha = 0.05$, $\lambda = 0.60$, $\phi = 145.0°$, $pb = -50.0$, $H_2 = 1.00$ and various Ca.

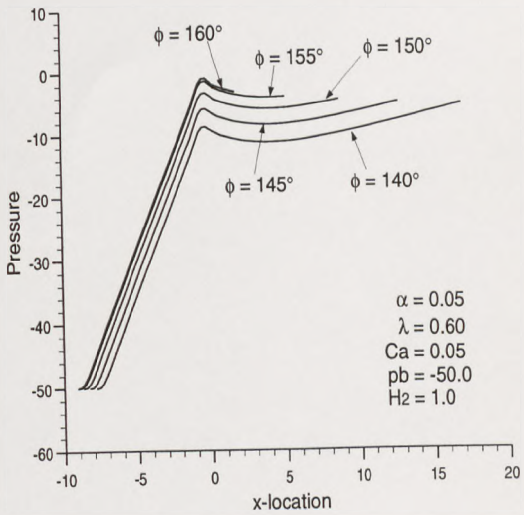

Figure 5.23: Pressure profiles for $\alpha = 0.05$, $\lambda = 0.60$, $Ca = 0.05$, $pb = -50.0$, $H_2 = 1.00$ and various ϕ.

5.3 Finite element stability analysis

The finite element linear stability analysis described in chapter 2 is now applied to the slot coating problem with an unpinned downstream meniscus. Using the grid described above there are now 4846 degrees of freedom (as opposed to 3412 freedoms with the 2-dimensional base flow). For each wavenumber, N, (and set of base flow, fluid and geometry parameters) an eigenvalue, Σ, is produced to indicate the stability. If, for a given base flow, the eigenvalue is negative for each wavenumber the base flow is stable. If one or more of the eigenvalues is positive then the base flow is unstable to the disturbance and ribbing appears. The following figures, 5.24-5.27, show such plots of eigenvalue against wavenumber as parameters vary.

Figure 5.24 shows a plot of the eigenvalue against wavenumber for various λ with $\alpha = 0.0575$, $Ca = 0.05$ $\phi = 145°$, $pb = -50.0$ and $H_2 = 1.00$. For $\lambda = 0.80$ the eigenvalue is negative for all wavenumbers and so the disturbance decays and the base flow is stable. A critical flux, $\lambda*$, exists ($\lambda = 0.60$) for which $\frac{d\Sigma}{dN} = \Sigma = 0$ for a particular value of N and $\Sigma < 0$ for all other N. The base flow is therefore 'neutrally stable' and all flows for which $\lambda < \lambda*$ are unstable. $\lambda = 0.40$ is an example of such an unstable base flow since $\Sigma > 0$ for N in the range $0.16 < N < 0.34$. The base flow is stable to disturbances with wavenumber $N < 0.16$ and $N > 0.34$ (as $\Sigma < 0$ for all such values of N).

The effect of the variation of α on the stability of the base flow is shown in figure 5.25 for $\lambda = 0.60$, $Ca = 0.05$ $\phi = 145.0°$, $pb = -50.0$ and $H_2 = 1.00$. Increasing the downstream lip angle has a stabilising effect and a critical α, $\alpha*$, exists such that the base flow is stable for $\alpha > \alpha*$ and unstable for $\alpha < \alpha*$.

Figure 5.26 shows the a plot of eigenvalue against wavenumber for various downstream static contact angles, ϕ, with $\lambda = 0.60$, $\alpha = 0.0575$, $Ca = 0.05$, $pb = -50.0$ and $H_2 = 1.00$. Increasing ϕ clearly has a stabilising effect and a critical ϕ, $\phi*$, exists such that the base flow is stable if $\phi > \phi*$ and unstable if $\phi < \phi*$.

Plots of eigenvalue against wavenumber for various Ca are shown in figure 5.27 for $\lambda = 0.60$, $\alpha = 0.05$ $\phi = 145.0°$, $pb = -50.0$ and $H_2 = 1.00$. Increasing Ca has a stabilising effect and a critical Ca, $Ca*$, exists such that the base flow is stable if $Ca > Ca*$ and unstable if $Ca < Ca*$. For the above conditions, $Ca* = 0.08$. This is opposite to the effect of increasing Ca in forward and reverse roll coating where increasing Ca

destabilises the downstream free surface to ribbing (see chapters 3 and 4).

Note that changing H_2, β and pb had no effect on the eigenvalue plots and consequently no effect on the stability of the downstream interface.

These results could be qualitatively predicted by using a stability hypothesis (S.H.), as described in chapters 1, 3 and 4. This theory gives a simple condition to be applied at the downstream interface for its stability, namely

$$\frac{T}{r_d^2}\frac{dr_d}{dx} > \left(\frac{dp}{dx}\right)_d^R, \tag{5.20}$$

where $(dp/dx)^R$ is given by equation (5.9), r_d is the radius of curvature of the downstream meniscus and T the surface tension of the fluid. If the pressure profiles in figures 5.20-5.23 are re-examined, it is clear that increasing λ, α, Ca and ϕ all reduce the pressure gradient at the outlet and so by using (5.20), their effect on the stability of the flow could be predicted. Once again, this illustrates the significance of the stability hypothesis in giving insight into the various mechanisms which affect the stability of an interface.

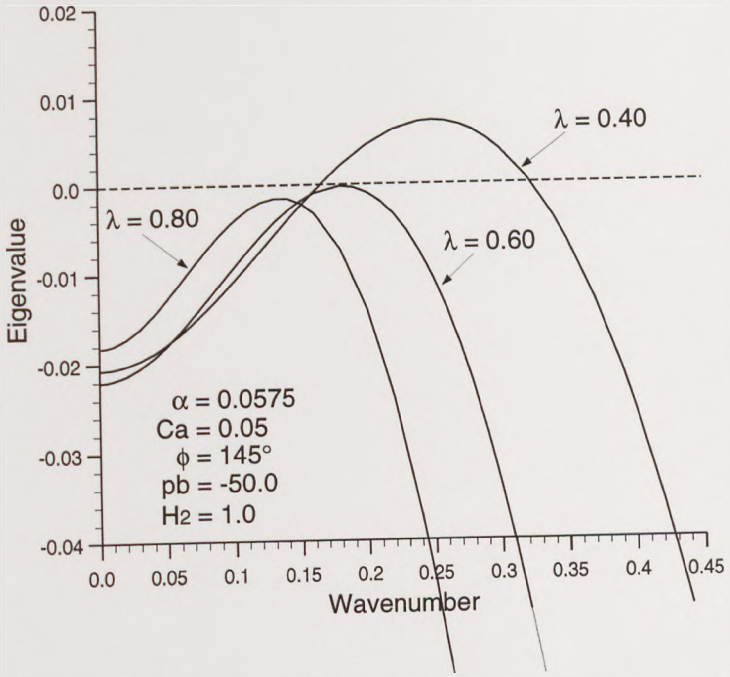

Figure 5.24: Growth rate (eigenvalue) against wavenumber for various λ with $\alpha = 0.0575$, $Ca = 0.05$ $\phi = 145^o$, $pb = -50.0$ and $H_2 = 1.00$.

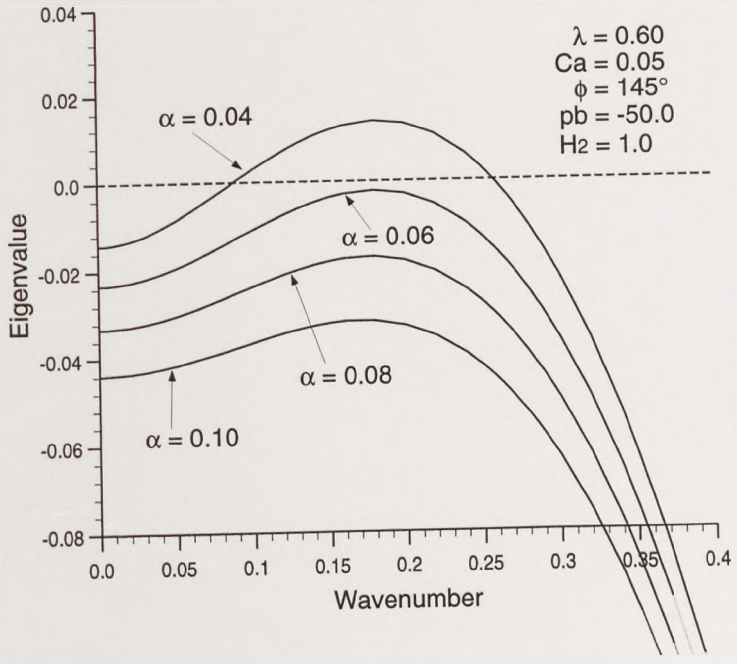

Figure 5.25: Growth rate (eigenvalue) against wavenumber for various α with $\lambda = 0.60$, $Ca = 0.05$ $\phi = 145.0^o$, $pb = -50.0$ and $H_2 = 1.00$.

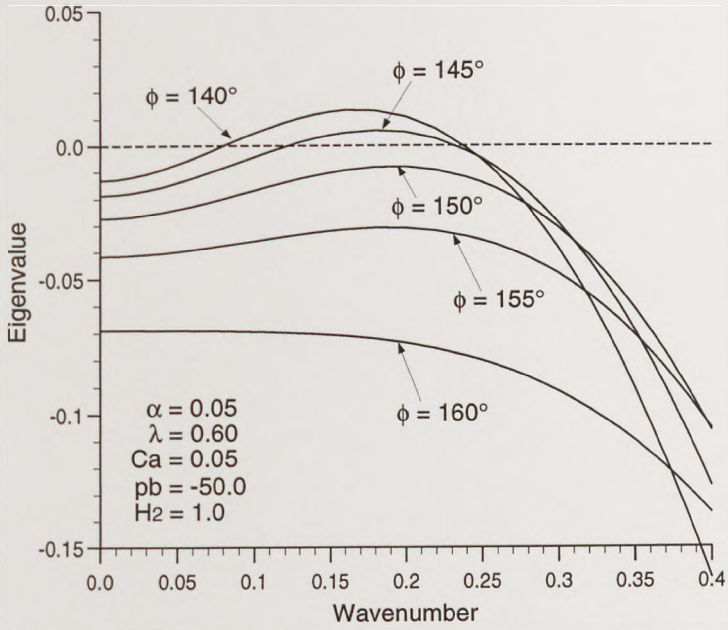

Figure 5.26: Growth rate (eigenvalue) against wavenumber for various ϕ with $\lambda = 0.60$, $\alpha = 0.0575$, $Ca = 0.05$, $pb = -50.0$ and $H_2 = 1.00$.

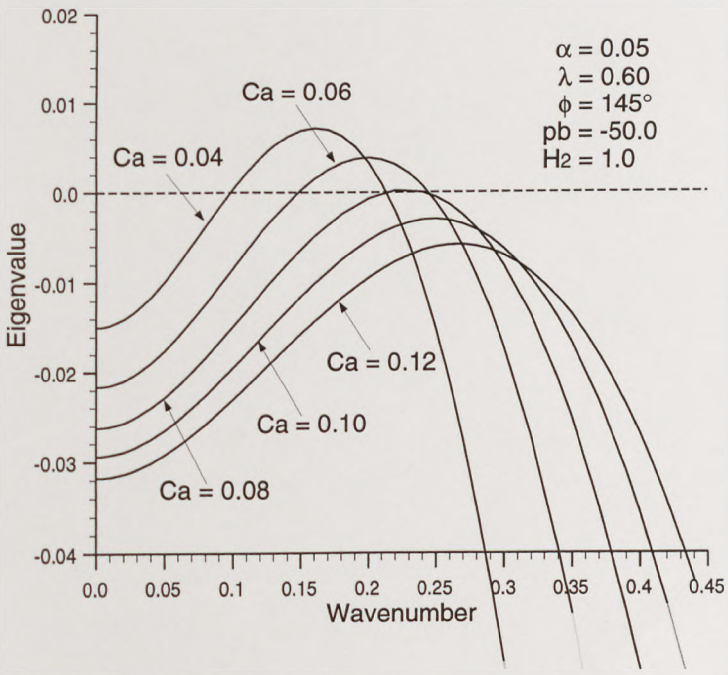

Figure 5.27: Growth rate (eigenvalue) against wavenumber for various Ca with $\lambda = 0.60$, $\alpha = 0.05$ $\phi = 145.0°$, $pb = -50.0$ and $H_2 = 1.00$.

5.4 Conclusions

In this chapter a finite element code has been used to analyse the two free surface, slot coating problem with a pinned downstream. The results show how the pressure profile and upstream meniscus location are affected by the various fluid and geometrical parameters. These numerical results are then compared with predictions obtained analytically using a model based on lubrication theory and, as with reverse and forward roll coating (chapters 3 and 4 respectively), lubrication theory is seen to accurately model the flow and accurately predict the upstream meniscus location and pressure profile.

Experiments by Kapur [1998], which show that ribbing cannot occur when the downstream wetting line is pinned, prompted the numerical investigation of the unpinned case. The effect of the various fluid and geometrical parameters is considered on the pressure profiles, on both the upstream and downstream meniscus locations and on the stability of the downstream free surface (using the linear stability theory described in chapter 2).

In summary, it is found that:

- Changing H_2, β and pb have no effect on the stability of the downstream interface.
- Increasing the flux (λ), the downstream lip angle (α), the downstream static contact angle (ϕ) and the capillary number (Ca) all promote the stability of the interface (for the parameters used).
- These results are in accord with predictions from the stability hypothesis.

Chapter 6

Conclusions

Contents

6.1 General review 193

6.2 Suggestions for future work 196

6.1 General review

The aim of this chapter is to review the work contained in this thesis and provide suggestions for future work.

In chapter 1, coating flows were introduced and features common to them all, namely contact lines and free surfaces, described. A review of the relevant literature was presented with particular reference to reverse, forward and slot coating flows together with the types of instabilities that occur in practice which limit their use to certain regions of parameter space. Various numerical methods capable of solving such free surface flows were outlined in chapter 2, including a thorough description of the finite element formulation using the method of weighted residuals. The particular form used throughout this thesis is more commonly known as Galerkin's method, where the weighting functions are the same as the interpolation functions used to approximate the dependent variables. A numerical technique based on linear stability theory for analysing the stability of these flows was then described, the case of zero Reynolds number (which is relevant to this thesis) being examined in detail.

Chapter 3 concerned an investigation of the ribbing instability in inlet flooded, reverse roll coating. By considering a 3-dimensional perturbation to a 2-dimensional base flow modelled using lubrication theory, regions of instability in the $Ca - S$ control space were established and found to be in accordance with experimental observation. For each h_0/R, there is a maximum value of Ca, Ca^{max}, below which the flow is stable for all values of speed ratio, S. For $Ca > Ca^{max}$, increasing S has a stabilising effect and it was shown that for particular values of S, there are two ranges of Ca for which the base flow is stable (separated by an unstable range). For each Ca, there was also shown to to be a speed ratio beyond which no ribs occur (and a particular value of S, S^{min}, such that no ribbing occurs if $S > S^{min}$ for any Ca). As h_0/R is increased, the region of stability increases such that S^{min} decreases and Ca^{max} increases.

Results obtained using this linear stability analysis were then compared with predictions from a stability hypothesis, that is a simple, 2-dimensional, force balance argument to determine the stability of the flow. Using this simple theory, it was shown that the effect of the various parameters on the stability of the downstream free surface can be ascertained by examining their influence on the pressure gradient there and the meniscus location. This stability hypothesis was also shown only to be sufficient for predicting stability and the agreement with the linear stability analysis improved with decreasing

h_0/R.

Results from the linear stability analysis were also compared to those obtained using the numerical methods outlined in chapter 2, from which it was seen that the analytical approach overpredicted the critical capillary number for the onset of instability.

A variation of inlet flooded, reverse roll coating was then examined in which the nip was fed from above by a large reservoir of fluid (i.e. by a hydrostatic head). Initially, using a model based on lubrication theory, the effect of the hydrostatic head on the base flow was examined from which it was seen that increasing the height of the head or Stokes number, St, increased the thickness of the final film and moved the meniscus further downstream. After applying linear stability theory to the base flow, the influence of gravity on the ribbing instability was determined again by means of critical curves in the $Ca - S$ control space. It was thus observed that at low St, increasing the height of the head had a stabilising influence whereas at high St it had a destabilising influence. The effect of increasing St was to destabilise the base flow.

Finally, an improved model of the dynamic contact line, developed by Shikhmurzaev [1993a], was described in which the dynamic contact angle was no longer kept constant, but became a function of various fluid and geometrical parameters. The limit of this theory for small capillary number was incorporated into the analytical model. Increasing the static contact angle, θ_s, was seen to have two effects, the first of which was to reduce S^{min} thus increasing the prospect of stability. However, increasing θ_s also reduces Ca^{max} which reduces the range of stability.

In chapter 4, instabilities in forward roll coating were investigated. As with the reverse roll coater described in chapter 3, the inlet flooded case was examined using linear stability analysis, a stability hypothesis and the numerical approach based on the finite element technique. It was seen that increasing both Ca and S have a destabilising effect whereas increasing h_0/R has a stabilising effect. This is unlike the reverse case, where increasing S has a stabilising effect. Again the stability hypothesis was sufficient only for predicting stability and the agreement with the linear stability analysis improves with decreasing h_0/R. However, it was seen that the numerical approach gave very good agreement with the analytical predictions for the onset of ribbing. This is in contrast to the reverse case, where the analytical approach overpredicts the critical capillary number, which the author attributes to the the presence of a dynamic contact

line. In particular, the main difference between the analytical and numerical modelling of the base flow for the reverse roll coater lies in the need to impose a slip condition in the numerics to avoid a stress singularity, whereas the analytical model does not include effects local to the wetting line and so is less accurate.

Inlet starved forward roll coating was then examined, in which the coater is fed by a film of non-dimensional thickness H_i. As with the inlet flooded case, the ribbing instability can still manifest on the downstream free surface and reducing H_i was seen to destabilise the flow to ribbing, a result obtained using the analytical linear stability approach. As with the flooded case, the downstream stability hypothesis underpredicts the critical capillary number for the onset of this instability.

Malone [1992] and then Gaskell *et al* [1998] noted from experiments the presence of an instability termed *bead break* in which increasing Ca and S moved the upstream menicus to the same side of the nip as the downstream before it accelerated rapidly to the downstream free surface, at which point the coating bead collapsed. This instability was verified analytically here using 3-dimensional linear stability theory, from which it was shown that reducing H_i also destabilises the flow to bead break. It was then shown that a stability hypothesis applied on the upstream free surface gives an accurate description of the stability there (unlike at the downstream free surface).

In chapter 5, the slot coating geometry was examined. This coating flow has many more geometrical parameters than forward and reverse roll coating and many experimentalists have noted that these parameters affect the size and shape of the coating window in which a defect free film can be produced. A geometrically flexible finite element code was written in order to describe the flow, for which it was possible to use various lip shapes and a roll of variable location and radius. Initially, as had always been the case in the past, the numerical mesh incorporated a pinned downstream wetting line and the effect of the various fluid and geometrical parameters on the pressure profiles and upstream meniscus locations were examined. These numerical results were seen to compare favourably with predictions obtained analytically using a model based on lubrication theory, in which the main source of error was the approximation to the pressure at the downstream free surface.

Sartor [1990] showed that the downstream wetting line did not always pin, but could also climb along the die shoulder or regress into the coating gap. This has been con-

firmed experimentally by Kapur [1998] who also noted that ribs could only occur when operating in the unpinned regime. This provided the motivation for a computational study of the case in which the downstream, static contact line had retreated from the lip edge towards the inlet. The pressure profiles and meniscus locations were compared with those in the downstream pinned case, and the numerical linear stability analysis (described in chapter 2) was then used to determine the effect of the many fluid and geometrical parameters on the stability of the downstream free surface. It was seen that changing H_2, β and pb did not influence the stability of the downstream free surface. However, increasing the flux, downstream lip angle, downstream static contact angle and capillary number all promoted the prospect of stability (over the parameter range explored). Note that the capillary number effect is opposite to that in forward and revere roll coating where increasing Ca has a destabilising effect.

To conclude, it was shown that, as with forward and reverse roll coating, many of the effects of the fluid and geometrical parameters on the stability of the downstream free surface could be predicted by examining their effect on the two terms (pressure gradient and surface tension/geometry terms) in the stability condition derived via a stability hypothesis.

6.2 Suggestions for future work

All the coating flows investigated in this thesis have been for the case of Newtonian fluids. However, many industrial applications involve non-Newtonian fluids and so their effects should be examined.

The linear stability theory applied to the various coating methods examined assumes that the effects of inertia can be neglected. For the analytical approach, this is because the base flows are modelled using lubrication theory. The numerical approach can be used to obtain steady state solutions for non-zero Reynolds number but the linear stability analysis then becomes much more involved, with increased difficulty in solving for the *leading* eigenvalues (which determine the stability) because of the presence of singular matrices and *infinite* eigenvalues (see chapter 2). However, although more computationally expensive, these inertia effects may become important in certain regions of parameter space and should be explored.

For the reverse roll coating problem in particular, it still remains to examine the stabil-

ity of the two free surface case. This will have an effect on the ribbing instability and also enable the bead break instability to manifest under certain operating conditions.

For the slot coating geometry, there are many possible geometries still to consider as well as the investigation of instabilities on the upstream free surface. This would require a new numerical mesh for the cases when the upstream free surface is pinned at the downstream edge of the upstream die lip and swells at the upstream edge. Also, there is considerable interest within the manufacturing community toward the use of two and more layer slot coating, the study of which provides the opportunity for several new areas of investigation - interfacial mixing, interfacial instability etc.

As discussed in chapter 1, all coating flows must contain a dynamic wetting line. In principal, this region can be modelled more accurately by including Shikhmurzaev's [1993a] full model, as opposed to the asymptotic theory (see chapter 3) or models which require the dynamic contact angle to be specified (see chapter 1). Including this model would make the dynamic contact angle and slip region dependent on all the hydrodynamic and geometrical parameters, a dependence which should be included in the numerical codes and examined.

Finally, to obtain a better understanding as to how instabilites form and develop, numerical, time dependent models should be formulated. This would also enable the parameters at which time-dependent instabilities occur to be determined e.g. for inlet flooded reverse roll coating, a time dependent instability known as *cascade* occurs at large S.

Appendix A

An examination of the force balance on a perturbed interface

From the downstream stability hypothesis used in chapters 3 and 4 it was determined that an approximate way to ascertain if the base flow is stable is to compare the capillary and fluid pressures at the meniscus; if the former dominate the latter then the flow is stable. However, it was shown that this force balance, which neglects curvature in the third dimension, is only a sufficient condition for predicting stability. The aim of this section is to investigate how accurately a 3-dimensional pressure balance predicts stability i.e. one which includes meniscus curvature in the $x-z$ plane which depends on each wavenumber, N. It is expected that for stable wavenumbers, i.e. those for which $\Sigma(N) < 0$, surface tension forces will dominate i.e. $g(D, N)$ will be positive.

Note that the following graphs are obtained using the linear stability analysis of inlet flooded reverse roll coating for $S = 0.500$ and $h_0/R = 10^{-4}$. The curves shown identify all qualitative changes in $g(D, N)$ and $\Sigma(N)$ for all S and h_0/R and are also typical of inlet flooded forward roll coating.

Figure A.1 ($Ca = 0.01 < Ca*$) shows an example of stability as $\Sigma < 0$ for all N. $g(D) > 0$ throughout the domain and so surface tension effects are dominating pressure gradient effects to give stability, as expected. Further, $g(D, N = 0) > 0$ and so the S.H. (i.e. the 2-dimensional force balance) also gives an accurate prediction of stability.

Figure A.2 ($Ca = 0.0193 < Ca*$) shows another example of stability as again, $\Sigma < 0$ for all N. However, $g(D, N = 0) = 0$ and $g(D) > 0$ for all other N. Hence the 3-dimensional force balance gives an unexpected result for $N = 0$, predicting neutral stability, but is as expected for all other N. Since $g(D, N = 0) = 0$, the S.H. predicts that the base flow is neutrally stable and so gives an inaccurate description of the stability.

For $0.0193 < Ca < Ca*$ (e.g. $Ca = 0.0260$ - see figure A.3), again $\Sigma < 0$ for all N. However, $g(D) < 0$ in the region AB and so, unexpectedly, stable wavelengths are present where pressure gradient forces dominate surface tension forces. Elsewhere, $g(D) > 0$ and so surface tension forces dominate pressure gradient forces as expected. Note that $g(D, N = 0) < 0$ and so the S.H. predicts that the base flow is unstable, an inaccurate description of the stability.

It can be proved that for $Ca** < Ca < Ca*$, where $Ca**$ is the critical capillary number predicted by the stability hypothesis, there is always one unexpected region of stable wavelengths for which pressure gradient effects dominate surface tension effects:

Proof:

*For $Ca** < Ca < Ca*$, $g(D, N = 0) < 0$ and $\Sigma < 0$ for all N. Therefore, as $g(D)$ is a monotonically increasing function (with N), there will be a value of $N = N_1$ for which $g(D) > 0$ for all $N > N_1$.*

□

Figure A.4 ($Ca = 0.0342 = Ca*$) is an example of neutral stability as $\frac{d\Sigma}{dN} = \Sigma = 0$ for a particular value of N, $N = 0.50$, and $\Sigma < 0$ for all other N. For $N > 0.76$, $g(D) > 0$ (as expected). However, for $N < 0.76$ (region AB), $g(D) < 0$ - an unexpected result as there is now a region of stable wavelengths for which pressure gradient forces dominate surface tension forces. Again, $g(D, N = 0) < 0$ and so the S.H. inaccurately predicts instability.

Figure A.5 ($Ca = 0.05 > Ca*$) shows an example of instability as $\Sigma > 0$ for some N. For all the unstable wavelengths (i.e. for $0.38 < N < 1.09$), $g(D) < 0$ and so pressure gradient effects are dominating surface tension effects as expected. For $N > 1.25$, $\Sigma < 0$ and $g(D) > 0$, again as expected. However for $N < 0.38$ (region AB) and $1.09 < N < 1.25$ (region CE), $\Sigma < 0$ and $g(D) < 0$ i.e. so there are now two unexpected regions of stable wavelengths for which the pressure gradient forces dominate the surface tension forces. Note that $g(D, N = 0) < 0$ and so the S.H. now gives an accurate description of the stability.

In fact, it can be proved that there are always two of these unexpected regions of

stable wavelengths when the base flow is unstable (i.e. when $Ca > Ca*$):

Proof:

It is first proved that $g(D)$ and $g'(D)$ always have the same sign (for $N \neq 0$): If $g(D)$ and $g'(D)$ did not always have the same sign then the graph of $g(X)$ would have a turning point (as $g(-\infty) = 0$). Since $\frac{dg}{dX} = 0$ at a turning point, (3.39) gives

$$\frac{d^2g}{dX^2} = 4\pi^2 N^2 g(X). \tag{A.1}$$

Supposing $g(X) > 0$ (at the turning point) then, via (A.1), $g''(X) > 0$ (at the turning point) and so the turning point is a minimum (assuming $N \neq 0$). However, as $g(-\infty) = 0$, a maximum must then also be present (which is not possible for $g(X) > 0$ as for a maximum, $g''(X) < 0$ thus contradicting (A.1)). Hence there can be no turning points (a similar argument applies if $g(X) < 0$ at the turning point).

Now if the linear stability analysis predicts instability (as in figure A.5), then $g(D, N = 0) < 0$. Hence at $N = 0$, both Σ and $g(D)$ are negative. On increasing N, there is a wavenumber at which $\Sigma = 0$ (point B). However, when $\Sigma = 0$, $g'(D) < 0$ (see equation (3.41)) and so (via the above proof) there is a region AB for which both Σ and $g(D)$ are negative.

At point C, $\Sigma = 0$, so again $g'(D) < 0$. As N increases, Σ will become negative and so a region CE will exist (again via the above proof) where both Σ and $g(D)$ are negative.

□

Hence it is clear that the simple idea of determining stability via a force balance is no more accurate for the 3-dimensional flow field than for the 2-dimensional flow field. For an accurate description of the stability it is necessary to carry out a linear stability analysis, although the 2-dimensional stability hypothesis remains a useful, insightful guide for determining the onset of instability.

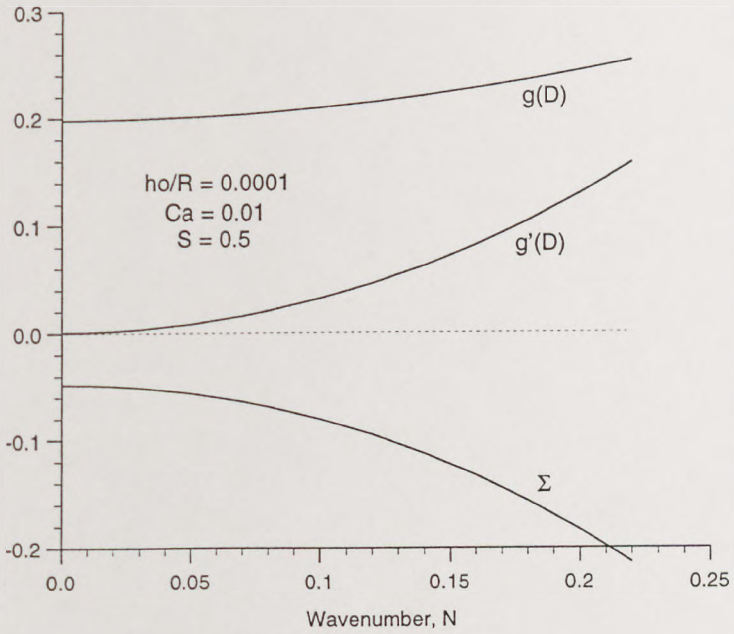

Figure A.1: Solution for the perturbed flow, showing Σ, $g(D)$ and $g'(D)$ against wavenumber (N) for $h_0/R = 10^{-4}$, $Ca = 0.01$ and $S = 0.5$.

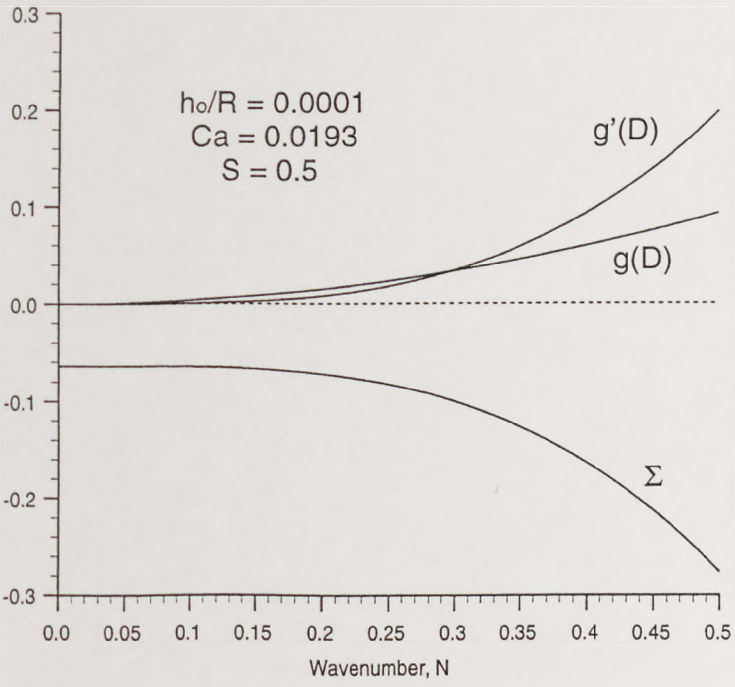

Figure A.2: Solution for the perturbed flow, showing Σ, $g(D)$ and $g'(D)$ against wavenumber (N) for $h_0/R = 10^{-4}$, $Ca = 0.0193$ and $S = 0.5$.

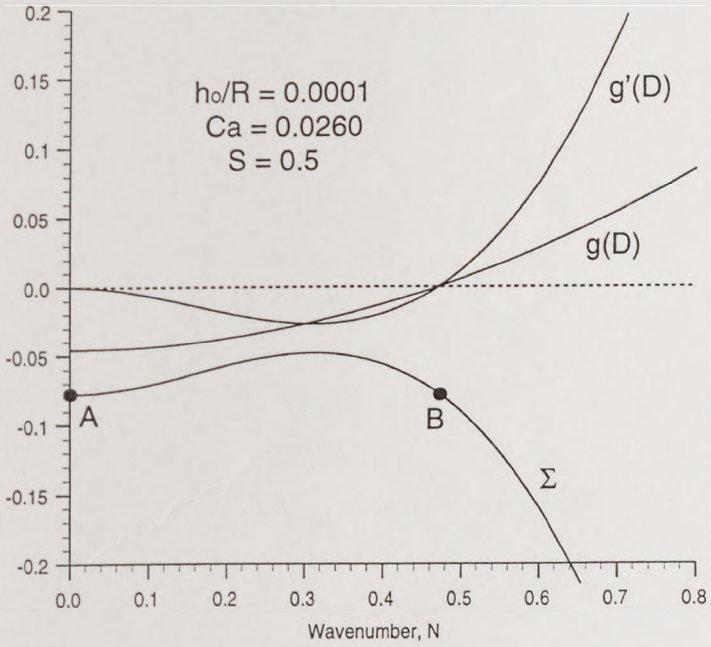

Figure A.3: Solution for the perturbed flow, showing Σ, $g(D)$ and $g'(D)$ against wavenumber (N) for $h_0/R = 10^{-4}$, $Ca = 0.0260$ and $S = 0.5$.

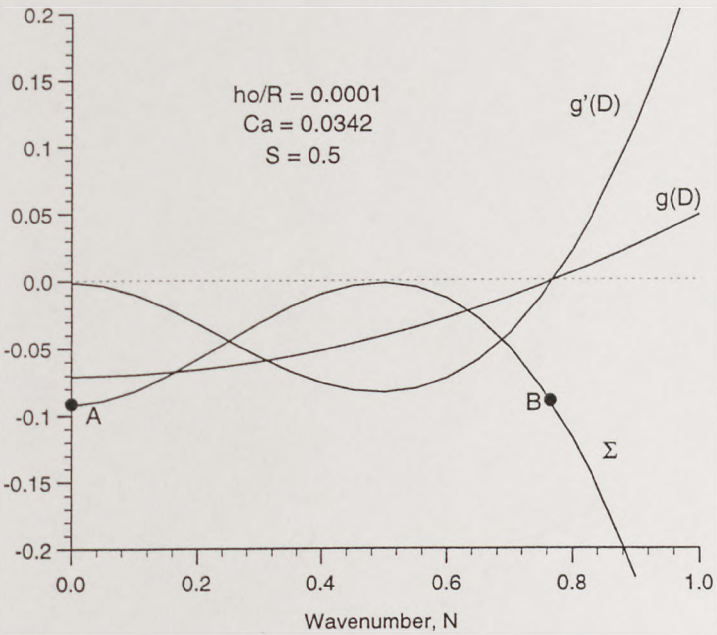

Figure A.4: Solution for the perturbed flow, showing Σ, $g(D)$ and $g'(D)$ against wavenumber (N) for $h_0/R = 10^{-4}$, $Ca = 0.00342$ and $S = 0.5$.

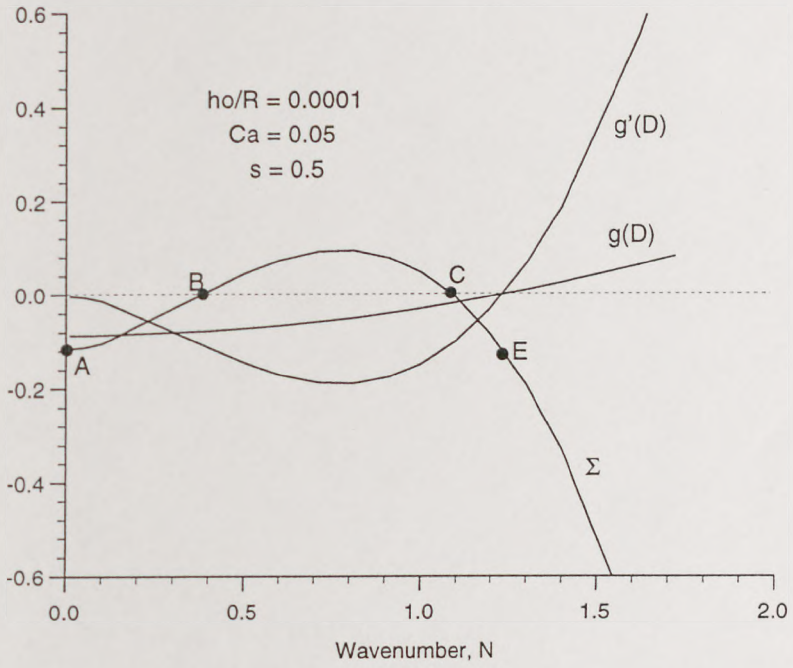

Figure A.5: Solution for the perturbed flow, showing Σ, $g(D)$ and $g'(D)$ against wavenumber (N) for $h_0/R = 10^{-4}$, $Ca = 0.05$ and $S = 0.5$.

References

ADACHI, K., TAMURA, T., NAKAMURA, R., "Coating flows in a nip region and various critical phenomena", AIChE Journal, Vol.34 No.3 pp.456-464 [1988]

AITKEN, J.G., UK paptent 957743 [1964]

AURIN, W., "Hot melt pressure sensitive adhesive coating equipment", in "Proceedings of the 1985 polymers, limitations and coating conference", pp.43-49 Atlanta Tappi [1985]

BABUSKA, I., AZIZ, A.K., "Lectures on the mathematical foundations of the finite element method", Mathematical foundations of the finite element method with applications to partial differential equations (Ed. Aziz, A.K.), Academic Press, New York, pp.1-135 [1972]

BATCHELOR, G.K., "An introduction to fluid dynamics", Camb.Univ.Press [1967]

BEGUIN, A.E., "Method of coating strip material", US patent 2681294 [1954]

BENKREIRA, H., EDWARDS, M.F., WILKINSON, W.L., "Roll coating of purely viscous liquids", Chem.Eng.Sci., Vol.36 pp.429-434 [1981]

BENKREIRA, H., EDWARDS, M.F., WILKINSON, W.L., "A Semi-empirical model of the forward roll coating flow of Newtonian fluids", Chem.Eng.Sci., Vol.36 pp.423-427 [1981]

BENKREIRA, H., EDWARDS, M.F., WILKINSON, W.L., "Mathematical modelling of the reverse and metering roll coating flow of Newtonian fluids", Chem.Eng.Sci., Vol.37 No.2 pp.277-282 [1982]

BENKREIRA, H., EDWARDS, M.F., WILKINSON, W.L., "Ribbing instability in the roll coating of Newtonian fluids", Plastics and rubber processing and applications Vol.2 No.2 pp.137-144 [1982]

BIRKHOFF, G., HAYS, D.F., "Free boundaries in partial lubrication", J.Math.Phys. (M.I.T.), Vol.42 No.2 [1963]

BIXLER, N.E., "Stability of a coating flow", PhD thesis, University of Minnesota, Minneapolis [1982]

BIXLER, N.E., SCRIVEN, L.E., "Downstream development of three-dimensional viscocapillary film flow", Ind.Eng.Chem.Res., Vol.26 pp.475-483 [1987]

BLAKE, T.D., RUSCHAK, K.J., "A maximum speed of wetting", Nature, Vol.282 pp.489-491 [1979]

BOOTH, G.L., "Coating equipment and processes", Lockwood publishing co., New York [1970]

BRETHERTON, F.P., "The motion of long bubbles in tubes", J.Fluid Dyn., Vol.10 pp.166-188 [1961]

BROUGHTON, G., EGAN, L.W., STURKEN, C., "The reverse roll principle of coating", Tappi Journal, Vol.33 No.7 pp.314-317 [1950]

BROWN, R.A., "On the multiple equilibrium shapes and stability of an interface pinned on a slot", J.Colloid and Interface Sci., Vol.78 No.2 [1980]

BRUYN, J.R., PAN, L., "Delayed onset of ribbing instability due to finite size effects", Phys. Fluids, Vol.7 No.9 [1995]

BURLEY, R., JOLLY, R.P.S., "Entrainment of air into liquids by a high speed continuous solid surface", Chem.Eng.Sci., Vol.39 pp.1357-1372 [1984]

BURLEY, R., KENNEDY, B.S., "An experimental study of air entrainment at a solid/liquid/gas interface", Chem.Eng.Sci., Vol.31 pp.901-911 [1976]

CAMERON, E., ALFRED, P., HILLS, R., "High speed coating apparatus", US patent 3413143 [1968]

CAMPBELL, D.F., "Slot orifice coating in 1980", in , "Proceedings of the paper synthetics conference", Cincinnati, Ohio pp.309-313, Atlanta Tappi [1980]

CARPENTER, J.K., STEEN, P.H., "Inertial effects in the fluid mechanics of planar-flow melt-spinning", in AIChE 1990 Spring National Meeting, Orlando, FL [1990]

CARTER, G.C., PhD thesis, University of Leeds [1985]

CARTER, G.C., SAVAGE, M.D., "Ribbing in a variable speed two-roll coater", Math.Engin.Ind., Vol.1 No.1 pp.83-95 [1987]

CARVALHO, M.S., SCRIVEN, L.E., "Deformable roll coating: modeling of steady flow in gaps and nips", 1st European Coating Symposium, Leeds [1995]

CARVALHO, M.S., SCRIVEN, L.E., "Deformable roll coating flows: steady state and linear perturbation analysis", J.Fluid Mech., Vol.339 pp.143-172 [1997]

CHENG, D.C.H., SAVAGE, M.D., "Onset of ribbing in direct rolling of Newtonian fluids", T.L.P. Report No.40, Warren Spring Laboratory, UK [1978]

CHRISTODOULOU, K.N., "Computational physics of slide coating flow", PhD thesis, University of Minnesota, Minneapolis [1990]

CHRISTODOULOU, K.N., SCRIVEN, L.E., "Finding leading modes of a viscous free surface flow: an asymmetric generalized eigenproblem", J.Sci.Comp., Vol.3 No.4 [1988]

COHEN, D., "Two-layer slot coating: flow visualization and modeling", M.S. Dissertation, University of Minnesota [1993]

COYLE, D.J., "The Fluid Mechanics of Roll Coating: Steady Flows, Stability, and Rheology", PhD Thesis, University of Minnesota, Minneapolis [1984]

COYLE, D.J., MACCOSKO, C.W., SCRIVEN, L.E., "Film-splitting flows in forward roll coating", J.Fluid Dyn., Vol.171 pp.183-207 [1986]

COYLE, D.J., MACCOSKO, C.W., SCRIVEN, L.E., "Film-splitting flows of shear-thinning liquids in forward roll coating", AIChE J., Vol.33 No.5 pp.741-746 [1987]

COYLE, D.J., MACCOSKO, C.W., SCRIVEN, L.E., "Stability of symmetric film-splitting between counter-rotating cylinders", J.Fluid Mech., Vol.216 pp.437-458 [1990]

COYLE, D.J., MACCOSKO, C.W., SCRIVEN, L.E., "The fluid dynamics of reverse roll coating", AIChE Journal, Vol.36 No.2 pp.161-174 [1990a]

COYLE, D.J., MACCOSKO, C.W., SCRIVEN, L.E., "A simple model of reverse roll coating", Ind.Eng.Chem.Res., Vol.29 pp.1416-1419 [1990b]

COYLE, D.J., MACCOSKO, C.W., SCRIVEN, L.E., "Reverse roll coating of non-Newtonian liquids", Journal of Rheology, Vol.34 No.5 pp.615-636 [1990c]

COYLE, D.J., "Roll Coating Processes",, , "An intoduction to coating and drying technology", [1991]

COYNE, J.C., ELROD, H.G., "An exact asymptotic solution for a separating film", J.Lub.Tech., pp.651-652 [1969]

COYNE, J.C., ELROD, H.G., "Conditions for the rupture of a lubricating film. Part 1: Theoretical model", J.Lubric.Technol., Vol.92 pp.451-456 [1970]

COYNE, J.C., ELROD, H.G., "Conditions for the rupture of a lubricating film. Part 2: New boundary conditions for the Reynolds equation", J.Lubric.Technol., Vol.92 pp.156-167 [1970]

DALMAZ, G., "Formation and separation of thin viscous film in Hertzian line contacts", J.Lub.Tech., Transactions of the ASME, Vol.102 pp.466-477 [1980]

DANIELS, N., GASKELL, P.H., SAVAGE, M.D., "The ribbing instability in reverse roll coating", Proceedings of the Second European Coating Symposium, Strasbourg, France (Ed. Bourgin, P.), pp.102-111 [1997]

DECRE, M., GAILLY, E., BUCHLIN, J.M., "Meniscus shape experiments in forward roll coating", Phys.Fluids, Vol.7 No.3 pp.458-467 [1995]

DECRE, M., GAILLY, E., BUCHLIN, J.M., "Meniscus control by string in roll coating experiment", AIChE Journal, Vol.42 No.6 pp.1583-1589 [1996]

DOWSON, D., TAYLOR, C.M., "Cavitation in bearings", Ann.Rev.Fluid Mech, Vol.11 pp.35-66 [1979]

DURST, F., WAGNER, H., "Liquid film coating", Ch11a, Chapman and Hall, UK [1997]

DUSSAN V, E.B., DAVIS, S.H., "On the motion of a fluid-fluid interface along a solid surface", J.Fluid Mech., Vol.65 part 1 pp.71-95 [1974]

DUSSAN V, E.B., "The moving contact line: the slip boundary condition", J.Fluid Mech., Vol.77 part 4 pp.665-684 [1976]

DUSSAN V, E.B., "On the spreading of liquids on solid surfaces: static and dynamic contact lines", Ann.Rev.Fluid Mech., Vol.11 pp.371-400 [1979]

ELLIOT, G.E.P., RIDDIFOLD, A.C., "Dynamic contact angles. Part 1: The effect of impressed motion", J.Colloid Int.Sci., Vol.23 pp.389-398 [1967]

FALL, C., "Surface ribbing of a thin viscous fluid film emerging from a spreader or roller", ASME Journal of Lubrication Technology, Vol.100 [1978]

FALL, C., "A theoretical model of striated film-rupture", Journal of Lubrication Technology, Vol.104 pp.164-167 [1982]

FALL, C., "A theoretical model of striated film-rupture applied to the cylinder plane", Journal of Tribology - Transactions of the ASME, Vol.107 pp.419-422 [1985]

FUKAZAWA, K., BENJAMIN, D.F., SCRIVEN, L.E., "Reverse roll coater model", poster presentation for AIChE, University of Minnesota, Minneapolis [1992]

GASKELL, P.H., Private communication [1990]

GASKELL, P.H., INNES, G.E., SAVAGE, M.D., "An experimental investigation of meniscus roll coating", J.Fluid Mech., Vol.355 pp.17-44 [1998]

GASKELL, P.H., KAPUR, N., SAVAGE, M.D., "Bead break instability", submitted to J.Fluid Mech. [1998]

GASKELL, P.H., KAPUR, N., THOMPSON, H.M., SAVAGE, M.D., ABBOTT, S., "Reservoir fed, reverse roll coating: a flow visualisation study", In preparation [1998]

GASKELL, P.H., LODGE, R.C., SAVAGE, M.D., "Experimental investigation of asymmetric transfer-jets, film splitting and flow rates in classical forward roll coating", Physics of Fluids [1996]

GASKELL, P.H., SAVAGE, M.D., SUMMERS, J.L., THOMPSON, H.M., "Modelling and analysis of meniscus roll coating", J.Fluid Mech., Vol.298 pp.113-137 [1995]

GASKELL, P.H., SAVAGE, M.D., THOMPSON, H.M., "Stagnation-saddle points and flow patterns in Stokes flow between contra-rotating cylinders", J.Fluid Mech., Vol.370 pp.221-247 [1998]

GIAVEDONI, M.D., SAITA, F.A., "Interfacial viscosity in viscous free surface flows. A sample case.", Ind.Eng.Chem.Res., Vol.31 pp.2222-2231 [1992]

GIAVEDONI, M.D., SAITA, F.A., "Differential pressure in slot coating - viscocapillary limit values versus computed predictions", Chem.Eng.Commun., Vol.125 pp.27-45 [1993]

GIBBS, J.W., "The scientific papers of J.Willard Gibbs. Volume 1: Thermodynamics", Dover reprint, Dover, New York pp.328 [1961]

GLAISTER, P., "A numerical scheme for steady-supercritical flows with boundary fitted coordinates", Int.J.Num.Methods for Heat and Fluid Flow, Vol.5 No.5 pp.923-931 [1995]

GOKHALE, V.V., "Bounds for region of ribbing instability in some free surface coating flows", Research laboratories, Eastman Kodak Company, Rochester, New York 14650 [1981]

GOLUB, G.H., VAN LOAN, C.F., "Matrix computations", John Hopkins University Press, Baltimore, Maryland [1983]

GRALD, E.W., CHAKRABARTI, M., SUBBIAH, S., "The spectral element method and its application to modelling coating flows", AIChE 7th Int.Coat.Proc.Sci.Tech.Symp. [1994]

GREENER, J., MIDDLEMAN, S., "A theory of roll coating of viscous and viscoelastic fluids", Polymer Eng. and Science, Vol.15 p.1 [1975]

GREENER, J., MIDDLEMAN, S., "Reverse roll coating of viscous and viscoelastic fluids", Ind.Eng.Chem.Fundam., Vol.20 pp.63-66 [1981]

GREENER, J., SULLIVAN, T., TURNER, B., MIDDLEMAN, S., "Ribbing instability of a 2 roll coater : Newtonian fluids", Chem.Eng.Commun., Vol.5 pp.73-83 [1983]

GURCAN, F., "Flow bifurcations in rectangular, lid-driven cavity flows", PhD thesis, University of Leeds [1996]

GURFINKEL CASTILLO, M.E., PATERA, A.T., "Three dimensional ribbing instability in symmetric forward-roll film-coating processes", J.Fluid Mech., Vol.335 pp.323-359 [1997]

GUTTOFF, E.B., KENDRICK, C.E., "Dynamic contact angles", AIChE J., Vol.28 pp.459-466 [1982]

HASEGAWA, T., SORIMACHI, K., "Wavelength and depth of ribbing in roll coating and its elimination", AIChE J., Vol.39 No.6 pp.935-945 [1993]

HENS, J., BOIY, L., "Operation of the bead of a pre-metered coating device", Numer.Eng.Sci., Vol.41 No.7 pp.1827-1831 [1986]

HIGGINS, D.G., "Coating methods - survey", Encyclopedia of Polym.Sci.Tech., Vol.3 pp.765 [1965]

HIGGINS, B.G., SCRIVEN, L.E., "Capillary pressure and viscous pressure drop set bounds on coating bead operability", Chem.Eng.Sci., Vol.35 pp.673-682 [1980]

HIGGINS, B.G., "Downstream development of two-dimensional viscocapillary film flow", Ind.Eng.CHem.Fundam., Vol.21 pp.168-173 [1982]

HIGGINS, B.G., BROWN, R.A., "Multiple equilibrium shapes of partially constrained menisci: A quasi-static mechanism for instability of a coating bead", Chem.Eng.Sci., Vol.39 No.9 pp.1339-1345 [1984]

HIRT, C.W., NICHOLS, B.D., "Volume of fluid (VOF) method for the dynamics of free boundaries", J.Comp.Phys., Vol.39 pp.201 [1981]

HIRT, C.W., CHEN, K.S., "Simulation of slide coating flows using a fixed grid and volume-of-fluid front-tracking technique", AIChE 8th International Coating Process Science and Technology Symposium, New Orleans, USA [1996]

HO, W.S., HOLLAND, F.A., "Between-rolls metering coating technique: A theoretical and experimental study", Tappi, Vol.61 No.2 pp.53-56 [1978]

HOOD, P., "Frontal solution program for unsymmetric matrices", Int.J.Numer.Meth.Eng., Vol.10 pp.379-399 [1976]

HOPKINS, M.R., "Viscous flow between rotating cylinders and a sheet moving between them", Brit.J.Appl.Phys., Vol.8 pp.442 [1957]

HUH, C., MASON, S.G., "The steady movement of a liquid meniscus in a capillary tube", J.Fluid Mech., Vol.81 pp.401 [1977]

HUH, C., SCRIVEN, L.E., "Hydrodynamic model of steady movement of a solid/liquid/fluid contact line", J.Colloid and Interface Sci., Vol.35 No.1 pp.85 [1971]

IRONS, B.M., "A fromtal solution program for finite element analysis", Int.J.Numer.Meth.Eng., Vol.2 pp.5-32 [1970]

ISAACSON, E., KELLER, H.B., "Analysis of numerical methods", Wiley, New York [1996]

KAGEYAMA, T., YOSHIDA, M., "Extrusion coating apparatus", US patent 2120132 [1986]

KANG, Y.T., LIU, T.J., "Minimum film thickness for reverse roll coating", Chem.Eng.Sci., Vol.46 No.11 pp.2958-2960 [1991]

KAPUR, N., Private communication [1998]

KAPUR, N., "Flow phenomena in fixed-gap and gravure roll coating systems", PhD thesis (to be submitted), University of Leeds [1998]

KELMANSON, M.A., "Boundary integral equation solution of viscous flows with free surfaces", J.Eng.Math., Vol.17 pp.329-343 [1983]

KISTLER, S.F., SCRIVEN, L.E., "Coating Flows", Computational analysis of polymer processing (Eds Pearson and Richardson), Applied Science Publishers, London and New York, pp.243 [1983]

KISTLER, S.F., SCRIVEN, L.E., "Coating flow theory by finite element and asymptotic analysis of the Navier-Stokes system", Int.J.Num.Methods in Fluids, Vol.4 pp.207-229 [1984]

KOCHUROVA, N.N., SHVECHENKOV, Y.A., RUSANOV, A.I., "Determination of the surface tension of water by the oscillating jet method", Colloid J. (USSR), Vol.36 pp.785 [1974]

LANDAU, L., LEVICH, B., "Dragging of a liquid by a moving plate", Acta Physicochimica URSS, Vol.XVII, No.1-2 pp.42 [1942]

LEE, R.L., GRESH, P.M., SANI,R .L., "Smoothing techniques for certain primitive variable solutions of the Navier-Stokes equations", Int.J.Numer.Meth.Eng., Vol.14 pp.1785-1804 [1979]

LEE, K., LIU, L., LIU, T., "Minimum wet thickness in extrusion slot coating", Chem.Eng.Sci., Vol.47 No.7 pp.1703-1713 [1992]

LIAO, S.J., CHWANG, A.T., "General boundary-element method for non-linear problems", Int.J.Num.Meth.Fluids, Vol.23 No.5 pp.467-483 [1996]

LIPPERT, H.G., "Slot die coating - a technical update on recent techniques and design developments", in , "1987 Polymers, limitation and coating conference book1", Atlanta Tappi [1987]

LODGE, R.C., Private communication [1994]

MALONE, B., "An experimental investiagtion of roll coating phenomena", PhD thesis, University of Leeds [1992]

MICHALLAND, S., "Etude des differents regimes dynamiques de l'instabilite de l'impremeur", Thesis L'Ecole Normale Superieure, Paris, France [1992]

MICHALLAND, S., RABAUD, M., COUDER, Y., "Instabilities of the upstream meniscus in directional viscous fingering", J.Fluid Mech., Vol.312 pp.125-148 [1996]

MOFFATT, H.K., "Viscous and resistive eddies near a sharp corner", J.Fluid Mech., Vol.18 [1964]

MILL, C.C., SOUTH, G.R., "Formation of ribs on rotating rollers", J.Fluid Mech., Vol.28 [1967]

MUNCH, C., "Process and apparatus for applying solutions", US patent 1847065 [1932]

NICKELL, R.E., TANNER, R.I., CASWELL, B., "The solution of viscous incompressible jet and free surface flows using finite element methods", J.Fluid Mech., Vol.65 part 1 pp.189-206 [1974]

NING, C., TSAI, C., LIU, T., "The effect of polymer additives on extrusion slot coating", Chem.Eng.Sci., Vol.51 No.12 pp.3289-3297 [1996]

O'BRIEN, W.G., "Beveled edge metered bead extrusion coating apparatus", US patent 4445458 [1984]

OLIVER, J.F., HUH, C., MASON, S.G., "Resistance to spreading of liquids by sharp edges", J.Colloid Interface Sci., Vol.59 No.3 pp.568-581 [1977]

PAN, L., DE BRUYN, J.R., "Spatially uniform travelling cellular patterns at a driven interface", Phys.Rev.E, Vol.49 pp.483-493 [1994]

PATERA, A.T., "A spectral element method for fluid dynamics: Laminar flow in a channel expansion", J.Comp.Phys., Vol.54 No.3 pp.468-488 [1984]

PEARSON, J.R.A., "The instability of uniform viscous flow under rollers and spreaders", J.Fluid Mech., Vol.7 [1960]

PITTS, E., GREILLER, J., "The flow of thin liquid films between rollers", J.Fluid Mech., Vol.61 [1961]

RABAUD, M., HAKIM, V., "Shape of stationary and travelling cells in the printer's instability", Instabilities and nonequilibrium structures III (ed. Tirapegui and Zeller), Klewer Academic, pp.217-223 [1991]

RABAUD, M., MICHALLAND, S., COUDER, Y., "Dynamical regimes of directional viscous fingering: spatiotemporal chaos and wave propagation", Phys.Rev.Lett., Vol.64 pp.184-187 [1990]

REES, S., Private communication [1993]

REES, S., PhD thesis, University of Leeds [1995]

REINELT, D.A., "Interface conditions for two-phase displacement in Hele-Shaw cells", J.Fluid Mech., Vol.183 pp.219-234 [1987]

REINELT, D.A., "The primary and inverse instabilities of directional viscous fingering", J.Fluid Mech., Vol.285 pp.303-327 [1995]

REYNOLDS, O., "On the theory of lubrication and its applications to Mr Beauchap Towers' experiments, including an experimental determination of the viscosity of olive oil", Phil.Trans.Roy.Soc.A, Vol.177 [1886]

RICHARDSON, C., "A theoretical investigation of reverse roll coating", PhD Thesis, University of Leeds [1996]

RICHARDSON, S., "A , "stick-slip", problem related to the motion of a free jet at low Reynolds numbers", Proc.Camb.Phil.Soc., Vol.67 pp.477-489 [1970]

ROWLINSON, J.S., WIDOM, B., "Molecular theory of capillarity", Clarendon Press, Oxford pp.174-181 [1982]

RUSCHAK, K.J., "Limiting flow in a pre-metered device", Chem.Eng.Sci., Vol.31 pp.1057-1060 [1976]

RUSCHAK, K.J., "Boundary conditions at a liquid/air interface in lubrication flows", J.Fluid Mech., Vol.119 pp.107-120 [1982]

RUSCHAK, K.J., "A 3D linear stability analysis for 2D free boundary flows by the finite element method", Computers and fluids, Vol.11 No.4 pp.391-401[1983]

RYSKIN, G., LEAL, L.G., "Numerical solution of free boundary problems in fluid mechanics. Part 1: The finite difference technique", J.Fluid Mech., Vol.148 pp.1-17 [1984]

SAITO, H., SCRIVEN, L.E., "Study of coating flow by the finite element method", J.Comput.Phys., Vol.42 pp.53-76 [1981]

SARTOR, L., "Slot coating: fluid mechanics and die design", PhD thesis, University of Minnesota, Minneapolis [1990]

SATAS, D., "Web processing and converting technology and equipment", Van Nostrand Reinhold, New York [1984]

SAVAGE, M.D., "Cavitation in Lubrication; Part 1. On boundary conditions and cavity-fluid interfaces; Part 2. Analysis of wavy interfaces", J.Fluid Mech., Vol.80 [1977]

SAVAGE, M.D., "Mathematical models for coating processes", J.Fluid Mech., Vol.117 pp.443-455 [1982]

SAVAGE, M.D., "Mathematical model for the onset of ribbing", AIChE Journal, Vol.30 No.6 pp.999-1001 [1984]

SAVAGE, M.D., "Meniscus instability and ribbing", Industrial Coating Research, Vol.2 pp.47-58 [1992]

SAVELSKI, M.J., SHETTY, S.A., KLOB, W.B., CERRO, R.L., "Flow patterns associated with the steady movement of a solid/liquid/fluid contact line", J.Colloid Int.Sci., Vol.176 pp.117-127 [1995]

SCHNEIDER, G.B., "Analysis of forces causing flow in roll coaters", Trans.Soc.Rheol., Vol.6 pp.209 [1962]

SCHWARTZ, A.M., TEJEDA, S.B., "Studies of dynamic contact angles on solids", J.Colloid Int.Sci., Vol.38 pp.359-375 [1972]

SCHWEIZER, P.M., "Visualisation of coating flows", J.Fluid Mech., Vol.193 pp.285-302 [1988]

SCHWEIZER, P.M., "Liquid film coating", Ch7, Chapman and Hall, UK [1997]

SHIKHMURZAEV, Y.D., "The moving contact line on a smooth solid surface", Int.J.Multiphase Flow, Vol.19 No.4 pp.589-610 [1993a]

SHIKHMURZAEV, Y.D., "A two-layer model of an interface between immiscible fluids", Physica A, Vol.192 pp.47-62 [1993b]

SHIKHMURZAEV, Y.D., "Mathematical modelling of wetting hydrodynamics", Fluid Dynamics Research, Vol.13 pp.45-64 [1994]

SHIKHMURZAEV, Y.D., "Dynamic contact angles and flow in the vicinity of moving contact line", AIChE Journal, Vol.42 No.3 pp.601-612 [1996]

SHIKHMURZAEV, Y.D., "Moving contact lines in liquid/liquid/solid systems", J.Fluid Mech., Vol.334 pp.211-249 [1997]

SILLIMAN, W.J., SCRIVEN, L.E., "Separation flow near a static contact line: Slip at a wall and shape of a free surface", J.Comput.Phys., Vol.34 pp.287-313 [1980]

STEIBER, W., "Das schwimmlager, hydrodynamische theorie des gleitlagers", Berlin V.D.I. [1933]

STEWART, G.W., "Introduction to Matrix Computations", Academic Press, New York [1973]

SUMMERS, J.L., Private communication [1995]

SUMMERS, J.L., GASKELL, P.H., THOMPSON, H.M., SAVAGE, M.D., "Transfer jets, flow structures and transformations in stokes flow between contra-rotating cylinders", In preparation [1998]

SWIFT, H.W., "The stability analysis of lubricating films in journal bearings", Proc.Inst.Civ.Engrs., Vol.223 pp.267 [1931]

TANNER, R.I., NICKELL, R.E., BILGER, R.W., "Finite element methods for the solution of some incompressible non-Newtonian fluid mechanics problems with free surfaces", Comput.Meth.Appl.Mech.Eng. Vol.6 pp.155-174 [1975]

TAYLOR, G.I., "Cavitation of a viscous fluid in narrow passages", J.Fluid Mech., Vol.16 pp.595-619 [1963]

THOMPSON, H.M., "A theoretical investigation of roll coating phenomena", PhD thesis, University of Leeds [1992]

WALKER, D.J., "A computational and theoretical investigation of slide and forward roll coating phenomena", PhD Thesis, University of Leeds [1995]

WANG, F.J., DOMOTO, G.A., "Free-surface Taylor vortices", J.Fluid Mech., Vol.261 pp.169-198 [1994]

WILSON, M., "Free surface flows between co-rotating and contra-rotating cylinders", PhD thesis, University of Leeds [1997]

YOUNG, T., "An essay on the cohesion of fluids", Phil.Trans.R.Soc.Lond., Vol.95 pp.65-87 [1805]

YU, W., LIU, T., "Reduction of the minimum wet thickness in extrusion slot coating", Chem.Eng.Sci., Vol.50 No.6 pp.917-920 [1995]

ZHOU, M.Y., SHENG, P., "Dynamics of immiscible fluid displacement in a capillary tube", Phys.Rev.Lett., Vol.64 pp.882-885 [1990]